Topics In Electron Dynamics In Moderate Magnetic Fields

A dissertation presented
by

Robert Ellis Frederick Parrott

to
The Department of Physics
in partial fulfillment of the requirements
for the degree of
Doctor of Philosophy
in the subject of

Physics

Harvard University
Cambridge, Massachusetts
May 2006

Thesis advisor
Professor Eric J. Heller

Author
Robert Ellis Frederick Parrott

Topics In Electron Dynamics In Moderate Magnetic Fields

Abstract

The dynamics of charged particles in moderate magnetic fields can present a theoretical challenge in many systems. Weak magnetic fields may break symmetries in a system, but the dynamics of the particle are usually only slightly perturbed. Alternatively if the field is very strong, the underlying system tends to become one dimensional, particularly in the case of the Quantum Hall Effect in mesoscopic systems, or plasma systems in strong magnetic fields, where the particles follow flux lines. In this thesis we consider systems where neither extreme holds.

The first Chapter analyzes high Rydberg antihydrogen states in a strong magnetic field, where the effect of the magnetic field can be as important as the Coulomb well. We find that the system can be considered in the center-of-mass coordinates with a conserved quantum number, the *pseudomomentum*. The states that are produced can be highly asymmetric, and when placed in an ionizing electric field, the dynamics complicated. We identify two extreme cases of the motion, and using classical simulations find a relation between an ionization field and transverse anti-atom size.

The next Chapter considers semiclassical dynamics of electrons in a large chaotic quantum dot in a perpendicular magnetic field. The device allows the conductance of the system to be probed in energy and magnetic field, and strong interference bands are identified in the (E, B) plane. We identify these bands as due to scarred states in the large dot, and connect the features of the bands to changes in the dynamics of periodic orbits in the system.

The last three Chapters extend the SPM tip imaging theory in 2DEGs to include more general tip imaging mechanisms. We consider how a realistic SPM tip scatters electrons classically, and then what type of fringe patterns such a deflection produces, deriving a formula that connects the scattering angle to the fringe pattern local to the tip. We then consider an SPM tip imaging of the magnetic focussing of electrons in a 2DEG, and characterize the results in terms of the novel effects of a soft weak tip on the electron flow.

Contents

Dedicated to Elisabeth

Citations to Previously Published Work

Large portions of Chapter 2 have appeared in the paper:

> "Strongly magnetized antihydrogen and its field ionization", D. Vrincineau, B.E. Granger, R. Parrott, H.R. Sadeghpour, L.S. Cederbaum, A. Mody, J. Tan, and G. Gabrielse, Phys. Rev. Lett. **92**, 133402-1 (April 2004).

Portions of Chapters 5 and 7 have appeared in the paper:

> "Imaging electrons in a magnetic field", K.E. Aidala, R.E. Parrott, E.J. Heller, and R.M. Westervelt. Physica E in press (available at http://arxiv.org/abs/cond-mat/0603035).

Chapter 1

Introduction and Summary

The work in this thesis concerns for the most part motion of electrons in a magnetic field, in a regime where the field is small enough that the system isn't highly degenerate, such as in the Quantum Hall effect, but where the effect of the magnetic field is more than just perturbative. In this regime the dynamics of particles can be very complex, and simpler analytic models can fail to have much predictive power. In addition a number of themes run throughout the thesis. Because of complexity of the dynamics involved with motion in moderate magnetic fields, much of the work in the thesis is numerical. This includes classical, semiclassical, and quantum approaches, the combination of which provides a more complete picture of the dynamics involved. The use of billiard models is a common theme; using analytic discrete maps allows one to manage the complexity of the magnetic dynamics in smooth potentials. The work focusses on experimental results and applicability, in collaboration with the Gabrielse, Marcus, and Westervelt groups at Harvard. And, being a very visual thinker, I rely heavily on figures and two-dimensional plots of theoretical results to convey the physics.

The thesis is structured into three main projects:

- Analysis of the ionization of antihydrogen in a strong magnetic field (Chapter 2),
- Modelling of the spectrometry of scarred states in a large quantum dot (Chapter 4), and
- Development of a more general model of SPM tip imaging processes, with application to experimental results in a magnetic focussing geometry ((Chapters 5, 6, and 7).

In addition we include a Chapter on wavepacket methods in magnetic fields which are utilized in Chapters (4) and (7), and we derive a novel Hamiltonian approach to the guiding center approximation in the Appendices.

Chapter 2: Ionization of Antihydrogen in Parallel Fields

Of significant interest in the understanding of antimatter is the production of stable antihydrogen at cold temperatures, so that its spectrum and fundamental properties can be observed and compared to normal hydrogen [38], using precise laser spectroscopy [116]. However, to do so, hot antiprotons and positrons must be cooled and allowed to bind in a matter free environment.

In the last few years, slowing of the antimatter has allowed the production and observation of antihydrogen at 4 K; this was first achieved by the ATHENA collaboration [32] by counting antiparticle annihilations over a relatively large region. In contrast, the ATRAP group observed the production of antihydrogen [29, 30] by allowing antiprotons to pass through plasma clouds of positrons [26], forming bound pairs. This required a special nested Penning trap technique [28] that allowed the hot positrons to cool to 4 K and form a single species plasma cloud in the Penning trap [13, 84]. The cooled plasma cloud was allowed to interact with a number of trapped antiprotons, and then a field was applied that would remove unbound antiprotons. A large ionizing field was then applied, and the number of antiprotons counted. This count indicated the number of antihydrogen atoms formed with extremely low background noise.

We begin by considering a model of a circular guiding center atom, where the transverse kinetic energy is completely wrapped up in the cyclotron motion, and decoupled from the axial motion. In this model, the motion of the particle is one-dimensional and axial, and parameterized by the transverse radius of the atom ρ_m; in the presence of an ionizing axial field,

$$H = \frac{mv_z^2}{2} - \frac{e^2}{\sqrt{z^2+\rho_m^2}} - eE_z z.$$

The axial well disappears at the radius

$$\rho_{m,max} = a\left(\frac{4}{27}\right)^{1/4}\frac{1}{\sqrt{E_z}}$$

providing a measure of the typical anti-atom size than can survive an ionizing field E_z.

Including the dynamics of the full two-particle system, the assumption of cylindircal symmetry cannot be made. However, one can identify a conserved quantity, the *pseudomomentum* K

$$\vec{K} = \dot{\vec{R}} - \frac{eB}{c}\vec{r}\times\hat{z}$$

which is a constant of the motion in uniform ionizing and magnetic fields. Utilizing this, we can parameterize the problem, and derive an effective potential in the center-of-mass system,

$$V = \frac{(\vec{K} + \frac{eB}{c}\vec{r}\times\hat{z})^2}{2M} + U(r) - eE_z z.$$

This enables the identification of ionization saddle points in the full system. This potential also allows for the possibility of stable bound states far from the Coulomb well, "giant dipole" states. An analysis of the experimental parameters and reasonable distributions of the displacement ρ of the anti-atom leads to an estimate for the experimental distribution of the pseudomomenta. In general the anti-atoms have $K < 1$ a.u. and are bound close to the Coulomb well; experimentally no stable giant dipole states are present. Simulations of the states reveal that for higher Rydberg states the anti-atoms are either cylindrical in nature, with nearly decoupled transverse and axial motions, or become fairly ergodic, with energy exchanged readily between the transverse and axial motions.

Classical simulations of anti-atoms in ionizing fields at varying K reveals that for small K, the guiding center model holds surprisingly well, even when angular momentum is not conserved. This indicates that for many configurations, there is an adiabatic invariant at play (this invariant is identified in the Appendices). For smaller radii and for increasing K values, the more ergodic, fully three-dimensional ionization saddle point becomes relevant. With increasing temperature, the effective anti-atom sizes will also shrink, but due to the rapid change in well depth of the Coulomb interaction, the decrease in anti-atom size is not large. The experimentally relevant anti-atom size versus ionizing field, as predicted by the guiding center and ergodic models, turns out to be within 20%, and the results of classical simulations lie in between the two extremes for relevant fields strengths and K values. This provides an experimentally relevant measure of the atom sizes produced in the ATRAP experiments.

Chapter 3: Mesoscopic Wavepackets

The use of wavepackets in quantum dynamics simulations has gained increasing popularity recently, spurred on by the increase in time resolved experimental techniques, or "femtochemistry" (see [41] for an overview). In the past, wavepackets have been used mostly as a pedagogical example, often to justify the use of time independent approaches in scattering theory [98]. However, the need of time resolved quantum simulations and their use in semiclassical approaches [48, 46, 60, 99, 70] has renewed interest in wavepacket approaches. Some measures of scars [47] even rely on wavepacket theory to define correlation functions in the system [54].

Wavepacket techniques have a number of advantages over time independent techniques, particularly in open systems. Time independent approaches dealing with open systems face difficulties in coupling to the continuum, and must use techniques such as R-matrix theory or a "self-energy" based on outgoing Green functions to couple to the continuum [21]. Because the wavefunction remains for the most part localized in space, wavepacket approaches avoid these difficulties. The problem of the continuum is elegantly dealt with by, for example, defining an absorbing region of the grid which attenuates amplitude as it enters. Resonances are naturally dealt with as well. In time independent theory, resonances are associated with complex energies, requiring specialized techniques like complex absorbing potential or complex scaling. In time dependent approaches, resonances arise naturally as long dwell times. The use of FFT and vectorized multiplication makes the codes very fast. And finally wavepacket results, being time dependent, provide an intuition that is lost in time independent approaches.

We consider wavepacket approaches in the context of mesoscopic systems. We show how to propagate wavepackets efficiently in magnetic fields, and how to construct absorbing boundary conditions to simulate the "black velvet" of the continuum. Flux into various areas can be calculated by measuring the amplitude and velocity across a flux surface, or by measuring the probability removed in some absorbing region. By tracking the history of these quantities we can extract the energy resolved flux (ERF) across a flux surface or into a "continuum" absorbing region. This allows us to calculate scattering coefficients for the system.

These approaches can be used to simulate the conductance through a system (see Chapter 4) directly, or can be used with a parameterically moved tip potential to simulate the imaging experiments performed in the Westervelt group (see Chapter 7). After laying out the theory of wavepacket propagation, we detail the simulation of an example system. Finally, we present some results of wavepacket tip scan simulations, to demonstrate the types of problems for which the method has been used.

Chapter 4: Spectroscopy of Scarred States in a Large Quantum Dot

Signs of classical chaos in mesoscopic systems, in particular quantum dots, have been observed in lateral quantum dots before [74, 73], as well as in resonant tunneling diodes [114, 81, 33, 34, 31]. Spectroscopic analysis is natural in resonant tunneling diodes [78, 80], while spectroscopy below the Fermi energy in quantum dots is a relatively recent development [90, 91], used in particular to study the correlation functions of the local density of states (LDOS) in the emitter [56, 75]. These studies used vertical quantum dots to probe the LDOS at the electrode wall. A very narrow resonance in the vertical dot was due to impurity-assisted tunneling mechanisms [97, 90], where an impurity between tunneling barriers in a quantum dot creates a narrow, isolated energy state that mediates most or all of the transmission through the system. However, the creation and use of a lateral single electron quantum dot, with a single sharp resonance, as a spectrometer is of significant interest for probing the transport of lateral devices at and below the Fermi sea.

Scarred wavefunctions [47, 54] are eigenfunctions of a system that are strongly influenced by classically unstable periodic orbits in the system. They usually have a spatial character reminiscent of the underlying classical periodic orbit. In addition, the scars usually are due to unstable orbits with a reasonably small Lyapunov exponent Γ, so that

$$\Gamma T \leq 1$$

where T is the period of the orbit.

Scars can play an important role in the spectra of atomic systems [85] and in the conductance of mesoscopic devices, such as lateral quantum dots [74]; in particular, scars have been shown to play a crucial role in resonant tunneling diodes [114, 79]. Some have even claimed (somewhat questionably) to have imaged scarred wavefunctions in billiards [19]. Often the observation of scars in a system is due to a bifurcation of some sort, where a classically stable orbit becomes unstable. The scar often contributes over a relatively small range of parameters, while the Lyapunov exponent is still relatively small. However, conductance mediated completely by scars has been seen [79] for resonant tunneling diode systems. As we shall see below, conductance mediated almost completely by scarring, as well as changes in the level of stability, may be seen in lateral quantum dot systems as well.

Inspired by some experimental results found in a study done by Dominik Zumbuhl in the Marcus group at Harvard, we study the dynamics of an electron in a large, leaky quantum dot [58, 57]. A lateral quantum dot device was fabricated that coupled a small spectrometer (in fact a small quantum dot) to a larger quantum dot, which was energized in such a way as to make a leaky, Fabry-Perot -like cavity in two dimensions. By “leaky”, we mean that the large dot has junctions to the leads that are open to many transverse modes, so that the an electron can enter or leave the large dot with relative ease. The small quantum dot acts as a device that could measure the local density of states LDOS(E, B) in the large dot at the tunnel junction. The small dot is a single electron dot, and can contain at most a single electron at any given time. Hence the small dot possesses a single narrow resonance at a specific energy E_R with a narrow line shape; this means that this small dot conducts appreciable current only over a narrow range of energies about E_R, and hence acts as a spectrometer. This feature of the small dot allows the experiment to run at large bias, and allows the current and hence the transmission through the system to be measured up to 1 meV below the Fermi sea, and hence to resolve the transmission of the system without the need to convolve over the Fermi function. While such devices had been created before [56] and used to measure the local density of states LDOS(E, B), this was performed in a vertical quantum dot, and did not possess any large scale interference structure.

The small and large dots were connected in series as a two-terminal device, with the tunnel junction between the two at the center, and the current through system was measured. The experimentally measured currents revealed bands of strong interference oscillations in energy versus perpendicular magnetic field, implying that the device was probing the effects of periodic orbits within the large quantum dot, and that as the energy or magnetic field was modified, the phase accumulated along the orbit changed rapidly, creating oscillations in the current.

In a toy model sense, the phase accumulated around the orbit due to the normal dynamics of the particle has a contribution from the energy $\phi_E = kL = \sqrt{2mE}L/\hbar$, where L is the length of the orbit, and from the flux enclosed by the orbit $\phi_B = qAB/\hbar$ where the area enclosed A has a directionality consistent with the "right-hand rule." The total phase is hence $\phi = \sqrt{2mE}L/\hbar + qAB/\hbar$ where we've ignored any topological phase. The interference bands should lie along lines of constant phase, and hence should have slope $\frac{dE}{dB} = -\frac{L}{2qA}\sqrt{\frac{2m}{E}}$. Linearizing, and asking over what distance in the parameters E or B we see a complete cycle in phase, we conclude that the band spacings are

$$\Delta E = \frac{h^2}{m\lambda L}$$

in energy, and in magnetic field

$$\Delta B = \frac{h}{qA}.$$

We begin by modelling the resonant quantum dot "spectroscope," and conclude that the main effect of the large dot, which acts as a Fabry-Perot cavity, is to modify the tunneling current as

$$I = \frac{2\eta}{1+\eta} I_o,$$

where I_o is the tunneling current if the large dot were removed (i.e. the tunneling current assuming a completely open emitter) and $\eta \equiv T/T_o$, the ratio between the transmission into the emitter with and without the large open quantum dot in place. With this approach we can focus on the spectrum LDOS(E, B) of the large quantum dot to determine the variations in the total tunneling current through the device.

We model the large quantum dot as a rectangular magnetic billiard to begin. This model does a surprisingly good job of reproducing the slope and spacing of the oscillations in the main interference band, and predicts some features of secondary bands. However, the model fails to predict the slope of the oscillations at low B field, the placement of bands, and why the main interference band is strongly attenuated below 50 milliTesla. This is because the billiard model does not adequately model the geometry of the tunnel junction region. In addition, we will show that the billiard orbits have the wrong stability.

We improve the accuracy of our approach by using a wavepacket simulation of the system, performed in an effective potential that is created using a DFT simulation [95] of the device from the gate geometry and voltages. These simulations reproduce the experimental result with remarkable accuracy, predicting all of the salient features of the system below 200 milliTesla. A small discrepancy in the oscillation spacing is consistent with a systematic error in the DFT model, which predicts a dot with a smaller area than in the real device. This has to do with how the device is cooled down with positive charge on the gates, which creates an image charge close to the 2DEG layer, and hence sharper features in the effective potential.

Since the wavepacket simulation reproduces well the experiment, we may conclude that the interference bands are a single-particle effect, and that the true effective potential has an important effect on the dynamics of the system. To determine how this is the case, we search for classical periodic orbits in the effective potential. We find that periodic orbits are present at all fields, but when we filter for only those orbits which are relatively short and penetrate well into the tunnel junction region, we find that the placement of the interference bands in B depend on the details of the dot potential. The tunnelling rate depends strongly on the overlap of the resonant wavefunction in the spectroscope and at the emitter wavefunction. The more deeply an orbit penetrates into the tunnel junction region, the stronger the interference band signal is.

The periodic orbits which contribute to the tunneling are almost all unstable, in part due once again to the geometry of the tunnel junction region. Thus the interference band signal is due to scars throughout the experimental range of the parameters. The dropout of an interference band is not due here to an increase in the Lyapunov exponent of the orbits, but instead to how they enter the tunnel junction region. To our knowledge, this is the first study that shows this, and it highlights the strong dependence of the tunneling current on the LDOS at the tunnel junction. The measurement is closer to a scanning tunneling microscopy measurement than to a resonant diode system in that sense.

In addition, a change in the slope of the main interference bands, present in both experiment and wavepacket simulation, is shown to be due not to the transition from stable to scarred states, but instead due to change in stability of the periodic orbits. A topological change in the relevant orbit at this B value is associated with a change from loxodromic (mixed stable and unstable) to hyperbolic (completely unstable) stability.

Chapters 5 and 6: Tip Scattering and Fringe Theory

The use of a scanning probe microscopy (SPM) tip to interact with electron flow has been shown over the past few years to be useful for imaging the electron flow through an open system. It has been used to image otherwise classical point-to-point electron flow in a weak magnetic field at low resolution [20], while at higher resolution it has more recently been used to image coherent electron flow, revealing remarkable classical branching effects and coherent fringes due to backscattering [101, 103, 100, 67, 68, 104].

These later experiments, mostly in the Westervelt group at Harvard, have had remarkable success in probing the coherent nature of the electron flow. The experimental setup is usually a two-terminal device, with a single source QPC [10, 111] on one side, and some open structure and the SPM tip on the other side. The signal in the experiment comes from the tip backscattering electrons back through the source QPC; thus the signal of interest is present in the reflectance R. Measuring the conductance G means that you are in effect measuring the transmission T, since by the Landauer-Büttiker formalism [64, 14, 21] the transmission $T = \frac{h}{2e^2}G$. Since the device is a two-terminal device, the unitarity relation $T = 1 - R$ holds. Thus by measuring the conductance you are also measuring the reflectance $R = 1 - \frac{h}{2e^2}G$, and hence the signal in the reflectance is available from conductance measurements.

This description of the setup implies a number of limitations. In general, to measure the reflectance R the system must be a two-terminal system, and thus the source and target QPCs must be colocated. Because of this, the imaging of electron flow in magnetic fields is possible only for very weak fields. The reliance on backscattering from the tip means that the tip potential must be well over the Fermi energy, and so weak deflections by the tip are not measurable in this setup. Thus the technique, while impressively useful for analyzing native electron flow in a $B = 0$ system, is not of general use. This motivates us to consider the feasibility more general tip scattering and fringing effects without these limitations. The results will be put to use here to interpret experimental imaging of the magnetic focussing setup [2, 110] and in a case in the old configuration where, because of geometry, the source and target QPCs may be considered as if they were at different locations.

We model the effective potential due to the SPM tip as a local radially symmetric potential "bump", which is monotonically decreasing from the center; the ratio of the potential maximum to the Fermi energy, $\eta \equiv V_o/E_F$, proves to be a useful parameter. We then develop the basic classical scattering theory of the electron off the bump, calculating as usual the scattering angle $\theta_{sc}(b)$, where b is the impact parameter. One can derive a transcendental equation for the location of the caustic structures in the flow created by the scattering potential; we calculate the caustics from this for attractive $\eta < 0$, weak repulsive $0 < \eta \leq 1$, and strongly repulsive $\eta > 1$ potentials, and characterize the asymptotics of the caustic in each case. For the attractive and weak repulsive cases, the scattering potential sheds asymptotically linear caustics. These converge to what appears to be a focussing point; in the attractive case, this focussing point is near a cusp. Treating the tip as a lens, which is consistent for the linear caustics, we derive the effective focal length of the tip,

$$f = -\tilde{b} \csc \tilde{\theta}$$

where $\tilde{b}$ is the impact parameter for which $\theta_{sc}(b)$ is a maximum, and $\tilde{\theta}$ is that maximum angle.

The lens approximation can be used to predict the effect on the caustic in a lensing system, and such a lensing system can be used to reduce flow diffusion over a bumpy potential background. We then consider quantum scattering, and finding the Born approximation inappropriate, evaluate the scattering system in the far-field by partial wave expansion. While such a partial wave expansion does reproduce the linear caustics, it fails to reproduce the shadowing effect of the tip in the forward direction seen classically. This implies that a near-field quantum or semiclassical scattering theory would be most appropriate.

Turning to semiclassical effects, we consider how the action $S(q, q'; E)$ of tip-deflected trajectory changes as the tip is moved slightly. Introducing a semiclassical "point tip" approximation, we can segment the trajectory action into two parts, and conclude that the gradient of the action $\nabla_{\vec{r}_{tip}} S = \vec{p}_1 - \vec{p}_2$. When we consider the fringing due to the change in phase of a single trajectory, beating against some fixed background amplitude, we find the fringe spacing is

$$\Delta r = \frac{\lambda}{2} \left| \csc \frac{\theta_{sc}}{2} \right|$$

while the fringes run perpendicular to the bisector of the incoming and outgoing angles. This result allows the local scattering process to be "read" off from the fringes. It also holds in weak to moderate magnetic fields without modification. This is a central result of the generalized fringe theory.

Another interesting result is that when the beating of a deflected trajectory versus a backscattered trajectory is strong enough in amplitude to be seen, fringes of spacing $\frac{\lambda}{2}|\sec \theta_{sc}/2|$ will run perpendicular to the other fringes, forming a checkerboard pattern. We then work out the fringe patterns from geometric considerations in a number of experimentally relevant cases. It is possible, using geometric considerations, to extract the tip position with respect to the actual scattering process; however, the mapping may not be one-to-one. Finally we analyze experimentally seen "elliptical fringes" using the results of the chapter, and find that the experiment and theory are quite consistent.

Chapter 7: Deflection Imaging of Magnetic Focussing

Imaging coherent electron flow in the absence of a magnetic field has been accomplished recently in the Westervelt group [101, 103, 100, 67, 68, 104] with significant new insights into the nature of the flow in two-dimensional electron gases (2DEG)s. However, these experimental configurations, because the source and target QPCs are colocated, are unable to image electron flow at anything but weak magnetic fields. While there has been an imaging study of electron flow between two separate QPCs in the presence of a weak magnetic field [20], the experiment was at low resolution and could not resolve coherent structure. Imaging has also been performed in the Quantum Hall regime [115, 94, 36], but the imaging mechanism is substantially different. Imaging techniques for coherent electron flow in moderate magnetic fields and open point-to-point geometries would be of use in designing future devices for spintronics and quantum information processing, and for measuring spin-orbit coupling and electron scattering.

In Chapter (7) we describe the imaging of coherent electron flow in the magnetic focussing geometry first used in metals [92, 105] and two decades later in 2DEGs [110]. This geometry has been used to measure electrons emitted from a quantum dot [37] and spin-polarized electrons resulting from strong spin-orbit coupling and birefringent reflection [88, 17]. The imaging process uses a deflecting scanning probe microscope (SPM) tip which doesn't backscatter and a three-terminal device, with a source and target QPC nearly 3 μm away, a new approach to imaging for Westervelt group experiments. We consider the system in the context of an experiment performed by Kathryn Aidala in the Westervelt group at Harvard. We will begin by describing the experimental setup and results, and discuss how the experiment is conceptually different from other experiments.

We will then develop the theory to be used to analyze the system, including classical, semiclassical, and quantum dynamics methods to simulate the tip scan process and to examine the flow of the electron in the system. While the magnetic focussing system has been considered theoretically before [110, 106, 107, 108], the inclusion of an SPM tip is new. The role of branching, seen in earlier works [101, 100, 103] continues to play a role in the determining the focussing peaks in the transmission as the magnetic fields is varies, $T(B)$. The classical caustics formed in the flow of electrons in a clean system give rise to the focussing peaks centered at fields

$$B_n = \frac{2\hbar k_F n}{eL}.$$

In the bumpy disordered case the same holds true, but the branching of the electron flow splits and shifts the focussing peak into many smaller peaks in general; at higher disorder the peaks cease to be discrete. At finite temperatures interference effects are negligible, and the structure of the focussing signal $T(B)$ is determined mainly by classical processes.

The tip scan process in the system we show to be strongly dependent on the particular shape and strength of the effective tip potential. In particular, the signal in the transmission is highly non-monotonic in the tip strength η: for some cases the signal is highest for a very weak tip. In addition the transmission signal varies little once the tip backscatters, $\eta > 1$.

There are consistent classical signals in the tip scan system: as a weak tip passes over nascently transmitted flow, the transmission is reduced, while bordering these regions there are strips where the tip deflects more new flow into the QPC than obstructs it. These patterns are present in both classical and quantum simulations. The scanning of a weak tip, attractive or repulsive, can use this effect to map the nascent transmitted flow in the system. It is important to point out that the

the tip will map only transmitted flow when used in this manner. This is different from the use of a backscattering tip to map the flow in two terminal systems at zero field [101, 100, 103].

Larger tip strengths will induce fringing, but in the clean system the fringing is often hard to discern from the classical signal and is easily washed out by thermal averaging. However, the branching due to smooth disorder present in realistic systems tends focus the flow into “bundles” of transmitted trajectories. By “bundle” we mean a small continuous neighborhood of trajectories in phase space that remains nearby to a central trajectory over the course of the flow to the target QPC. While these bundles aren’t necessarily the caustic branches seen previously, they do form discrete regions in phase space of transmitted trajectories. This bundling enhances fringing; each trajectory in the bundle accumulates nearly the same phase as it propagates through the system, and as such discretizes the amplitude into “bundles” as well. If we parameterize trajectories by their initial angle α, then the nascent semiclassical amplitude at the target QPC may be approximated

$$A_o = C \int d\alpha A(\alpha) e^{i\phi(\alpha)} \approx C \sum_{\text{traj } j} A_j e^{i\phi_j} \tag{1.1}$$

where C is some constant, and the sum is over the typical bundle trajectories j. Weak tips will diminish or remove one of the terms when placed over a bundle, lowering the transmission but not creating a tip position dependent interference effect (i.e fringe).

When a strong tip deflects flow into a new bundle (or bundles), this new discrete amplitude term is a function of tip position, $A'(\vec{r}_{tip})e^{i\phi(\vec{r}_{tip})}$. Varying the tip position will vary the phase of the bundle in accordance with the arguments in Chapter (6), where we now use the typical bundle trajectory, with the amplitude sum over nascent bundles serving as the background amplitude. The interference of the new bundle amplitude with the nascent amplitude produces the fringes we see. When these bundles happen to coincide, or nearly coincide with caustic branches, the response may be very large, and the fringe signal stronger than expected.

Lastly, we note that the varying of the tip strength can be used as a calibration for the system. By measuring the range of fringes seen, one can empirically derive a typical scattering function $\theta_{sc}(b)$ and use this to understand the effective tip potential. The flow direction determined from weak tip scattering, along with the fringe direction for stronger tips, can be used to calculate the wavelength of the electron. Finally, it may be possible to use the differential signal of alternating weak attractive and repulsive tips to gain further information about the electron flow density from the tip scan data.

Appendices

In the Appendices we describe the basic non-relativistic classical theory of particle motion in a strong magnetic field, particularly when the system is cylindrically symmetric about the direction of $\vec{B}$, and in addition for the case of bouncing ball motion along a wall. The aim is to develop some basic analytic and geometric results of the classical trajectories of electron in a magnetic fields, for use in other Chapters.

With a focus on the guiding center approximation [82], we begin in Appendix (B) by developing the theory in action-angle coordinates via a canonical transformation. Under the guiding center approximation, the cyclotron action and the orbital action are independently conserved, and such an analysis highlights this fact. The guiding center holds to be exact in a number of basic cases. This approach is useful for considering the classical mechanics of hydrogen atoms in high Rydberg states and relatively strong magnetic fields, particularly in the case where the effective atomic potential is cylindrically symmetric. In addition it is useful for considering the classical and quasiclassical motion of charged particles in a two-dimensional electron gas (2DEG), moving under the influence of a weak to moderate magnetic field.

By expressing the system via a canonical transformation to guiding center action-angle variables, we derive a Hamiltonian version of the guiding center approximation in Appendix (C), something rarely if ever seen in the Literature. The breakdown of the guiding center approximation can then be considered as the breakdown of this independence of orbital and cyclotron actions. The casting of the electron motion in terms of otherwise independently conserved actions provides a direct way of quantifying how the guiding center approximation breaks down, which is more difficult in Cartesian coordinates.

Lastly we consider such a guiding center type of motion, but in the presence of a billiard wall located at some position $y = b$ in Appendix (D). The wall breaks translational invariance in the y direction, but not the x-direction. The properties of such skipping orbits can be handled in a general way [51], but here we explicitly derive the needed relations for application to magnetic focussing tip scan systems in Chapter (7).

Chapter 2

Ionization of Antihydrogen in Parallel Fields

Of significant interest in the understanding of antimatter is the production of stable antihydrogen at cold temperatures, so that its spectrum and fundamental properties can be observed and compared to normal hydrogen [38] using precise laser spectroscopy [116]. However, to do so, hot antiprotons and positrons must be cooled and allowed to bind in a matter-free environment.

In the last few years, slowing of the antimatter has allowed the production and observation of antihydrogen at 4 K; this was first achieved by the ATHENA collaboration [32] by counting antiparticle annihilations over a relatively large region. In contrast, the ATRAP group observed the production of antihydrogen [29, 30] by allowing antiprotons to pass through plasma clouds of positrons [26], forming bound pairs. This required a special nested Penning trap technique [28] that allowed the hot positrons to cool to 4 K and form a single species plasma cloud in the Penning trap [13, 84]. The cooled plasma cloud was allowed to interact with a number of trapped antiprotons, and then a field was applied that would remove unbound antiprotons. A large ionizing field was then applied, and the number of antiprotons counted. This count indicated the number of antihydrogen atoms formed with extremely low background noise.

A schematic of the experimental setup is shown in Figure (2.1). The antihydrogen atoms are formed by allowing antiprotons to pass back and forth through a plasma of positrons held in place in the nested Penning trap. This formation process must be a three-body process [39, 42, 35] in order to conserve both energy and momentum. Once formed, the bound system is neutral and will drift within the center of the Penning trap at thermal velocities. These bound Rydberg atoms are qualitatively different from those produced by photon excitations from the ground state [71, 72] and studied theoretically [25, 18, 22] because they have a significantly higher angular momentum, and

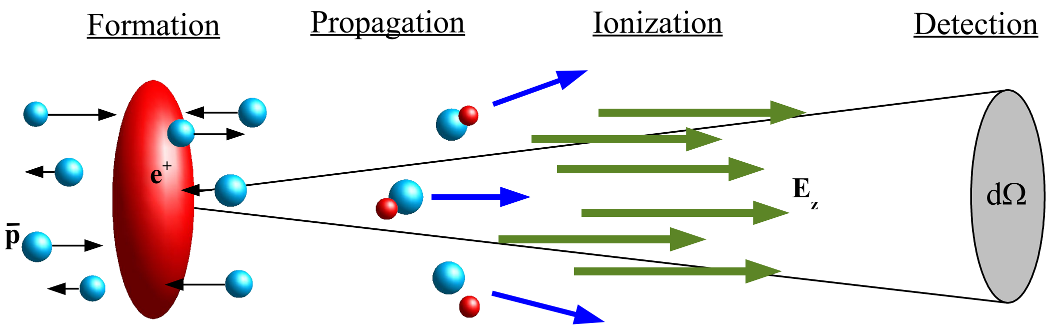

Figure 2.1: A schematic overview of the experimental setup used to observe antihydrogen production.

will usually have a significant drift motion across the magnetic field lines, creating strong effects due to electromotive forces. The atoms so produced may remain at an excited Rydberg state if unable to de-excite by collisions, or they may indeed de-excite to the ground state by diffusive collision [35] or by axial replacement collision [42].

A fraction of the anti-atoms will drift to the right in the figure, into a region of strong axial electric field. The bound system will not respond to this ionizing field and will continue drifting, but the internal motion will be modified. If the anti-atom is ionized, the antiproton will be accelerated towards a detector at the end of the trap. Stable anti-atoms will continue drifting with some transverse component of momentum, and will annihilate on the side walls of the detector with a negligible probability of reaching the detector. In this manner the system registers only bound atoms that were ionized by the axial field E_z.

This observation of antihydrogen at low temperatures in a Penning trap prompted work on estimating the size of the atoms observed [113]. The ATRAP results depend significantly on the final ionization field used, indicating that the ionization energy of the antihydrogen atom can be measured. However, these anti-atoms are confined by the strong magnetic field of the Penning trap ($\sim$ 5 Tesla), and thus do not ionize like normal atoms.

In this Chapter we explore the ionization of antihydrogen in strong magnetic fields, in particular how the size of the anti-atom relates to its ionization field. Once such a relationship is established, the antiproton production signal as a function of ionization field can be used to determine the size of the anti-atoms formed in the experiment. To begin, we model the anti-atom by assuming that the guiding center approximation holds; from this assumption we can derive a relation between the ionization energy and the smallest such circular guiding center atom that remains stable. Next we consider the full antihydrogen system in the Penning trap, and parameterize the Hamiltonian given known conserved quantum numbers, in particular the pseudomomentum K [23].

This allows us to derive a more general expression for the position of the ionization saddle point. We then determine the distribution of K as a function of the temperature, and use this to predict the experimental distribution. Finally we numerically simulate the ionization process for anti-atoms in different ionization fields, and determine the expected transverse size of the anti-atoms as a function of ionizing field.

2.1 Circular Guiding Center Model

We consider a model where we assume that the guiding center approximation (see Appendix C) holds, and external effects of the magnetic field are assumed to be cylindrically symmetric; we will call such atoms "Circular Guiding Center atoms", or GCA atoms. Such an atom is depicted in Figure (2.2a) and in Figure (C.1), and described in Section (C.5) in action-angle variables.

2.1.1 Effective 1D Model

Upon formation at a temperature T, the atom will have as a typical size the Thomson radius [40]

$$b = \frac{1}{kT}, \tag{2.1}$$

which at 4 K is $b \approx 4\ \mu$m. If the anti-atom is allowed to collide with other particles, the size may become smaller. The thermal positron will have typical cyclotron velocity $v_e = \sqrt{\frac{2kT}{m}}$ which implies a thermal cyclotron radius $r_c = \frac{c}{eB}\sqrt{2mkT}$. As a weak criterion, the radius of the anti-atoms $\rho \gg r_c$ for the guiding center approximation to hold. With the experimental temperature $T = 4$ K and field $B = 5.3$ Tesla, this implies a cyclotron radius $r_c = 10$ nm.

For a circular GCA atom, the guiding center assumption reduces the system to essentially two coordinates, the magnetron radius ρ_m and the axial position z, and we can find a relation between these values by using conservation of angular momentum and of energy. From Section (C.5) the GCA in this context implies that the cyclotron action $J_c = \frac{m\omega_c r_c^2}{2}$ is conserved. This is the same as the canonical angular momentum of the cyclotron motion, since it is conjugate to the cyclotron angle θ_c. Since the system is cylindrical, the total angular momentum, and hence $J = J_c + J_m$ is also conserved, hence so is $J_m = \frac{m\omega_m \rho_m^2}{2}$. With two invariant momenta in a 3D system, we can reduce the system to 1D. From equation (C.14), the magnetron frequency is

$$\omega_m = \frac{\alpha^2 e^2}{(z^2 + \rho_m^2)^{3/2}}.$$

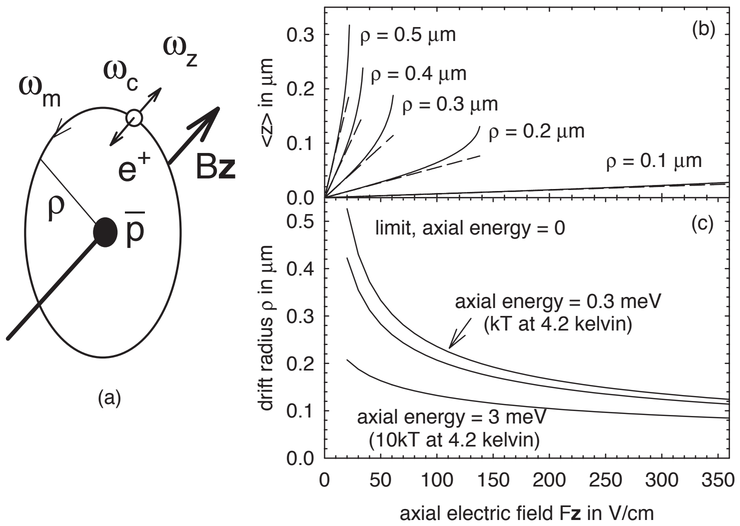

Figure 2.2: A circular guiding center anti-atom in (a) is polarized by an applied axial ionizing field. In (b) we approximate how the circular GCA atom is axially polarized and in (c) estimate the radius ionzied at the field E_z. From [113].

Near the axial center of the atom, $z \sim 0$ this implies

$$\omega_m \approx \frac{e^2}{m\omega_c\rho_m^3}. \tag{2.2}$$

The stable atom will oscillate axially as well as engage in magnetron motion; if we approximate the effective Lorentzian well, a Coulomb well at a finite displacement, as harmonic, the positron moves with frequency

$$\omega_z = \sqrt{\frac{e^2}{m\rho_m^3}} = \sqrt{\omega_c\omega_m}. \tag{2.3}$$

Referring back to the Hamiltonian for the GCA atom, equation (C.11), if the atom were formed with energy $\mathcal{E}_{z,o}$ at $z = 0$, then since each angular momentum is invariant, the problem reduces to a 1D problem axially, with available energy $\tilde{\mathcal{E}}_z = \mathcal{E}_{z,o} - e^2/\rho_m$

$$\tilde{\mathcal{E}}_z = \frac{mv_z^2}{2} - \frac{e^2}{\sqrt{z^2 + \rho_m^2}} \tag{2.4}$$

The system is effectively 1D under the GCA approximation; the cylindrical symmetry provided for one invariant, while the GCA provided the other.

2.1.2 Ionization

Now that we've reduced the system to 1D, we can ask what happens when an ionizing axial electric field E_z is applied. The potential with the ionizing field reads

$$V(\rho_m; z) = -\frac{e^2}{\sqrt{z^2 + \rho_m^2}} - eE_z z. \tag{2.5}$$

where V is parameterized by ρ_m. If the applied field is weak enough, and the atom cool enough that the axial well serves only to displace the local axial harmonic well, then we can solve for the new center of the harmonic well. This shifted well is $V' \approx \frac{m\omega_z^2 z^2}{2} - eE_z z$, with shifted minimum

$$z' = E_z \rho_m^3 / e$$

which implies a polarizability $\alpha \approx \rho_m^3$ where the polarization $ez' = \alpha E_z$. This is shown as the dotted lines in Figure (2.2b). A more careful consideration of the shift in the potential well in equation (2.4) yields the solid lines in Figure (2.2b). These are the solutions of the equation

$$E_z + \frac{ez}{(z^2 + \rho_m^2)^{3/2}} = 0.$$

For small $z \ll \rho_m$ this gives the previous expression for the new potential minimum.

A circular GCA atom can be bound only if there exists a local minimum in the potential. This implies that, for circular GCA atom with a radius ρ_m that one needs an ionizing field

$$E_z = \frac{2}{\rho_m^2 \sqrt{27}}$$

in order to remove a local minimum. Inverting, we have

$$\rho_{m,max} = a \left(\frac{4}{27}\right)^{1/4} \frac{1}{\sqrt{E_z}} \tag{2.6}$$

where $\left(\frac{4}{27}\right)^{1/4} \approx 0.62$ and a is a units conversion factor, $a = 1$ for a.u., while in S.I. $a = 3.975\ \mu\text{m}\sqrt{\text{V/cm}}$.

This expression relates the maximum transverse size for the circular GCA atom to the ionizing field at $T = 0$; it is the top curve in Figure (2.2c). At finite temperatures an atom of size ρ_m will ionize at weaker fields, hence the typical thermal atom will be smaller at the same field strength. The reduced maximum ρ_m versus E_z are shown for finite axial energies in Figure (2.2c). The positron energies will be thermal axially, and so one could predict a thermal distribution of sizes at a given ionizing field using such a measure.

2.2 Antihydrogen Hamiltonian

A neutral two-body system can not be separated in the presence of a magnetic field. However, there is a conserved quantum number in the presence of a uniform magnetic field, the *pseudomomentum* K [16, 5, 89, 23]. As the bound atom moves through the Penning trap, the pseudomomentum K will be conserved, along with the total energy E, assuming that the ionizing fields are changed slowly.

2.2.1 Pseudomomentum

Consider the system in uniform fields with a positively charged particle at position $\vec{r}_+$ and negatively charged at $\vec{r}_-$. Then the Hamiltonian reads, with uniform fields $\vec{E}$ and $\vec{B} = B\hat{z}$, a central potential $V(r)$, and in the symmetric gauge ($\vec{A} = \vec{B} \times \vec{r}/2$ or $A_\theta = rB/2$),

$$H = \frac{(\vec{p}_+ + \frac{eB}{2c}\vec{r}_+ \times \hat{z})^2}{2m_+} + \frac{(\vec{p}_- - \frac{eB}{2c}\vec{r}_- \times \hat{z})^2}{2m_-} + U(r) - e\vec{E} \cdot \vec{r} \tag{2.7}$$

where the relative coordinate is defined as $\vec{r} \equiv \vec{r}_+ - \vec{r}_-$. This leads to equations of motion

$$\begin{aligned} \dot{\vec{p}}_+ &= m_+\ddot{\vec{r}}_+ - \frac{eB}{2c}\dot{\vec{r}}_+ \times \hat{z} = -\vec{\nabla}_+ U(r) + e\vec{E} + \frac{eB}{2c}\dot{\vec{r}}_+ \times \hat{z} \\ \dot{\vec{p}}_- &= m_-\ddot{\vec{r}}_- + \frac{eB}{2c}\dot{\vec{r}}_- \times \hat{z} = -\vec{\nabla}_- U(r) - e\vec{E} - \frac{eB}{2c}\dot{\vec{r}}_- \times \hat{z}. \end{aligned} \tag{2.8}$$

Unlike the electrostatic case, the transverse part of the center of mass motion doesn't decouple; adding the momenta, we have $\dot{\vec{P}} = \frac{eB}{2c}\dot{\vec{r}} \times \hat{z}$, and

$$0 = M\ddot{\vec{R}} - \frac{eB}{c}\dot{\vec{r}} \times \hat{z}. \tag{2.9}$$

This implies that neither the center-of-mass canonical $\vec{p}$ nor kinetic $m\vec{v}$ momentum are conserved in this system, and hence that we cannot seprate the center-of-mass coordinates from the relative coordinates. We may define a momentum-like quantity, however, that is conserved in uniform fields for this neutral system, the *pseudomomentum* $\tilde{\vec{K}}$,

$$\begin{aligned} \tilde{\vec{K}} &\equiv M\dot{\vec{R}} - \frac{eB}{c}\vec{r} \times \hat{z} \\ &= \vec{P} - \frac{eB}{2c}\vec{r} \times \hat{z}. \end{aligned} \tag{2.10}$$

The $\tilde{\vec{K}}$ here will soon be redefined to incorporate the transverse electric field as well.

With a conserved quantity $\tilde{\vec{K}}$ we can perform a *pseudoseparation* [23] of the relative coordinates from the center-of-mass coordinates; in the full Hamiltonian, we may replace $M\dot{\vec{R}}$

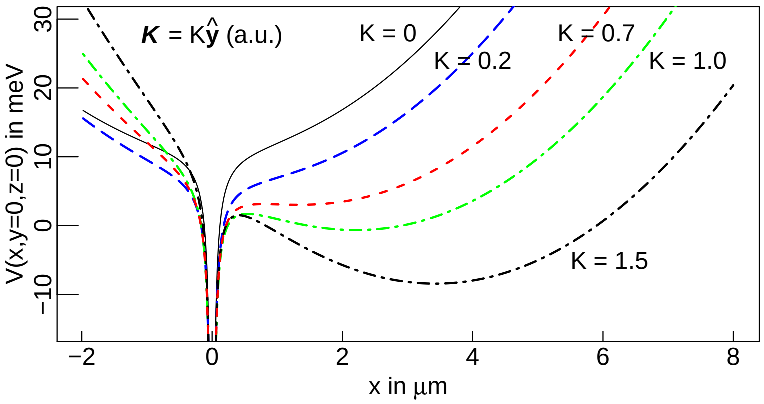

Figure 2.3: Slices of the pseudopotential $V(x, y = 0, z = 0)$ at different values of the pseudomomentum $\vec{K}$. When $K = 0$, then V is cylindrically symmetric. As K is increased, the potential develops another well at a distance $\rho_o = \frac{cK}{eB}$ along the x-axis.

by $\tilde{\vec{K}} + \frac{eB}{c}\vec{r} \times \hat{z}$ and in the process remove the center-of-mass coordinates explicitly from the Hamiltonian. Rearranging the kinetic energies in terms of the center-of-mass and relative momenta,

$$\begin{aligned} E_T = H &= \frac{M\dot{\vec{R}}^2}{2} + \frac{(\vec{p} + \frac{e\gamma B}{2c}\vec{r} \times \hat{z})^2}{2\mu} + U(r) - e\vec{E} \cdot \vec{r} \\ &= \frac{(\tilde{\vec{K}} + \frac{eB}{c}\vec{r} \times \hat{z})^2}{2M} + \frac{(\vec{p} + \frac{e\gamma B}{2c}\vec{r} \times \hat{z})^2}{2\mu} + U(r) - e\vec{E} \cdot \vec{r} \end{aligned} \tag{2.11}$$

where we've defined the total mass $M \equiv m_+ + m_-$, the reduced mass, $\mu = m_+ m_-/M$, and the scaling factor $\gamma = (m_- - m_+)/(m_+ + m_-)$ (assuming antihydrogen here). For antihydrogen, $\mu = 0.9995 m_e$ and $\gamma = 0.9989$, while for positronium, $\mu = m_e/2$ and $\gamma = 0$.

Thanks to the conserved pseudomomentum, this Hamiltonian is a function solely of the relative coordinates, but is now parameterized by $\tilde{\vec{K}}$. So we may reinterpret the Hamiltonian as describing a single particle system with reduced mass μ, charge e, moving in an axial magnetic field γB. The kinetic energy of the center of mass appears as an offset harmonic potential now, as part of the pseudopotential $V(\vec{r})$; the total energy is unchanged, so we may interpret

$$E_T = H = T(\dot{\vec{r}}) + V(\vec{r}) \tag{2.12}$$

where

$$\begin{aligned} T &= \frac{(\vec{p} + \frac{e\gamma B}{2c}\vec{r} \times \hat{z})^2}{2\mu} \\ V &= \frac{(\tilde{\vec{K}} + \frac{eB}{c}\vec{r} \times \hat{z})^2}{2M} + U(r) - e\vec{E} \cdot \vec{r}. \end{aligned} \tag{2.13}$$

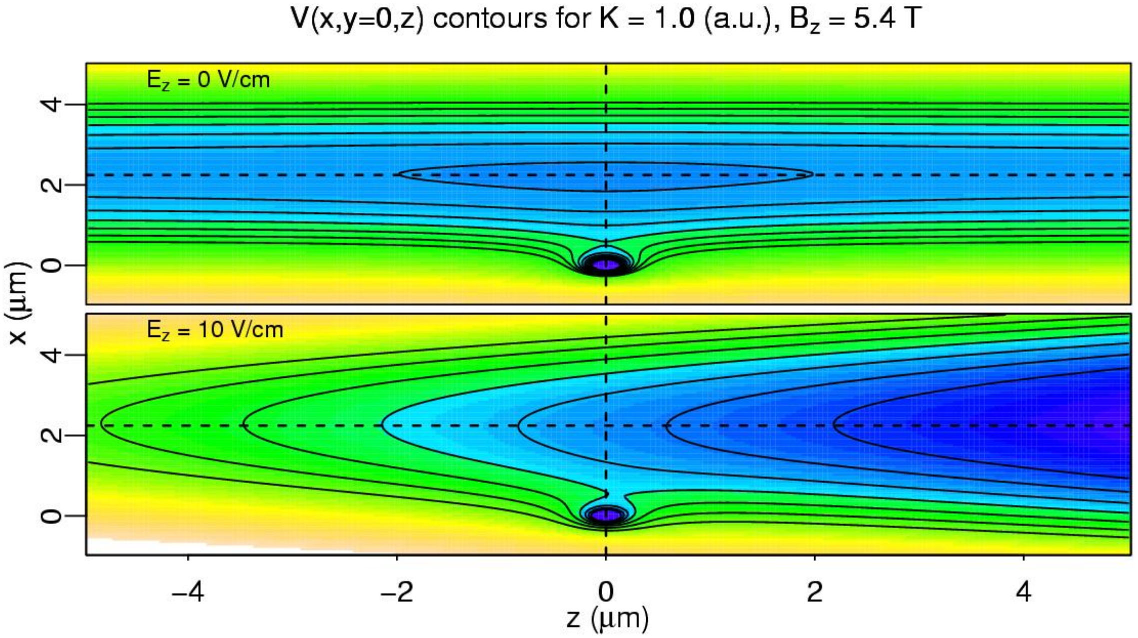

Figure 2.4: Slice of the pseudopotential $V(\vec{r})$ through the $y = 0$ plane, showing both Coulomb singularity and the giant dipole well. The giant dipole well is shallow enough that even a small axial ionizing field E_z will wash it away.

The quadratic nature of the center-of-mass kinetic energy term in the pseudopotential implies that we can refactor the transverse part of the dipole potential, and pull it into the definition of the pseudomomentum. After some algebra, we can add a constant to the pseudomomentum,

$$\vec{K} \equiv \tilde{\vec{K}} - M\vec{v}_D = \dot{\vec{R}} - \frac{eB}{c}\vec{r} \times \hat{z} - M\vec{v}_D \tag{2.14}$$

where $v_D \equiv \frac{c\vec{E}\times\hat{z}}{B}$; this is equivalant to performing a Galilean transformation into a frame moving at the drift velocity v_D. The energy shift $H' = H - \Delta E$ from this refactoring of the Hamiltonian is essentially the energy cost of performing this transformation in the presence of $\vec{B}$,

$$\Delta E = -(M\vec{v}_D^2/2 + \vec{K} \cdot \vec{v}_D). \tag{2.15}$$

After this refactoring, the pseudopotential is simplified

$$V = \frac{(\vec{K} + \frac{eB}{c}\vec{r} \times \hat{z})^2}{2M} + U(r) - eE_z z. \tag{2.16}$$

The advantage in subsuming the transverse dipole term into the pseudomomentum is that it removes two parameters (E_x, E_y) from the problem, since a system at a given $(\tilde{\vec{K}}_\perp, \vec{E}_\perp)$ can always be mapped to another system with $(\vec{K}_\perp, 0)$.

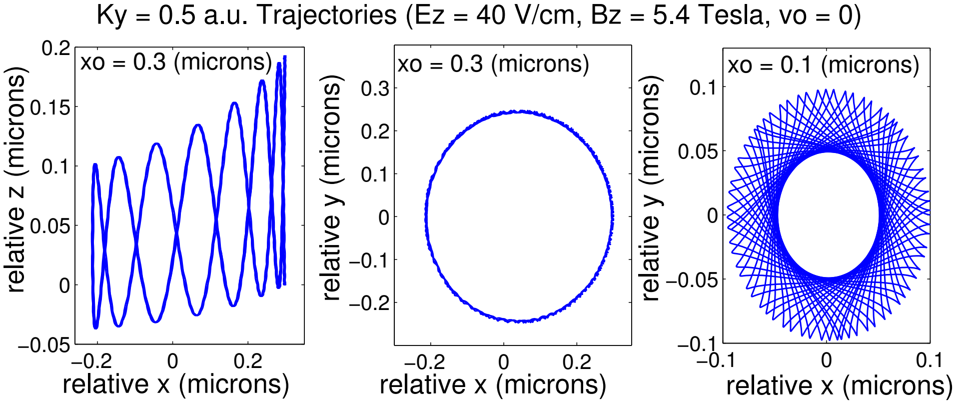

Figure 2.5: Classical positron trajectories in the relative coordinates for an anti-atom with significant pseudomomentum $\vec{K} = 0.5\hat{y}$ and an axial ionizing field. The asymmetry in x is due to the pseudomomentum, while that in z is due to the ionizing field. The first two plots are for a larger $\sqrt{\langle\rho\rangle^2} \sim 250$ nm size anti-atom, while on the right the radius of the anti-atom is comparable to the cycltoron radius r_c.

Figure (2.3) shows slices of the pseudopotential in $(x, 0, 0)$ for a pseudomomentum in $\hat{y}$. The main effect of the pseudomomentum here is to add an offset harmonic potential, of frequency $\omega_p \equiv \sqrt{\frac{\mu}{M}\frac{eB}{\mu c}}$ and some offset proportionate to K to the Coulomb well. In Figure (2.4) we plot contours of the pseudopotential in $(x, 0, z)$ with a significant pseudomomentum, showing the "giant dipole" well at some distance from the Coulomb well. The well has finite depth with no axial field, but is washed out by a small axial ionizing field.

It is often convenient to describe the effect of the pseudomomentum in terms of the center of the resulting transverse harmonic well; defining

$$\vec{\rho}_o \equiv \frac{c}{eB}\vec{K} \times \hat{z}, \tag{2.17}$$

the Hamiltonian reads (with $\vec{\rho}$ indicating a purely transverse coordinate)

$$H = \frac{(\vec{p} + \frac{e\gamma B}{2c}\vec{r} \times \hat{z})^2}{2\mu} + \frac{(eB)^2}{2Mc^2}(\vec{\rho} - \vec{\rho}_o)^2 + U(r) - eE_z z \tag{2.18}$$

which is shifted in energy by $\Delta E = -\frac{P_z^2}{2M} - (M\vec{v}_D^2/2 + \vec{K} \cdot \vec{v}_D)$ from the original total energy E_T. For a harmonic interaction, the motion of the system can be solved for exactly [23], but this isn't the case for a Coulomb bound system.

2.2.2 Trajectories on the Pseudopotential

In Figure (2.5) we depict an anti-atom in a strong magnetic field with an ionizing field at two different radii. The left two plots are for an anti-atom that has been made quite asymmetrical

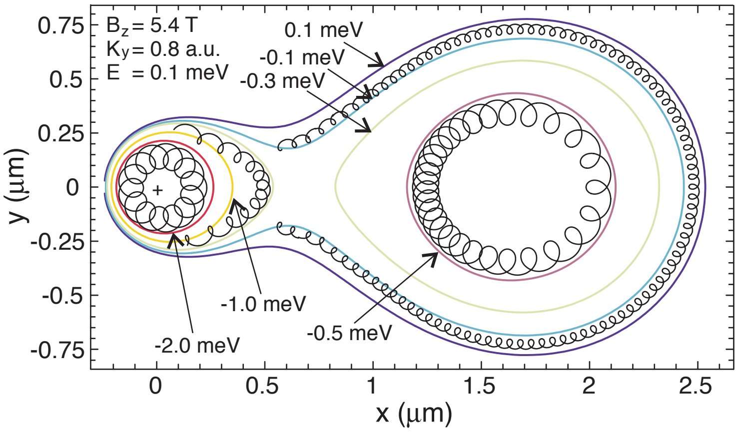

Figure 2.6: Classical positron trajectories for the anti-atom at $K_y = 0.8$ superimposed on the equipotentials of the pseduopotential on the $z = 0$ plane. The radii of the cylotron motion has been increased for visibility. Except in regions where the guiding center approximation breaks down, the guiding center follows equipotentials of the pseudopotential. From [113].

by the pseudomomentum and the axial ionizing field, but which remains guiding center-like: the two adiabatic invariants, J_c and J_m (i.e. the angular momenta) are nearly conserved, even though the system is highly non-cylindrical. The action of the pseudomomentum term is to pull the orbit off-center from the Coulomb well; however the conservation of the cyclotron action, and the small cyclotron radius, restricts the region of motion, and the positron remains in a region where the potential is roughly the same magnitude, and hence the kinetic remains roughly the same. This is in contrast to the panel on the right, where the GCA breaks down, since $\rho_m \sim r_c$.

One hallmark of the guiding center approximation is that when the motion is strongly guiding center, the guiding center position tends strongly to follow equipotenial contours. This can be most readily seen by considering the drift motion from equation (B.29),

$$\vec{v}_D \equiv \frac{c\vec{E} \times \vec{B}}{B^2}.$$

Since $\vec{E} = -\nabla V$, then we can write

$$\vec{v}_D \equiv \frac{c}{B}\hat{z} \times \nabla V.$$

The motion of the guiding center will be perpendicular to the gradient of the pseudopotential in the transverse plane. Since the gradient is perpendicular to the equipotentials, this means that the guiding center follows equipotentials in the transverse plane.

This can also be seen by considering action angle coordinates. From Appendix (C), the

Hamiltonian guiding center approximation can be written in 2D by

$$H = J_c\omega_c + V(Q, \theta_c, P, J_c).$$

The motion of canonical coordinate Q is

$$\dot{Q} = \frac{\partial H}{\partial P} = \frac{\partial V}{\partial P}.$$

while for the momentum P it is

$$\dot{P} = -\frac{\partial H}{\partial Q} = \frac{\partial V}{\partial Q}.$$

But $Q \propto X_{gc}$ and the canonical momentum to Q, $P \propto Y_{gc}$. Thus $\dot{\vec{R}}_{gc} = \left(\frac{\partial V}{\partial Y_{gc}}, -\frac{\partial V}{\partial X_{gc}}\right) = \nabla_{\vec{R}_{gc}} \times \hat{z}$; the motion of the guiding center moves perpendicular to its local gradient, and hence follows equipotentials.

In Figure (2.6) we show a variety of trajectories in the $z = 0$ plane of the system. The GCA dictates that the guiding center follow equipotentials of V, which for most of the trajectories in the figure is true. Nearer to the Coulomb well this breaks down, as it does additionally near the saddle point region. Note that there is an entire set of states which exist solely in the giant dipole well, a set of states which orbit the Coulomb well, and a number of states which interact with both wells. In general, only those states near the Coulomb well will persist for any measurable length of time in the actual experiment, since they ionize for fields as small as $E_z \approx 2$ V/cm.

2.2.3 Hydrogenic Scaled Coordinates

We can simplify the expressions by first moving to atomic units, where we choose to set $\mu = 1$ instead of the electron mass. Then, writing the magnetic field strength in terms of the cyclotron frequency $\omega_c = eB/\mu c$, the Hamiltonian reads

$$H = \frac{1}{2}\left(\vec{p} + \frac{\gamma\omega_c}{2}\vec{r} \times \hat{z}\right)^2 + \frac{\eta\omega_c^2}{2}(\vec{\rho} - \vec{\rho}_o)^2 - \frac{1}{r} - E_z z. \tag{2.19}$$

where we've defined the parameter $\eta \equiv \mu/M$. In these units, ω_c has the same value as the magnetic field B/c.

We can scale out the magnetic field by scaling [52]

$$\begin{aligned} \vec{r} &= (\gamma\omega_c)^{-2/3}\tilde{\vec{r}} \\ \vec{p} &= (\gamma\omega_c)^{1/3}\tilde{\vec{p}} \\ L_z &= (\gamma\omega_c)^{-1/3}\tilde{L}_z \\ H &= (\gamma\omega_c)^{2/3}\tilde{H} \\ t &= (\gamma\omega_c)^{-1}\tilde{t} \end{aligned}$$

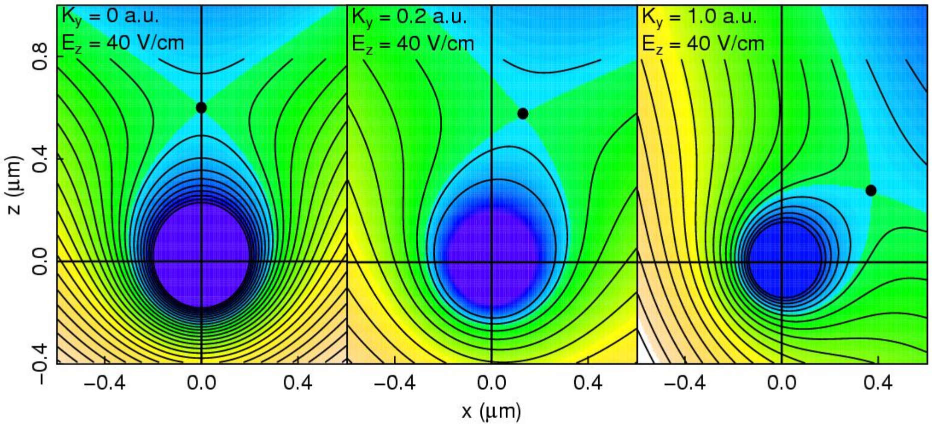

Figure 2.7: Slices of the pseudopotential $V(\vec{r})$ through the $y = 0$ plane, for regions around the Coulomb well for varying pseudomomentum $\vec{K} = K_y\hat{y}$ values. The saddle point for $\vec{K}_\perp = 0$ is unchanged from the $\vec{B} = 0$ case, but as K_y increases, the saddle point is pulled away from the z-axis toward the center of the giant dipole well $\vec{\rho}_o = \rho_o\hat{x}$.

$$E_z = (\gamma\omega_c)^{4/3}\tilde{E}_z \tag{2.20}$$

so that the scaled equation reads

$$\boxed{\varepsilon = H = \frac{1}{2}\left(\vec{p} + \frac{1}{2}\vec{r}\times\hat{z}\right)^2 + \frac{k}{2}(\vec{\rho}-\vec{\rho}_o)^2 - \frac{1}{r} - E_z z.} \tag{2.21}$$

where the dimensionless constant $k = \eta/\gamma^2 = \mu/(M-\mu) \approx 5.4 \times 10^{-4}$.

Thus the new Hamiltonian has only three parameters, $(\varepsilon, E_z, \rho_o)$, since the polar orientation of ρ_o is arbitrary.

Considering a specific set of parameters in scaled atomic units, we choose a magnetic field $B = 5.4\text{T} = 2.30 \times 10^{-5}$ in atomic units. Setting this as our B scale, then we have conversion factors to scaled atomic units: $E_z \to 2.981 \times 10^{-6} E_z$ where E_z was in V/m, $K \to 35.187$ K, where K is in atomic units, $x \to 15.29x$ where x is in μm, or $x \to 8.0767 \times 10^{-4}x$ where x is in atomic units, and $\varepsilon \to 5.554 \times 10^4\varepsilon$ in eV.

For a strong magnetic field, the angular momentum is almost entirely tied up in the magnetic field, $L_z = \frac{\mu}{2}\omega_c\gamma\rho^2$, or in scaled units $L_z = \frac{\rho^2}{2}$.

2.3 Ionization and Saddle Points

The pseudomomentum term of the pseudopotential restricts ionization to take place in the axial direction. However, a non-zero pseudomomentum (or equivalently a transverse electric field) will force the saddle point away from the z-axis.

In zero magnetic field, the classical ionization saddle point is simple to calculate; the saddle will occur by definition when $\frac{\partial V}{\partial r} = \frac{\partial V}{\partial z} = 0$. For axial E_z, this implies that

$$\begin{aligned} \vec{\tilde{r}}_{B=0} &= 1/\sqrt{E_z}\hat{z} \\ \tilde{\varepsilon}_{B=0} &= 2\sqrt{E_z} \end{aligned} \tag{2.22}$$

2.3.1 $E_z = 0$ Saddle

In the presence of a magnetic field, but no axial ionizing field, there may also be a saddle between the Coulomb well and a "giant dipole" well. This saddle is visible in the top panel of Figure (2.4), between the Coulomb well at the bottom, and the giant dipole well in center. This saddle will lie on the $z = 0$ plane, and for a pseudomomentum $\vec{K} = K\hat{y}$, will lie on the x-axis; this case was shown in Figure (2.3).

This saddle will occur when the potential on the x-axis

$$V(x,0,0) = \frac{1}{2}k(x - x_o)^2 - \frac{1}{x}$$

has a local maximum, so when $0 = k(x - x_o) + \frac{1}{x^2}$ or when

$$kx^2(x - x_o) + 1 = 0.$$

In order for this solution to be a local maximum, the second derivative of the potential must be positive. Thus $k - \frac{2}{x^3} > 0$. This implies that for a saddle to exist, that in scaled coordinates $x_o > 3(4k)^{-1/3} \sim 23.2$, or that $K > K_{crit}$ where

$$K_{crit} = \frac{3e}{c}\left(\frac{MB}{4}\right)^{1/3}.$$

The inflection point will exist at a distance $x_{crit} = \left(2Mc^2/B^2\right)^{1/3}$.

The saddle that joins the giant dipole and Coulomb wells may not lead to ionization, since in the $E_z = 0$ case the entire system is bound. However, if a state can escape the nearby confines of the Coulomb well through this saddle region, (for weaker magnetic fields by just following the equipotential contours), then once away from the confines of the Coulomb well, it may be ionized by stray fields.

2.3.2 General Saddle Analysis

For a hydrogen atom in a magnetic field, the saddle is similarly found. From the pseudopotential $V(\vec{r})$, the saddle conditions imply,

$$0 = \frac{\partial V}{\partial \vec{\rho}} \quad = \quad k(\vec{\rho} - \vec{\rho_o}) + \frac{\vec{\rho}}{r^3}$$

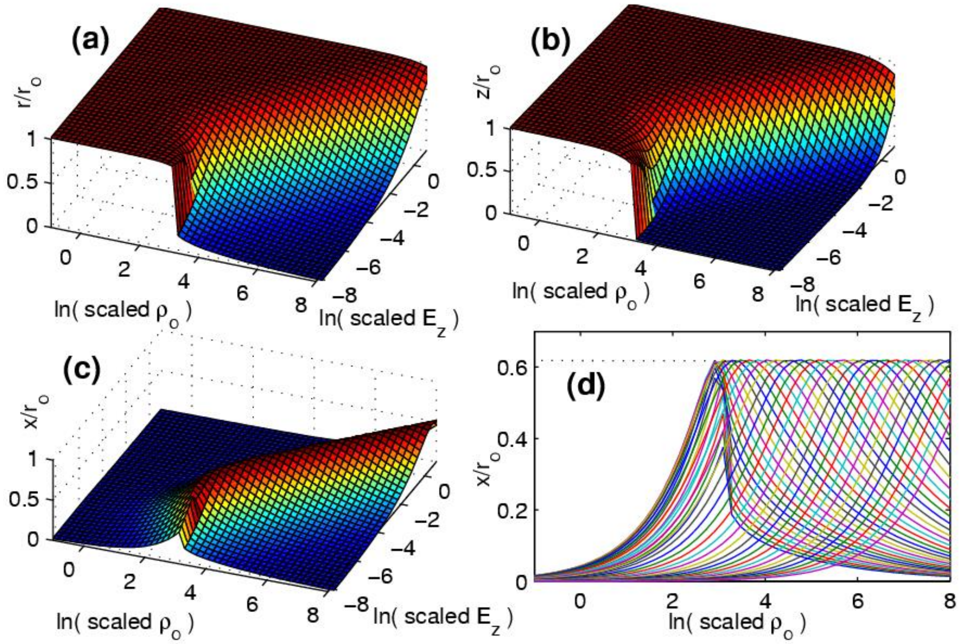

Figure 2.8: Saddle point positions scaled by the $B = 0$ values, $r_o = 1/\sqrt{E_z}$, versus scaled parameters $\tilde{\rho}_o$ and $\tilde{E}_z$. For $B = 5.4$T field, the conversion factors from scaled parameters are: $E_z = 3353\tilde{E}_z$ to V/cm, and $x = 0.0655\tilde{x}$ to μm.

$$0 = \frac{\partial V}{\partial z} \quad = \quad \frac{z}{r^3} - E_z \tag{2.23}$$

Without loss of generality, we can take $\vec{\rho}$ to lie in the same direction as $\vec{\rho}_o$. We can further simplify by scaling the lengths by the $B = 0$ saddle radius $r_{B=0} = 1/\sqrt{E_z}$. So we must solve

$$\begin{aligned} \tilde{k}(\tilde{\rho} - \tilde{\rho}_o) + \frac{\tilde{\rho}}{\tilde{r}^3} &= 0 \\ 1 - \frac{\tilde{z}}{\tilde{r}^3} &= 0 \end{aligned} \tag{2.24}$$

where $\tilde{k} \equiv k E_z^{-3/2}$ and $\tilde{\rho}_o \equiv \sqrt{E_z}\rho_o$. The scaled radius $\tilde{r}$ is found by solving the polynomial

$$\left(\tilde{k}\tilde{r}^5 + \tilde{r}^2\right)^2 - \left(1 + \tilde{k}\tilde{r}^3\right)^2 + \tilde{k}^2\tilde{\rho}_0^2\tilde{r}^4 = 0 \tag{2.25}$$

from which the ρ and z variables follow,

$$\begin{aligned} \rho &= \frac{1}{\sqrt{E_z}}\left(\frac{\tilde{k}\tilde{\rho}_o}{\tilde{k} + \tilde{r}^{-3}}\right) \\ z &= \frac{1}{\sqrt{E_z}}\,\tilde{r}^3. \end{aligned} \tag{2.26}$$

For $\tilde{k} \ll 1$ (i.e. when the electric field scaled by B, $E_z \gg k^{2/3} \cong 7 \times 10^{-3}$), we can find an approximate closed form solution for the saddle point,

$$\begin{aligned} r &= \frac{1}{\sqrt{E_z}} \left(1 - (\tilde{k}\tilde{\rho}_o)^2\right)^{-1/4} \\ z &= r \\ \rho &= \frac{\tilde{k}\tilde{\rho}_o}{\sqrt{E_z}} \left(1 - (\tilde{k}\tilde{\rho}_o)^2\right)^{-3/4} ; \end{aligned} \tag{2.27}$$

linearizing for small $\tilde{\rho}_o$ as well, $z = r$ and $\rho \cong \frac{\tilde{k}\tilde{\rho}_o}{\sqrt{E_z}} \left(1 + \frac{3}{4}(\tilde{k}\tilde{\rho}_o)^2\right)$.

In Figure (2.8) we explore the position of the general saddle points for a variety of axial electric fields E_z and pseudomomenta, here as the offset ρ_o. In each case there is an abrupt knee for the saddle point values for small ionizing field E_z. This occurs when the pseudomomentum is strong enough to create a saddle of its own, $\ln(\rho_o) \sim \ln(23.2) \sim 3.1$.

2.3.3 $K = 0$ Saddle Analysis

At $K = 0$, which implies the center of the harmonic well in the pseudomomentum is at $\rho_o = 0$, the pseudopotential is cylindrically symmetric. The canonical angular momentum for the pseudoparticle about the z-axis,

$$\begin{aligned} L_z &= \left|\vec{r} \times \left(\vec{v} + \vec{A}\right)\right| \\ &= v_\theta \rho + \frac{1}{2}\rho^2 \end{aligned} \tag{2.28}$$

is conserved (here $\rho = \sqrt{x^2 + y^2}$, and we have expressed the vector potential in the symmetric gauge, $\vec{A} = \vec{B} \times \vec{r}/2$ so that $A_\theta = \rho B/2$). Furthermore, it is conserved in any frame of reference rotating about the z-axis, and has the same value in any such frame.

If we choose to rotate about the z-axis at an angular velocity $\omega = -1/2$, the Coriolis forces from the rotation will just cancel the magnetic forces, effectively reducing the magnetic field to an attractive harmonic potential; the rotating frame Hamiltonian is

$$H_R = \frac{p_\rho^2 + p_z^2}{2} + \frac{L_z^2}{2\rho^2} + \frac{1 + 4k}{8}\rho^2 - \frac{1}{r} - E_z z. \tag{2.29}$$

The total energy exceeds the energy in the old frame by the amount of work needed to spin up the the new frame,

$$\varepsilon_R = \varepsilon_L - \omega L_z = \varepsilon_L + \frac{L_z}{2}. \tag{2.30}$$

Since L_z is conserved we can treat the angular KE term as an additional term in the pseudopotential, and reduce the problem to two degrees of freedom,

$$V(\rho, z) = \frac{L_z^2}{2\rho^2} + \frac{1 + 4k}{8}\rho^2 - \frac{1}{r} - E_z z, \tag{2.31}$$

which is now parameterized by the angular momentum L_z.

In this formulation, the effect of the pseudomomentum term is to modify the magnetic confining potential by an additionak $4k$. In the antihydrogen case, this is a small change, and for $K = 0$ it makes sense to ignore the coupling of the center-of-mass motion to the relative motion.

We can perform a saddle point analysis in (ρ, z) taking into account the conservation of angular momentum, In this case, the saddle point is parameterized by L_z, so partials in $V_{\text{eff},R}$ are

$$\begin{aligned} \frac{\partial V_{\text{eff},R}}{\partial z} &= \frac{z}{r^3} - E_z = 0 \\ \frac{\partial V_{\text{eff},R}}{\partial \rho} &= \frac{\rho}{r^3} - \frac{L_z^2}{\rho^3} + \frac{1+4k}{4}\rho = 0 \end{aligned} \tag{2.32}$$

so that

$$\begin{aligned} z &= E_z r^3 \\ \rho^2 &= \frac{L_z}{\sqrt{1+4k+r^{-3}}} \end{aligned} \tag{2.33}$$

Combining $r^2 = \rho^2 + z^2$, we get a twelfth order polynomial in r,

$$r^4(E_z^2 r^4 - 1)^2 \left(1 + (1+4k)r^3\right) - L_z^2 = 0. \tag{2.34}$$

whose solutions provide positions (ρ, z) of the saddle points of the potential at a given L_z. Physically, these saddle points are in fact rings at a certain distance from the z-axis and z position where the pseudoparticle can just make it over the potential hill without costing too much energy pushing up the centrifugal barrier.

For guiding center atoms, the relative transverse position oscillates by a small amount about the mean value $\bar{\rho}$, which is nearly the initial radius; this is tantamount to stating that the magnetic part of the angular momentum is much larger than the kinetic part. In this case, we can take the radius of the saddle point to be $\bar{\rho}$, and solve the cubic equation for z^2,

$$E_z^2(z^2 + \bar{\rho}^2)^3 + z^2 = 0. \tag{2.35}$$

The sign of z is the sign of E_z. This is the same result we derived for the cicular GCA atoms in Section (2.1).

2.4 Distribution of Pseudomomenta

In order to estimate the experimental distribution of pseudomomenta, we consider how an initial population of thermal center-of-mass velocities $\dot{\vec{R}}$ combined with a random distribution of initial transverse positions $\vec{\rho}$. The pseudomomentum is

$$\vec{K} = M\dot{\vec{R}}_\perp - e\rho \times \vec{B}$$

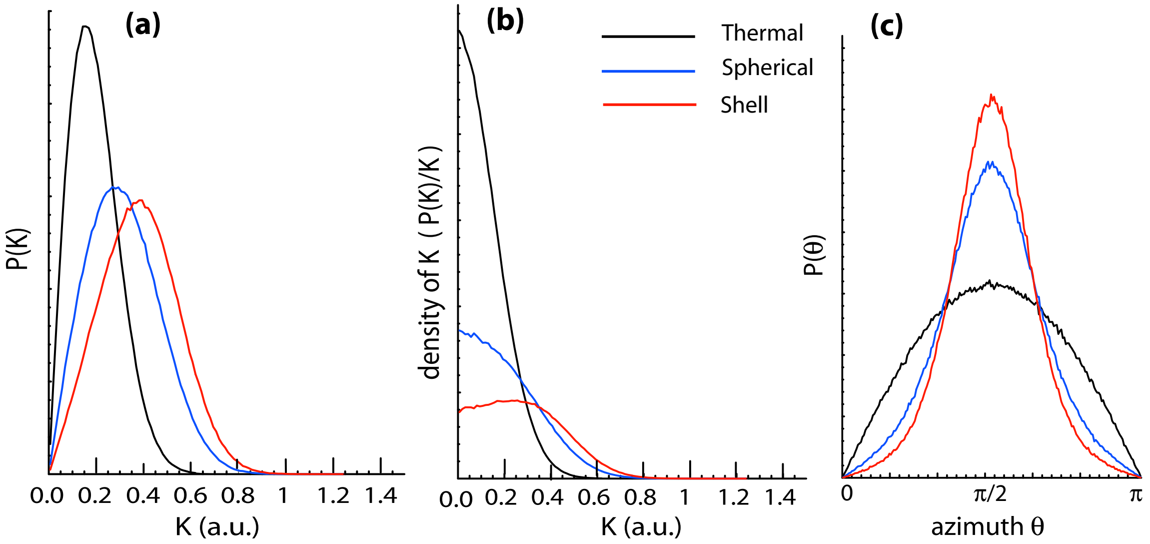

Figure 2.9: Distributions in $K_\perp$ for a temperature $T = 4.2$ K and atom size $r = b/4 = 1/4kT$ using a thermal distribution for the center-of-mass veloicity $\dot{\vec{R}}$ and shell (in red) or spherical (in blue) distributions in atom sizes; the completely thermal (in black) distribution is where we've set $r = 0$. Clearly the shell distribution creates the most skewed distribution in $K_\perp$.

And thus we wish to calculate the distribution in $K_\perp = |\vec{K}_\perp|$. This can be written as

$$f(K_\perp) = \int\int dV_x dV_y \int\int d^2\rho_o f(\vec{V}) f(\vec{\rho}_o) \delta \left[K_\perp - |M\vec{V} - e\vec{\rho}_o \times \vec{B}| \right] \tag{2.36}$$

where we take $f(\vec{V}) = f(V_x)f(V_y)$ to be a Maxwell-Boltzmann distribution in the center-of-mass velocity at temperature $T = 4$ K, and $f(\vec{\rho}_o)$ is the distribution in atom sizes.

The distribution in initial atom sizes, $f(\vec{\rho}_o)$ is an unknown, probably complicated quantity that depends on the collisional dynamics of atoms and particles in strong magnetic fields. Previous work [42] indicates that if the anti-atoms have enough time so that collisions with unpaired positrons may take place, then anti-atoms formed at large radii will gradually reduce in size. This process however encounters a dynamics bottleneck at energies $E = \alpha kT$, where $\alpha \sim 4$. This is due to competition between the collisional dynamics, which tends to favor the bound system becoming even more bound as it becomes deeper, with the shrinking cross section of the anti-atom. The bottleneck binding energy $E = \alpha kT$ provides a useful energy scale, and hence the relevant length scale is $r = b/\alpha$, where b in the Thomson radius, equation (2.1). At $\alpha = 4$ and $T = 4$ K, this length scale $r \sim 1\ \mu$m.

How the atom sizes are populated, given this length scale, is not obvious. One model is to assume that all the anti-atoms have collided and reduced in size down to the bottleneck size, at

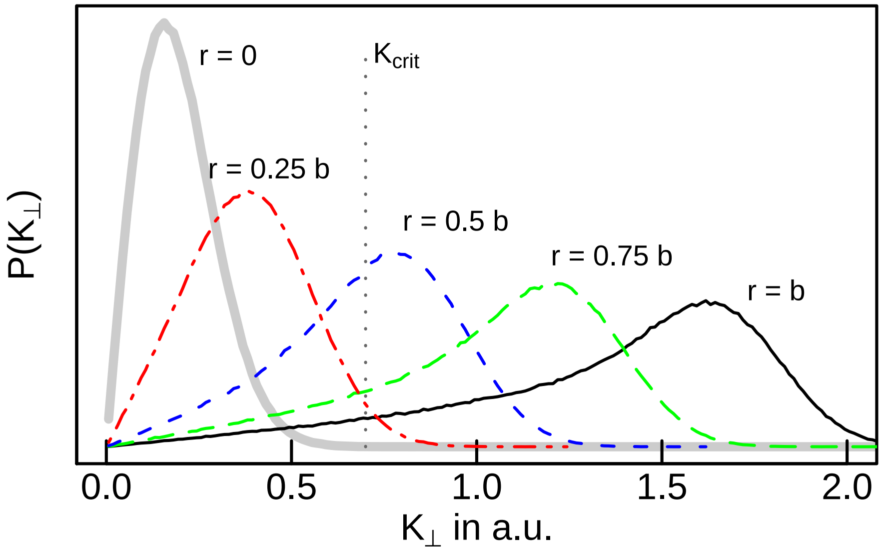

Figure 2.10: Distributions in $K_\perp$ at $T = 4$ K and a shell distribution in anti-atom sizes, for various sizes in terms of the Thomson radius $b = 1/kT$. The assumed approximate bottleneck radius, $r = b/4$, implies that the anti-atoms almost all have $K < 1.0$ and can't sustain a giant dipole bound state. The completely thermal distribution is shown as a wide gray line.

which they remain, forming a shell distribution of radius r,

$$f(\vec{\rho}_o) = \frac{1}{2\pi}\delta(r - |\vec{\rho}_o|)$$

Another model is that the anti-atoms have shrunk to radius r rapidly, but will slowly shrink the rest of the way, forming a uniform disk-shaped distribution in the $\vec{\rho}_o$ plane up the radius r,

$$f(\vec{\rho}_o) = \frac{1}{\pi r^2}\Theta(r - |\vec{\rho}_o|).$$

A third model is that the anti-atoms have shrunk to radius r rapidly as in the previous case, but that the distribution is spherical in space, with radius $\sqrt{\vec{\rho}_o^2 + z^2}$ up the radius r,

$$f(\vec{\rho}_o, z) = \frac{3}{4\pi r^3}\Theta(r - |\vec{\rho}_o + z\hat{z}|).$$

In Figure (2.9a) we plot three different distributions for experimentally relevant values, $T = 4$ K, $\alpha = 4$ and a combined mass $M = m_e + m_p$. These were calculated numerically by populating a large number of configurations in $\dot{\vec{R}}$ and $\vec{\rho}_o$, then determining the distribution of these configurations in $K_\perp$. The distribution with the $K_\perp$ values closest to $K_\perp = 0$ (in black) is a purely thermal distribution in center-of-mass velocities $\dot{\vec{R}}$, i.e. the case where the typical atom size $r = 0$. For distributions that are more weighted in the atom sizes, the distribution in $K_\perp$ moves

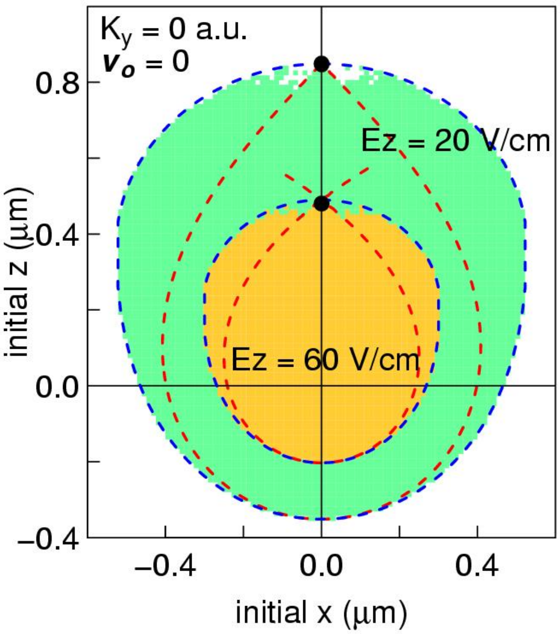

Figure 2.11: Regions in the parameter space (x_o, z_o) which are bound in the $K = 0$ case, with initial speed $v = 0$. Hence this represents the largest possible anti-atom at these fields E_z and K. The colored region indicate a stable configuration. The blue contour indicates the saddle contour assuming that the atom is a good GCA atom, while the red contour is the energy contour at the saddle energy.

toward larger values. In Figure (2.9b) we plot the the density of atoms with $K_\perp$. here we can we how the shell distribution (in red) clearly weights towards a maximum that is at a finite value of $K_\perp$. Figure (2.9c) indicates that the distribution in the angle θ with respect to the magnetic field is clearly weighted away from axial motion for non-thermal distributions. Since the detector is at one axial end of the Penning trap, this indicates that non-thermal distributions will have a lower signal at the detector for these distributions.

In Figure (2.10) we plot the distribution in $K_\perp$ where the atom size distribution is taken to be a shell at $|\vec{\rho}_o| = r$, for various atom sizes r; the $r = 0.25\ b$ curve is the same as the shell curve in Figure (2.9a). Even using the most skewed distribution, that assumes that all the anti-atoms are trapped at the energy bottleneck radius, $r \approx b/4$, few of the anti-atoms produced are capable of sustaining a giant dipole bound state, and almost all are below $K = 1.0$.

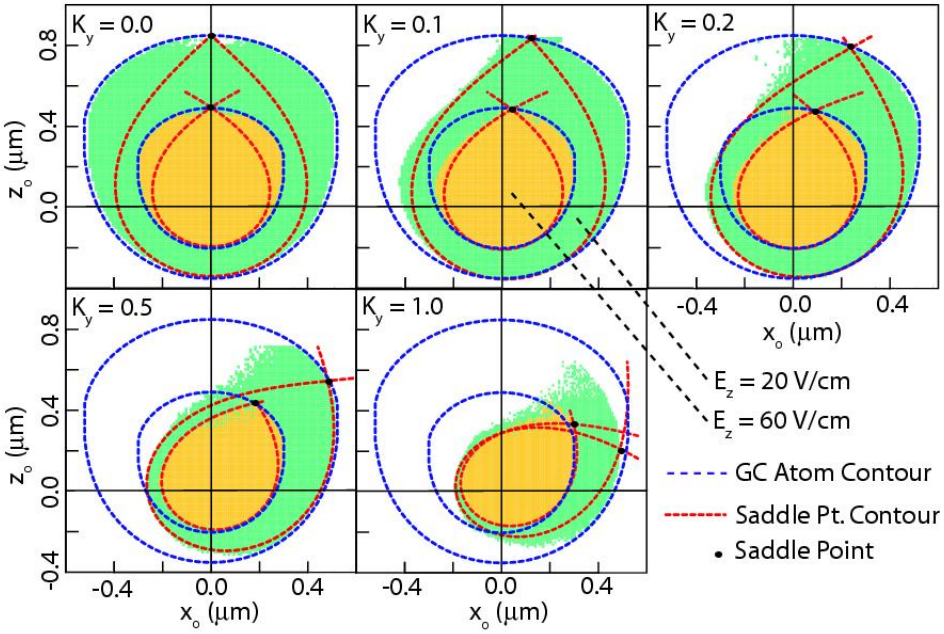

Figure 2.12: Regions in the parameter space (x_o, z_o) which are bound, for a variety of K values up to $K = 1$, with initial speed $v = 0$. The blue contours indicates the saddle contour assuming that the atom is a good GCA atom, while the red contour is the energy contour at the saddle energy; the black points are the saddle points.

2.5 Ionization Simulations

We have considered so far two models of the ionization of antihydrogen atoms in a strong magnetic field. The first model assumed that the anti-atoms were cylindrically symmetric and that the transverse motion of the positron was dominated by the effect of the magnetic field. The second model considered the ionization saddle point of the system, as derived from the full Hamiltonian including asymmetric effects due to the electromotive force as the anti-atoms move across magnetic flux lines. However this model implicitly assumes that, for the global saddle points to be relevant, the motion of the positron in the reduced system is nearly ergodic, and hence that the particle can escape though the saddle point if it has sufficient energy. In addition, we saw that experimentally relevant anti-atom configurations have a pseudomomentum $K < 1$. As we shalll see, for anti-atoms that are experimentally relevant, both the guiding center and saddle point models are relevant, sometimes even within the same configuration. In this Section we will simulate the classical ionization of anti-atoms in the center-of-mass system, by launching the positron in the effective potential at varying energies and positions.

2.5.1 Low Temperature Atoms

To begin we consider the simplest case, that of a cylindrically symmetric $K = 0$ anti-atoms in the presence of ionizing field $E_z = 20$ and $E_z = 60$ V/cm. The method is as follows: at each initial point on a grid, the particle is placed at position (x_o, y_o) with no initial speed, and allowed to propagate over many thousands of cyclotron periods. Since there is no initial kinetic energy, the results represent the largest expected atom size. If the positron remains within the Coulomb well, it is marked as essentially bound, and the initial grid position indicated on the figure by a colored square. While the state might not be bound, but have a very long dwell time, because of the reasonably steep slope of the potential everywhere but at the saddle point, the error in atom size is negligible. In addition, due to the ionizing axial fields, no state is truly bound; in the quantum sense then, bound really means a long-lived metastable state.

From the results in Figure (2.11), the approximation of a circular guiding center atom is a good one for a cold atom at $K = 0$, and only breaks down near the lip of the saddle region. The outer contour, which assumes that the angular momentum tied up in the cyclotron motion is conserved (or that J_c is strictly conserved) does in this case define the “size” and shape of the atom. The circular GCA contour and the saddle energy contour represent the two models of ionization in the Figure, and define the two limits of atom size.

In Figure (2.12) we consider the same type of simulations but with K varied up to $K = 1$. The $K = 0$ case corresponds to Figure (2.11). As the system becomes more asymmetric, the stable regions becomes depopulated away from the saddle point. However, on the side of the saddle point on the x-axis, the guiding center atom approximation remains surprisingly good, even at $K = 0.5$, which has a significantly asymmetric saddle energy contour. Even at $K = 1.0$, when the saddle lies almost to the x-axis, states that have initial position near the saddle remain bound, because the guiding center motion maintains a distorted tube-like motion well away from the Coulomb well (see again Figure 2.5). Nearer to the Coulomb well, the guiding center approximation breaks down, and the saddle energy contour, shown in red, demarcates the edge of the stable atom.

2.5.2 Thermal Atoms

In Figure (2.13) we consider the effect of an initial thermal speed for the particle, as compared to a particle launched from rest at position (x_o, z_o). The panel on the left, with $v_o = 0$ is the same as for Figure (2.11). When a particle is launched with very little initial velocity, we are almost ensuring that the particle will behave as a good guiding center atom, since the cyclotron radius is small. In the panel on the right, the particle is launched with a thermal speed $v = \sqrt{2kT/m}$ in the y-direction. Near the Coulomb well, this enhances the mixing of cyclotron and magnetron

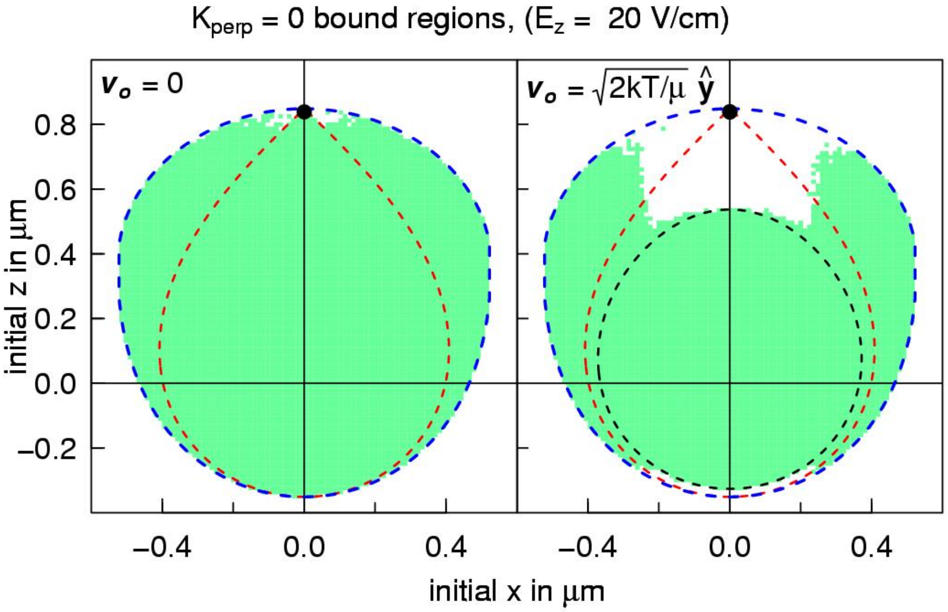

Figure 2.13: Regions in the parameter space (x_o, z_o) which are bound, for $K = 0$. The panel on the left is for a particle with no initial speed, while on the right is for a thermal particle at 4 K. The red contours are the potential contours at the saddle energy, and will be the strict edge of the bound region if the motion were completly ergodic at $v_o = 0$. The blue contours are the saddle boundary with angular momentum conservation taken into account. The inner black contour on the right panel is the saddle energy contour when the extra kinetic energy is subtracted. The figure highlights that the guiding center approximation works well for larger radii and then rapidly breaks down at around 0.25μm. This breakdown radius holds well for a wide range of initial velocities.

angular momenta (and actions), producing a more ergodic trajectory. Because the additional near invariant of the magnetron action J_m is not conserved, the particle can move in all three dimensions nearly ergodically, and escape the system. In this region the correct atom boundary is the energy contour at $E = E_{saddle} - \frac{mv_o^2}{2}$.

Further from the Coulomb well, the guiding center motion is preserved despite the large cyclotron radius. This transition occurs at about $\rho \approx 250$ nm. This value of the GCA breakdown is fairly large as compared to the rough approximation from Section (2.1) that the magnetron radius $\rho_m \gg r_c \approx 10$ nm. However it matches the value found in Figure (C.2) in Section (C) for completely transverse motion.

We have for the most part considered anti-atoms in an extreme regime; setting the initial speed $v = 0$ produces an atom at very low temperature, and leads to a prediction of a fairly large region of stable configurations. If we instead consider the more realistic case of anti-atoms which are formed via axial collisions with other particles in the trap, then we may assume that they have an

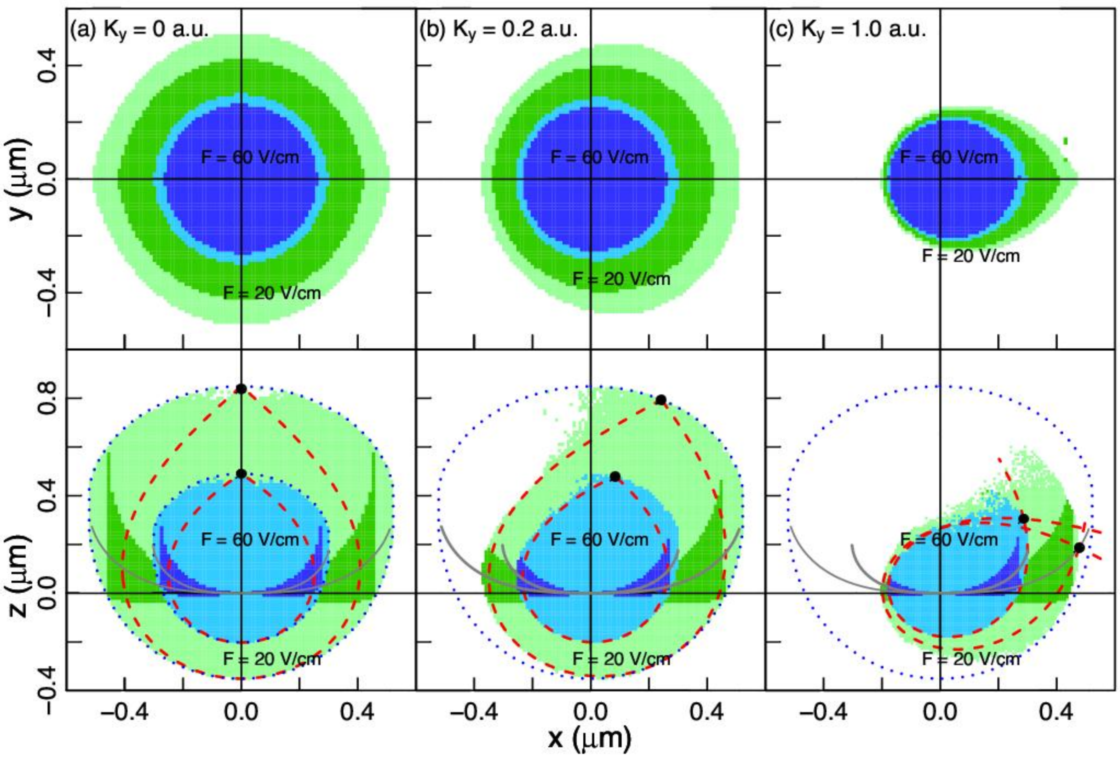

Figure 2.14: Anti-atom sizes in an ionizing electric field F with a pseudomomentum K, including axial thermal energy. Anti-atoms formed with no initial velocity are in lighter shades, and those formed with an axial thermal energy kT are shown in darker shades. The edge of the stable region, assuming a circular GC atom is shown as the dotted blue lines, while the potential contour for the saddle energy is the dashed red line. The center of the axial well, deformed by the ionizing field, is shown as the gray solid lines in the lower panels. At thermal axial energies, bound atoms take on a narrow, pancake-shape at reasonable ionizing fields, much smaller than the configurations when $v_{z,o} = 0$.

axial thermal energy kT above the bottom of the axial well (since the axial and transverse motions are strongly decoupled). In Figure (2.14) we consider atoms formed with axial energy kT in the presence on an ionizing field.

In the top row of panels, we launch trajectories as before with no initial velocity, and track whether the anti-atoms ionize classicalyl for various initial positions; this data is shown in the lighter shades. Here we plot in the $z = 0$ plane, adiabatically advanced by the ionizing field; this is the surface that intersects the bottom of the axial well for all (x, y), and will be the surface along which the atom is widest. The surface is shown as a grey lines in the lower panels. For $K = 0$ it is circular, as would be suspected. The darker shades indicate regions where the electron have been lanuched with not only at a transverse thermal speed, but at an axial energy $-kT/2$ below the

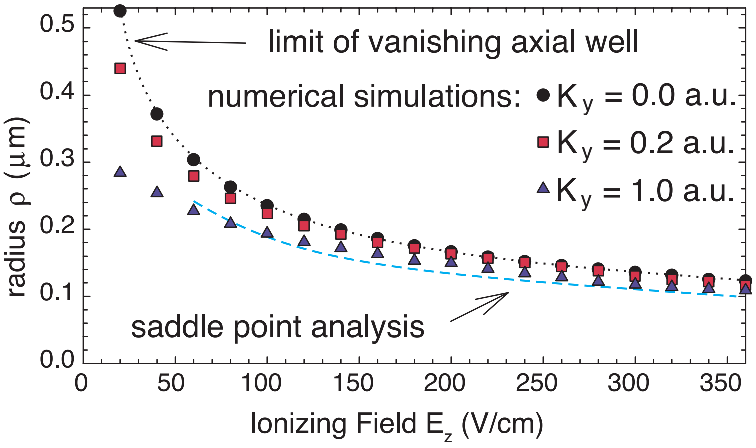

Figure 2.15: Anti-atom size versus ionizing field E_z from simulation and analytic models. In all cases, for the K values expected experimentally the results agree, and the simulated results for various K values lie in between the curves predicted by the two models. From [113].

continuum. Because the axial well for large radii becomes fairly shallow, the $v = 0$ estimates for the atom size overestimates the viable size of the thermal anti-atom. This is not due to any GCA breakdown, just due to the finite axial well depth. As K is increased, the cross-section of the atom is distorted by the K pseudopotential, but remains close to circular out to $K = 1$.

In the lower panels we plot the region where the positron does not ionize on the $y = 0$ plane, as in previous figures. However, the inclusion of axial thermal energy makes the effective axial atomic size very different. Whereas in previous figures the axial extent of the anti-atom could be quite large, when thermal axially, the atom is significantly narrower in the z-direction, and narrows as it approaches the Coulomb well. When we consider positrons close to the Coulomb well, we should not take this approximation too seriously. However, far from the well, where the guiding center and axial motions are strongly decoupled, the axial well will appear to be harmonic at thermal energies. It then will be populated according to equipartition of energy, with a portion $\sim kT$ of the total energy. This available axial energy implies that the effective radius of the anti-atoms is smaller when the GCA holds. However, when the Coulomb well couples transverse and axial energies well enough, as in the $K = 1$ and the left-hand side of the $K = 0.2$, then there is no discernible difference in atom-sizes ρ.

2.5.3 Atom Sizes

Our simulations of the ionization of experimentally relevant anti-atom configurations can provide a measure of the typical radial size ρ of anti-atoms formed experimentally. In addition, the two models of ionization, assuming ergodic or guiding center behavior, can be used as limits on the atom size as well. As we have seen, if the ionizing field is fairly weak, so that the axial well persists for a radius $\rho > 250$ nm, then the anti-atom may be considered a guiding center system, and the guiding center saddle approximation used. In the other extreme. If the ionizing field is strong, such that at any stable radius ρ the Coulomb well mixes the radial and axial energies, then we may assume that dynamically the positron can find the full three-dimenstional saddle point, and ionize in a reasonably short amount of time. As we have seen, the true dynamics usually lies in between these two cases.

This approach is summarized in Figure (2.15) for a system with no initial kinetic energy $v = 0$. The generalization to thermal atoms is straightforward. The upper dotted line indicates the radius at which the axial well vanishes, which is the maximum possible radius if the guiding center motion holds, and radial motion negligible. The lower dashed line is the maximum radius assuming that the particle can otherwise find the ioniziation saddle point region. In between lie the typical simulated $\sqrt{\langle \rho_{max}^2 \rangle}$ maximum radii of the positron motion at varying K values. This Figure paints a consistent picture of the radial extent of cold anti-atoms as a function of ionizing field, and provides the needed relation to predict the size of anti-atoms in the experiment.

Chapter 3

Mesoscopic Wavepackets

In this Chapter we describe the use of numerical quantum dynamics methods, known as "wavepacket" propagation, to simulate the transmission of particles through a semiconductor nanostructure in a two-dimensional electron gas (2DEG) or similar 2D system. These methods have been employed extensively in the past, primarily in quantum chemistry and optics, but are well suited to single particle 1-2D systems in mesoscopic physics as well.

We begin by outlining the basic theory of wavepacket propagation, and then focus on the use of wavepackets to determine the energy resolved flux through a system, and hence the transmissive properties of the system. Next we present an example simulation of a quantum dot simulation as a small tutorial on the approach. We then consider the application of wavepacket approaches to simulate tip scan experiments in 2DEG systems, as pioneered by the Westervelt group, including examples of such tip-scan systems.

3.1 Basic Wavepacket Properties

3.1.1 Free Wavepackets

The Gaussian wavepacket in simple quadratic systems was worked out near the inception of quantum theory itself, and worked out by Kennard [55] in 1927. The most common way to model a localized wavefunction is the minimum uncertainty wavepacket with linear momentum, which is a symmetric Gaussian wavepacket

$$\langle \vec{x}|\psi\rangle = \frac{1}{\sigma\sqrt{\pi}} e^{i\vec{k}_o\cdot\vec{r}-\frac{(\vec{r}-\vec{r}_o)^2}{2\sigma^2}} \tag{3.1}$$

where the expectation values of the position $\langle \vec{r} \rangle = \vec{r}_o$ and the fluctuation in position is $\Delta r = \sigma/\sqrt{2}$. In momentum space this is

$$\langle \vec{k} | \psi \rangle = \frac{\sigma}{\sqrt{\pi}} e^{i\vec{k}\cdot\vec{r}_o - \frac{\sigma^2(\vec{k}-\vec{k}_o)^2}{2}} \tag{3.2}$$

where the mean values of momentum $\langle \vec{k} \rangle = \vec{k}_o$ while the fluctuation in momentum is $\Delta k = 1/\sqrt{2}\sigma$. Since $\Delta r \Delta k = \frac{1}{2}$, this is a minimum uncertainty state. When we say “wavepacket” in general, this is the form we mean.

This wavepacket has the property that upon propagation by some propagator

$$\hat{\mathcal{U}}(t) = e^{-i\hat{H}t/\hbar} \tag{3.3}$$

that the expectation values of the motion obey [41]

$$\begin{aligned} \frac{\partial}{\partial t}\langle r \rangle &= \frac{\langle r \rangle}{m} \\ \frac{\partial}{\partial t}\langle k \rangle &= -\frac{1}{\hbar}\langle \frac{\partial V}{\partial r} \rangle \end{aligned} \tag{3.4}$$

which can be calculated from the Schrödinger equation. The center of the wavepacket moves as the classical value, as expected from Ehrenfest’s theorem. However the second equation indicates that the change in momentum isn’t classical, since in general $\langle \frac{\partial V(r)}{\partial r} \rangle \neq \frac{\partial V(\langle r \rangle)}{\partial \langle r \rangle}$. However, in many cases the wavepacket does follow the classical motion of the particle reasonably closely.

In free space, even the the last holds, since $V = 0$. We can propagate the wavepacket analytically in momentum space [11]

$$\begin{aligned} \langle \vec{k} | \psi(t) \rangle &= \langle \vec{k} | e^{-i\hat{T}\frac{t}{\hbar}} | \psi_o \rangle \\ &= e^{-i\frac{\hbar^2(k_x^2+k_y^2)}{2m}\frac{t}{\hbar}} \langle \vec{k} | \psi_o \rangle \\ &= \frac{\sigma}{\sqrt{\pi}} e^{-iEt/\hbar + i\vec{k}\cdot\vec{r}_o - \frac{\sigma^2(\vec{k}-\vec{k}_o)^2}{2}} \end{aligned} \tag{3.5}$$

where $E = \frac{\hbar^2 k^2}{2m}$. Since the change over time is in phase only , the expectation values of momentum quantities remains unchanged (i.e. $\langle \vec{k}(t) \rangle = \vec{k}_o$ etc.) Transforming back to spatial coordinates, we find

$$\langle \vec{r} | \psi(t) \rangle = \frac{1}{\tilde{\sigma}(t)\sqrt{\pi}} e^{-iEt/\hbar} e^{i\vec{k}_o\cdot(\vec{r}-\vec{r}_o)} e^{-\frac{1}{2\tilde{\sigma}(t)^2}\left(\vec{r}-(\hbar\vec{k}_o t/m+\vec{r}_o)\right)^2} \tag{3.6}$$

where the width of the wavepacket is changing over time as

$$\tilde{\sigma}(t) = \sigma\sqrt{1 + it/t_D} \tag{3.7}$$

and t_D is the diffusing or spreading time

$$t_D \equiv m\sigma^2/\hbar \tag{3.8}$$

The expectation values of the position is now $\langle\vec{r}\rangle = \vec{r}_o + \hbar\vec{k}_o t/m = \vec{r}_o + \vec{v}t$, indicating the wavepacket center moves with velocity $\vec{v} = \hbar\vec{k}_o/m$ as expected; the wavepacket moves along a classical straight line trajectory with velocity $\vec{v}$. The expectation value of the wavepacket width is

$$\Delta r(t) = |\tilde{\sigma}(t)|/\sqrt{2} = \sigma\sqrt{1+(t/t_D)^2}. \tag{3.9}$$

The uncertainty relation is now $\Delta r\Delta k = \frac{1}{2}\sqrt{1+(t/t_D)^2} \rightarrow \frac{t}{2t_D}$, and is only minimum uncertainty at $t = 0$.

We end by noting that the propagator may be transformed to position space as well [59]; explicitly this is

$$\hat{\mathcal{U}}_{\vec{r}}(t) = -\frac{im}{2\pi t}e^{i\frac{m}{2\hbar t}[(x-x_o)^2+(y-y_o)^2]} \tag{3.10}$$

3.1.2 Wavepackets in a Uniform Magnetic Field

In a magnetic field in free space the evolution of the wavepacket remains classical, but the width oscillates. For any such quadratic Hamiltonian, that the semiclassical and quantum propagators are equivalent, and a Gaussian wavepacket remains Gaussian for all time [44]. Thus we can use classical intuition to consider the wavepacket in a uniform magnetic field.

The wavepacket can be thought of as built up of many semiclassical trajectories with a range of energies and momenta. In a uniform field, however, all the trajectories will return to their starting point after a cyclotron period, $T = 2\pi/\omega_c$. Thus the wavepacket will recur completely after a single cyclotron period. After a half a period, each trajectory will have its velocity reversed, and thus $\langle\vec{v}(T/2)\rangle = -\langle\vec{v}_o\rangle$. At this time the width of the wavepacket will have increased in size perpendicular to the velocity, but remain the same parallel to the velocity. This oscillation in wavepacket widths clearly will be periodic in the cyclotron period as well.

From [55], the equations of motion for the wavepacket can be written in terms of the center of the wavepacket,

$$\begin{aligned}\langle x\rangle &= \frac{1+\cos\omega_c t}{2}x_o + \frac{\sin\omega_c t}{2}y_o + \frac{\sin\omega_c t}{\omega_c}v_{x,o} + \frac{1-\cos\omega_c t}{\omega_c}v_{y,o}\\ \langle y\rangle &= -\frac{\sin\omega_c t}{2}x_o + \frac{1+\cos\omega_c t}{2}y_o - \frac{1-\cos\omega_c t}{\omega_c}v_{x,o} + \frac{\sin\omega_c t}{\omega_c}v_{y,o}\end{aligned} \tag{3.11}$$

which following from the classical equations of motion, and widths of the wavepacket

$$\begin{aligned}\Delta x &= \frac{1}{\sqrt{2}}\sqrt{\sigma^2\cos^2\omega_c t + \frac{2(1+\sin\omega_c t)^2}{(m\sigma\omega_c)^2}}\\ \Delta y &= \frac{1}{\sqrt{2}}\sqrt{\sigma^2\cos^2\omega_c t + \frac{2(1+\sin\omega_c t)^2}{(m\sigma\omega_c)^2}},\end{aligned} \tag{3.12}$$

where we've assumed that the wavepacket began as a circular wavepacket of width σ.

3.2 Channel Wavepackets

Many mesoscopic systems have narrow incoming or outgoing leads with a single transverse mode open. In addition, in moderate magnetic fields, the incoming states tend to be bunched up against the wall of an incoming lead as an edge state. Useful for setting up such simulations is a "channel wavepacket." The idea is to create a quasi-1D wavepacket in the channel $V(x)$, with some distribution in the longitudinal momentum, $f(k_y)$, which at each k_y occupies the lowest transverse mode of the system. Here we assume that the channel is long enough that evanescent waves are not present. We begin by considering a system in the Landau gauge, separated so that the magnetic field creates an effective transverse potential that modifies the channel potential [21],

$$\hat{H} = \frac{1}{2m}\left(\hat{p}_x^2 + (\hat{p}_y - eBx)^2\right) + V(x) \tag{3.13}$$

and separating $\psi(x, y) = e^{ik_y y}\phi_{k_y}(x)$, we have an effective 1D Hamiltonian

$$\hat{H}_x = \frac{\hbar^2 k_y^2}{2m} + \frac{\hat{p}_x^2}{2m} + \tilde{V}(k_y, x) \tag{3.14}$$

where the effective transverse potential $\tilde{V}(k_y, x)$ is momentum dependent,

$$\tilde{V}(k_y, x) = V(x) + \frac{m\omega_c^2}{2}(x - x_k)^2 \tag{3.15}$$

with displacement

$$x_k = \frac{\hbar k}{eB}.$$

The apparent effect of the magnetic field is to provide a momentum dependent force, as usual. In this way, we solve for the transverse modes $\phi_{k_y}(x)$ and transverse energies $E_x(k_y)$, now parameterized by k_y. In the absence of a magnetic field, these values are fixed and independent of momentum.

Given the separated transverse solutions, we know that the longitudinal solutions have free particle form, $\propto e^{ik_y y}$. So we may construct a channel wavepacket with energy distribution $f(E)$

$$\psi = \frac{1}{\mathcal{N}}\int_0^\infty dk_y \phi_{k_y}(x) e^{ik_y y} f^{1/2}[E(k_y)] \tag{3.16}$$

where $E(k_y) = E_x(k_y) + \frac{\hbar^2 k_y^2}{2m}$.

In the absence of a magnetic field, it is straightforward to build a Gaussian channel wavepacket

$$\psi = \frac{1}{\mathcal{N}}\phi_o(x) e^{ik_y y - \frac{(y-y_o)^2}{2\sigma^2}}$$

In the presence of a magnetic field, we need to build a wavepacket by hand by summing up over many longitudinal momenta,

$$\psi = \frac{1}{\mathcal{N}} \sum_{k_y} \phi_{k_y}(x) e^{ik_y y} f^{1/2}[E(k_y)] \tag{3.17}$$

as above. In each case, it is simplest numerically to normalize such a wavefunction on the grid, using $\mathcal{N} = \sum_{i,j} |\psi_{ij}|^2$.

3.3 Numerics

3.3.1 Wavepackets On the Grid

To begin we place the initial wavepacket $\langle \vec{x} | \psi_o \rangle$ on the grid. To do so for an analytic form in position space of the wavepacket (i.e. Gaussian), we evaluate the analytic form of the wavepacket on each grid point,

$$\tilde{\psi}_{i,j} = \psi_o(x_i, y_j)$$

and then normalize it

$$\psi_{i,j} = \tilde{\psi}_{i,j} \left[\sum_{i,j} |\tilde{\psi}_{i,j}|^2 \right]^{-1}$$

so that the wavefunction on the grid is normalized to the grid,

$$1 = \sum_{i,j} |\psi_{i,j}|^2.$$

If the initial state is defined in momentum space $\langle \vec{k} | \phi_o \rangle$, then we can prepare it in momentum space

$$\tilde{\phi}_{i,j} = \phi_o(k_{x,i}, k_{y,j})$$

and then take the FFT of it,

$$\tilde{\psi}_{i,j} = \mathcal{F}_x^{-1} \mathcal{F}_y^{-1} \tilde{\phi}_{i,j}$$

where we represent the Fourier transform from position space to momentum space by the operator $\mathcal{F}$. Then we normalize in position space as before. We note that on a small grid, this approach may produce a wavepacket that has significant amplitude throughout the position grid; in this case it is better to use an analytic position-space approximation for the initial state instead if possible.

3.3.2 Numerical Propagation

To propagate wavepackets numerically ,we exploit the fact the the kinetic energy operator $\hat{T} = \frac{\hat{p}^2}{2m}$ is diagonal in a momentum basis while the potential operator $\hat{V}$ is diagonal in a position basis. This allows us to use the "split-operator" method, by approximating

$$\hat{\mathcal{U}}(\delta t) = e^{-i(\hat{T}+\hat{V})\delta t/\hbar} \approx e^{-i\hat{V}\delta t/\hbar} e^{-i\hat{T}\delta t/\hbar}, \tag{3.18}$$

which is the quantum equivalent to Euler's method of propagation. To improve convergence, we can switch to a Leap-Frog approach,

$$\hat{\mathcal{U}}(\delta t) \approx e^{-i\hat{V}\delta t/2\hbar} e^{-i\hat{T}\delta t/\hbar}\, e^{-i\hat{V}\delta t/2\hbar}. \tag{3.19}$$

If before propagation, we "prepare" the initial state, $\tilde{\psi}_o = e^{i\hat{V}\delta t/2\hbar}\psi_o$ and correct the final state $\psi(t) = e^{-i\hat{V}\delta t/2\hbar}\tilde{\psi}(t)$, then we can use the Euler propagator from equation 3.18 instead, reducing the number of operations while increasing the accuracy of the propagation. Note that ψ now is not quite the physical ψ at each time step, but instead would need to be corrected as in the final step; however, the error is using the slightly unphysical ψ is very small, and the computational savings usually worthwhile in ignoring the discrepancy.

If an operator $\hat{A}$ is diagonal in some basis, so is $e^{\hat{A}}$ in that basis. Thus we may express the propagator factors as diagonal in the momentum and position bases. The work then comes down to changing bases from position to momentum. If we discretize the wavefunction on a grid, then we can make use of the Fast Fourier Transform (FFT) to change between momentum and position bases efficiently. We again will represent the Fourier transform from position space to momentum space by the operator $\mathcal{F}$. Then the numerical propagation of the wavepacket is

$$\psi(t) \approx e^{-i\hat{V}\delta t/2\hbar} \left[\mathcal{F}^{-1} e^{-i\hat{T}\delta t/\hbar} \mathcal{F} e^{-i\hat{V}\delta t/\hbar}\right]^N \left(e^{i\hat{V}\delta t/2\hbar}\psi_o\right) \tag{3.20}$$

where $N = T/\delta t$, the total number of steps. Each multiplication is done as a vector operation, since the operators are diagonal in each basis, and the basis transformation from position to momentum and back is performed by FFT. The basic process is quite efficient numerically.

3.3.3 Numerical Propagation in a Uniform Magnetic Field

In a uniform magnetic field, the propagator cannot be segmented into T and V parts alone. However, in a uniform field the Hamiltonian will be separable into terms that are diagonal in the mixed basis sets (x, y), (k_x, y) and (x, k_y). In the symmetric gauge (for example) the Hamiltonian may be written as

$$\hat{H} \;=\; \frac{1}{2m}\left[(\hat{p}_x + m\omega_c y/2)^2 + (\hat{p}_y - m\omega_c x/2)^2\right] + V(x)$$

$$= \left[\frac{\hat{p}_x^2}{2m} + \frac{\omega_c}{2}\hat{p}_x y\right] + \left[\frac{\hat{p}_y^2}{2m} - \frac{\omega_c}{2}\hat{p}_y x\right] + \left[\frac{m\omega_c^2\rho^2}{2} + V(x,y)\right] \quad (3.21)$$

where $\rho = \sqrt{x^2+y^2}$. This last form helps to identify how we want to split the Hamiltonian. Defining the operators

$$\begin{aligned} \hat{T}_{k_x,y} &\equiv \frac{\hat{p}_x^2}{2m} + \frac{\omega_c}{2}\hat{p}_x y \\ \hat{T}_{x,k_y} &\equiv \frac{\hat{p}_y^2}{2m} - \frac{\omega_c}{2}\hat{p}_y x \\ \hat{V}_B &\equiv \frac{m\omega_c^2\rho^2}{2} + V(x,y) \end{aligned} \quad (3.22)$$

we note that these are diagonal in either the position basis, or in a mixed position and momentum bases. Defining the partial Fourier operators, $\mathcal{F}_x$ and $\mathcal{F}_y$ which only transform one of the variables to momentum space, the numerical propagation looks like

$$\psi(t) \approx e^{-i\delta t/\hbar \hat{V}_B/2}\left[\mathcal{F}_y^{-1} e^{-i\delta t/\hbar \hat{T}_{x,k_y}} \mathcal{F}_y \mathcal{F}_x^{-1} e^{-i\delta t/\hbar \hat{T}_{k_x,y}} \mathcal{F}_x e^{-i\delta t/\hbar \hat{V}_B}\right]^N \left(e^{i\delta t/\hbar \hat{V}_B/2}\psi_o\right). \quad (3.23)$$

Again the bulk of the work is done in FFT numerics, which are quite fast. Propagating in a magnetic field takes about ~ 1.7 the time as $B = 0$ propagation, since the 1D FFT transforms are a little faster than the full 2D transforms.

A significant advantage of the split operator approach is that it is inherently symplectic and unitary in nature. While other methods approximate the kinetic energy operator in terms of off-diagonal matrix elements, in transforming via FFT to the correct basis, we avoid any errors in the propagation due to taking numerical derivatives. The evolution operators $e^{-i\hat{T}\delta t/\hbar}$ and $e^{-i\hat{V}\delta t/\hbar}$ are unitary, and as such the probability on the grid is conserved throughout the propagation. This invariance has significant advantages in the same way that symplectic evolution for classical systems has the advantage of being an area-preserving map. On the grid, the evolution process represents a Hamiltonian discrete map, and thus is exact “on the grid” (space and time grid). The error comes from the time discretization of the evolution operators, due to the finite time step and finite grid. Decreasing the time step is of linear cost, and in practice adequate convergence can be achieved with a reasonably large time step; in fact the limit on the time step size tends to come instead from limiting the reflection from any absorbing regions, discussed below.

The main disadvantage of the approach is that to take advantage of the FFT, the grid needs to be of fixed spacing, and due to the periodic nature of the FFT, any amplitude that leaves the grid on one side enters on the other. While this can usually be handled by creating “walls” at the edges or with absorbing boundary conditions, the same problem is true in momentum space. This creates the odd behavior that significantly hard walls or magnetic fields can move the wavepacket in momentum space off of the k-space grid. This results in the amplitude wrapping around to negative momenta. Thus the particle can reverse direction without a potential present in a completely unphysical way. Since the maximum k value is

$$k_{max} = \frac{\pi}{\Delta x}$$

by increasing the number of points on the grid for the same spatial system size, one can increase the k grid size. However, this scales as N^4, and means that the grid must have a minimum size to accommodate reasonable momenta, and that in strong magnetic fields or billiard systems the grid spacing must be small enough that the grid size may become prohibitively large.

3.3.4 Absorbing Boundaries

In order to avoid the problems that the periodicity of the FFT present, we need to remove amplitude from the system when it leaves the system, or else it will wrap around and enter from the opposite side. To do so, we introduce a complex absorbing potential (CAP) $W(\vec{r})$ that lies only outside of the interaction region. As an example (though a very useful one) we choose a harmonic potential that ramps up for positive $x > x_S$,

$$W_x \equiv \Theta(x - x_S)\alpha(x - x_s)^2. \tag{3.24}$$

We add this potential on the negative imaginary axis to the Hamiltonian

$$\hat{\hat{H}} = \hat{H} - iW. \tag{3.25}$$

When propagating the wavepacket, the propagator in position space acquires an additional factor,

$$\hat{\mathcal{U}}'(\delta t) \approx e^{-W\delta t/\hbar} e^{-i\hat{V}\delta t/\hbar} e^{-i\hat{T}\delta t/\hbar}. \tag{3.26}$$

Thus the effect of this complex absorbing potential is to attenuate the amplitude of the wavefunction in the absorbing region. This additional term is clearly non-unitary, since the new Hamiltonian is non-Hermitian.

While the connection with complex absorbing potentials in clear, in general we will treat the attenuation factor as an additional, non-physical numerical process. The attenuation operator for a semi-harmonic CAP at $x = x_S$ is explicitly

$$\hat{A} = e^{-\alpha\delta t/\hbar\Theta(x-x_S)(x-x_s)^2} \tag{3.27}$$

and is diagonal in the position basis. The propagation method is to propagate as normal, and then attenuate at the end of each propagation cycle,

$$\psi(t) \approx e^{-i\hat{V}\delta t/2\hbar}\left[\hat{A}\,\mathcal{F}^{-1}e^{-i\hat{T}\delta t/\hbar}\mathcal{F}e^{-i\hat{V}\delta t/\hbar}\right]^N \left(e^{i\hat{V}\delta t/2\hbar}\psi_o\right). \tag{3.28}$$

After each attenuation, it makes sense to compute the lost probability

$$\Delta P(t) = |(1 - \hat{A})\psi(t)|^2. \tag{3.29}$$

This measures the rate of loss into the absorbing region, and can be integrated over time,

$$P_{lost} = \sum_{n}^{N=T/\delta t} \Delta P(t_n), \tag{3.30}$$

to calculate the total probability lost into the absorbing region.

In general one would want a number of complex absorbing regions in order to discriminate probability loss into different regions, hence the attenuation step would be

$$\tilde{\psi} = \hat{A}_1 \hat{A}_2 .... \hat{A}_m \psi(t), \tag{3.31}$$

where by applying each separately we can keep track of the probability loss in each absorbing region. In this case, we would measure a number of probability loss values $P_{loss,n}$.

Since every other operator acting on the wavefunction is unitary, and the wavefunction initially has unit probability, then probability is conserved to machine precision. In other words,

$$1 = \sum_{i,j} |\psi_{i,j}|^2 + \sum_{n} P_{loss,n} \tag{3.32}$$

holds exactly at each time step, by construction. This is a real advantage of the split-operator method, since the probabilities $P_{loss,j}$ can be used to determine aggregate scattering coefficients.

Numerical Dephasing

As a related technique, one can simulate dephasing by exponentially removing amplitude from the system. The attenuation operator can be modified by adding an overall imaginary constant potential, such that we have a trivial attenuation operator

$$\hat{A}_o = e^{-\delta t / t_\phi}, \tag{3.33}$$

where t_ϕ is the dephasing time. If one knows the incoherent scattering coefficients of a system, then one can build a mixed coherent/incoherent simulation of the system by attenuating globally in this fashion, and then accounting for particle conservation incoherently in the scattering coefficients.

3.4 Flux Measurements

To measure the scattering coefficients in the system, we need to measure the flux or equivalent through surfaces. Because we are often dealing with magnetic fields, we will derive the flux operator from first principles; we will adapt the approach from [53, 9] but generalize it. The occupation of some region can be characterized by some function Θ_S, where $\Theta_S = 1$ if the particle is in the region, i.e. beyond some surface S, and 0 elsewhere. Then the change in occupancy of the region follows from the Heisenberg equation

$$\frac{d}{dt}\Theta_S = \frac{i}{\hbar}[\hat{H}, \Theta_S]. \tag{3.34}$$

The time derivative of the occupancy of some region is the total flux into the region, so the flux operator across some surface S may be written as

$$\hat{\Phi}_S \equiv \frac{i}{\hbar}[\hat{H}, \Theta_S]. \tag{3.35}$$

We choose the obvious choice for the function $\Theta_S = \Theta(\vec{r} - \vec{r}_S)$, the step function, or Heaviside function, and $\vec{r}_S$ is some parametric function that traces the surface boundary. Then we have that the flux operator is

$$\hat{\Phi}_S = \frac{i}{\hbar}[\hat{H}, \Theta_S] = \frac{im}{2\hbar}[\hat{v}^2, \Theta(\vec{r} - \vec{r}_S)]$$

since Θ_S is a function of position alone. The momentum operator is

$$\hat{p} = i\hbar\nabla$$

while the velocity operator is

$$\hat{v} = \frac{1}{m}(i\hbar\nabla - q\vec{A}/c)$$

with $\vec{A}$ the vector potential. The momentum operator and the function Θ_S have the commutator relation

$$[\hat{p}, \Theta(\vec{r} - \vec{r}_S)] = i\hbar\nabla\Theta(\vec{r} - \vec{r}_S) = i\hbar\hat{n}\delta(\vec{r} - \vec{r}_S)$$

where $\hat{n}$ is the outgoing normal to the surface. From this one can easily show that the commutator for the flux operator becomes

$$[\hat{v}^2, \Theta(\vec{r} - \vec{r}_S)] = \frac{\hbar}{im}\left[\vec{v}_\perp\delta(\vec{r} - \vec{r}_S) + \delta(\vec{r} - \vec{r}_S)\vec{v}_\perp\right] \tag{3.36}$$

and hence the flux operator is

$$\hat{\Phi}_S = \frac{1}{2}\left[\hat{\vec{v}}_\perp\delta(\vec{r} - \vec{r}_S) + \delta(\vec{r} - \vec{r}_S)\hat{\vec{v}}_\perp\right] \tag{3.37}$$

where $\hat{\vec{v}}_\perp = \hat{n}\cdot\hat{\vec{v}}$ is the velocity operator normal to the surface S.

We can use this definition of the flux operator to track the flux across some surface in our system. In the following, we assume that there is just one relevant incoming or outgoing mode, or that the experimentally relevant quantity is a sum over these modes. Hence we don't take care to track any indices on these modes. It would be straightforward to extend the following to include projections over modes of the "leads" of the continuum regions.

3.4.1 Flux Surface Measurements

In general it is easier on a grid to define flux surfaces that align with the grid directions. To calculate $\vec{v}$ on a (for example) flux surface at $y = y_j$, we must compute both $\frac{\partial \psi}{\partial y}$ and ψ on the surface. Numerically, it is better to use a fourth order or higher numerical derivative. Taking the grid spacing to be $(\Delta x, \Delta y)$, then if we take our surface at the center at index j, then the derivative at fourth order is

$$\frac{d\psi_{i,j}}{dy} \approx \frac{1}{12\Delta y} \left[8(\psi_{i,j+1} - \psi_{i,j-1}) - (\psi_{i,j+2} - \psi_{i,j+2})\right] \tag{3.38}$$

so that the velocity across the surface is

$$v_{i,j}(t) \approx \frac{1}{m\psi_{i,j}} \left[i\hbar \frac{d\psi_{i,j}}{dy} - \eta q B_z x_i \psi_{i,j} \right] \tag{3.39}$$

where in the symmetric gauge $\eta = 1/2$, in the Landau gauge in the y-direction, $\eta = 1$, and in the x-direction $\eta = 0$. The charge current density across the surface is hence

$$j_{i,j}(t) = \frac{q}{\Delta x} v_{i,j}(t) |\psi_{i,j}(t)|^2 \tag{3.40}$$

and the total probability flux is

$$\Phi_{y=y_j}(t) = \sum_i v_{i,j}(t) |\psi_{i,j}(t)|^2. \tag{3.41}$$

3.4.2 Energy-Resolved Flux

While we can calculate the flux over time as the particle propagates, the energy resolved flux, needed to calculate scattering coefficients in energy, requires the entire history of the amplitude on the surface. Thus we must track both the amplitude $\psi_{i,j}(t)$ and the velocity $v_{i,j}(t)\psi_{i,j}(t)$ on the surface. Once that's done, we calculate the Fourier transforms

$$\psi_{i,j}(E) = \int_0^T e^{iEt/\hbar} \psi_{i,j}(t) dt$$

and (using the shorthand that $\hat{v}\psi \rightarrow v\psi$)

$$v\psi_{i,j}(E) = \int_0^T e^{iEt/\hbar} v_{i,j}(t) \psi_{i,j}(t) dt,$$

The energy resolved flux is hence

$$\Phi(E)_{y=y_j} = \sum_i \psi^*_{i,j}(E) v\psi_{i,j}(E). \tag{3.42}$$

If we take the inverse Fourier transform of this, we get the time correlation function of flux across the surface,

$$\Phi_{y=y_j}(\tau) = \frac{1}{2\pi}\int_0^\infty e^{-iE\tau/\hbar}\Phi_{y=y_j}(E)dE. \tag{3.43}$$

We also note that by the Fourier power relations that

$$P_{S,total} = \int_o^T \Phi_S(t)dt = \int_o^{E_{max}} \Phi_S(E)dE \tag{3.44}$$

since the total probability through the surface must be the same in either representation. This provides a useful check of convergence and of the numerics.

3.4.3 Flux Measurement By Absorbing Boundaries

The tracking of amplitude on a flux surface in the preceding fashion is very convenient since the data that needs to be kept to resolve the flux in energy is minimal. However, a drawback to the method is that it uses numerical derivatives to calculate flux. For quickly changing, or more relevantly, recurring flux, this can lead to significant numerical instabilities, and can even lead to negative probability measurements.

When such a problem can't be surmounted by changing the grid spacing, one may need to resort to a different, more accurate but much more compute and memory intensive approach. Following Jäckle and Meyer [53, 9], the absorbing region can be used to measure energy resolved flux instead of an explicit flux surface. The edge of the absorbing region becomes the ad-hoc flux surface in this case. We consider the absorbing region as an additional complex potential W such that

$$\hat{\hat{H}} = \hat{H} - iW.$$

We demand that W vanishes outside the interaction region; in analogy with the flux operator derivation, we may define (for instance)

$$W_x \equiv \Theta(x - x_S)\alpha(x - x_s)^2 \tag{3.45}$$

for an absorbing region at that positive x edge of the interaction region. We assume that the system has been tuned so that the complex absorbing potential (CAP) $-iW$ is non-reflecting. Then if the CAP is outside the interaction region, we can write the flux through the surface at x_S as

$$\begin{aligned}\hat{\Phi}_S &= i[\hat{H}, \Theta_S] \\ &= i[\hat{\hat{H}}, \Theta_S] \\ &= 2W + i(\hat{\hat{H}}^\dagger - E)\Theta_S - i\Theta_S(\hat{\hat{H}} - E).\end{aligned} \tag{3.46}$$

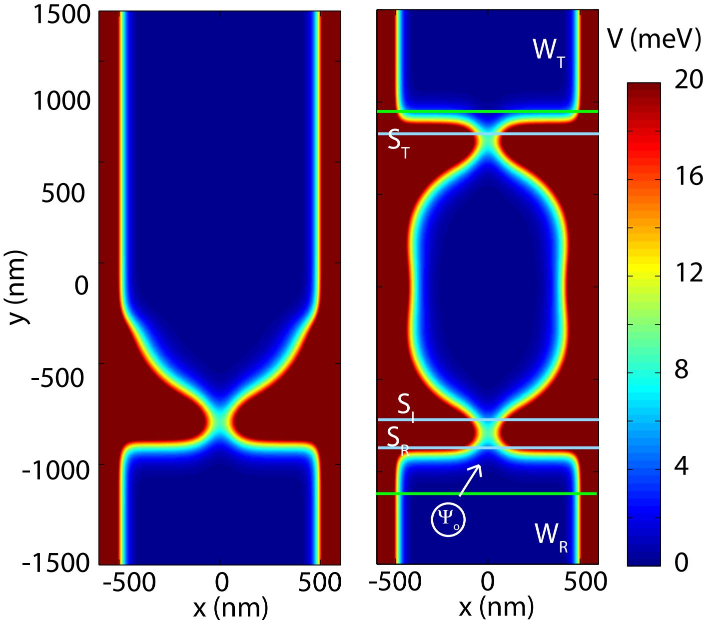

Figure 3.1: The lateral quantum dot stadium potential used as an example. CAPs W_T and W_R start at the green lines, and the light blue lines are the flux surfaces. The initial wavepacket starts at the bottom and travels toward the QPC where one mode transmits into the stadium dot.

By inserting in the wavefunction for the wavepacket and assuming that the wavepacket was localized at time $t = 0$ one can show that [53, 9] the transmission coefficient into the absorbing region is

$$T_\mu = \frac{4\pi}{f(E)} \text{Re} \int_0^\infty g_\mu(\tau) e^{-iE\tau/\hbar} d\tau, \tag{3.47}$$

where $g(\tau)$ is correlation function in the absorbing region indexed by μ,

$$g_\mu(\tau) \equiv \int_0^\infty \langle \psi(t+\tau) | W_\mu | \psi(t) \rangle, \tag{3.48}$$

and $f(E)$ is the energy distribution of the initial state. Thus the coefficient normalizes the outgoing transmission by the energy distribution of the initial state. If we are dealing with ratios between transmission coefficients, then we can ignore the normalizing factor. This is useful for calculating the change in transmission with and without a structure in place, as in Chapter (4).

3.5 Wavepacket Simulations

In this Section, we consider a typical mesoscopic application of a wavepacket code. The system to be measured is a two-terminal system comprised of a stadium-shaped quantum dot coupled to the leads by QPCs each with a single open mode at the energy of interest. The system is depicted in Figure (3.1) in the right panel, and is reminiscent of an experiment by Marcus *et.al.* [74]. Here the system has $N_x = 256$ and $N_y = 512$ grid points, and with $\Delta t = 2000$ (a.u.) is run for $N_t = 4000$ time steps. To the system we add a perpendicular magnetic field $B_z = 50$ milliTesla, and we take the electron mass as that in GaAs, $m = 0.067$.

In performing scattering simulations, one must define what the is difference between the system without the scatterer, and with the scatterer. In nuclear or atomic systems, or more generally in open systems, the system without the scatterer is usually taken to be a free system. In mesoscopic systems, when analyzed using Green function techniques and finite size leads [21], the non-scattering system is taken to be empty leads, but of a finite width. To do the same with wavepackets would take some effort, as each mode would need a wavepacket to be run. When a single-mode or tunneling QPC is involved however, this effort is unnecessary: only one mode of the QPC is available, and as long as the wavepacket can populate that mode, then a single wavepacket is adequate. Furthermore, when the QPC is single moded, and the conductance plateau wider than the range of energies we are interested in, then we can utilize the QPC as the "lead"; the density of states $g(E)$ is flat and the transmission $T = 1$ when on the first plateau.

Thus we will take our non-scattering system to be a single QPC on the first plateau, with known conductance $G = 2e^2/h$. This system is created by removing any mechanism for reflecting beyond this single QPC. In our example system, this setup is shown in the left panel of Figure (3.1). In Chapter (4) we accomplish this by removing any structure beyond the QPC. In Chapter (7) we can turn off the magnetic field to eliminate reflection.

Incident Flux and the Non-Scattering System

In this example simulation, we consider the system with and without the dot in place, but with the incoming QPC in place. A wavepacket with width $\sigma = 88$ nm, corresponding to a energy width with temperature of $kT = 10$ K is launched at an angle toward the incoming QPC. The flux through the QPC is measured up to a time $t_{inc} = 3.5 \times 10^5$ (a.u.), after which the wavepacket has entered the system; this incident time is identified by eye, or by plotting the probability in the system as a function of time, as in Figure (3.2A). In addition, we can read that the total probability to enter the system is $P_{inc} = 0.00218$, which is exact "on the grid." This value can be used to check the accuracy of flux surface measurements. The time resolved flux across the incident flux surface is shown in Figure (3.2C) for both cases; the integral of this plot over time is $\int \Phi_i(t)dt = 0.00210$, indicating a small 4% total error in the flux surface measurement (as is to be expected with a fairly coarse grid).

The energy resolved incident flux is shown in Figure (3.2B) for the non-scattering and

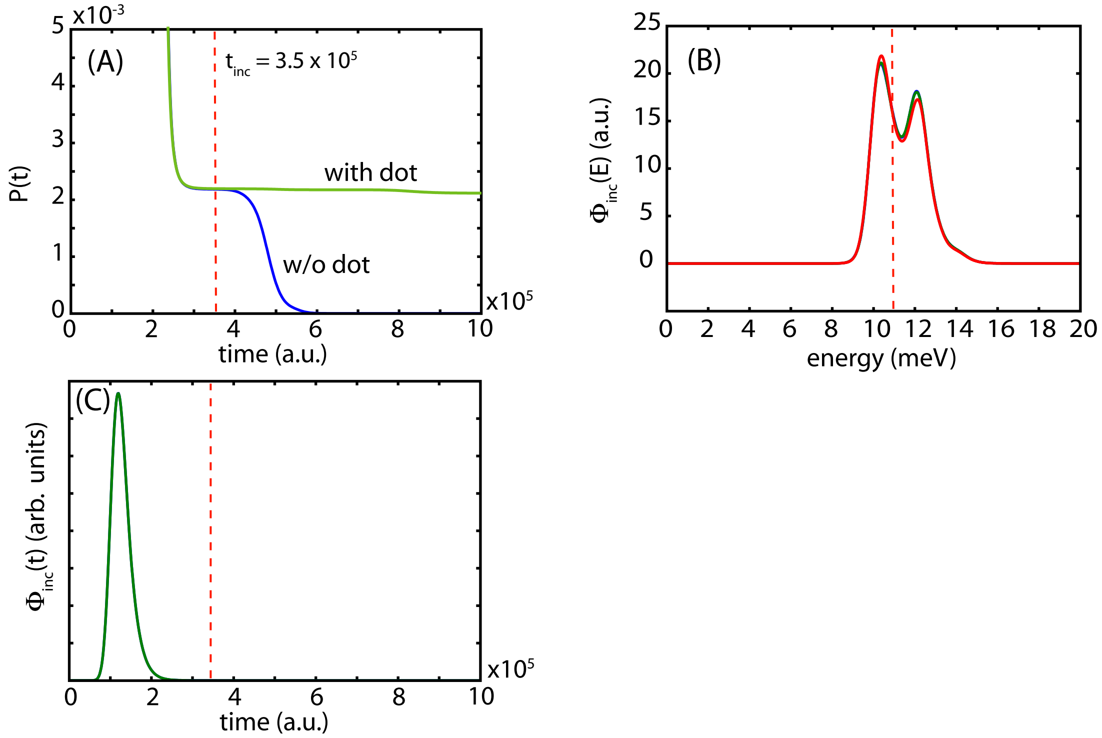

Figure 3.2: Incident flux of the wavepacket over time or energy. (A) is the probability left in the system over time; the plateau indicates that the wavepacket has entered, but has not yet left the interaction region, and sets the $t_{inc} \approx 3.5 \times 10^5$ (a.u.). (B) shows the energy distribution of incident flux. Since the wavepacket itself has a non-uniform energy distribution, the first plateau at $E = 11$ meV is multiplied by the distribution. (C) shows the incident flux through the initial QPC as a function of time.

scattering case, as calculated by the flux surface approach, and as calculated in the non-scattering case by the absorbing boundary approach. All three cases show the plateau structure of the QPC, here with first plateau at $E \approx 11$ meV, multiplied by the energy distribution of the initial wavepacket. Both flux surface measurements are almost exactly the same, but the absorbing boundary measurement differs by a small amount. The error in the flux surface measure is due to the numerical derivative taken at the flux surface, and will decrease (somewhat) with an increase in the fineness of the grid.

The Scattering System

Now that we have a handle on the incident flux and the "non-scattering" quantities to which we compare the scattered results, we can propagate the wavepacket into the full system. For

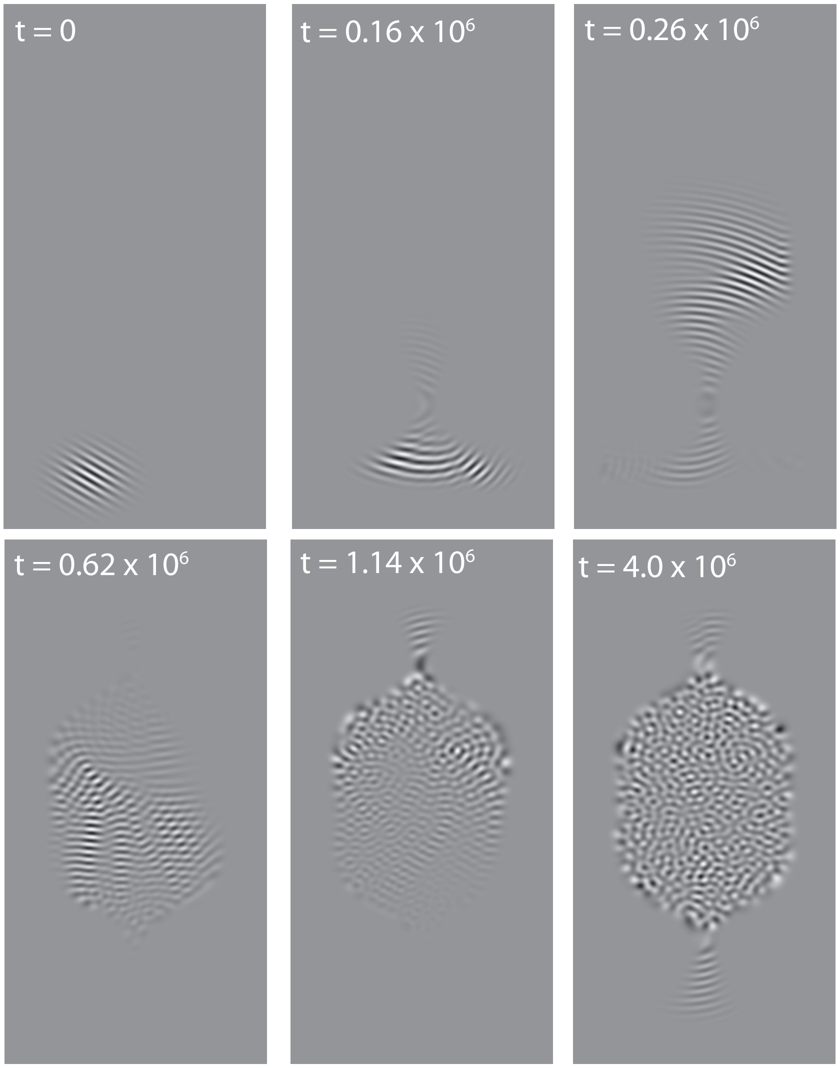

Figure 3.3: States of the wavepacket in the stadium dot over time. By the end, the states within the dot are fairly chaotic in appearance.

short times the flux measurements will be nearly the same (as we have seen already) because the electron has yet to “see” the changes in the potential further away from the initial position. In Figure (3.3) we plot a series of snapshots of the real part of the electron wavefunction over time. The initial wavepacket in the first frame collides with the source QPC in the second, and bounces within the dot in a fairly classical fashion to begin, but after a time settles down to a more chaotic appearance in the dot.

In Figure (3.4) we plot the transmission coefficient for the dot, with respect to the source

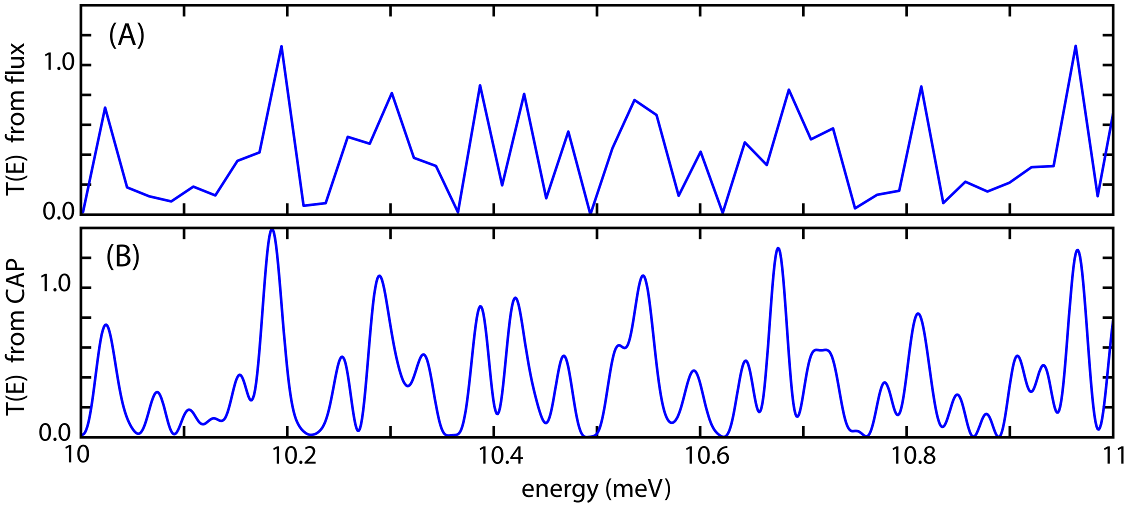

Figure 3.4: Transmission coefficient through the dot, as compared to the case with only the incident QPC, calculated by (A) flux surface measurement and (B) absorbing boundaries (CAP) approaches. In both cases the spectrum is resolved and agrees over this range of energies, but there is a normalization issues in both cases, of the same magnitude. This normalization error is due to the fact that the dot will retain amplitude for long times beyond those that are numerically measurable with this approach.

QPC alone, as calculated by flux surface measurements (A) or absorbing potential (B) approaches. In the flux surface case,

$$T_{flux}(E) = \frac{\Phi_T(E)}{\Phi_I(E)},$$

where we scale the transmitted flux by the incident flux through the source QPC. Since the incident flux in the scattering case is the same as the transmitted flux in the non-scattering (i.e. open) case, either can be used here. In the absorbing potential approach,

$$T_{CAP}(E) = \frac{\Phi_T(E)}{\Phi_{o,T}(E)},$$

where $\Phi_{o,T}(E)$ is the transmitted flux, as calculated by CAP, with the open dot. In both cases there is a normalization issue, since $T(E) \leq 1$ for all energies. However, this normalization issue is present in both cases. It is most likely due to the fact that the closed leaky dot will retain amplitude out to long times, which cannot be pragmatically measured numerically.

We have three choices to resolve this issue. We can push the numerics to try to converge the spectrum in the region of interest. We can add in dephasing to reduce the amplitude in the dot, which will artificially widen the peaks somewhat, and cause the correlation function $g(\tau)$ in the absorbing boundary or the flux $\phi_T(t)$ to converge more rapidly, throwing off the normalization in a more controlled fashion. Lastly, we can assume that the normalization error is slowly changing in E, and ignore it. The latter approach is the approach of choice when the most important signal is not the absolute spectrum itself, but the spectral structure, particularly when considering the system over a range of parameters such as B as in Chapter (4) or tip position, as in the next Section or Chapter (7).

The normalization error in $T(E)$ is rarely an issue in very open systems with short dwell times, but when long dwell times and sharp resonances are important, the truncation of the dynamics of the system in time becomes an issue in the energy spectrum. The systematic resolution of this convergence is still, to our knowledge, an open problem.

3.6 Tip Scan Simulations

To simulate a tip scanning experiment, we use the approach of the last Section, but add a localized potential that approximates the SPM tip, and parametrically move it around for each run. This will be very CPU intensive, and thus we may need to compromise on the grid size and the accuracy of the spectrum, since in such a simulation it is not the spectrum $T(E)$ that we are interested in, but spatial patterns $T(x, y)$ at finite temperature. One may simulate finite temperature using a thermal wavepacket to automatically thermally average the results [50], or the flux can be energy resolved as in previous Sections, and then thermally average explicitly.

One advantage of the tip scan approach is that the placement of the tip will minimally effect the flux through the source QPC or similar structure; thus any error in determining the incident flux into the system is a systematic error that is uniform across $T(x, y)$, and thus will not effect the spatial pattern appreciably. In general the signal in the spatial pattern will also be much larger than the error in the reflectance measurement as well. The upshot is that, to within an overall error across the entire scan, the signal of spatial variation in the transmission is clean and robust.

In Figures (3.5) and (3.6) we present some results of tip scan simulations, using flux surface measurements to determine the conductance. Since these are both two-terminal systems, we use the reflectance R to measure the conductance through the system. This has the advantage that the amplitude beyond the QPC in the open system does not need to be carefully measured as it is absorbed, since we can use the reflectance R back through the source QPC instead.

Figure (3.5) depicts the results of a tip scan simulation in a Young's double-slit system, as conceived of by the Westervelt group at Harvard. The position coordinate is the tip position. The coherent point source is a single moded QPC, and two other QPCs form the double slit. While the classic interference pattern is visible as one scans in the x-direction, longitudinal back-scattering fringes are visible as well, with spacing $\lambda_F/2$ (see Chapter 6).

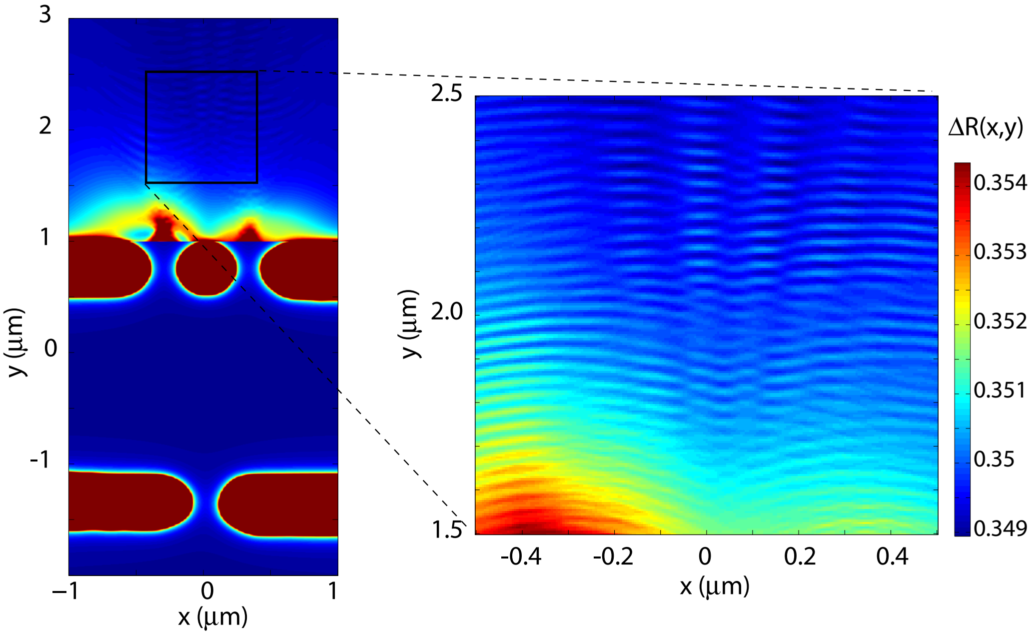

Figure 3.5: A tip scan simulation of a Young's double-slit experiment in a 2DEG system. The Lorentzian tip is $2\sigma = 160$ nm wide and at center $V_o = 4E_F$ (i.e. $\eta = 4$ from Chapter 5), but resolves fringes ~ 30 nm $= \lambda_F/2$ in size.

Figure (3.6) shows a two-terminal system in which a circular gate of radius 500 nm has been placed at a distance of 1800 nm from the source QPC, and energized in order to provide a large back-scattering amplitude. In (A) we show a simulation version of the potential, overlaid by a low resolution tip scan simulations $R(x, y)$; there has been included a small strong scatterer to the left of the circular gate as well. The caustics shed by the large scatterer are visible as hyperbola-like structures beyond the gate (see Chapter 5 for similar structures). In (B) we show the experimental layout of the experiment, along with some data showing ellipse shaped fringe structures. See Chapter (6) for more such experimental results. In (C) and (D) we present a higher resolution simulation of the tip scan $R(x, y)$; three patterns are visible here: circular fringes due to back-scattering, elliptical fringes due to trajectories which reflect off the circular gate, and more complex structures due to trajectories that scatter from the strong impurity on the left. See Chapter (6) for a semiclassical theory that can be used to understand the patterns.

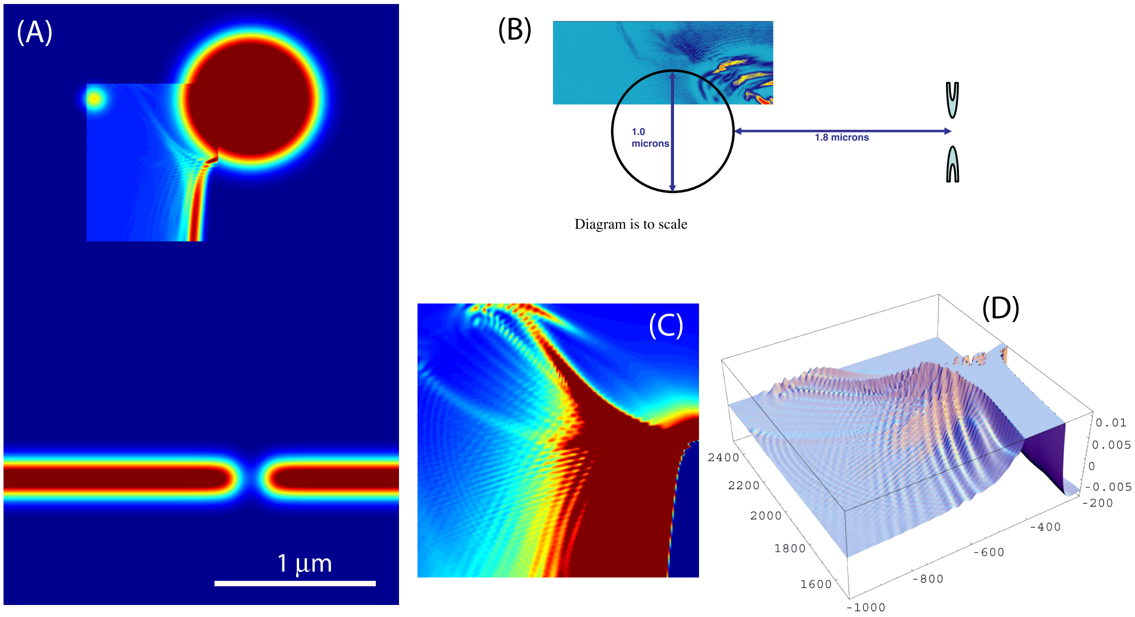

Diagram is to scale

Figure 3.6: (A) A tip scan simulation of a system with a large circular scatterer and a small impurity. The tip scan is inset. (B) the equivalent experimental system and elliptical fringes. (C) close up of the simulated fringe structure. (D) 3D rendering of the simulation. At least three types of fringes are evident. The tip parameters were equivalent to Figure (3.5).

Chapter 4

Spectroscopy of Scarred States in a Large Quantum Dot

Inspired by some experimental results found in a study done by Dominik Zumbuhl in the Marcus group at Harvard, we study the dynamics of an electron in a large, leaky quantum dot [58, 57]. A lateral quantum dot device was fabricated that coupled a small spectrometer (in fact a small quantum dot) to a larger quantum dot, which was energized in such a way as to make a leaky, Fabry-Perot -like cavity in two dimensions. By "leaky", we mean that the large dot has junctions to the leads that are open to many transverse modes, so that the an electron can enter or leave the large dot with relative ease. The small quantum dot acts as a device that could measure the local density of states LDOS(E, B) in the large dot at the tunnel junction. The small dot is a single electron dot, and can contain at most a single electron at any given time. Hence the small dot possesses a single narrow resonance at a specific energy E_R with a narrow line shape; this means that this small dot conducts appreciable current only over a narrow range of energies about E_R, and hence acts as a spectrometer. This feature of the small dot allows the experiment to run at large bias, and allows the current and hence the transmission through the system to be measured up to 1 meV below the Fermi sea, and hence to resolve the transmission of the system without the need to convolve over the Fermi function. While such devices had been created before [56] and used to measure the local density of states LDOS(E, B), this was performed in a vertical quantum dot, and did not possess any large scale interference structure.

The small and large dots were connected in series as a two-terminal device, with the tunnel junction between the two at the center, and the current through system was measured. The experimentally measured currents revealed bands of strong interference oscillations in energy versus perpendicular magnetic field, implying that the device was probing the effects of periodic orbits within the large quantum dot, and that as the energy or magnetic field was modified, the phase accumulated along the orbit changed rapidly, creating oscillations in the current.

In a toy model sense, the phase accumulated around the orbit due to the normal dynamics of the particle has a contribution from the energy

$$\phi_E = kL = \sqrt{2mE}L/\hbar,$$

where L is the length of the orbit, and from the flux enclosed by the orbit

$$\phi_B = qAB/\hbar$$

where the area enclosed A has a directionality consistent with the "right-hand rule". The total phase is hence

$$\phi = \sqrt{2mE}L/\hbar + qAB/\hbar \tag{4.1}$$

where we've ignored any topological (i.e. Maslov) phase. The oscillations in interference bands should lie along lines of constant phase, and hence should have slope

$$\frac{dE}{dB} = -\frac{L}{2qA}\sqrt{\frac{2m}{E}}. \tag{4.2}$$

The rate of change of the phase as we vary the energy is

$$\frac{d\phi}{dE} = \frac{mL}{\hbar^2 k} \tag{4.3}$$

thus if we linearize about a given energy, the oscillation will cycle with an energy spacing

$$\Delta E = \frac{2\pi\hbar^2 k}{mL} = \frac{h^2}{m\lambda L}. \tag{4.4}$$

As a function of magnetic field, the rate of change of the phase is simpler:

$$\frac{d\phi}{dB} = \frac{qA}{\hbar} \tag{4.5}$$

with linearized spacing

$$\Delta B = \frac{h}{qA}. \tag{4.6}$$

The semiclassical assumption, that the fastest varying parameter is the phase, holds well in this system, and so locally we can predict the slope without knowing how the area or length varies. For small magnetic field, we can immediately predict that the slope of the lines will become horizontal, and that the spacing of the oscillations will be due to the variation in energy alone.

In this Chapter, we begin by describing the device, and then derive a simple model of resonant tunneling through the spectrometer which highlights its role as a probe of the local density of states LDOS(E,B). We then use a billiard model of the large quantum dot to predict the structure of the interference bands with some success. Failures in the billiard model prompt us to consider wavepacket simulations in a more realistic potential, which produces striking agreement with experiment. Finally we consider the classical dynamics of the system and search for periodic orbits in order to gain a deeper intuition of the features of the data and the system.

4.1 Experimental Setup and Results

The device used in the experiment is shown in Figure (4.1). The device consists of two lateral quantum dots produced in a 2DEG at the junction of between a GaAs/AlGaAs heterostructure. The gates applied to the surface of the GaAs chip are energized so as to create a confined region of the order of the Fermi wavelength. The material and large quantum dot portion of the device has been described in [117]. In particular, the 2DEG was located 105 nm below the surface, the bulk electron density was measured to be $n \sim 10^{11}\text{cm}^{-2}$, and the mobility was $\mu \sim 10^5\text{cm}^2/\text{Vs}$, implying a mean free path $l \sim 1.5$ μm, and implying ballistic transport in the large dot; the electron effective mass is $m = 0.067 m_e$ in this material. The current from the large dot through the small dot was measured in series; the two open quantum points in the far end of the large quantum dot were held at variety of open transverse modes, and the leads from the QPCs tied together, implying a two-terminal measurement of the series resistance of the small and large dots. A perpendicular magnetic field was applied to the system, and swept in strength from -1 to 1 Tesla.

In the experiment, the energy resolution of the measurement, whether limited by temperature or by the line width of the spectrometer, is fine enough to resolve most spectral structure in the large dot (i.e. $kT \sim \Gamma \lesssim \Delta$). The large dot, with area $A \sim 1$ μm^2, will hence contain about 2000 electrons at any given time, and the level spacing in the large dot, $\Delta = \frac{2\pi\hbar^2}{mA} \sim 7$ μeV. The temperature of the experiment was mostly 45 mK, and since $1\ kT = 86.2\ \mu$ eV, we have $kT = 3.9$ μeV. The tunneling rate was measured to be $\Gamma = \frac{\gamma_L \gamma_R}{\gamma_L + \gamma_R} \cong 1$ μeV. Assuming the tunneling rates on each side are about the same, this implies that each has rate $\gamma \cong 2$ μeV, which is the half-width of the energy measurement. The energy resolution due to the dot is hence $\cong 4$ μeV. At the Fermi energy the resolution is $kT \sim 4\mu$eV due to temperature effects, while below the Fermi level the energy resolution 4μeV, now limited by the resolution Γ of the small dot. In either case the energy resolution is somewhat finer than the level spacing Δ in the large dot, implying that the small dot can resolve individual energy levels of the large dot, if it were closed and the levels quantized. Since the large dot is usually leaky and open ion the experiment, the spectrometer can be thought of as resolving most of the resonances in the large cavity of the dot.

In Figure (4.1a), we show a micrograph of the device, and in (b) depict the relative posi-

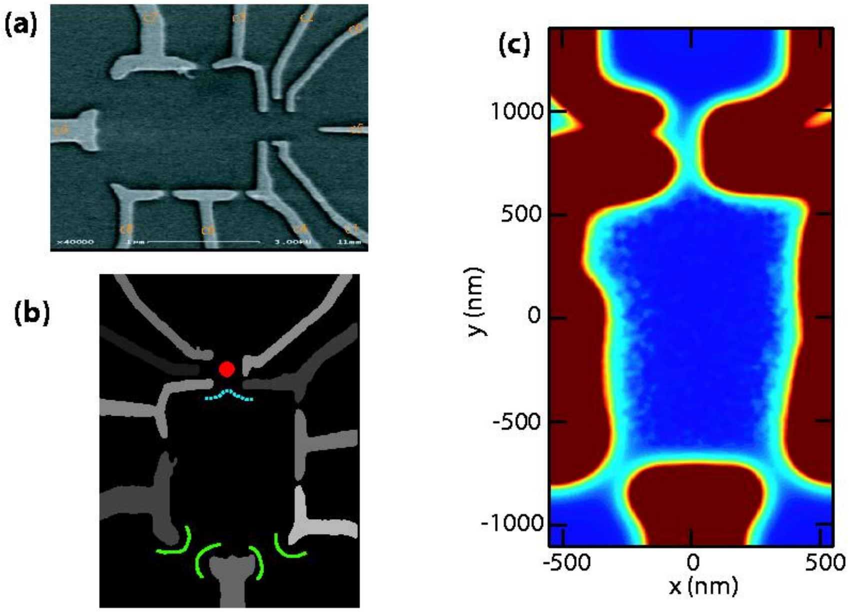

Figure 4.1: The lateral quantum dot device used in the experment. (a) shows a micrograph of the device, with the small quantum dot on the right; the scale bar is 1 micron. (b) shows a trace map of the device, with the location of the spectrometer indicated by a red circle. The dashed cyan line shows the approximate location of the edge of the classical allowed region of the tunnel barrier. In (c) we see a DFT simulation of the dot taken from realistic voltages on the traces, and real dimensions and parameters of the heterostructure; here the small dot is opened up instead of closed.

tions of the spectrometer dot, shown as a red circle, the quantum point contacts between the large dot and the leads, shown in green, and the classical turning point of the tunnel junction between the small dot and the large dot. In (c) we show a DFT simulation [95] of the effective single-particle potential of the large dot based on realistic parameters of the device and gate voltages. Note the asymmetrical shape of the dot, particularly near the tunnel junction, and how the classical turning point near the tunnel junction becomes concave then rapidly convex. It is also apparent that the edges of the dot lie at least 100 nm inward from the location of the gates, but apart from the rapid change transition near the edges, the dot is fairly flat. Here the device has been simulated with the small dot completely open, which is not how it operates in the actual experiment.

A diagram of the energy levels is shown in Figure (4.2), showing the relative energies of the Fermi edges in the incoming and outgoing leads, as well as the energy levels of the large dot and the single spectrometer energy level of the small single electron dot. The current through the device at finite bias is plotted in Figure (4.3) for two different runs. The bias voltage is 1 meV across both dots, and the Fermi energy of the incoming lead is 7.1 meV. Since almost all the voltage drop will be

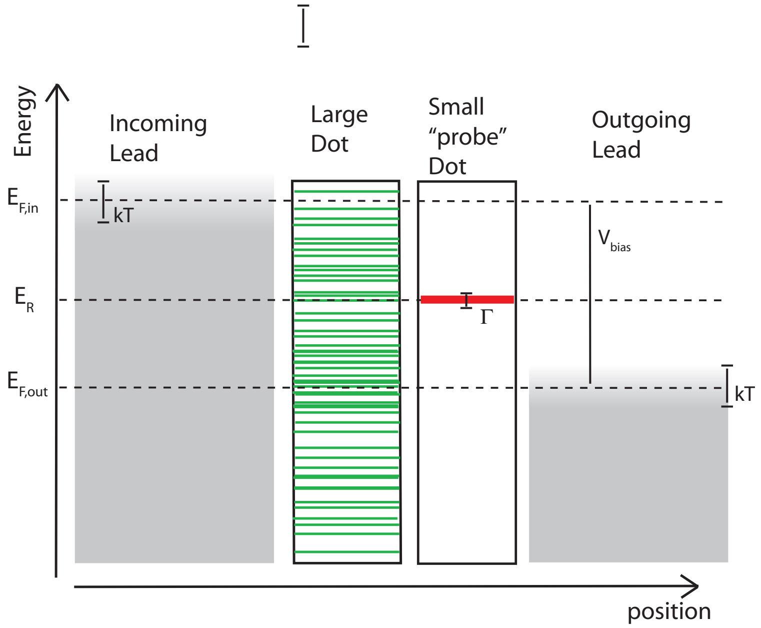

Figure 4.2: Energy diagram for flow through the two-terminal device. On the left is the Fermi sea of the incoming lead with Fermi energy $E_{F,inc} = 7.1$ meV and temperature kT. On the right is the outgoing lead, at bias $V_{bias} = 1$ meV below the incoming lead. In the center are the many energy levels of the large dot, and the single energy level of the spectrometer dot, at energy E_R with width Γ. When E_R is between the Fermi edges of each lead, the current that flows is due to electrons with energy within Γ of the spectrometer energy.

across the spectrometer, the Fermi energy within the large quantum dot is also 7.1 meV. Comparing the data to the schematic in Figure (4.2), we can read the data as follows: at the upper edge of the data where there is finite current we are looking at the edge of the Fermi sea of the incoming lead. As the spectrometer energy is lowered, the incoming states will be filled while the outgoing states are empty, and the distribution difference, $f_i(E) - f_o(E) = 1$ for most of the figure. At the bottom edge of the current data, where the current drops to near zero, we are now seeing the edge of the Fermi sea of the outgoing lead; beyond that states are occupied in both leads, and we measure no net current through the device. This is also clearly visible in Figure (4.4a,c).

In a typical, non-Fabry-Perot-like device one would expect to see universal conductance fluctuations between the two Fermi edges; this type of experiment has been done before [56] and saw just that. The inclusion of the large quantum dot could create strong resonances in the cavity, and the sign of these resonances would be strong oscillations in the signal, as is seen. Around $B = 0$, there is an oscillation in the current as the energy of the spectrometer is changed, covering ~ 4 cycles in 1 meV; this implies a path length $L \sim 3200$ nm, approximately twice the length of

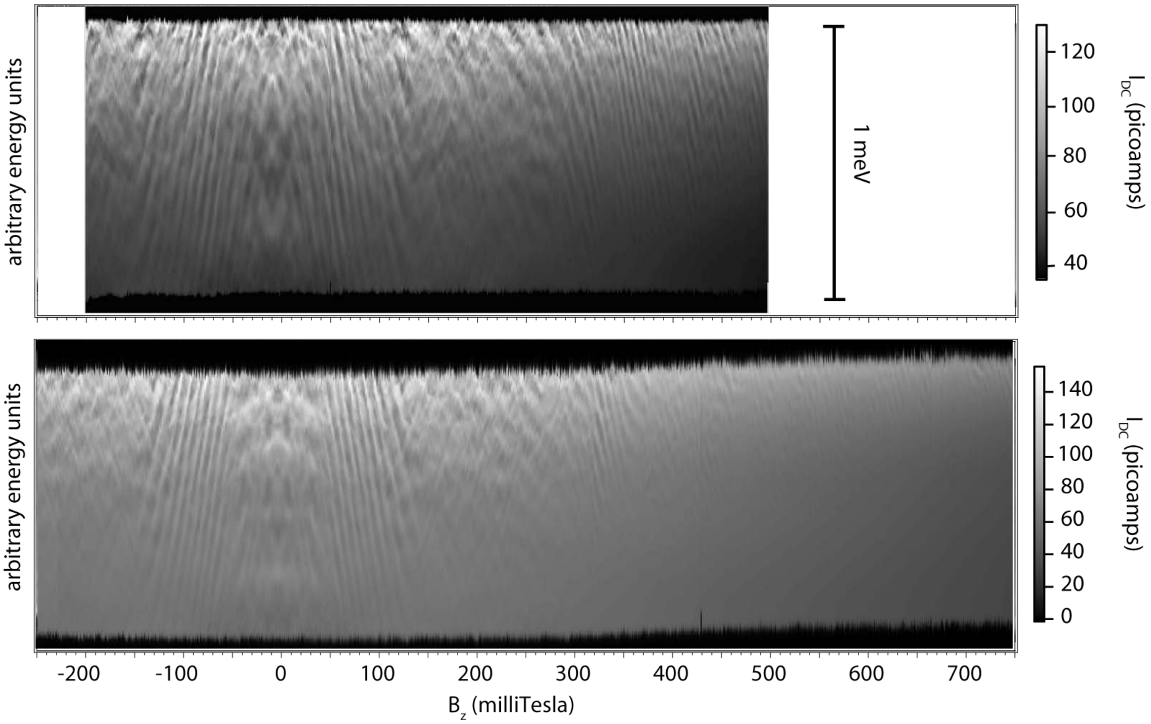

Figure 4.3: Two sets of experimental currents, plotting versus magnetic field and spectrometer energy; the y-axis is a voltage of a particular gate, and hence isn't particularly relevant. What matters is that the current spans 1 meV vertically before dropping to near zero. The Fermi surface of the incoming lead is at the top edge of the data, and the Fermi surface of the drain at the bottom; the bias was 1 meV. The interference bands are visible in both sets of data for various regions of magnetic field.

the dot, and thus is consistent with the hypothesis that the oscillations are due to certain resonant trajectories in the large dot. Near $B = 0$, the bands have a small but finite slope, implying that the relevant trajectory has a finite but small area.

Turning to the strong interference bands around 100 milliTesla, we refer to Figure (4.4), which shows the lower data set for smaller magnetic fields in 3D, and slices through the data for the region with the strongest interference bands. In (a) the data is shown in 3D, highlighting the strong interference bands around 100 milliTesla. In (c) we plot a slice of the current data at $B = 70$ milliTesla, indicating the peak spacings, and the Fermi edges. There are ~ 5 oscillations over the course of 1 meV, implying a path length 1.25 times longer than at $B = 0$, or $L = 4000$ nm. In (b) we plot a slice of the data at $E = 7.0$ meV, just below the Fermi sea of the incoming lead; the peak spacings are indicated as red dashed lines. The spacing in magnetic field of the bands is $\Delta B \sim 9$ milliTesla, and given that the bands have negative slope in the (B, E) parameter plane, this implies

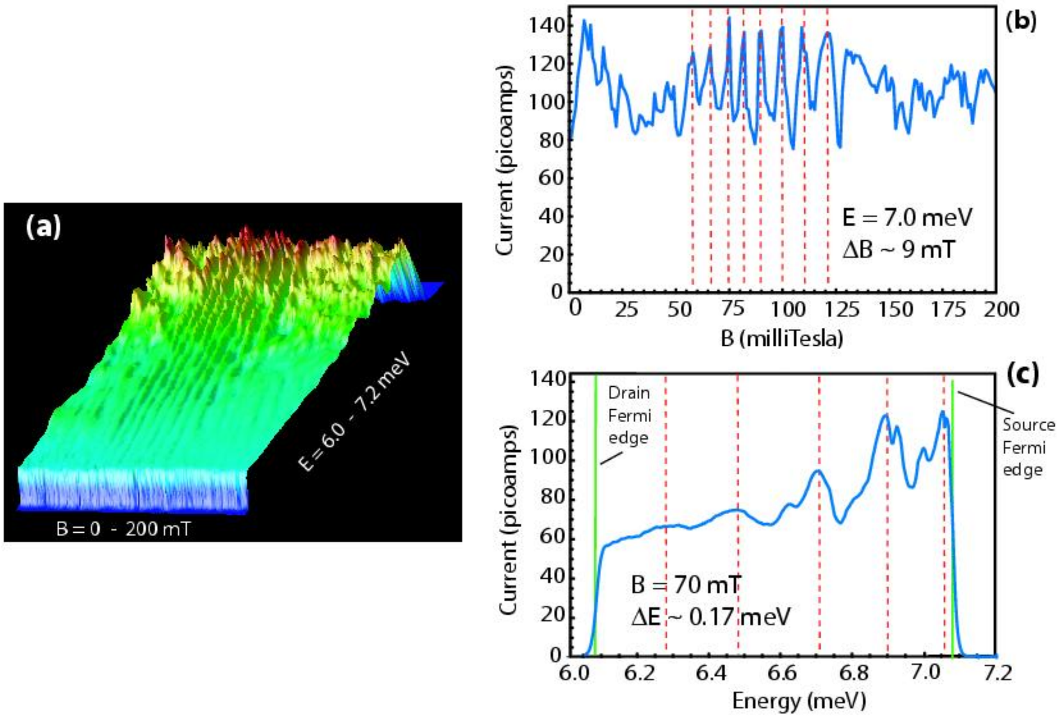

Figure 4.4: In (a) we plot the experimental current in 3D, showing the the Fermi edges of the data, the interference bands, and the dropoff in amplitude as the energy drops below the Fermi energy. In (b) we plot a slice of the current at an energy of 7.0 meV, just below the Fermi energy. The oscillations are clear and marked with red dotted lines, with a typical spacing around $B = 70$ milliTesla of $\Delta B \sim 9$ milliTesla. In (c) we plot a slice of the current at the field $B = 100$ milliTesla. The oscillations are still pronounced but less obvious, with a typical spacing of $\Delta E \sim 0.17$ meV. In addition, we mark the edges of the Fermi sea of the source and drain in green.

that the area enclosed is $A \sim 0.5\ \mu\text{m}^2$. These values are consistent with a diamond shaped orbit that encloses a little under half of the area of the large quantum dot, which is $\sim 1\ \mu\text{m}^2$.

In addition to being consistent with semiclassical considerations, these bands are quite robust. Opening the QPCs of the large dot from one to many transverse modes has negligible effect on the interference bands, and they persist at temperatures up to 1 K, where most of the small scale signal has been washed out.

4.2 Model Of Resonant Tunnelling

In the experimental results, the most interesting aspects are the existence and nature of the interference bands in magnetic field and spectrometer energy. These bands result from the dynamics in the large dot, which may be thought of as a resonant cavity. The bands are due to the coupling between the resonant states of this cavity and the single state of the spectroscope, or "probe" dot, via the tunnel junction. We expect that at small to moderate magnetic fields, and over a small range of energies, the state in the probe dot, and the states in the lead on the other side of the probe dot, will not vary strongly, so that the coupling between the probe dot and the lead will vary slowly with energy and magnetic field. Since we are mostly interested in the signal due the resonant states in the large dot, we may justifiably focus on the contribution to tunneling due to the dynamics of the large dot.

Normally resonant tunneling theory starts by assuming the Hamiltonian may be separated into transverse and longitudinal parts, and that the tunneling process, which takes place longitudinally, does not mix these states. For the process of tunnelling through a lateral single electron quantum dot, this assumption does not hold, since the tunnel junction strongly mixes modes. However, since there is a single available mode in the probe dot, the tunneling into the dot from any mode can be combined into a single incoming and outgoing transmission amplitude

$$\bar{t} = \sum_{m} t_{m \to o}, \tag{4.7}$$

and we may continue to use the formalism. Here we have ignored any level splitting due to spin; we assume in this model that the spin degeneracy will simply double the final transmission. For simplicity, we also assume that at any given parameter, there is a single dominant tunneling mode in the leads and cavity, or that the basis states may be changed to provide a single dominant mode (in the case of a tunnel junction on a half-plane, the dominant mode would be the equivalent of a "p"-wave in the leads [8]).

The tunneling through the resonant dot may be treated in terms of the transmission into and out of the small quantum dot (depicted schematically in Figure (4.5)). The tunneling process is nearly completely coherent, and so the combined transmission amplitude should be written as

$$t = \frac{t_1 t_2}{1 - r_1' r_2} = \frac{t_1 t_2}{1 - e^{i\theta}\sqrt{R_1 R_2}}, \tag{4.8}$$

where t and r are the transmission and reflection amplitudes of each tunnel junction, and θ is the phase accumulated for one round trip in the small quantum dot. In standard fashion [21], one can define an attempt frequency $\nu \equiv \frac{1}{\hbar}\frac{dE}{d\theta}\Big|_{E=E_R}$ at the resonant energy, which is the rate at which the electron attempts to tunnel. (If the tunnel barriers were treated as delta function barriers, this

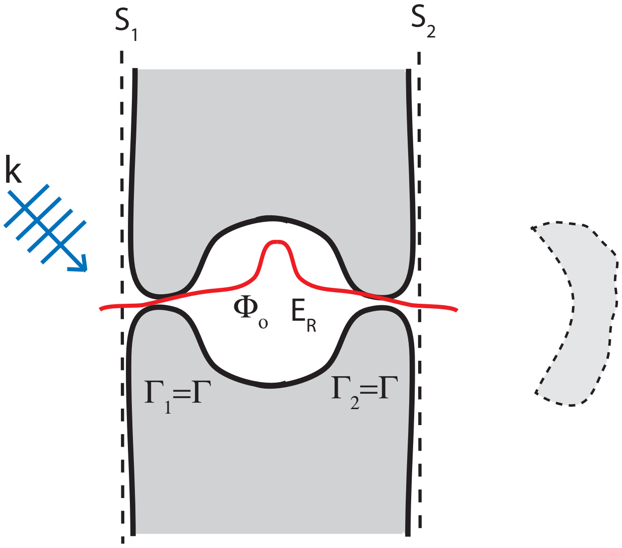

Figure 4.5: Schematic layout of the resonant quantum dot, where the tunneling rates are assumed equal in the incoming and outgoing tunnel junctions when the resonant cavity is removed.

would be equal to $v/2w$, the speed divided by twice the dot size). We then define the escape rate, $\Gamma \equiv \nu T$, the rate at which the electron tunnels out of the dot into a given lead; a Lorentzian approximation about the resonant energy for the transmission $T = |t|^2$ through the entire barrier yields the expression

$$T(E) \cong \frac{\Gamma_1\Gamma_2}{\Delta E^2 + \left(\frac{\Gamma_1+\Gamma_2}{2}\right)^2} \tag{4.9}$$

after noting that $T/R \ll 1$. Here $\Delta E \equiv E - E_R$, the energy difference from the resonant energy.

If we remove the opposing walls of the large dot, walls which make it operate as a leaky resonant cavity, then the tunneling through the spectrometer dot is fairly symmetrical. For simplicity, we set the transmission coefficients of each cavity to be $\bar{T}$, and the escape rates of each tunnel junction to be $\Gamma = \nu\bar{T}$, and arrive at the simplified result for the “bare” transmission,

$$T_o(E) = \frac{\Gamma^2}{\Delta E^2 + \Gamma^2}. \tag{4.10}$$

The current

$$I = \frac{2e}{h}\int_E^{\mu} T(E)f(E)dE \tag{4.11}$$

is, at low temperatures and on resonance,

$$I_o = \frac{2e}{\hbar}\frac{\Gamma}{2}. \tag{4.12}$$

If instead we include the effects of the leaky resonant cavity of the large dot, the transmission in to that cavity, T_2, will be strongly affected by the change in the density of states and in the states themselves. To parameterize this effect, we define the ratio between the transmission with and without the large cavity present, $\eta(E,B) \equiv T_2(E,B)/\bar{T}$, which will include all the effects of the altered states in the resonant cavity. Inserting that into the equation for the total transmission, and noting that the attempt frequency ν will not be affected by the change in external states, we have the altered transmission

$$T(E) = \frac{\eta\Gamma^2}{\Delta E^2 + \Gamma^2\left(\frac{\eta}{1+\eta}\right)^2}. \tag{4.13}$$

Since the resonance is taken to be very sharp, then the variation in η over the resonance will be small, and we can take $\eta(E,B) = \eta(E_R,B)$ instead. Integrating over energy, we get the modified current,

$$I = \frac{2e}{\hbar}\frac{\eta\Gamma}{1+\eta} = \frac{2\eta}{1+\eta} I_o. \tag{4.14}$$

Thus in order to understand the change in the current through the spectrometer due to the walls on the large dot, I/I_o, we need to understand the parameter $\eta(E_R,B)$ alone.

As for the transmission coefficients of the tunnel barriers, we can calculate the overlap matrix elements between the resonant state Φ_o and some external state of the lead or cavity, ψ, using the Bardeen tunneling formula [7] for each tunnel junction [83]. This is appropriate when the expected reflection amplitude for a tunnelling particle from the leads is small. The overlap matrix element is

$$\langle\Phi_o|\psi\rangle = \frac{\hbar^2}{2m}\int_S \Phi_o\nabla\psi^* - \psi^*\nabla\Phi_o dS \tag{4.15}$$

from the Bardeen tunneling formula. If we take the surface of integration to be in the classically allowed region of the cavity or leads, then the expression may be recast in terms of Φ_o and the derivative of ψ [78]

$$\langle\Phi_o|\psi\rangle = \frac{\hbar^2}{m}\int_S \Phi_o\nabla\psi^* dS. \tag{4.16}$$

From Fermi's Golden Rule, the transition rate is $W = \frac{2\pi}{\hbar}\sum_{states}|\langle\Phi_o|\psi_m\rangle|^2\delta(E_R - E)$ so that, for a single state m

$$W_{o\to m} = \frac{2\pi\hbar^3}{m^2}\left|\int_S \Phi_o\nabla\psi_m^* dS\right|^2, \tag{4.17}$$

and the total transition rate is the sum of the transition rates into each state.

The transfer Hamiltonian formalism can be compared to the scattering formalism [21] to yield the transmission through the tunnel junctions to a state ψ_m

$$T_{o\to m} = (2\pi)^2|\langle\Phi_o|\psi_m\rangle|^2 = \frac{(2\pi)^2\hbar^4}{m^2}\left|\int_S \Phi_o\nabla\psi_m^* dS\right|^2. \tag{4.18}$$

Note that this, with the earlier expression for W, implies that $W = \frac{\hbar}{(2\pi)^3}T$. Here we recognize that, when the surface is taken in the classically allowed region beyond the tunnel junction, that $\nabla\psi \sim ik_\perp\psi$, and hence the matrix element is proportional to the momentum times the overlap of the wavefunctions on the surface S. Since the resonant state of the small dot, Φ_o, will change little with energy and B, the dominant dependence of the transmission will be on the perpendicular momentum and the LDOS on the surface S. Only those states which have significant amplitude to cross the surface S will contribute to the transmission. Furthermore, when the cavity walls are activated, the eigenstate of the spectrometer Φ_o will change negligibly; hence the parametric function η will depend solely on the change in the LDOS near the tunnel junction due to adding the cavity walls. In this way the spectrometer acts as a direct probe of the LDOS of the large quantum dot at the tunnel junction.

In terms of the Green function within the large cavity, $G(r, r'; E)$, the transmission can be expressed as [78]

$$T = -\frac{1}{\pi}\left(\frac{2\pi\hbar^2}{m}\right)^2 \Im \int_S dxdx'\Phi_o(x)\Phi_o^*(x')\frac{\partial^2}{\partial x\partial x'}G(x, y_S, x', y_S; E), \tag{4.19}$$

where the y_S is the position of the surface S. Semiclassically, the Green function is the sum over classical trajectories [45, 12]

$$G_{sc}(r, r'; E) = \frac{2\pi}{(2\pi i\hbar)^{3/2}}\sum_j A_j e^{\frac{iS_j}{\hbar} - \frac{i\pi\mu_j}{2}} \tag{4.20}$$

where A_j is the classical amplitude of the jth orbit. The second derivative of G_{sc} near the turning point may be found by considering the contribution from each direct trajectory, coupled to the accompanying trajectory which was reflected by the tunnel barrier; the resulting expression [78] is

$$\frac{\partial^2 G_{sc}}{\partial x\partial x'} = 4i\frac{2\pi}{(2\pi i\hbar)^{3/2}}\sum_j k_y k_y' A_j e^{\frac{iS_j}{\hbar} - \frac{i\pi\mu_j}{2}}. \tag{4.21}$$

Thus the term for each trajectory is multiplied by $4i$ times the initial and final momentum at the tunnel mouth, as expected. The semiclassical transmission reads

$$T_{sc} = 4\frac{(2\pi)^{3/2}\hbar^{5/2}}{\pi m^2}\Re\int_S dxdx'\Phi_o(x)\Phi_o^*(x') \sum_{j \text{ from } x\rightarrow x'} k_y k_y' A_j e^{\frac{iS_j}{\hbar} - \frac{i\pi\mu_j}{2} + i\pi/4}, \tag{4.22}$$

where we sum across each trajectory from x to x' on the surface S at the tunnel junction. This expression could be directly used to accurately calculate the transmission through the tunnel junction.

For simplicity and clarity, we can approximate the tunnel barrier as a delta function, and hence write $\Phi_o = ae^{-Kl}\delta(x - x_o)$, where a represents an effective width of Φ_o across the tunnel barrier, and e^{-Kl} is a typical factor for the evanescence of the resonant state into the tunneling region, with l a typical distance into the tunneling region, and $K = \sqrt{2m(U-E)}/\hbar$. Then the integration across the mouth of the tunnel barrier is trivial, and we have the transmission through the tunnel barrier

$$T = \left(4\frac{(2\pi)^{3/2}\hbar^{5/2}}{\pi m^2}a^2 e^{-2Kl}\right)\sum_j k_y k_y' A_j \cos\left[S_j/\hbar - \pi\mu_j/2 + \pi/4\right], \tag{4.23}$$

where the sum is over closed orbits. For a magnetic billiard, it is often the case that the shortest closed orbits are also the periodic orbits, and so this type of equation is directly applicable. From this expression, it is clear that the most quickly varying factor in the transmission is due to the semiclassical phase accumulated along the trajectory, and that when this phase varies by 2π, the transmission due to a particular orbit will oscillate from a maximum to zero and back. The relevance of the orbit comes primarily from the component of the momentum perpendicular to the tunnel barrier, but also depends on the classical amplitude A.

This derivation is convenient, but not necessarily correct, since taking the tunnel barrier width to zero does not correctly take the semiclassical limit; in particular the expression for the amplitude is suffering. However, it does highlight the central role of the phase and perpendicular momentum in to the tunnel junction region. A more correct, although significantly more complicated, treatment is available [78]. In addition, being a semiclassical derivation for finite length periodic orbits, this expression is only for the oscillatory part of the transmission; the Weyl term would come from summing up over infinitely small trajectories.

4.3 Magnetic Billiard

A simple and analytically accessible model of the quantum dot is that of a rectangular billiard in the presence of a perpendicular magnetic field. The trajectories in this system are relevant to those in the quantum dot, as long as the trajectories don't come near the corners of the dot where there are open quantum point contacts. The rectangular magnetic billiard model will prove to be a reasonably accurate tool to model the dynamics in the cavity. Because of symmetry considerations, the dominant (i.e. shortest) closed orbits that touch the center of the magnetic billiard will also be periodic orbits; this implies that examining the lowest order periodic orbits of the magnetic billiard will provide the bulk of the insight.

4.3.1 Motion in the Magnetic Billiard

In the magnetic billiard, because motion between the walls is free and the walls are hard, speed and kinetic energy are conserved quantities. Since the motion within the billiard is free motion

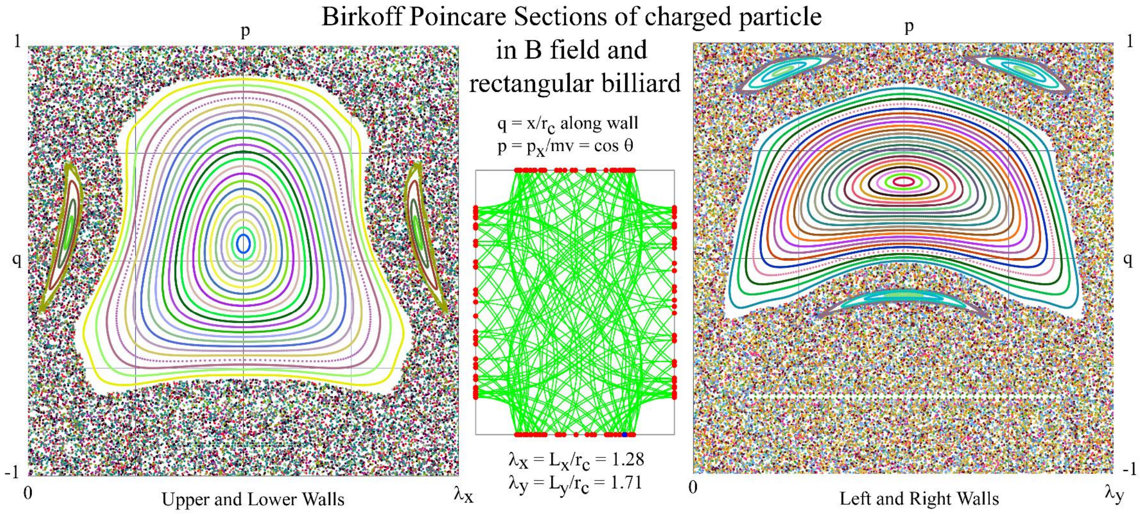

Figure 4.6: Poincaré section of the magnetic billiard for a field value that produces a stable periodic orbit surrounded by a large integrable island. Also visible on the section for the side walls is a line of parabolic states due to football shaped orbits which spans the width of the billiard. The trajectory shown is one on the outer part of the integrable island.

within a uniform magnetic field, we can define the dynamics of the entire system by the dynamics on the walls alone; the reasonable choice is hence to use Birkhoff coordinates for this system. Since speed is a conserved quantity (i.e. kinetic momentum, and not canonical momentum), we can scale out the speed of the particle (mv actually), and hence the energy. Furthermore, the ratio between the magnetic field strength B and the velocity v determines the cyclotron radius, so we may just as easily measure distance in units of the cyclotron radius

$$r_c = \frac{v}{\omega_c} = \frac{mv}{|q|Bc} = \frac{\sqrt{2mE}}{|q|Bc}. \tag{4.24}$$

If we do so, then the number of free parameters of the system has dropped to just two, the dimensions of the rectangular billiard in units of r_c. It must be noted that values that depend on the transit from one wall to another, in particular the time of flight and the action, do not reduce to two parameters, and depend on a third parameter (energy, magnetic field or speed). However, the length and area enclosed by an orbit do scale with only two parameters, since they scale as length only.

4.3.2 Discrete Map

In cyclotron radius scaled units, the system is described on the walls by a discrete map in the phase space variables (p, q, n), the position and momentum along a wall, as well as the wall

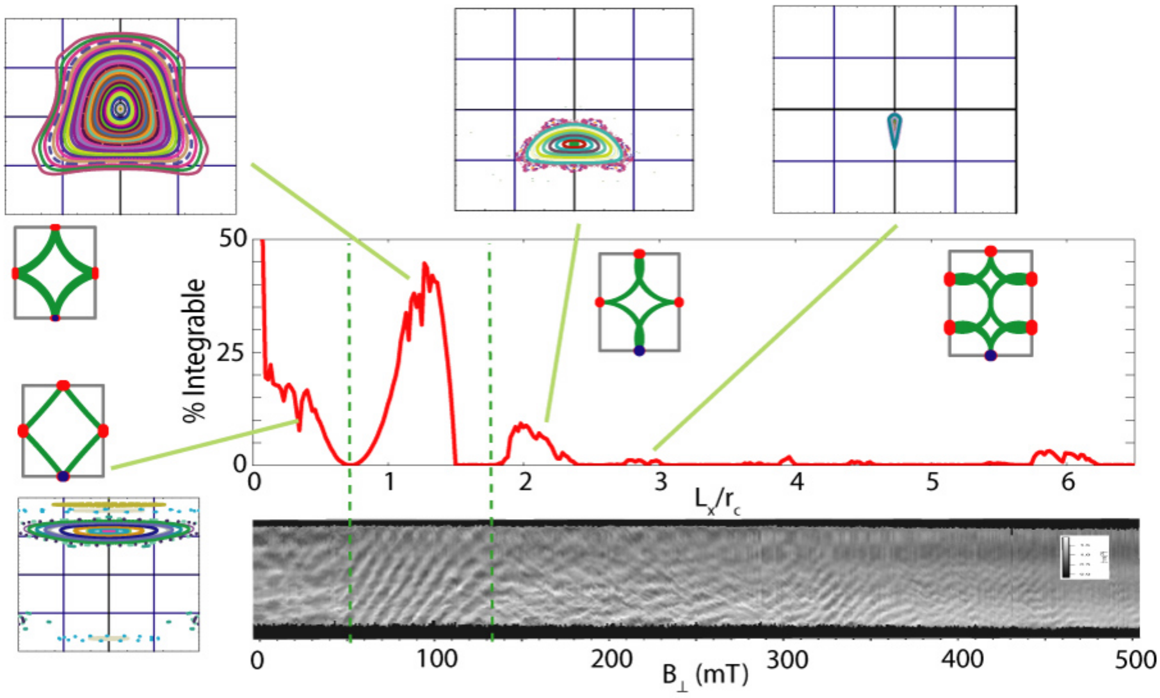

Figure 4.7: Plot of the percentage of phase space that is integrable as a function of the scaled billiard size (read B) as compared to the experimental data.

number; this wall number index is needed if we allow for non-square rectangular billiards. The full discrete map can be thought of as a conditional map involving individual maps, each of which maps from a state on the present wall to a state on $\Delta n = 0...3$ walls around the billiard. In scaled units, the maps are

$$\begin{aligned}
\mathbb{M}_0 &= \left(q + 2\sqrt{1-p^2},\ p\right) \\
\mathbb{M}_1 &= \left(\sqrt{1-\left[\sqrt{1-p^2}-(L_x-q)\right]^2}-p,\ \sqrt{1-p^2}-[L_x-q]\right) \\
\mathbb{M}_2 &= \left(L_x-(q+\sqrt{1-p^2}-\sqrt{1-(p+L_x)^2}\ ),\ -p-L_y\right) \\
\mathbb{M}_3 &= \left(L_x+p+\sqrt{1-\left[q+\sqrt{1-p^2}\right]^2},\ -q-\sqrt{1-p^2}\right)
\end{aligned} \tag{4.25}$$

where the map is iterated as $(q_{i+1}, p_{i+1}) = \mathbb{M}_{\Delta n}(q_i, p_i)$. Here L_x is the length of the present billiard wall, and L_y is the length of the next billiard wall. The full map $\mathbb{M}$ applies the physically relevant map from these.

A Poincaré surface of section for a field value with a large integrable island is shown in Figure (4.6). At the center of the large island is a diamond shaped periodic orbit, which strikes the center of each wall; the other islands, two on the upper and lower walls and three on the side walls, are due to less symmetrical orbits that do not strike the center of the upper wall. Along the side walls are also a set of parabolic orbits with marginal stability, which resemble a set of football shaped orbits spanning the width of the billiard; these are visible in the Poincaré section of the side walls as a horizontal strip of orbits. With any small perturbation this strip of orbits will turn into a set of small integrable islands and unstable separatrices strung together along this line like beads on a string.

This large integrable island will play a strong role in the tunneling current, since not only does it have a strong presence at the tunnel junction, but the momentum along the wall is small. This implies that the momentum into the wall is large. Because the orbits are fairly close together here, we also expect a significant classical amplitude.

One useful measure that may be pertinent to the experiment is how large these integrable islands in the Poincaré sections are, since if a particle is trapped on one of the islands it will continue to attempt to tunnel far more frequently than if the orbit were chaotic. To produce such a measure, it is straightforward to launch a single trajectory of the map in a known chaotic location of phase space, and then track the particle's trajectory for many thousands of iterations. We then discretize phase space into a grid, and count the number of times the trajectory enters a given grid cell. If the grid cell lies fully on the integrable island, then an initially chaotic trajectory will never sample any point in that grid cell. We then count the number of unoccupied grid cells, and obtain a measure of the integrable phase space.

In Figure (4.7) we consider the fraction of phase space that lies on a integrable island, as a function of the field, for a 4/3 rectangular billiard. For a variety of field values we also show the Poincaré section of the shorter wall and the dominant periodic orbit at the center of the integrable island. This is compared to the experimental data as well. The strong correlation between island size and interference band strength is convincing for magnetic fields of 50-130 milliTesla, which correspond to the diamond shaped periodic orbit at the center of the integrable island. This correlation fails below 50 milliTesla, because the islands persist well below 50 milliTesla, but the signal does not experimentally.

In Figure (4.8), we consider the Poincaré section at a higher field value, where the dominant periodic orbit has attained a holly-leaf shape, bouncing twice on the side walls. Although this is the dominant island at this field strength, the size of the island is greatly reduced from that at lower fields.

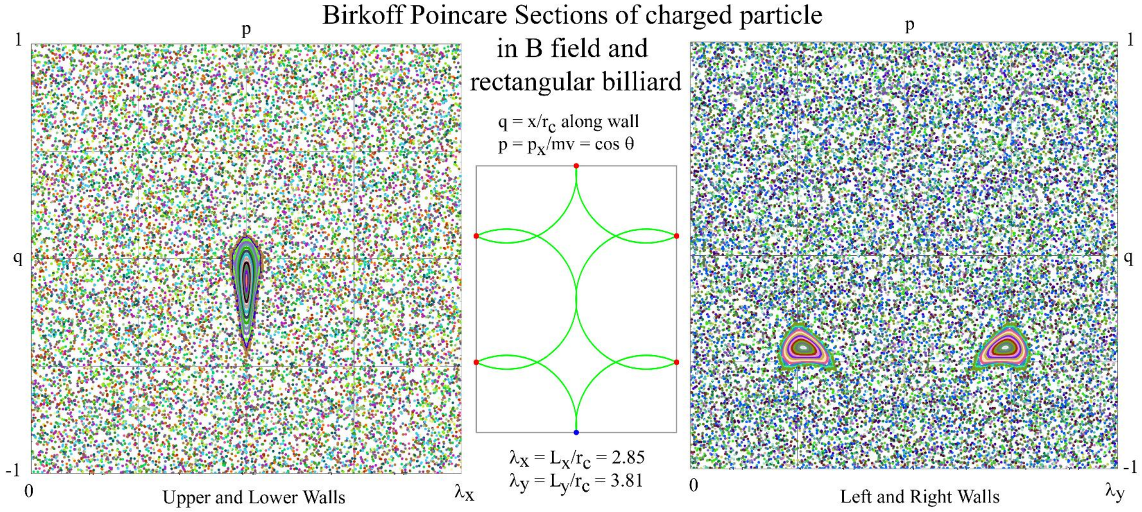

Figure 4.8: Poincaré section of the magnetic billiard for a stronger field value, showing a stable holly-leaf shaped orbit.

4.3.3 Pitchfork Bifurcation

We also note that in the region between $L_x/r_c = 1.5$ and 1.9, the integrable phase space volume drops to zero; this is due to a pitchfork bifurcation [69] that occurs for fields values just below this region. This is depicted in Figure (4.9), and in phase space in Figure (4.10) by a series of Poincaré sections around this process. The initial periodic orbit at lower fields splits into two asymmetrical periodic orbits, which leave the center of the side walls, and a third still symmetrical, but now unstable periodic orbit. This bifurcation occurs just before the field value when the trajectory strikes perpendicular to the wall, and hence when $p = 0$; beyond that field value the symmetric periodic orbit ceases to exist. The asymmetrical periodic orbit pair still exist beyond this value by adding a twist at one end. With increasing field even these orbits cease to exist.

The same process happens in reverse at higher fields; a stable symmetric periodic orbit exists for higher fields by twisting with each wall bounce. As the magnetic field is reduced, the symmetric trajectory strikes perpendicular to the side walls, and then ceases to exist. However asymmetrical orbits may exist for smaller fields, where the orbits twists at just one of the walls. The phase space portrait of these bifurcations is shown in Figure (4.10), with the periodic orbits indicated by small dots, red for stable and blue for unstable. The magnetic field values are relevant when the dot is scaled to the size of the experimental quantum dot cavity.

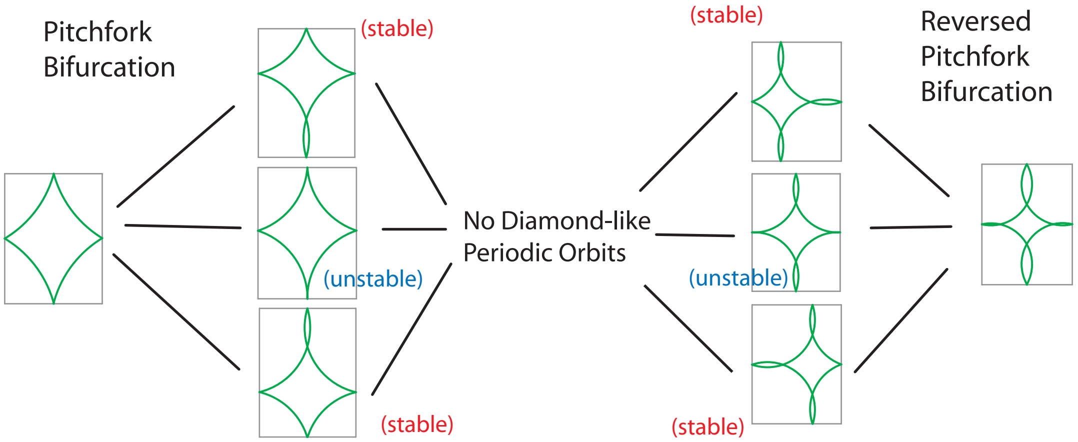

Figure 4.9: The pitchfork bifurcation of the diamond shaped orbit with increasing magnetic field. On the left is a stable periodic orbit at low field. As the field is increased, the angle with respect to the lower wall approaches $90°$, at which point the symmetric orbit ceases to exist, and only asymmetric orbits remain. At higher fields even these are no longer present. Coming down from larger field values, a reverse bifurcation takes place.

4.3.4 Soft Wall Discrete Map

Since an actual quantum dot is not a true hard-walled billiard, of interest is the dynamics of a billiard with soft walls. We can model this as a discrete map by composing the hard wall discrete map with another map which changes the position of the particle along the wall as if the particle had entered a half harmonic wall. For simplicity we ignore the magnetic field in the harmonic wall, assuming that the effect of the restoring force of the wall is much stronger than the field.

Motion in a harmonic potential can be scaled so that it is independent of energy; if we consider the angle of the harmonic motion, then given the momentum, the angle rotated by is $\eta t = 2\cos^{-1} p$, where $\eta = \omega/\omega_c$ is the scaled frequency of the harmonic potential comprising the soft wall. The particle will always emerge with the same momentum p along the wall, and will have covered a distance $\Delta q = pt$ after emerging from the wall. If the particle moves beyond the edge of the billiard while in the wall, we assume that it must bounce off the next wall and return with opposite momentum. Hence our soft wall map looks like

$$\begin{aligned} \mathbb{M}_{soft}(q,p) &= (q'',p'') \\ q' &= q + \frac{2}{\eta}\cos^{-1} p \end{aligned}$$

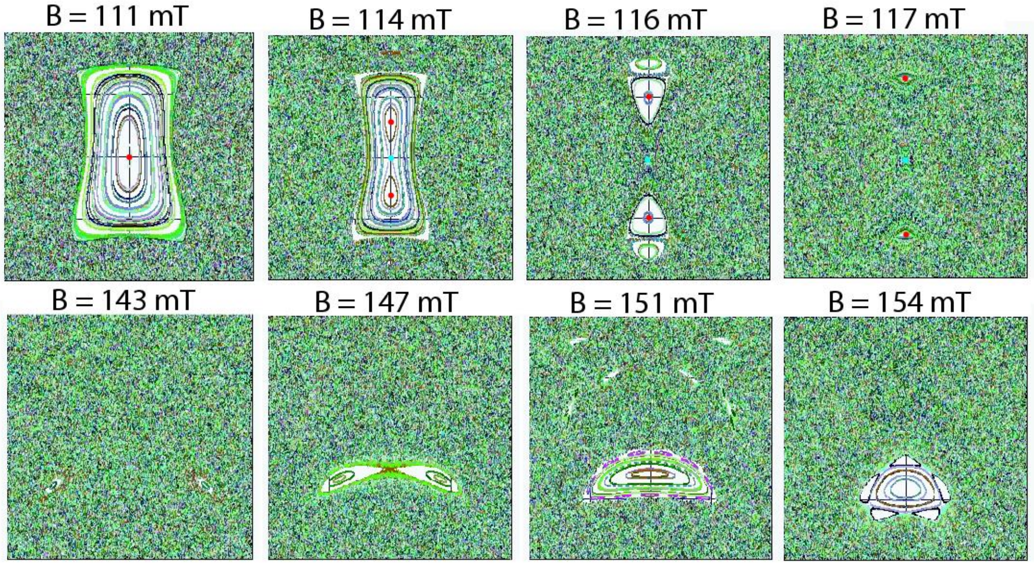

Figure 4.10: Poincaré section of the magnetic billiard at varying field values, showing the bifurcation process.

$$q'' = \begin{cases} q' & \text{if } 0 < q' < L \\ -q' & \text{if } q' < 0 \\ L - q' & \text{if } q' > L \end{cases}$$
$$p'' = \begin{cases} p' & \text{if } 0 < q' < L \\ -p' & \text{if } q' < 0 \text{ or } q' > L \end{cases} \tag{4.26}$$

warts and all. One can show that this is an area-preserving map as in the hardwall case. In this map, the parameter η plays the role of an inverse time, and $\sqrt{\eta}$ as a wall hardness , so that as η is increased, the wall seems harder and the particle spends less time in the wall. As $\eta \to \infty$, the hard wall case is recovered.

We show the dynamics of the map in Figure (4.11) at a field value that is the same as that in Figure (4.6), and which exhibits a very large integrable island. The soft wall map has an equivalently large island at this field, but also exhibits a pitchfork bifurcation for smaller fields. In addition, there is an inaccessible region of phase space, shown in the lower left corner of the first Poincaré section, due to the map; this region of phase space is shadowed throughout phase space as well, leaving a fractal of inaccessible phase space.

In Figure (4.12), we compare the integrable phase space volume of the soft wall map with the hard wall map, for a reasonably hard wall. In general the effect of the soft wall is to enhance

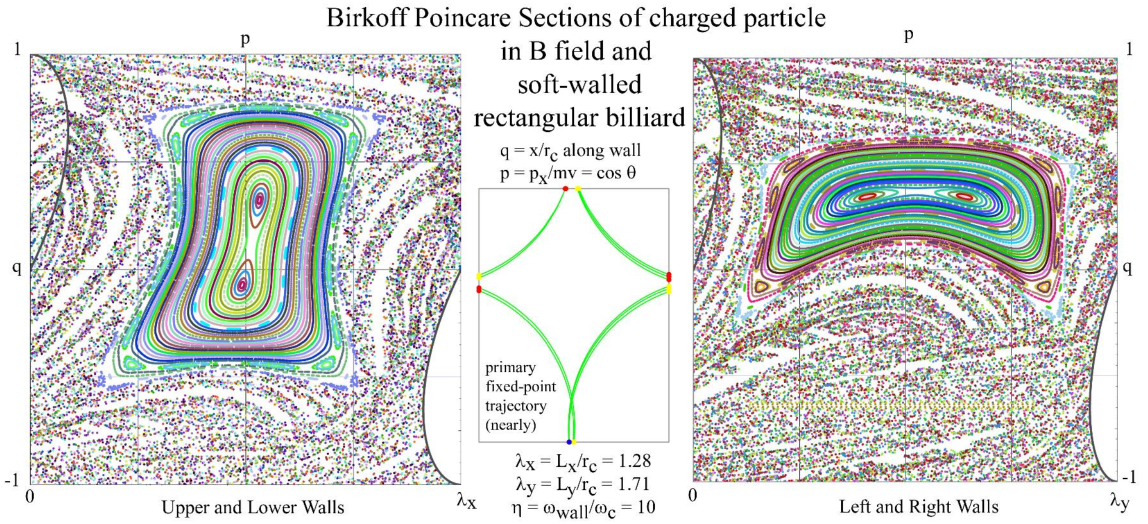

Figure 4.11: Poincaré section of the soft magnetic billiard for a field value that produces a stable periodic orbit surrounded by a large integrable island. The soft walls allow for a bifurcation at smaller field values than for the hardwall case.

the integrability of the system, and to remove the sharp drops in integrable volume due to the abrupt dropout of imporant stable periodic orbits. The data must be taken only qualitatively, however, due to the effect of the classical disallowed region and its shadow throughout phase space, as mentioned earlier. The relative classically allowed phase space will be smaller for the soft walled map, and hence the integrable percentage will appear larger relatively. In addition the sharp peaks are most likely due to the particles being injected into shadows of the classically disallowed region in a normally chaotic region of phase space.

4.3.5 Bumpy Wall Discrete Map

Besides soft walls, it is also relevant to examine the effect of bumpy walls on the dynamics of the particle in the billiard. This can be accomplished by adding an extra, position dependent but non-stochastic momentum kick with each wall bounce. We define a momentum kick function $\Delta p(q)$ with some relevant randomly assigned distribution of momentum kicks; often one wants to scale this function so that the distribution of kicks $\delta p = \sqrt{\langle \Delta p^2 \rangle}$ has some experimentally relevant value. The bumpy map looks like

$$\mathbb{M}_{bumpy} = (q,\ p + \Delta p(q))\,, \tag{4.27}$$

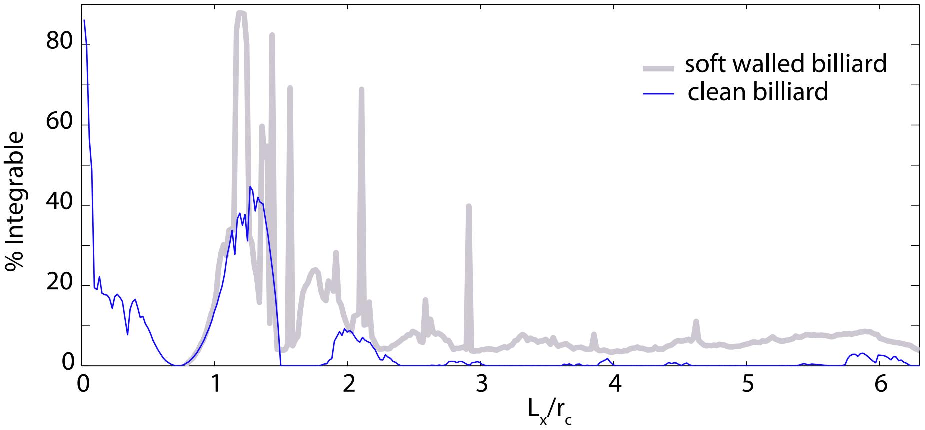

Figure 4.12: The percentage of phase space that is on a stable integrable island, when the walls are made soft. The effect is apparent but small, distorting and shrinking the integrable islands. As expected, a stronger average kick will distort phase space more than a weaker kick.

and is applied after the wall bounce maps $\mathbb{M}_{\Delta n}$. The bumpy wall map can be shown to be an area-preserving map, and hence relevant to a physical Hamiltonian. The momentum kick is with respect to the momentum along the wall only, and hence we assume an appropriate change in the perpendicular momentum so that energy is conserved. It is conceivable that for incoming momenta that are glancing and hence have momentum p close to the total momentum, that this map may change the energy of the particle. However, if we avoid the edges of the Poincaré section we can avoid this case.

In Figure (4.13) we plot the integrable phase space volume versus the field strength for the typical 4/3 rectangular billiard, for a bumpy wall map with varying average kick stengths. Most relevant about these results is that even for a 10% momentum kick, the integrable islands persist and remain of good size, indicating that even in a bumpy rectangular quantum dot, that integrable islands are present and contribute.

4.3.6 Periodic Billiard Orbits

At this point, we have a good idea of the dominant periodic orbits, but we need to know their properties at various field strengths in order to anticipate the tunneling current due to them. Most of these values can be determined by simple geometric considerations, and we record them here. We consider a rectangular box of size $(L_x, L_y) = 2r_c(\lambda_x, \lambda_y)$; we will work in these scaled box lengths. The main three periodic orbits that intersect the top of the box are the football, dia-

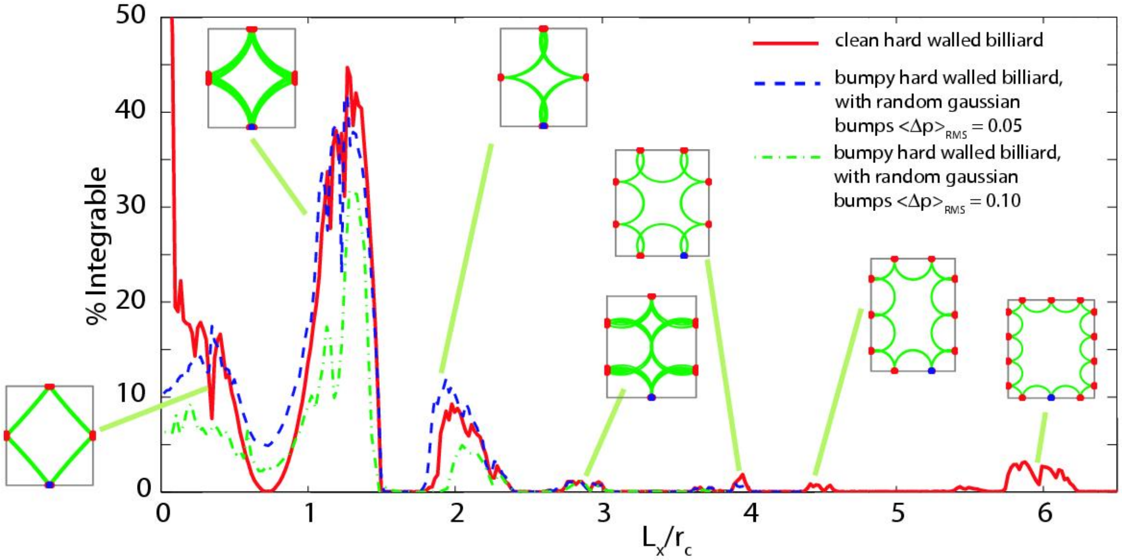

Figure 4.13: The percentage of phase space that is on a stable integrable island, when the walls are made bumpy. The effect is apparent but small, distorting and shrinking the integrable islands. As expected, a stronger average kick will distort phase space more than a weaker kick.

mond, and holly-leaf orbits; we will only consider the basic symmetrical version of each here for the simplicity of the analytic expressions. These main orbits are depicted in Figure (4.14); for concreteness we take the magnetic field to be in the $-\hat{z}$ direction (and hence $B < 0$), so that the cyclotron motion of a negatively charged particle will be clockwise.

In each case, we can safely assume that the orbit's length will increase monotonically with increasing field magnitude. The area of the orbit will not be as simple; while we can assume that it will change monotonically, the sign of the change is not trivial, and it may change sign as field magnitude increases. However, due to symmetry, we know that if the field strength B or the particle charge q changes, the sign of the area A will change as well; if we change both B and q, the dynamics will remain unchanged, and A will remain the same sign. Thus the quantity qBA will remain invariant with change of B direction or charge, as is the case with kL. Its derivative in B will become odd, however, with a change in B, implying that the slope of the interference bands will be odd in the magnetic field B, as is seen experimentally (see Figure 4.3).

From the following expressions for the length and enclosed area of the periodic orbits, the

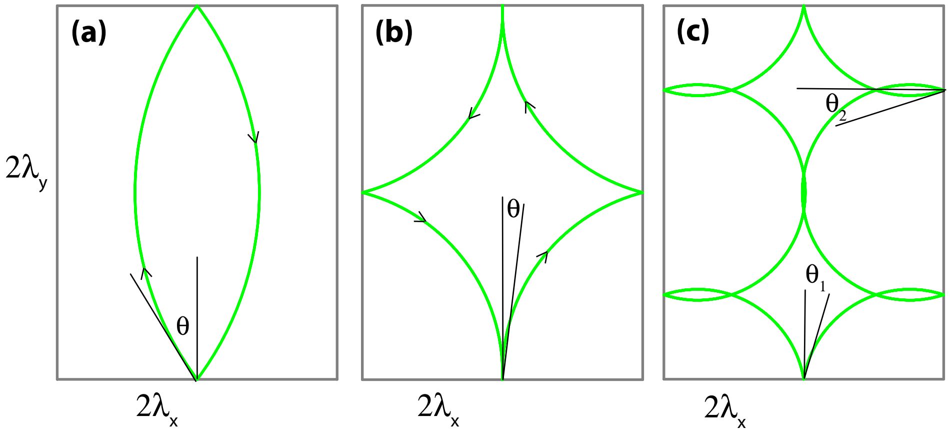

Figure 4.14: Main symmetrical periodic orbits of the magnetic billiard. Here we use a scaled billiard size $(2\lambda_x, 2\lambda_y)$.

unscaled action and phase follow as

$$\begin{aligned}
\phi(E,B) &= \frac{S}{\hbar} \\
&= \sqrt{2mE}Lr_c/\hbar + qBAr_c^2/\hbar \\
&= \frac{2mE}{\hbar qB}(L+A)
\end{aligned} \tag{4.28}$$

since $r_c = \frac{\hbar k}{qB}$. The time of flight depends only on the length, so that

$$T = \frac{mL}{|qB|} = \frac{L}{\omega_c}. \tag{4.29}$$

The monodromy matrix of the orbits is invariant of scaling,

$$M = \begin{pmatrix} \frac{\partial q'}{\partial q_o} & \frac{\partial q'}{\partial p_o} \\ \frac{\partial p'}{\partial q_o} & \frac{\partial p'}{\partial p_o} \end{pmatrix} \tag{4.30}$$

and hence the eigenvalues λ and $1/\lambda$ of the scaled system can be used to determine the stability and Lyapunov exponents of the unscaled orbits. The classical density in the time domain is the determinant of this matrix, $D(q_o, q', t) = |M|$, and hence is also invariant to scaling.

Football Orbit

This orbit bounces back and forth from the center of the top to the bottom wall; it is shown in Figure (4.14a). For small field it is almost a straight line back and forth. The angle with respect to vertical is

$$\theta = -\sin^{-1}(\lambda_y) \tag{4.31}$$

so that the initial momentum along the wall is $p = \sin(\theta)$, and will always be negative. The area and length are

$$\begin{aligned} L &= 4\sin^{-1}\lambda_y, \\ A &= -2\left[\sin^{-1}(\lambda_y) - \lambda_y\sqrt{1-\lambda_y^2}\right]. \end{aligned} \tag{4.32}$$

We note that since the particle always traverses the path in a clockwise fashion, that $A < 0$, and that the flux $AB \geq 0$ for this orbit. The requirements that θ have a real solution implies that the orbit exists when the distance to the far wall is not too large, i.e. when $\lambda_y < 1$; in addition, the orbit exists only when the particle doesn't touch the side walls, or when $\lambda_x + \lambda_y > 1$.

The monodromy matrix in general for the relevant map has a zero off-diagonal value, $\frac{\partial p'}{\partial q_o} = 0$, and as such the eigenvalues of the matrix are $\lambda_{1,2} = 1$, indicating that all existing football periodic orbits are direct parabolic, neither stable or unstable. Any change in the initial or final position of the football orbit on the upper or lower walls will not effect the initial of final momenta, as long as the orbit doesn't touch the side walls.

Diamond Orbit

This orbit bounces once on the center of each wall, curving in a clockwise fashion, as shown in Figure (4.14b). For small field it is almost a rhombus. The angle with respect to vertical is

$$\theta = \cos^{-1}\sqrt{\lambda_x^2+\lambda_y^2} - \tan^{-1}(\lambda_y/\lambda_x) \tag{4.33}$$

with initial momentum along the wall $p = \sin(\theta)$. For low fields $\theta > 0$, while for high fields, $\theta < 0$. The minimum angle occurs when the paths are straight lines, hence the size of the box $\to 0$ and only the second term remains, thus $\theta_{min} = \tan^{-1}(\lambda_y/\lambda_x)$. The maximum angle, at the highest field, will occur when the paths from wall center to wall center are half circles, which is an angle $\theta_{max} = \theta_{min} + \pi/2 = -\tan^{-1}(\lambda_x/\lambda_y)$. The minimum area is $A_{min} = 2\lambda_x\lambda_y$ while the minimum length is $L_{min} = 4\sqrt{\lambda_x^2+\lambda_y^2}$. The maximum length is easily found by remembering that each wall to wall path is a circle of diameter $\sqrt{\lambda_x^2+\lambda_y^2}$, so $L_{max} = 2\pi\sqrt{\lambda_x^2+\lambda_y^2}$.

The area and length in general are

$$\begin{aligned} L &= 8\sin^{-1}\sqrt{\lambda_x^2+\lambda_y^2}, \\ A &= \frac{\lambda_x\lambda_y}{2} - 4\sin^{-1}\sqrt{\lambda_x^2+\lambda_y^2} + \sqrt{(\lambda_x^2+\lambda_y^2)(1-\lambda_x^2-\lambda_y^2)}. \end{aligned} \tag{4.34}$$

For small fields the area is positive, unlike the football case, but may turn negative for large fields.

The monodromy matrix for this orbit is quite complicated, but can be found analytically; we only consider it when evaluated at the periodic orbit. We will choose to express it in terms of the angle of bounce on the lower and upper walls, θ_1, and on the side walls, θ_2. Noting that θ_2 can be found by rotating the billiard by $\pi/2$,

$$\theta_2 = \cos^{-1}\sqrt{\lambda_x^2+\lambda_y^2} - \tan^{-1}\frac{\lambda_x}{\lambda_y}. \tag{4.35}$$

The monodromy matrix

$$M = \begin{pmatrix} m_{11} & m_{12} \\ m_{21} & m_{22} \end{pmatrix}$$

has elements

$$\begin{aligned} m_{11} &= \csc^2\theta_1 \csc^2\theta_2 \left(\cos^2\theta_1(9\cos^2\theta_2 - 1) + \sin^2\theta_2 - 2\sin 2\theta_1 \sin 2\theta_2\right) \\ m_{12} &= -\left(\cos 2\theta_1 + \cos 2\theta_2 + 6\cos^2(\theta_1+\theta_2)\right)\cot\theta_1 \csc^2\theta_1 \csc^2\theta_2 \\ m_{21} &= 4\cot\theta_2(1 - 2\cot\theta_1\cot\theta_2) \\ m_{22} &= m_{11}. \end{aligned} \tag{4.36}$$

Taking the eigenvalues, we get a pair of solutions $\lambda = a \pm 2\sqrt{b}$, with

$$\begin{aligned} a &= -8\cot\theta_1\cot\theta_2 + \csc^2\theta_1 + \cot^2\theta_1(9\cot^2\theta_2 - \csc^2\theta_2) \\ b &= \cos(\theta_1+\theta_2)\left(\cos(\theta_1-\theta_2) + 3\cos(\theta_1+\theta_2)\right)^2 \cot\theta_1\cot\theta_2\csc^3\theta_1\csc^2\theta_2. \end{aligned} \tag{4.37}$$

In particular, we note that $b \to 0$ when either θ_1 or $\theta_2 \to \pi/2$, when the orbit strikes one of the walls perpendicularly. When this happens, the orbit becomes parabolic in stability, and a further change in angle will change the stability of the orbit, marked by a change in eigenvalues from real to complex. This confirms the process of bifurcation seen in earlier sections, and depicted in Figure (4.9).

Holly-Leaf Orbit

This orbit bounces once on the center of the lower and upper walls, curving in a clockwise fashion, and twice on each side wall, as shown in Figure (4.14c). The orbit does not exist for small or large fields, only existing when $\lambda \sim 2-3$. The angle with respect to vertical along the side walls must be found numerically by solving the equation

$$(\lambda_x + \sin\theta_2)^2 = 1 - (2\cos\theta_2 - \lambda_y)^2. \tag{4.38}$$

The angle from the vertical on the upper and lower walls follows,

$$\theta_1 = \mathrm{sign}(2\cos\theta_2 - \lambda_y)\cos^{-1}(\sin\theta_2 + \lambda_x). \tag{4.39}$$

The area and length are then

$$\begin{aligned} L &= 4\pi - 8\theta_2 - 4\theta_1 \\ A &= 4\lambda_x\lambda_y - 2\pi + 8\theta_2 + 4\sin\theta_2\cos\theta_2 + 4\theta_1. \end{aligned} \tag{4.40}$$

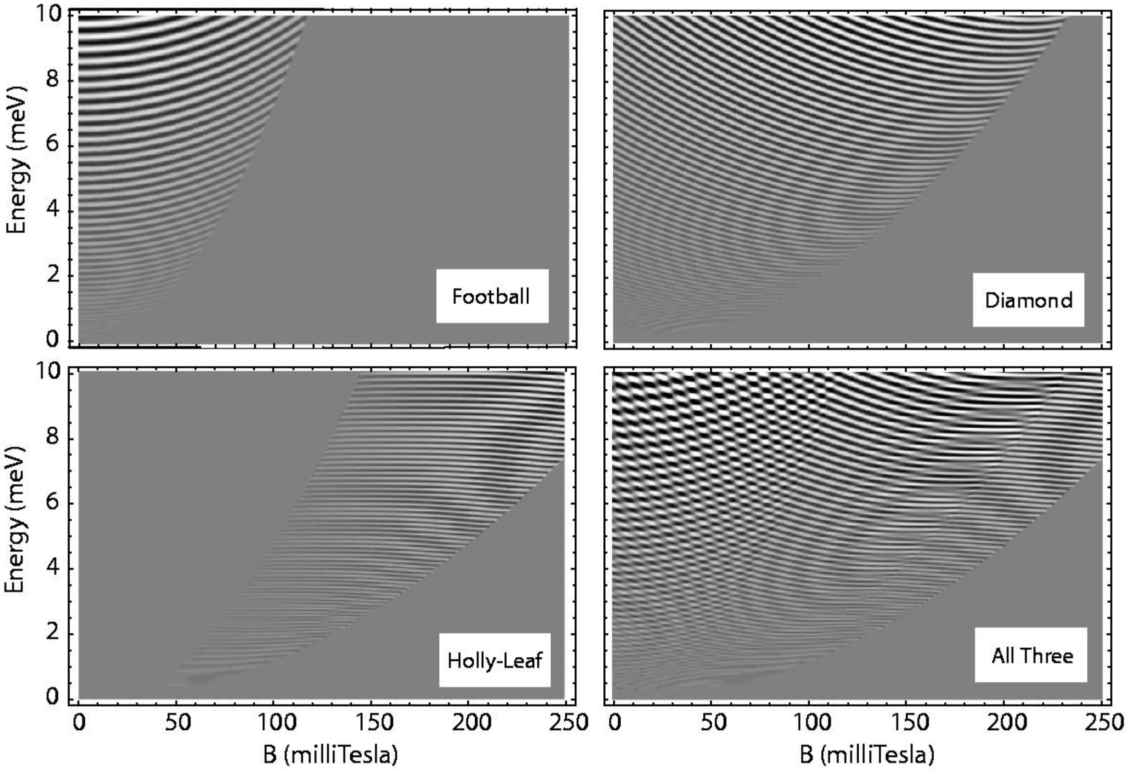

Figure 4.15: Tunnelling current factor $\xi(E, B)$ for each main periodic orbit type, over a range of energies and field values. In the last frame the contributions to the current are added from each orbit type. The billiard is scaled to a size very close to that of the large dot.

4.3.7 Billiard Interference Bands

Knowing the properties of these main periodic orbits as the magnetic field and energy are adjusted, we can determine the phase around the orbit and part of their weighting factors. For the sake of qualitative comparison, we will ignore Maslov indicies and take the classical amplitude to be uniform over the range of the orbit's existence. We define a function

$$\xi(E, B) \equiv C\ E\ \cos^2 \theta_o \cos(S(E, B)/\hbar), \tag{4.41}$$

where C is some constant. This function contains the main factors, due to the dynamics of the billiard, that contribute to the simplified model of the oscillatory part of the tunneling current, equation (4.23). Thus $\xi(E, B)$ serves as an useful qualitative measure of the tunneling current. These main factors include the orbit phase and the momentum into the tunnel junction; we assume that the classical amplitude is slowly varying for these orbits, and approximate it as unity. The other quickly

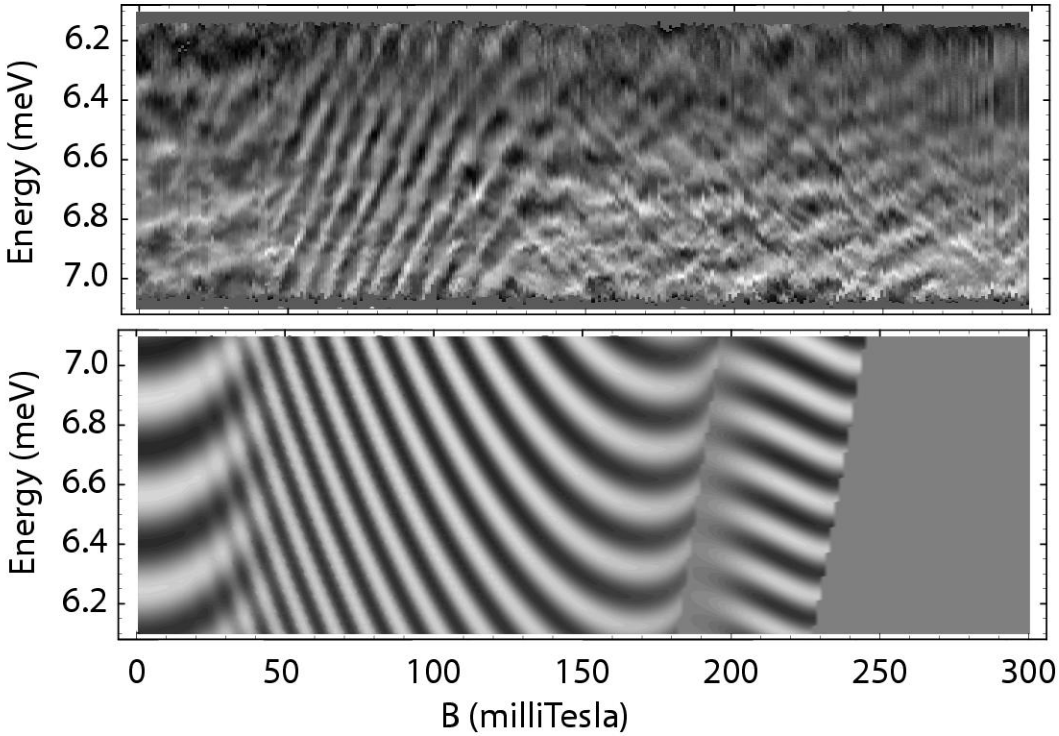

Figure 4.16: Tunnelling current factor $\xi(E,B)$ for each main periodic orbit type. For clarity, the contributions from each orbit are included only in a limited range of B values. The experimental current data is shown just above, but upside down in order to aid in comparison. For low fields the football shaped orbit has the correct ΔE spacing, but has the wrong band slope, while the diamond orbit reproduces the slopes quite well. The holly-leaf orbit is a reasonable match for bands at high B.

varying quantity in the tunneling current is due to the evanescent amplitude of the resonant states of the small dot, which we ignore here.

In Figure (4.15) we plot this function over a range of magnetic field values and energies for each of the main periodic orbits, and for the sum of these contributions. For the football shaped orbit, the oscillations have positive slope, tending to flat for small magnetic field. The diamond shaped orbits have mostly positive area, and hence negative slope, but flattening out and becoming positive in slope for large field values. The holly-leaf shaped orbit has small negative area, leading to mainly horizontal interference oscillations. The obvious candidate for the strong interference band around $B = 100$ milliTesla is the diamond shaped orbit, while for the interference pattern near $B = 0$ the football and diamond orbit are relevant. Interference bands further out in magnetic field are likely due to holly-leaf orbits and orbits with a higher number of bounces.

In Figure (4.16) we compare the billiard bands to the experimental data; these orbital bands have been somewhat clipped in B range to highlight the similarities. For low fields the football shaped orbit has a close ΔE spacing, but has the wrong slope to the oscillations, implying that the sign of A is wrong; that the real orbits have positive area instead. Referring back to Figure (4.3) however, there is evidence that there are oscillations with both positive and negative slope near $B = 0$; this could indicate a bifurcation of a direct orbit, due to the soft walls of the real dot, with one branch having positive area and the other negative area. A hard walled billiard couldn't reproduce such behavior.

The diamond shaped orbit matches the slope and spacing quite well for a billiard result. In addition, the gentle flattening of the slope of these experimental oscillations around $B \sim 125$ milliTesla is reproduced by the billiard, indicating a significant reduction in orbit area around this value of B. As we have shown, this change in slope is neighbored by a change in stability as well. For higher fields the holly-leaf orbit and its siblings provide a possible explanation for the various isolated sets of interference bands, particularly the bands in the region $B \sim 250$ milliTesla. The discrepancy in the location of the bands in B can be attributed to the more complex dynamics of the realistic, odd-shaped and soft-walled large dot.

We can understand intuitively why the diamond shaped orbit of the billiard would match better than other orbits. For low fields, the forces on the particle due to the magnetic field are small compared to the forces due to the soft walls when near the walls, but at higher fields the curvature of the trajectory due to the magnetic field is dominant. However, at high enough fields, the particle will reflect off the walls more often, and will "learn" that the billiard is odd-shaped and non-rectangular. The diamond shaped orbit is a mix of both cases; the magnetic field is strong enough that the curvature is mostly due to B, but the particle only samples the wall at four points, and thus, to lowest order, the dot appears rectangular. By matching the billiard to the dimensions of the dot, as sampled by the particle, the billiard model proves quite useful.

The main drawback of the billiard model in explaining the slopes and signal strength of the bands is that it fails to correctly predict the dropout of the diamond orbit below 50 millliTesla, as well the existence and placement of higher field bands. As we noted, these characteristics of the system are due to the non-rectangular, soft-walled nature of the quantum dot. As such, understanding the system further requires a more accurate dot. This we address in the rest of the Chapter.

4.4 Wavepacket Simulation

While the billiard model matches surprisingly well the qualitative aspects of the data, as well as the shape of interference bands, it fails to capture some of the more interesting aspects of

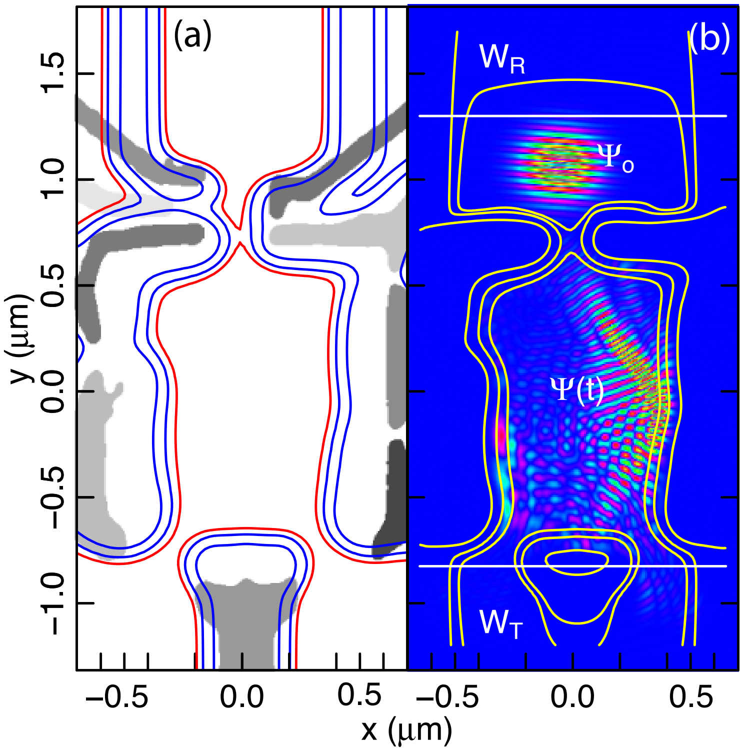

Figure 4.17: The simulated effective potential of the large quantum dot, and a wavepacket propagating into and through the large quantum dot.

the system, such as the dropoff of the interference bands with lowering magnetic field at around 50 milliTesla. One approach to improving on the billiard model might be to derive a more exact semiclassical treatment [78], and using a more realistic billiard system to attempt to understand the finer details of the system using semiclassical numerics. The drawback to this is that accurate semiclassics is usually difficult technically. Instead we choose to perform a full quantum simulation of the system.

To more accurately simulate the system in question, we employ a density-functional theory (DFT) numerical code [95] to get a more accurate effective potential of the large dot; the results were depicted in Figure (4.1c), and are shown in Figure (4.17a), with the potential contours superimposed on the gate pattern. The red contour is the contour at the Fermi energy, the classical turning point. Note that the effective walls of the system are upwards of 200 nm further in from the gates themselves in most places. The outgoing QPCs are simulated with gate voltages that allow for ~ 5 open transverse modes. In addition, the small quantum dot has been completely opened up, and in this case acts as only a tunnel junction to the leads; on the right, the remains of the small dot have been removed to avoid unphysical resonances in the results.

We can justify removing the small dot from the system as follows: while the small dot acts as a spectrometer in the actual device, this is necessary only because the current cannot be resolved in energy experimentally. Numerically, however we can measure the wavefunction amplitude in the system, and resolve the flux through the system in the energy domain without needing to include a spectrometer element. We have argued that the main signal in the current is due to the LDOS at the classical turning point at the tunnel junction with the large dot, and thus by determining $\eta = T/T_o$ for the tunnel junction between the small and large dots, we can use equation (4.13) with the experimentally measured tunneling rate Γ, or equation (4.14) with the experimental current with the large dot removed, to simulate the tunneling current in the real system. We note that this argument implicitly assumes that the tunneling process with or without the small dot will show nearly the same ratio T/T_o; explicitly, we assume that by changing the tunneling wavefunction Φ_o from that of the small dot to that of a lead, the ratio T/T_o will not change appreciably, and hence that this ratio is dominated by the dynamics in the large dot. This is along the same lines as the arguments made in Section (4.2).

Following the approach of Chapter (3), and as depicted in Figure (4.17b), a wavepacket is introduced with a mean velocity at the Fermi velocity and heading toward the tunnel junction with the large dot. The energy spread of the wavepacket is equivalent to a temperature of 20 K or 1.7 eV, much larger than the region of interest energetically. It propagates down and into the tunnel junction, and some portion of it transmits through the tunnel junction; the wavefunction through a flux surface at the tunnel junction, $|\psi(t)\rangle$ is tracked. To begin we remove the far end of the cavity of the large dot, and allow the wavefunction to propagate away into the leads, with no chance of reflection; the electron wavefunction in the absorbing region, marked as W_T in Figure (4.17b), is tracked in time, and later used to resolve the flux into this region in energy, $\Phi(E)$. We mark the time after which there is no flux moving through the tunnel junction, t_{inc}, after which we consider the particle “incident.” Because there is no reflection from the modified cavity, the measured flux is the incident flux, Φ_I of the cavity. We define the unperturbed system as the system without the cavity in place, where all the flux that tunnels into the large dot ends up in the outgoing leads. This is in keeping with the goal of determining the change of transmission of the system by including the cavity, with the same tunneling junction in place, T/T_o, and is consistent with the approach in Chapter (3).

Having measured the incident flux Φ_I, we again interpose the cavity, and run the same simulation. After the incident time t_{inc} we track the wavefunction that is reflected back through the tunnel barrier into the absorbing region, marked W_R, and determine the reflected flux Φ_R.

The propagation of the wavefunction, rattling around in quasiclassical paths, is depicted as $\Psi(t)$ in Figure (4.17b). Because the cavity is resonant, the particle's amplitude may take a good deal of time to leave and be absorbed in the absorbing regions. The reflected amplitude converges more quickly than the transmitted, because it is significantly smaller in amplitude, and so we measure it. Since the system is a two terminal system, and the flux measurement process employed accurately measures the total probability, then we know that

$$\Phi_I(E) = \Phi_T(E) + \Phi_R(E)$$

will hold well. Thus we may measure the transmission

$$\tilde{T}(E) = 1 - \frac{\Phi_R(E)}{\Phi_I(E)} \tag{4.42}$$

with good accuracy.

Note that we do not immediately identify $1 - \frac{\Phi_R(E)}{\Phi_I(E)}$ with T here. Since we took as the incident flux Φ_I that flux which had already entered the cavity through the tunnel junction, we are not measuring the transmission from the small dot into the leads by this simulation. Instead we are measuring the transmission of the cavity itself. The incident flux Φ_I as defined here is proportional to the cavity-less transmission of the tunnel barrier, T_o, while the transmitted flux Φ_T is in the same way proportional to the transmission of the barrier with both dots in place, T. By the assumption that the dynamics of the large cavity has little affect on the small dot, we can identify the simulated transmission as

$$\tilde{T} \equiv \frac{\Phi_T(E)}{\Phi_I(E)} = \frac{T}{T_o} = \eta. \tag{4.43}$$

As a side note, the resonant nature of the system demands a particular numerical approach. Because the electron rattles about in the large dot for a significant time, the measurement of flux across a flux surface becomes numerically unstable. The approach of tracking the entire history of the wavefunction in the absorbing regions can be shown to preserve exactly the total probability on the grid, and hence is necessary to overcome the numerical instability. The price paid is that the entire history of the amplitude must be stored and processed at the end of the run, using many times more memory and CPU time than the flux surface approach. The specifics on the numerics are discussed in Chapter (3).

In Figure (4.18) we show the results of a set of wavepacket simulations at the top, followed by the experimental data and the billiard results at the bottom. Wavepackets were propagated over a range of magnetic field values, and each resolved in energy to produce the plot. The resemblance to the experimental data is striking; all the features of the billiard model are captured, but the quantum simulations also capture the dropout of the main interference bands at $B \sim 50$ milliTesla and beyond

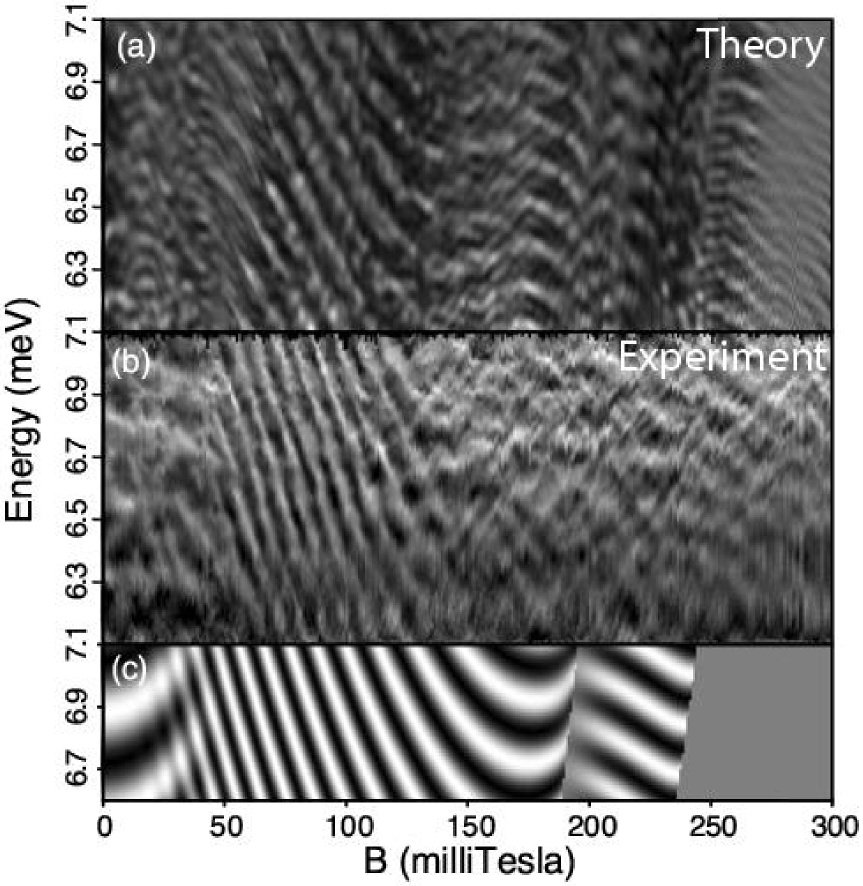

Figure 4.18: The simulation of the experiment taken at the Fermi energy, compared to the actual experimental data, with no fitting parameters. Oscillations as predicited by the toy billiard model are shown at the bottom for comparison. The discrepancy of 20% in the spacing of the bands in magnetic field can be attributed to the DFT simulation not correctly predicting the effective area of the large dot.

$B \sim 150$ milliTesla. In addition, the interference oscillations near $B = 0$ have the correct spacing and slope. Higher field bands at around $B \sim 250$ milliTesla also agree in theory and experiment.

There is a discrepancy in the simulation results, in that the bands don't wash out as much as the experimental data, but this is easily attributed to the fact that there is no dephasing or disorder in the quantum simulations, or experimental noise. In addition, the spacing ΔB of the main interference bands is off by 20% from the experimental value, while the energy spacing is much closer, about 7% off. This can be attributed to the fact the the experimental device was cooled with positive voltage applied to the gates, which created a negative imprint of the gate pattern on the donor layer in the sample, effectively bringing the gates "closer" to the 2DEG. This should have made the effective screening length of the gates shorter experimentally than in the simulation, and hence made the billiard appear flatter and a little larger in area. Such a circumstance is consistent with the band spacing error: a slightly larger dot should affect the area of orbits more than their length, and hence the spacing ΔB more than ΔE.

Having found a good match to the experimental data, we are still left asking about the actual classical picture of the process; quantum simulations are powerful, but do not always provide clear intuition. With that in mind we turn to classical periodic orbits and the search for scarred states.

4.5 Classical Periodic Orbits

Here we change gears completely and run trajectories in the realistic effective potential simulated by DFT in order to gain intuition about the periodic orbits involved. One important aspect of the tunnelling current is that an orbit must penetrate well into the tunnel junction in order to have significant tunneling amplitude; the question remains as to whether the system can support such orbits, and what their stability might be. Once a periodic orbit is found, we can track its evolution as the magnetic field or energy is changed. Orbits that exist with significant density and penetrate into the tunnel junction over a range of magnetic field values are good candidates for the source of the interference bands.

The process of searching for periodic orbits is as follows: a Poincaré surface of section is chosen as the line $y = b$ near the mouth of the tunnel junction in the effective potential, and particles of energy E are launched in random directions from classically accessible points along this line, each with some initial phase $(x_o, p_{x,o})$. When a particle returns to the Poincaré surface, it continues through the surface, and when it passes through the second time, the returning phase is recorded, (x, p). We may define a distance in phase space

$$\epsilon = \sqrt{\left(\frac{x - x_o}{L_x}\right)^2 + \left(\frac{p_x - p_{x,o}}{\sqrt{2mE}}\right)^2}$$

as a scaled measure of the distance of the new phase point from the original. We can then use a robust root finding algorithm [61] to minimize this distance, and hence find a periodic orbit. One potential problem with this approach is that it does not allow for periodic orbits which pass through the Poincaré surface twice or more at different points. However, given the influence of dephasing and impurity scattering in a real sample, our interest is focussed on the shortest and simplest orbits, and hence we can live with the problem.

Once an orbit has been found, it is rerun for the same initial condition, but the monodromy matrix at each time step is integrated as well, to determine the full monodromy matrix for the periodic orbit; this is done using a method from [12] and developed by [6], but adapted for a magnetic field. Once the monodromy matrix is calculated, quantities like the stability, Lyapunov exponents, and classical amplitude may be calculated as well from its matrix elements. In addition, the action of the orbit, as well as its length and area, may be directly calculated from the $\vec{r}(t)$ and $\vec{p}(t)$ trajectory values. The action is simply the sum

$$S = \sum_i \frac{p_{x,i} + p_{x,i-1}}{2}(x_i - x_{i-1}) + \frac{p_{y,i} + p_{y,i-1}}{2}(y_i - y_{i-1}),$$

and the length is just $L = \sum \sqrt{(x_i - x_{i-1})^2 + (y_i - y_{i-1})^2}$, and the area may be calculated by adding up all the areas of triangles from the origin to the one point and to the next, with directionality included, which follows from the cross product:

$$A = \frac{1}{2} \sum_i x_{i-1} y_i - x_i y_{i-1}.$$

In Figure (4.19) we show a series of periodic orbits at a variety of magnetic fields, all launched in the realistic potential at the Fermi energy 7.1 meV. The orbits were filtered for short length and relevance to tunneling into the small dot; these are a representative set. For small fields, there are two distinct short orbits, one that has small area, and one with larger negative area. The orbit with small area starts out tracing over its path, then evolves a twist, as shown in the figure. The other main orbit at these fields is likely responsible for the finite slope of the oscillations in the experimental data near $B = 0$.

At higher fields an oddly shaped diamond orbit forms, and at $B \sim 110$ milliTesla develops a twist near the far wall, then near 125 milliTesla develops a second twist. This orbit persists up to about 150 milliTesla. At higher B fields variants of the holly-leaf orbit are evident.

In Figure (4.20) we present the series of found periodic orbits for the large quantum dot system. The orbits have been filtered by length and by how far they penetrate into the tunnel junction region; only those orbits under 5μm in length and that penetrate well into the tunnel junction are shown. Each orbit is a dot, with the stability of the orbit indicated by color: red dots mean stable orbits, blue dots mean completely unstable (hyperbolic) orbits, and green dots indicate that the orbit has both stable and unstable directions (loxodromic). The area and Lyapunov exponent is plotted for the orbits.

The most striking feature of the data is that the periodic orbits tend to form trend lines as the field B is changed, with uniform or slowly varying parameters such as area or Lyapunov exponent (length as well, but since most orbits show little variation in length, we exclude that data here). These trend lines tend to take abrupt jumps in the parameters, often signaled by a change

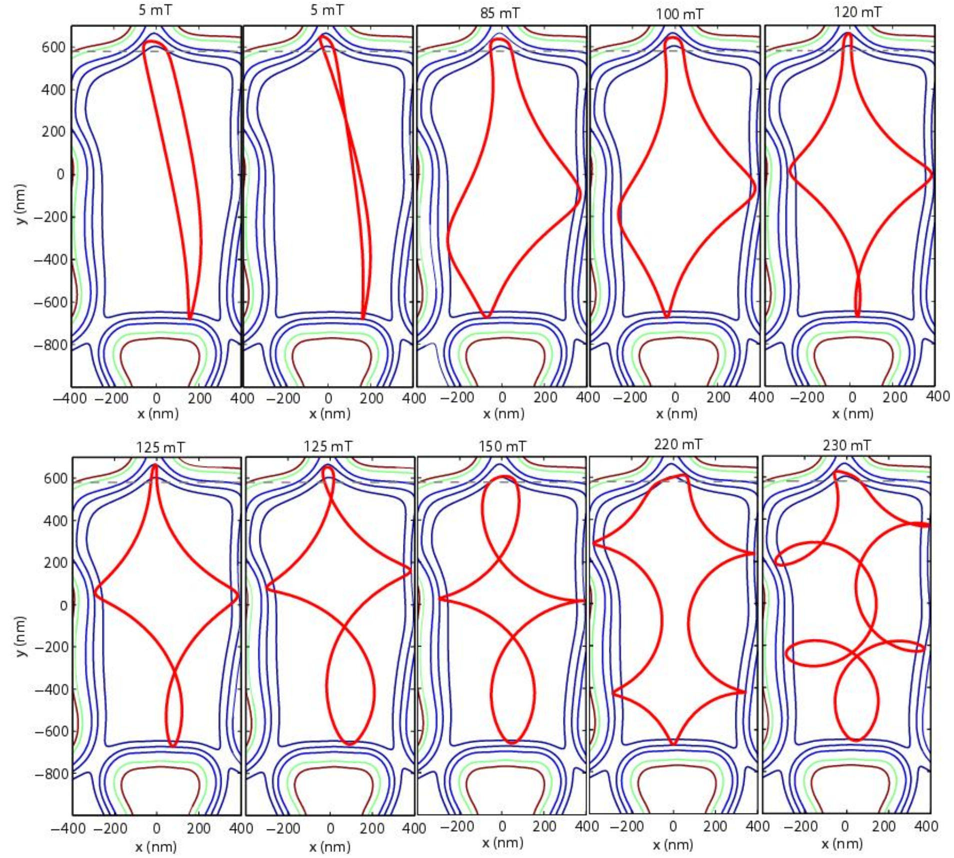

Figure 4.19: Periodic orbits of the large quantum dot from $B = 0$ up to 250 milliTesla, at energy $E = 7.1$ meV.

in stability. This likely indicates processes such as bifurcations taking place as the parameter B is changed. In addition, the trend lines sometimes trail off to nothing, indicating that the orbit has changed so that it does not penetrate as deeply into the tunnel junction region.

Also striking is the region $B = 10 - 50$ milliTesla where no orbits of reasonable short length penetrate into the tunnel junction region. This coincides closely with the experimental data and the quantum simulations. While periodic orbits obviously exist for these field values, because of the particular shape of the large dot, no simple periodic orbits penetrate deeply into the tunnel region, and furthermore don't form clear trend lines like orbits at higher field values. Since the spectrometer acts as a measure of the LDOS in the tunnel junction region, the signal from these orbits is exponentially reduced, and interference bands are not seen.

We wish to point out one additional feature of the results, which occurs at the dashed red line: at this field value $B \sim 125$ milliTesla, the diamond shaped periodic orbit abruptly changes

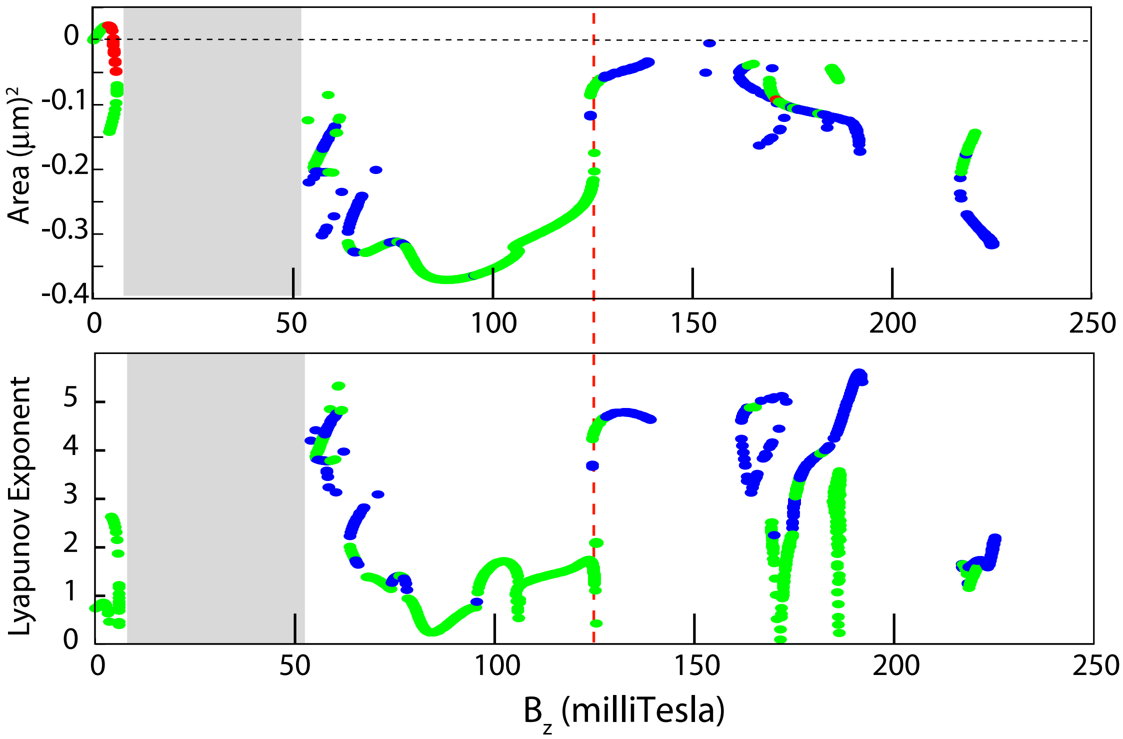

Figure 4.20: Periodic orbit areas and Lyapunov exponents for the realistic quantum dot potential. Each dot is a periodic orbit; the orbits have been filtered to show only those that penetrate deeply into the tunnel junction region. The color of each dot indicates the stability: red dots mean stable orbits, blue dots mean completely unstable (hyperbolic) orbits, and green dots indicate that the orbit has both stable and unstable eigenvalues of the monodromy matrix (loxodromic). Of note is the absence of orbits in the gray region below 50 milliTesla, and the abrupt change in area and Lyapunov exponent at $B \sim 125$ milliTesla.

area and stability, which occurs because one of the "arms" of the orbit adds a twist. This transition is shown in Figure (4.21), as is the evolution of the shape of the "diamond" orbit. The twist process is analogous to the billiard system. As the change occurs, the Lyapunov exponent drops rapidly, perhaps momentarily becoming stable, and then returns to being loxodromic, and then tending to hyperbolic in stability as B is increased. The twisting of the loop is accompanied by a very rapid change in area; the plot indicates that the trendline in orbit area actually turns back on itself and becomes double valued at this field.

This abrupt change in the the area of the orbit will be signaled in the current $I(E, B)$ by a change in the spacing ΔB of the inteference oscillations. Referring back to the experimental and quantum simulation data (Figures (4.18) and (4.3)), there is indeed such a change in ΔB at this

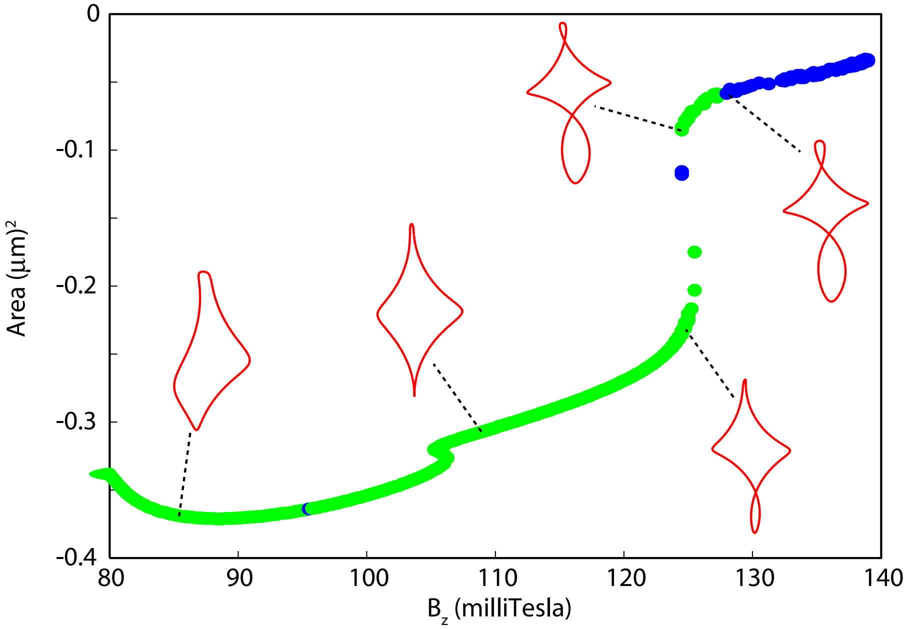

Figure 4.21: Periodic orbit areas and shapes for the main interference band, showing the evolution of the orbit shape. The color of the dots is explained in the text and in Figure (4.20).

value of magnetic field, appearing as a "knee" in the interference bands. As the area of the orbit becomes smaller, the increase in magnetic field needed to increase the flux by one quantum goes up, and the spacing increases; this increased spacing is seen in both experiment and quantum theory. In addition, the billiard shows a similar trend, not as an abrupt knee, but as a smooth levelling off and even change in slope of the oscillations.

These results suggest that we now understand the main features of the experimental data, and can safely interpret the features not only in terms of toy billiard orbits on the gross scale, but also in terms of realistic periodic orbits on the finer scale. Since these orbits are predominantly unstable, any quasiclassical resonant states that resemble these orbits are scarred states [47, 54]. So we go on to look for scars in the quantum dot.

4.6 Cavity Eigenstates

We begin our search for scarred states by solving for states in a clean regularly shaped billiard instead. After reporting some interesting numerical results, we will turn to the search for scarred states in the realistic quantum dot potential used earlier in the chapter.

4.6.1 Approach

We solve the time-independent Schrödinger equation,

$$\hat{H}\psi = E\psi \tag{4.44}$$

using finite differences on a fine grid. For a grid at points $\vec{r}_{i,j}$ and grid spacings $\Delta x, \Delta y$, the finite difference matrix in 2D reads, for zero magnetic field,

$$\begin{aligned} m_{i,j,i',j'} \quad = \quad & -\frac{\hbar^2}{2m}\Big[\\ & \Delta x^{-2}(\delta_{i,i'-1} + \delta_{i,i'+1} - 2\delta_{i,i'})\delta_{j,j'} + \\ & \Delta y^{-2}(\delta_{j,j'-1} + \delta_{j,j'+1} - 2\delta_{j,j'})\delta_{i,i'} + \Big] \\ & +V(\vec{r}_{i,j})\delta_{i,i'}\delta_{j,j'}, \end{aligned} \tag{4.45}$$

where $\delta_{a,b}$ is the Kronecker Delta. For a magnetic field, the matrix elements between points in space must also include the difference in phase due to the vector potential [21]. The nearest neighbor matrix elements must include the extra factor $e^{iq\vec{A}\cdot(\vec{r}_{i,j}-\vec{r}_{i',j'})}$ in order to include magnetic field. Writing this in shorthand as $a_{i,j,i',j'} = e^{iq\vec{A}(\vec{r}_{i,j})\cdot(\vec{r}_{i,j}-\vec{r}_{i',j'})}$, we have matrix elements

$$\begin{aligned} m_{i,j,i',j'} \quad = \quad & -\frac{\hbar^2}{2m}\Big[\\ & \Delta x^{-2}(a_{i,j,i'-1,j}\delta_{i,i'-1} + a_{i,j,i'+1,j}\delta_{i,i'+1} - 2\delta_{i,i'})\delta_{j,j'} + \\ & \Delta y^{-2}(a_{i,j,i,j'-1}\delta_{j,j'-1} + a_{i,j,i,j'+1}\delta_{j,j'+1} - 2\delta_{j,j'})\delta_{i,i'} + \Big] \\ & +V(\vec{r}_{i,j})\delta_{i,i'}\delta_{j,j'}. \end{aligned} \tag{4.46}$$

For constant magnetic field, the factor in the symmetric gauge can be simplified to $e^{\pm iaBx_i\Delta y}$ or $e^{\mp iaBy_i\Delta x}$, depending on which matrix elements it is.

4.6.2 Idealized-System Eigenstates

With the numerics in hand, we solve for the eigenstates of a very regular system at moderate and strong magnetic fields. In Figure (4.22) we depict eigenstates of a regular soft-walled rectangular dot at a field strength on the order of 100 milliTesla; both the field and the idealized quantum dot are comparable to the experimental system; in addition, for quasiclassical states we overlay the associated periodic orbits from the billiard system. Classically the system has a large stable island surrounding these types of periodic orbits, and quantum mechanically these quasiclassical states stand out. The symmetry of the system forces all states to have even or odd parity. Some states are fairly evenly spread over the classically allowed region, while others follow closely classical periodic orbits.

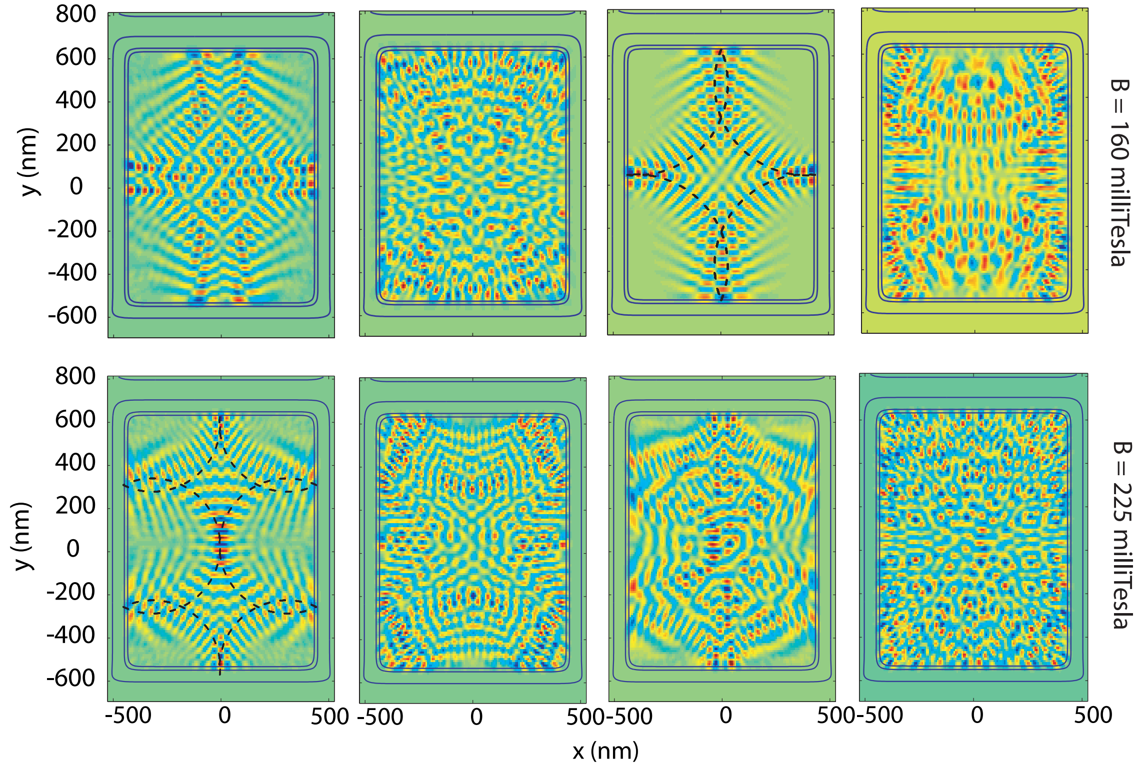

Figure 4.22: Eigenstates of a regular closed quantum dot in a perpendicular magnetic field. The states have energy near 6.5 meV, and the closed rectangular dot is 900 by 1200 nm in size, slightly larger than the real dot. In the upper row we have eigenstates for a field of $B = 160$ milliTesla, while the field is 225 milliTesla in the lower row. Shown along with the clearly quasiclassical states are states at nearby energies which show little quasiclassical qualities.

The obvious classical nature of these orbits, which tend to show up with a frequency of 1 in 10 - 20 states for these parameters, will be quickly washed away when symmetry is broken and the system pushed far from integrability, for example by a bumpy background or by distorting the perimeter of the system. These quasiclassical states become far less frequent, but are often still visible in the simulations.

In Figure (4.23) we show eigenstates for a comparable sized quantum dot with a regular soft-walled rectangular shape in a 1 and 5 Tesla field. In the top row we show typical bouncing ball-like eigenstates for the clean smooth system at 1 Tesla. At times these states can appear very classical in nature. In the middle and lower rows a weak background bumpiness has been added to the potential of the dot. As in the clean case there are edge states present that ring the boundary and show a bouncing ball-like spatial pattern. However, the symmetry breaking of the bumpy case also allows for solutions that are localized in space, often with most of the amplitude on rings of

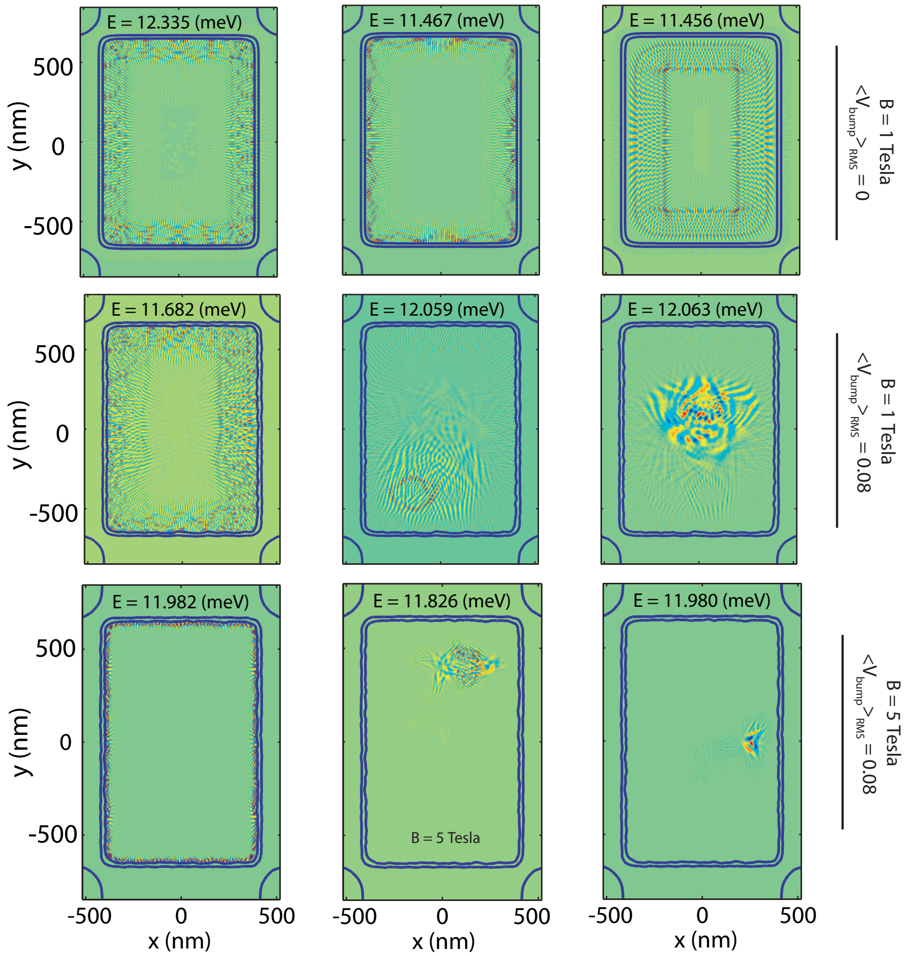

Figure 4.23: Eigenstates of a regular closed quantum dot in a strong perpendicular magnetic field of 1 and 5 Tesla. In the upper row the system is clean, while in the two lower rows a weak bumpy background has been added to the potential. This has the effect of breaking symmetry and allowing for localized “bulk” states.

the size of the cyclotron motion. As the field increases to 5 Tesla; these localized bulk states may remain somewhat dispersed in the bulk, or can be very localized, almost down the magnetic length $a_H \equiv \sqrt{\hbar/m\omega_c}$ [21].

4.6.3 Cavity Eigenstates

Having tested the method we turn to searching for scarred eigenstates in the realistic potential. As we know the periodic orbits in the billiard are much more likely to be stable than in the real potential, and the integrable islands non-existent, so the quasiclassical states will in turn be

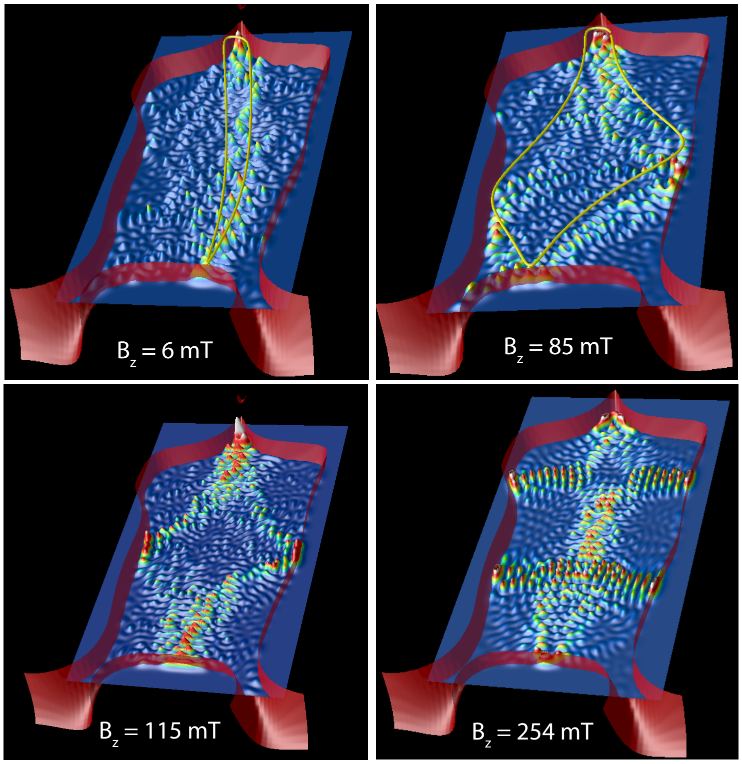

Figure 4.24: Eigenstates of a realistic closed quantum dot in a perpendicular magnetic field, plotted within a 3D rendering of the large dot potential. The first two have had the corresponding periodic orbit added for comparison. The state at 6 milliTesla is on the cusp of being stable, and may in fact be stable, but the other two states are unstable. The states at 85 and 115 milliTesla are the resonant states that contribute to the strong interference bands structure in the data. The state at 254 milliTesla would produce a stripe of bands at the higher field.

rare. For the system in question, which is about 40 wavelengths across, the frequency of scar-like orbits was about 1 in 200 for some field values, but 1 in 20 for others. The typical level spacing for the dot is 7μeV. Although the quantum dot is open and leaky, we have chosen to close the dot to find the states, and assume that the closed dot eigenstates and energies will be close to the open dot solutions for strong resonances. An alternative approach could be to use something like R-matrix theory or complex-scaling [77] to handle the non-Dirichlet boundary conditions of a leaky dot.

In Figure (4.24) we plot the found scarred states in three-dimensions within the potential surface of the large dot; the surface plotting of the scarred states aids in visualizing them, since they can be faint at times. In reality the first state at $B = 6$ milliTesla may in fact be stable, but is on the cusp either way. The next two states are classically unstable; these are the states that contribute to the strong interference bands in the experimental current. The last orbit will participate in creating stripes of banding at higher fields in the experimental current, such as seen around $B = 260$ milliTesla in Figure (4.3).

4.7 Conclusions

In this Chapter we have analyzed the results of an experiment with a small spectroscopic single-electron quantum dot coupled to a large leaky quantum dot which acted as a Fabry-Perot cavity. We have formulated an approach to the system that focusses on the small scale structure in the system, and found that factors due to the dynamics of the large dot will dominate the tunneling current when significant resonant states are present, and that the interference bands seen in the experimental signal are consistent with the kinds of periodic orbits the large dot could support. Using a toy billiard model, we find that the characteristics of the major interference bands are reasonably well matched by the predictions of the billiard model, but that the billiard model failed when particulars of the dynamics due to the dot shape came into play.

Using a realistic effective potential model of the large dot, quantum dynamics simulations reproduced with striking accuracy the patterns seen in the experimental data. This prompted a study of the periodic orbits of the realistic system. The strength of the signal of the bands is due to particular orbits that are structurally robust to changes in magnetic field, and that the loss in signal is not due to a change in stability of the orbits. Instead it is due to a reduced coupling to the spectrometer states because of the manner in which the periodic orbits reflect from the wall of the large dot near the tunnel junction. In addition, this study revealed that the orbits are for the most part unstable in character, and that rapid changes in the stability of the orbits can be seen as kinks or knees in the oscillations within the interference bands. Solving for eigenstates of the Schrödinger equation revealed scarred states matching the classical periodic orbits, indicating that the interference bands are due to these states, and that the device is in a sense “imaging” these scarred resonant states of the large dot.

Chapter 5

Tip Scattering Theory

In this Chapter we consider how an electron scatters from a localized radially symmetric potential in two-dimensions, a potential of the kind that might be generated in a two-dimensional electron gas (2DEG) when an SPM tip is introduced. This is of interest for the purposes of understanding SPM tip-scan experiments, of the kind done by the Westervelt group at Harvard [103, 101, 100, 102, 67], and in particular for understanding the next generation of these experiments.

In the past, SPM tip imaging experiments were almost always performed using a single source QPC and a tip that backscattered the electron. In this configuration, the particular shape of the potential due to the SPM tip is not important, as long as it can reverse or "backscatter" an electron trajectory back into the source. With the source and the target colocated, almost any trajectory that, when striking the tip, doesn't retrace its path, will not return to the source, and hence will not change the conductance through the system. In this sense, the target sees only the "glint" from the tip potential, and is insensitive to the actual shape of the effective potential (beyond that it can backscatter, and hence has a central value $V_o > E_F$).

When the source and target QPCs are at different locations, when the system is in the presence of a perpendicular magnetic field, or when large reflective structures in the system allow for alternate, non-backscattered paths, then the particulars of the tip potential become important. In this Chapter we consider classical tip scattering theory for such a tip in two dimensions, and apply it for two representative tip shapes. We then examine the caustic structure shed by the scattering process, and how such a tip can be approximated as a lens. Next we consider a quantum approach to tip scattering, and calculate tip scattering profiles in the far field, using partial wave expansion and a variable phase method.

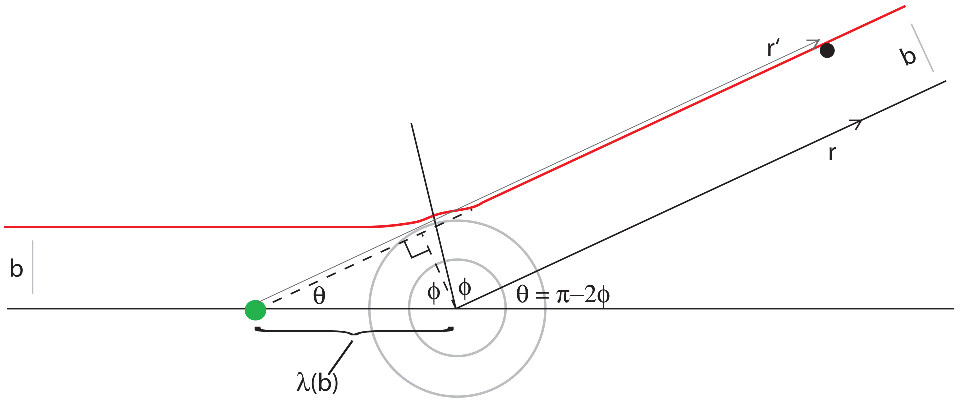

Figure 5.1: Classical scattering schematic, with an incoming particle of impact parameter b being scattered by a central potential $V(r)$ into some outgoing angle $\theta(b)$. Symmetry dictates that the outgoing trajectory lies a distance b from a central ray for large distance from the potential.

5.1 Classical Tip Scattering

In the backscattering imaging approach, the particular shape of the tip potential is not important, as long as the tip is capable of backscattering the electron. However, in the deflection case, where backscattering is not the main mechanism, the tip potential becomes important. In this section we'll study the tip potential, and in particular model the tip potential as a lens.

5.1.1 Classical Scattering

Consider a continuum of trajectory "rays" of the same speed in direction $\hat{x}$ impinging on a local potential bump or valley. We will assume that the potential hill is circularly symmetric, and monotonically increasing to a finite peak. Taking the origin at the center of the potential bump, we can use the fact that angular momentum is conserved to cast the problem as a one-dimensional problem. Following Landau and Lifschitz [62], the Hamiltonian in the absence of a magnetic field is

$$E = H = \frac{m\dot{r}^2}{2} + \frac{L^2}{2mr^2} + V(r) \tag{5.1}$$

where $V(r)$ is the tip potential. If a particle of speed v approaches with an impact parameter b, then $L = mbv$. Writing the potential as $V(r) = E\eta\mathcal{V}(r)$, where $\mathcal{V}(0) = 1$ is the unit normalized potential, then η is the fraction of the tip height to the total energy. We can use the fact that $L = mr^2\frac{d\phi}{dt}$ to express the scattering angle as

$$\Delta\phi = \int \frac{L}{mr^2}dt$$

$$= \int \frac{L dr}{mr^2 \sqrt{E - V(r) - \frac{L^2}{2mr^2}}}. \tag{5.2}$$

Here we take the convention that θ may be negative, in which case the particle crosses the x-axis; this will occur only for attractive potentials. The scattering process is depicted in Figure (5.1). Considering only the half of the trajectory from $r = \infty$ to the closest approach r_{min}, we can write the expression for the scattering angle as

$$\theta = \pi - 2b \int_{r_{min}}^{\infty} \frac{dr}{r^2 \sqrt{1 - \eta \mathcal{V}(r) - \frac{b^2}{r^2}}}. \tag{5.3}$$

The radius of closest approach is the radius at which the radial speed $\dot{r} = 0$; hence r_{min} is the (positive) root of the energy balance equation (after some manipulation)

$$1 - \eta \mathcal{V}(r_{min}) - \frac{b^2}{r_{min}^2} = 0. \tag{5.4}$$

Note that this is the expression under the square root in the denominator of the equation for the scattering angle.

In the case of no potential, then $r_{min} = b$, and it can be shown that the scattering angle is exactly zero. In the case of Rutherford scattering, with a Coulomb potential $V(r) = \pm\alpha/r$, then $r_{min} = \sqrt{b^2 + r_o^2} \pm r_o$, where the relevant length scale for the Coulomb system is $r_o \equiv \alpha/2E$, and the scattering angle may be found analytically to be $\theta = \pm 2 \sin^{-1} \frac{r_o}{\sqrt{b^2 + r_o^2}}$.

For the case of a Gaussian or Lorentzian potential bump, there is no exact analytic solution. In Figure (5.2) we analyze numerically the scattering off of a such a SPM tip-like potential. Writing the potentials as

$$\begin{aligned} V_{Gaussian}(r) &= E\eta \, e^{-r^2/2\sigma^2} \\ V_{Lorentzian}(r) &= E\eta \, \frac{\sigma^2}{r^2 + \sigma^2} \end{aligned} \tag{5.5}$$

we can scale by the typical size of the potential σ in each case, and $\eta = 1$ serves as the border between the backscattering and the purely deflecting cases. The point in parameter space $\eta = 1, b = 0$ is singular, as can be seen in plots (b) and (e); dynamically, the particle comes to rest at the top of the hill for these values, and since any tiny deviation will lead to a wide range of scattering angles, this point in parameter space is very unstable. This boundary is important for the scattering angle, because, as can be seen in (c) and (f) of the Figure, when $\eta < 1$ then direct trajectories with small impact parameter will forward scatter, while those trajectories will back scatter for $\eta > 1$. Hence only for $\eta < 1$ does the scattering profile have a maximum in scattering angle.

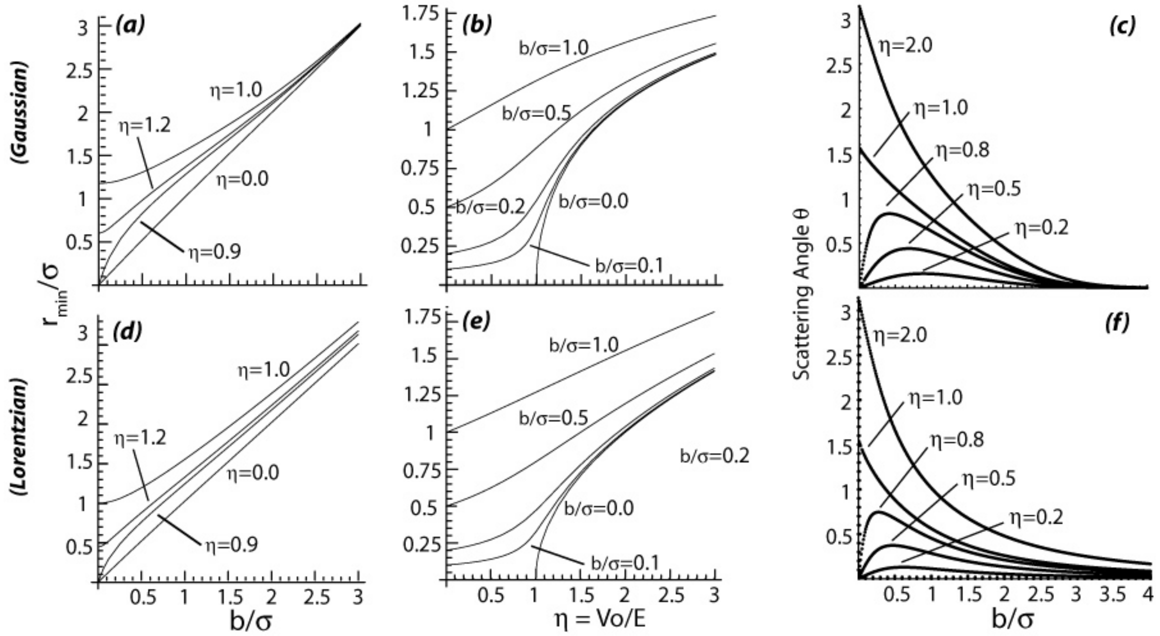

Figure 5.2: Classical scattering results for a Gaussian (a-c) and Lorentzian (d-f) potential bump. (a) and (d) plot the radius of nearest approach r_{min} versus impact parameter b for various central potential heights, while (b) and (e) plot r_{min} as a function of tip height. Plots (c) and (f) show the scattering angle as a function of impact parameter for a variety of potential heights. For both potential types, the scattering angle is monotonically decreasing when backscattering occurs ($\eta > 1$), but has a maximum peak when $\eta < 1$.

5.1.2 Small Angle Scattering

For a small perturbation, with impact parameter large enough that the trajectory of the particle is only slightly perturbed, one can approximate the particle path by the unperturbed trajectory, and calculate the resulting impulse on the particle as it passes by the scatterer. The momentum imparted to the particle perpendicular to the original path is $p_\perp = mv\sin(\theta) \cong \theta\sqrt{2mE}$ for small angles. Thus we can use the force on the particle, perpendicular to the original path, to calculate approximately the scattering angle; the resulting expression is ([62])

$$\theta_{sc} \cong -b\eta \int_b^\infty \frac{d\mathcal{V}(r)}{dr} \frac{dr}{\sqrt{r^2 - b^2}} \tag{5.6}$$

For a Gaussian potential (5.5), the integral evaluates to

$$\theta_{g,sc} \cong \sqrt{\frac{\pi}{2}} \frac{b\eta}{\sigma} e^{-b^2/2\sigma^2}$$

which has a single maximum when $b = \sigma$. For a Lorentzian potential hill (5.5), the integral evaluates to

$$\theta_{l,sc} \cong \frac{\pi \eta b \sigma^2}{2(b^2 + \sigma^2)^{3/2}}$$

which has a single maximum when $b = \sigma/\sqrt{2}$.

5.1.3 Caustics

The existence of a maximum in the expression for the scattering angle implies that there will be a caustic formed near that maximum angle. The existence of such a caustic far from the scattering center implies that the scatterer will cast relatively high density rays off in some direction. Thus knowing the far-field nature of these caustics will be important for the interpretation of conductance data for samples with an introduced SPM tip.

For a heuristic derivation of the caustics, we consider a uniform sheet of trajectories each with the same energy moving in the $\hat{x}$ direction to impinge on the scatterer. Here the impact parameter b directly corresponds to the initial value y_o. Taking the derivative of the final, far-field momentum $p_y = mv \sin(\theta)$ with respect to the initial position,

$$\begin{aligned} \frac{dp_y}{dy} &= \frac{d}{dy} mv \sin(\theta) \\ &= mv \frac{d}{db} \sin(\theta) \\ &= mv \cos(\theta) \frac{d\theta}{db}. \end{aligned} \tag{5.7}$$

Since we expect a caustic when $\theta = \pm\pi/2$ or when $\frac{d\theta}{db} = 0$. This "back of the envelope" derivation does succeed in identifying some caustics, but not all, and fails completely when the tip is near to strongly backscattering.

To rigorously derive the caustics, we ask at what points in space do neighboring trajectories cross, so at what points does $\vec{x}(b) - \vec{x}(b + \delta b) = 0$? For a given trajectory parameterized by b, we consider the line which the far-field outgoing trajectory follows. From Figure (5.1) we see that the outgoing trajectory is a line that appears to have originated at a point on the x-axis

$$\lambda(b) \cong -b \csc(\theta(b)) \tag{5.8}$$

from the origin. Defining the distance from the origin as r, the asymptotic outgoing position of the particle, parameterized by (b, r) is

$$\begin{aligned} x(b,r) &= r \cos(\theta(b)) - b \csc(\theta(b)) \\ y(b,r) &= r \sin(\theta(b)). \end{aligned} \tag{5.9}$$

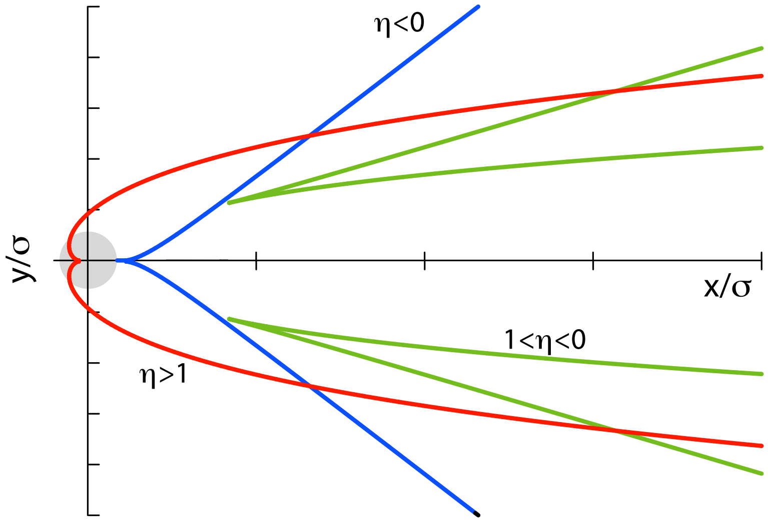

Figure 5.3: Classical caustics for a Lorentzian potential bump. Three types of caustics are possible: in red are backscattering caustics for which $\eta > 1$, in green are caustics for which $0 < \eta < 1$, and in blue are the caustics for which $\eta < 0$.

For the trajectories to cross at this point, then we need to solve

$$\begin{aligned} \delta x(b,r) &= 0 = \frac{dx}{db}\delta b + \frac{dx}{dr}\delta r \\ \delta y(b,r) &= 0 = \frac{dy}{db}\delta b + \frac{dy}{dr}\delta r \end{aligned} \tag{5.10}$$

for some relationship between r and b. After some algebra, we find the relation

$$\left[b\cot(\theta(b)) - r\right]\frac{d\theta}{db} = 1, \tag{5.11}$$

solutions of which, parameterized by b, can be used to determine the positions of the caustics.

Representative caustics for the Lorentzian case are plotted in Figure (5.3). Depending on the value of η, a caustic will be one of three types. For attractive potentials $\eta < 0$, the caustics form a “V” centered on the x-axis, with a cusp which acts like a focus lying on the x-axis. This is known as a “swallowtail” caustic [4]. These caustics are plotted in blue in the figure. The caustic is formed by trajectories with θ_{sc} near the maximum, and hence for which the transverse momentum imparted Δp_y is a maximum.

The caustics in the upper half-plane for both the Gaussian and Lorentzian case are plotted in Figure (5.4), for a range of η values. For a non-backscattering repulsive case $0 < \eta < 1$ (plotted in green), the caustics will lie solely on the outgoing side of the scattering center. These caustics

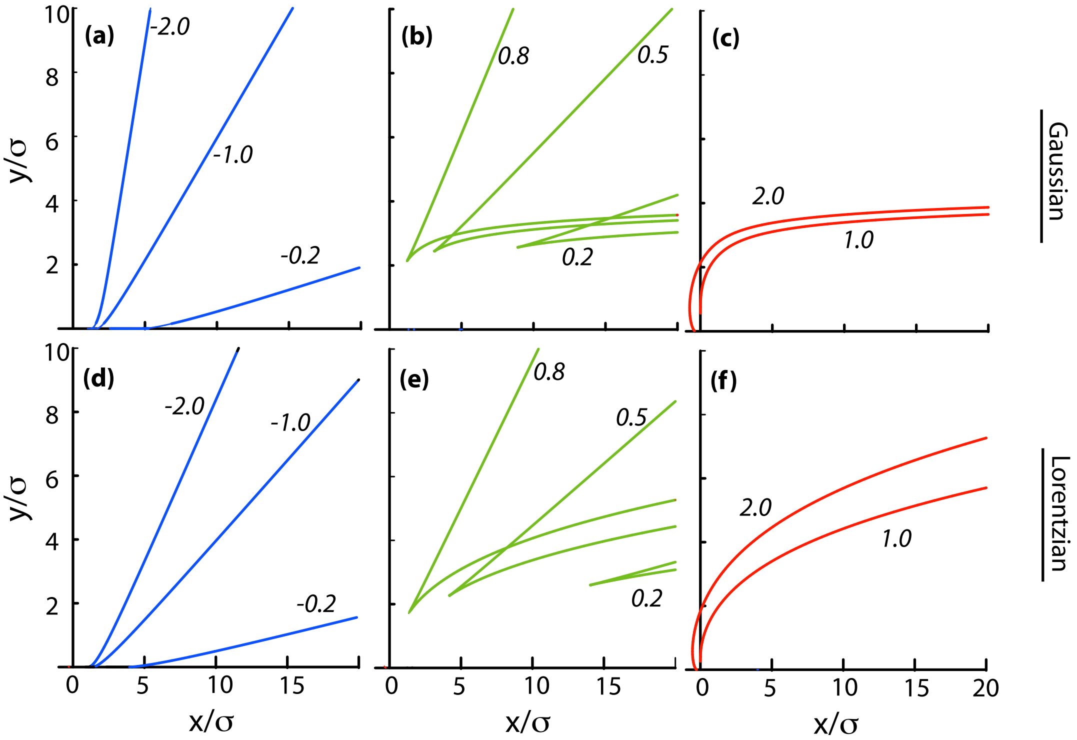

Figure 5.4: Classical caustics for a Gaussian (a) and Lorentzian (b) potential bump. Three types of caustics are clear in both cases: in red are backscattering caustics for which $\eta > 1$, in green are caustics for which $0 < \eta < 1$, and in red are the caustics for which $\eta < 0$.

are known as "open swallowtail" caustics. Each has two branches, with different asymptotic forms, which converge to a cusp at a distance that increases with decreasing potential strength, on either side of the x-axis. The outer branch of the caustic is equivalent to the caustic in the attractive case, and is caused by trajectories of near maximum scattering angle. The inner branch is caused by trajectories of larger impact parameter, in the region of small-angle scattering.

In the backscattering case $\eta > 1$ (plotted in red), the particle will backscatter for $b = 0$, implying that the the caustic will lie on the incident side of the potential, and curve parabola-like around the scatterer. This caustic is caused by the manifold sheet folding back onto itself, the "crease" starting from the classical turning point where $b = 0$; logically, this is called a "fold" caustic. In the asymptotic region, this caustic is also caused by the crossing of small-angle scattering trajectories. Because the Lorentzian potential drops off more slowly in radius than the Gaussian potential, these caustics in the small-angle regime change position more slowly with impact parameter, extending over the range of the plot twice as far as in the Gaussian case. In contrast, the caustics due to maximum scattering angle are wider in the Gaussian case, because the Gaussian potential is

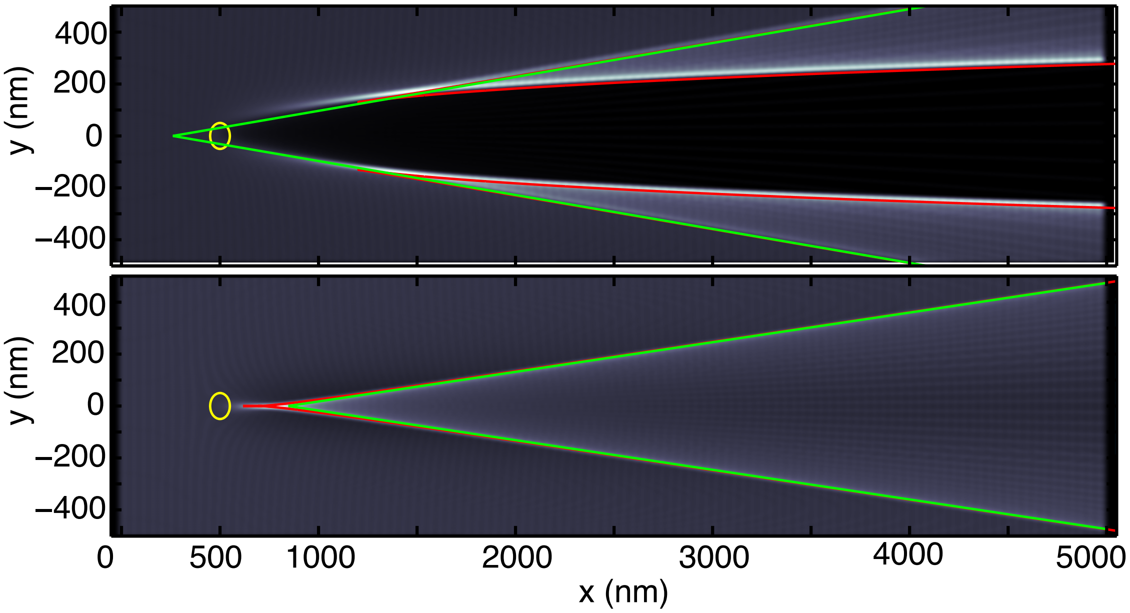

Figure 5.5: Classical caustics shed by a repulsive (a) or attractive (b) Lorentzian potential bump ($\eta = \pm 0.2$), superimposed on a numerical simulation of a trajectory manifold flowing over the scatterer. The analytic caustic solution are plotted in red on the manifold image, while the asymptotic approximations are in green.

less "pointed", and hence scatters with smaller angles, than the equivalent Lorentzian potential.

Next let us consider the asymptotic forms of the caustics. We begin by considering the case where $\theta \leq 0$, which is the case when the potential is attractive, $\eta < 0$, or the case $\theta \not\succeq 0$ which is relevant in the outer branch of the $0 < \eta < 1$ caustic. Then in either of these cases, $r - b\cot(\theta(b)) \to \infty$. In order to satisfy equation (5.11), $\left(\frac{d\theta}{db}\right)^{-1} \to \infty$ as well, so we have the condition

$$\frac{d\theta(b_c)}{db} = 0 \tag{5.12}$$

for a caustic to exist. This type of caustic is formed by the trajectories which scatter with the maximum angle. Note that in the backscattering case, there is no maximum angle, since all angles are classically scattered. We anticipate that there will be no such caustic in the backscattering case. In Figure (5.5), the solution is plotted in green, superimposed on numerical simulations of the classical flow in the system. The approximation is quite accurate until one gets close to the scatterer. Taking the center of the tip as the origin, and denoting by $\tilde{b}$ the impact parameter which produces the maximum scattering angle $\tilde{\theta} \equiv \theta(\tilde{b})$, then the equation for this caustic in position space is

$$y = \tan\tilde{\theta}\,(x + \tilde{b}\csc\tilde{\theta}), \tag{5.13}$$

a line with slope $\tan\tilde{\theta}$ crossing the axis at the point $-\tilde{b}\csc\tilde{\theta}$.

The preceeding approximation fails if the scattering angle $\theta \to 0$ as $b \to \infty$, which is the case for some of the caustics in the repulsive case. Thus we must consider caustics formed at small scattering angles. In the former case, the caustic was formed by trajectories with $b \sim \sigma$, because the caustic was the result of highly deflected trajectories. In this case, the caustic is formed by trajectories out on the tail of the potential, when $b \gg \sigma$. The expression will be sensitive to the functional form of the potential for large b, and we must proceed on a case-by-case basis.

For an algebraic dropoff in $\tilde{V}(b)$, we may assume a form $\theta(b) \approx ab^{-p}$ where $p > 0$. For small angle scattering, we approximate $\cot\theta \cong 1/\theta$, so that the relation for the caustics, equation (5.11), simplifies to

$$r = \frac{p+1}{ap}b^{p+1}. \tag{5.14}$$

Since $y \approx r\theta$ for small angle scattering, we may substitute in expressions for r and θ to determine that for large r, $y \cong b$. Similarly, since $r = \sqrt{(x + b\csc\theta)^2 + y^2}$ and y grows only as $r^{1/(p+1)}$, then for large r,

$$y = \left[\frac{ap}{p+1}(x + b\csc\theta)\right]^{\frac{1}{1+p}}. \tag{5.15}$$

Thus for an algebraic dropoff in potential, the caustic asymptotically follows a curve of form $y \propto \sqrt[p+1]{x}$.

In the case of a Lorentzian, we can use the small angle scattering approximation, where $\theta \approx b^{-2}$. In this case $a = \pi\eta\sigma^2/2$ and $p = 2$. Thus we expect an asymptotic form $y \propto \sqrt[3]{x}$ for the position of the caustics, in particular

$$y = \left[\frac{ap}{p+1}(x + b\csc\theta)\right]^{\frac{1}{1+p}}. \tag{5.16}$$

5.1.4 Classical Point Sources

In the case of mesoscopic systems, it is often useful to speak in terms of trajectories emanating from a point source, instead of a sheet of trajectories all with the same momentum. It is a simple matter to incorporate this case formally into the expressions for classical scattering by noting that the impact parameter for a point source at distance R is $b = R\sin\phi$, where ϕ in the incoming angle. Then we can reparameterize all the equations in terms of $b(\phi)$, and note that the outgoing scattering angle $\theta_{sc}(b)$ is now with respect to the incoming angle ϕ, so that we replace θ by $\theta' = \theta_{sc} + \phi$ in all the relevant expressions.

For the most part this makes the equations more unwieldy, so the best bet is to keep the parameterization in terms of b, and instead work in a coordinate system that is rotated by ϕ for each separate trajectory launched at angle ϕ. Thus, we have as the equations for the caustics the same equation formally as before,

$$[b \cot \theta_{sc}(b) - r] \frac{d\theta_{sc}}{db} = 1. \tag{5.17}$$

When we want to map this back into real positions, we need to use θ' instead,

$$\begin{aligned} x(b,r) &= r\cos(\theta') - b\csc(\theta') \\ y(b,r) &= r\sin(\theta') \end{aligned} \tag{5.18}$$

where $\theta' = \theta_{sc}(b) + \sin^{-1}(b/R)$.

The linear caustics far from the scattering center occur with impact parameter b_c and scattering angle $\tilde{\theta}_{sc}$, where $\frac{d}{db}\theta_{sc}(b_c) = 0$. With a point source, these linear caustics will occur at an angle $\phi(\tilde{b})$ further out from the x-axis, or at $\tilde{\theta} = \tilde{\theta}_{sc}(\tilde{b}) + \sin^{-1}(\tilde{b}/R)$. The difficultly in representation is avoided by first solving for the unrotated system, then identifying the crucial values of the impact parameter, and using these values to determine the caustics in real space.

5.1.5 Lens Approximation

We have seen how the caustics, for the non-backscattering case $\eta < 1$, have an outgoing asymptotic behavior that is linear in at least one of the arms. For $\eta < 0$ this is the only outgoing caustic, while for η positive but small, this linear caustic will be the dominant one in terms of flux (as $\eta \to 1$ this will change).

In a situation where this linear outgoing caustic is of prime importance, we can justifiably approximate the tip as a lens. The definition of a focal point of a perfect lens is the point at which all the rays from infinity converge. The outgoing rays then follow linear paths that (seemingly) originate from the focus. In our case of an imperfect lens, the focus will be defined as the point from which the caustics seemingly originate, having impinged on the lens from infinity. As depicted in Figure (5.5), the caustics do appear to originate from a seeming focal point on the x-axis; since the caustics carry a large portion of the flux, such a definition of the focus makes sense. From equation (5.13), the focus appears to lie on the x axis at the point

$$f = -\tilde{b} \csc \tilde{\theta} \tag{5.19}$$

where $\tilde{\theta}$ is the maximum angle of scattering, and $\tilde{b}$ is the impact parameter that scatters maximally, according to the scattering relation $\theta_{sc}(b)$.

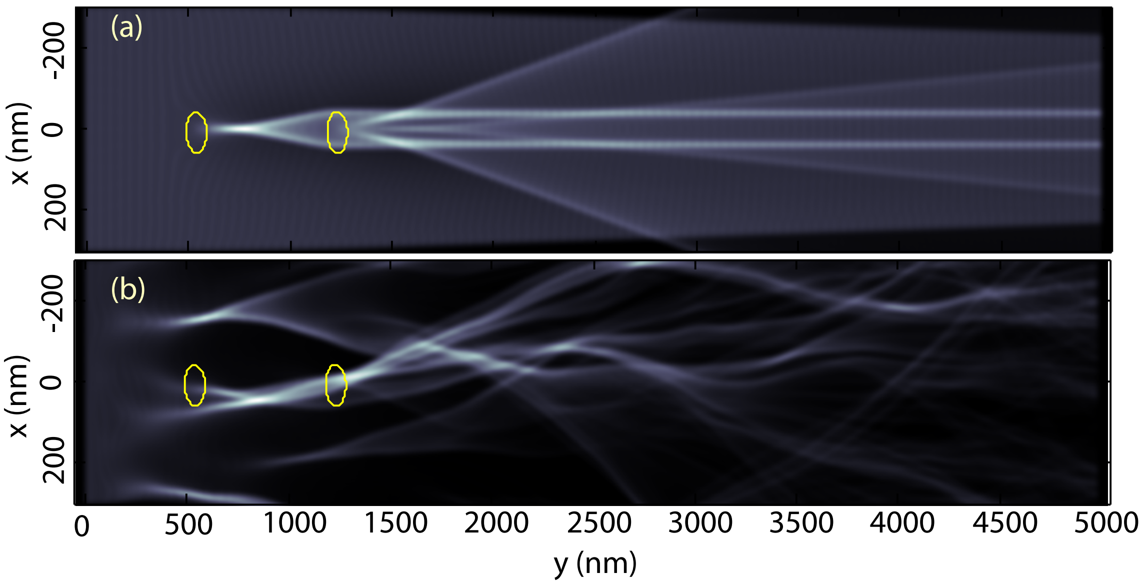

Figure 5.6: A system of convex "lenses" produced by applying a positive (attractive) tip voltage. The Lorentzian tip potentials are set to $\eta = -0.2$, are $2\sigma = 100$ nm in size, and are spaced at two focal lengths λ apart. A sheet of trajectories is propagated in a clean (a) and bumpy (b) background. The bumpy background is a random Gaussian distribution with correlation length $l_{corr} = 40$ nm and rms bump height $\sqrt{\langle V^2 \rangle} = 0.05 E_F$. In (a), we can see that the caustics from the first lens are focussed to infinity by the second lens. In (b), the lens system helps to contain the diffusive branching from the random background potential.

In Figure (5.6a) we depict a system of attractive ($\eta < 0$) "lens" tips, where the distance between the tips is two focal lengths. In this configuration with perfect lenses, incoming parallel rays will end up as outgoing parallel rays, but reflected about the y-axis. In the case of imperfect tip "lenses", the outgoing rays are not homogenous in space as would be the case for perfect lenses; however the linear caustics created by the first tip are "corrected" by the second tip, and run parallel beyond the lens system. Meanwhile, second order caustics are created with different slopes and focal lengths.

5.1.6 Tip Scattering with Random Background Potential

In Figure (5.6b) we show the same tip "lensing" system, but with a bumpy background included. In this case the collimating properties of the convex lens system helps to contain some of the diffusion due to small angle scattering, and appears to contain the branching flux somewhat,

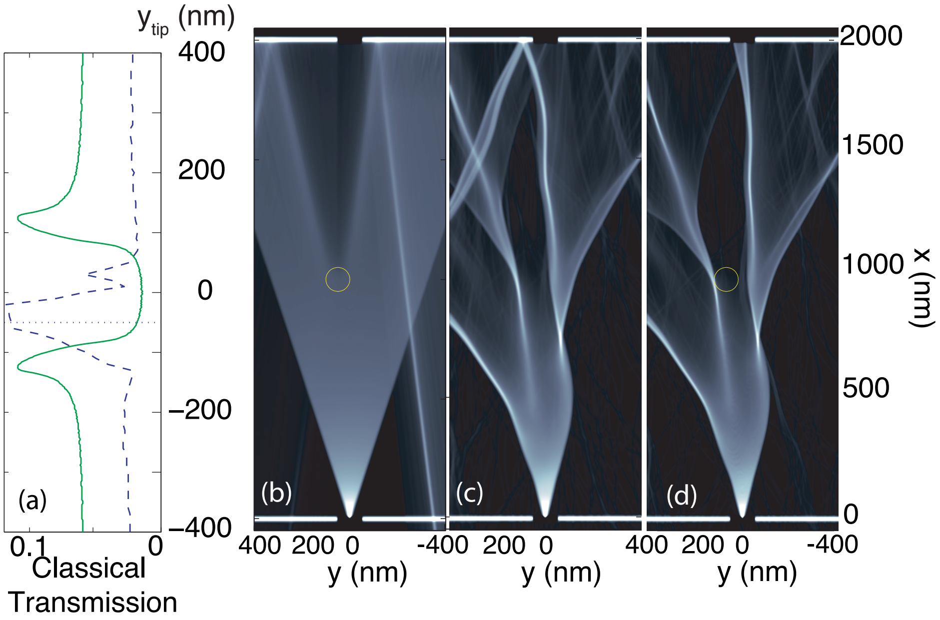

Figure 5.7: A classical simulation of flow in a QPC to QPC geometry, with the target QPC directly facing the injector. In (a) we plot the classical transmission as a function of tip position; values for large y are essentially the no-tip values. The solid green line is the transmission for a clean sample, while the dashed blue line is with disorder. The dotted line indicates the position of the tip in (b) - (d). The peaks in the plot indicate the passage of a caustic across the target QPC. In (b), a sheet of trajectories is shown in a system without disorder; the deflecting tip, indicated by the circle, acts like a diverging mirror, shedding caustics off at some angle. Here the tip shadows the target QPC, lowering the classical transmission. In (c) we see the same trajectory sheet, but with background disorder in the sample, and in (d) we see the same instance, but with the diverging tip in place. Here the tip is centered at a position with little flow, but gently deflects a branch into the QPC, dramatically changing the transmission, and hence conductance, of the sample. Here $E_F = 20$ meV, the tip is Gaussian with peak height $V_o = 0.2E_F$, and width $2\sigma = 100$ nm.

keeping it nearer the center axis. One could imagine using an array of attractive potentials, acting as convex lenses, to redirect and contain branching flow.

In the presence of a bumpy background potential, the tip can influence classical electron flow in more interesting ways [2]. In Figure (5.7) we depict another manner in which a tip can redirect and “focus” classical electron flux. In the absence of a bumpy background, a weakly repulsive tip will obscure a target QPC when placed between it and the source (Figure 5.7b), thus lowering the transmission (Figure 5.7a). As the tip is scanned in position, the caustics can sweep across the target QPC, causing a maximum in the transmission greater than if the tip weren’t present. In this sense the repulsive tip, by creating caustics, “focusses” the flux into the target QPC.

Alternatively, if a bumpy background is present, so that the electron flow is branched (Figure 5.7c), the weakly repulsive tip can either knock a branch out of the target QPC, or assist by deflecting a branch into it (Figure 5.7d). The accompanying change in the transmission through the system may be dramatic.

5.2 Quantum Tip Scattering

In this section we consider the full quantum scattering of an electron off a tip potential, under the single particle approximation in a 2DEG (see [65] or [1] for two-dimensional scattering theory). We write the time independent Schrödinger equation as

$$(\nabla^2 + k^2)\psi = \frac{2mV(\vec{r})}{\hbar^2}\psi \equiv \eta k^2 \mathcal{V}(\vec{r})\psi \tag{5.20}$$

with the quantum number k being equal to the free particle wavenumber

$$k = \sqrt{2mE_F}/\hbar = 2\pi/\lambda,$$

and $\eta\mathcal{V} = V/E_F$ is the normalized potential. Written in this form, the retarded free particle Green function is

$$G_o(k;\vec{x}_o,\vec{x}) = \frac{1}{4i}H_0^+(k|\vec{x}-\vec{x}_o|) \tag{5.21}$$

In the far field, $|\vec{x}-\vec{x}_o| \gg \lambda$, this simplifies to

$$G_o(k;\vec{x}_o,\vec{x}) \cong -\sqrt{\frac{i}{8\pi}}\frac{e^{ik|\vec{x}-\vec{x}_o|}}{\sqrt{k|\vec{x}-\vec{x}_o|}} \tag{5.22}$$

The Lippman-Schwinger equation reads in operator notation

$$\psi_k = \phi_k + \hat{G}_o\,[\eta k^2 \mathcal{V}]\,\psi_k \tag{5.23}$$

where ϕ_k is the unscattered incident plane wave incident with direction $\vec{k} = k\hat{x}$. Written out explicitly, this is

$$\psi_k(\vec{r}) = \frac{e^{ikx}}{(2\pi)^2} - \eta k^2\sqrt{\frac{i}{8\pi k}}\int d^2r'\,\frac{e^{ik|\vec{r}-\vec{r}'|}}{\sqrt{|\vec{r}-\vec{r}'|}}\mathcal{V}(\vec{r}')\psi_k(\vec{r}'). \tag{5.24}$$

In the far field and for a central potential, we may rewrite this as

$$\psi_k(\vec{r}) = \frac{e^{ikx}}{(2\pi)^2} - \eta k^2\sqrt{\frac{i}{8\pi k}}\frac{e^{ikr}}{\sqrt{r}}\int e^{-ikr'\cos\theta'}\mathcal{V}(r')\psi_k(\vec{r}')r'dr'd\theta' \tag{5.25}$$

where we take the origin at the center of the scattering potential. Writing in the usual way the full wavefunction as a sum of scattered and unscattered parts,

$$\psi_k(\vec{r}) = \phi_k + f_k(\theta)\frac{e^{ikr}}{\sqrt{r}} \tag{5.26}$$

we can identify the expression for the scattering amplitude in two dimensions,

$$f_k(\theta) = -\eta k^2 \sqrt{\frac{i}{8\pi k}} \int e^{-ikr'\cos\theta'} \mathcal{V}(r')\psi_k(\vec{r}')r'dr'd\theta' \tag{5.27}$$

.

5.2.1 First Born Approximation

For a perturbative tip, we assume that we may replace the full wavefunction on the right-hand side in the above $\psi_k(\vec{r}')$ by the unperturbed wavefunction ϕ_k. This is tantamount to truncating a series expansion in the Lippman-Schwinger equation to a single $\psi = \phi + \delta\psi$ and assuming that $|\delta\psi| \ll |\phi|$ when integrated over the potential region. Such an approximation is known as a Born approximation [63], and is valid under the conditions

$$\eta \ll (k\sigma)^{-2} \tag{5.28}$$

or when

$$\eta \ll (k\sigma)^{-1} \tag{5.29}$$

where σ is the extent of the potential in space. The former demands that the potential be small compared to the wavelength of the particle, while the latter demands that the action imparted to the particle on scattering be significantly smaller than $\hbar$.

When either condition holds, we may replace ψ by ϕ under the integral, and simplify the math greatly; with a central potential, the scattering amplitude simplifies to

$$f_k(\theta) = -2\pi\eta k^2 \sqrt{\frac{i}{8\pi k}} \int_0^\infty J_o[2kr'\sin(\theta/2)]\mathcal{V}(r')r'dr' \tag{5.30}$$

where θ is the scattering angle with respect to the x-axis.

For a Gaussian potential as we've considered before, the scattering amplitude may be integrated directly, with result

$$f_k(\theta) = -\eta\sqrt{\frac{i\pi}{2k}}(k\sigma)^2 e^{-(k\sigma)^2(1-\cos\theta)} \tag{5.31}$$

with total cross section

$$\Sigma(k) = \frac{\pi^2\eta^2}{k}(k\sigma)^4 e^{-2(k\sigma)^2} I_0[2(k\sigma)^2] \tag{5.32}$$

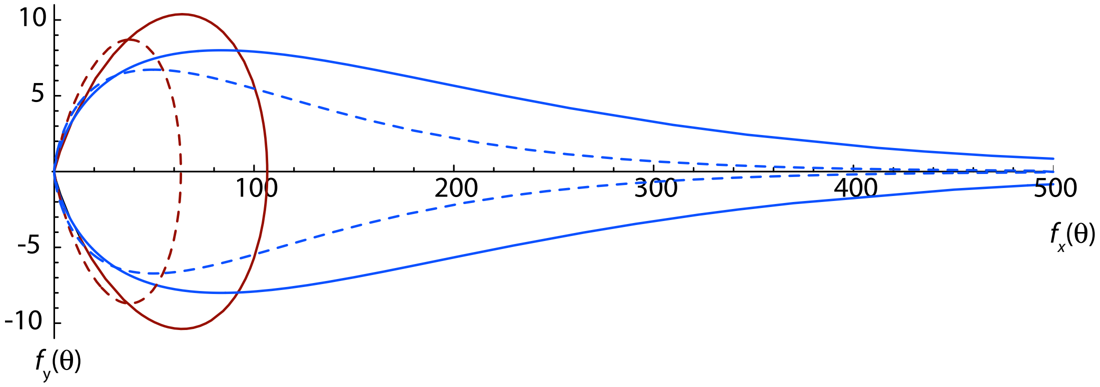

Figure 5.8: Scattering amplitude in the Born approximation off a localized "tip" potential modeled as a Lorentzian (blue) or a Gaussian (red). Solid lines are at a Fermi energy of 13.7 meV, while the dashed lines are at one half this energy. For the Lorentzian, the scattering amplitude is singular in the forward direction due to the Bessel function K_0. The tip width is 100 nm, and tip height $\eta = 0.2$, so that $k\sigma \approx 6.2$.

where I_0 is the modified Bessel function of the first kind [3], $I_n(x) = e^{-i\pi n/2} J_n(xe^{i\pi/2})$. For small argument, $I_0(x) \to 1$, so for low energy or small tip $\Sigma(k) \to \sigma\pi^2\eta^2(k\sigma)^3$. For large argument, $I_0(x) \to e^x/\sqrt{2\pi x}$, so asymptotically for large $k\sigma$ we have $\Sigma \propto \sigma(k\sigma)^2$.

For a Lorentzian the scattering amplitude evaluates to

$$f_k(\theta) = -\eta\sqrt{\frac{i\pi}{2k}}(k\sigma)^2 K_0[2k\sigma\sin(\theta/2)] \tag{5.33}$$

where $K_0(x)$ is a modified Bessel function of the second kind [3], $K_n(x) = \frac{\pi}{2} i^{n+1} H_n^{(1)}(ix)$.

For reference, for an exponential tip $V = E_F\eta e^{-r/a}$, the scattering amplitude evaluates to

$$f_k(\theta) = -\eta\sqrt{\frac{i\pi}{2k}}\frac{(k\sigma)^2}{[1+2(k\sigma)^2(1-\cos\theta)]^{3/2}} \tag{5.34}$$

while the cross section evaluates to

$$\Sigma(k) = \frac{\pi^2\eta^2}{k}(k\sigma)^4\frac{1+4(k\sigma)^2+6(k\sigma)^4}{[1+4(k\sigma)^2]^{5/2}}. \tag{5.35}$$

We note that in all of these cases, the total cross section scales as k^2 for large k, while for small energy scattering, the total cross section scales as k^3.

Figure (5.8) depicts the scattering amplitude in the Born approximation for a Lorentzian and Gaussian tip. In both cases, at these values the Born approximation predicts that scattering will be strongly focussed in the forward direction. In fact, in the Lorentzian case, there is an integrable singularity at $\theta = 0$ due to the modified Bessel function of the second kind K_0. In both cases the cross section increases monotonically with momentum k at the same potential size, which is evident from the figure.

It must be noted that usually the Born approximation is not valid for typical mesoscopic tip scattering experiments, unless the tip potential is quite weak. Typically $\sigma \approx 50$ nm and $\lambda_F \approx 40$ nm, so that $k\sigma \approx 16$. Hence the tip potential needs to be less than 5% of the Fermi energi for the Born approximation to hold with tip scattering. On the other hand, for impurity scattering, σ is usually orders of magnitude smaller, and hence the Born approximation is almost always appropriate, with the scattering usually being s-wave in nature.

5.2.2 Partial Wave Analysis

In the partial wave approach, we expand the wavefunction in an angular basis, and solve for the system separately at each azimuthal quantum number m. In this section we follow Lapidus [65]. In two dimensions, the angular basis is simply a Fourier series in angle, so we choose an orthonormal basis $\Theta_m(\theta) = \cos(m\theta)/\sqrt{\pi}$. We write out a general solution to the system at a given energy $\hbar^2 k^2/2m$ as a sum of separated solutions

$$\psi_k(\vec{r}) = \sum_m R_m(r)\Theta_m(\theta) \tag{5.36}$$

and for each term solve the Schrödinger equation for the radial functions $R_m(r)$,

$$\frac{1}{r}\frac{d}{dr}\left(r\frac{dR_m}{dr}\right) + \left(k^2 - \frac{m^2}{r^2}\right)R_m = \frac{2mV(r)}{.}\hbar^2 R_m \tag{5.37}$$

In the absence of a nearby potential, this has a linear combination of Bessel functions $J_m(kr)$ and $N_m(kr)$ as the general solution (in the absence of any potential, the $N_m(kr)$ part must be removed in order for the wavefunction to be finite at $r = 0$). Hence far from the scatterer, we may write the radial partial wave solution

$$\begin{aligned} R_m(r) &= a_m(k)J_m(kr) + b_m(k)N_m(kr) \\ &\cong \frac{A_m(k)}{\sqrt{kr}}\cos\left(kr - \pi(m+1/2)/2 + \delta_m(k)\right) \end{aligned} \tag{5.38}$$

where we've used the asymptotic expansion of the Bessel functions [3] to recast the amplitudes in terms of a phase shift $\delta_m(k)$ and an overall amplitude $A_m(k)$. Using the expansion of a plane wave in terms of Bessel function and angular eigenfunctions,

$$e^{ikx} = \sum_{m=-\infty}^{\infty} i^{|m|} e^{im\theta} J_{|m|}(kr) \tag{5.39}$$

one can eliminate the A_m (see [65]), with partial scattering amplitudes

$$f_m(\theta) = \sqrt{\frac{1}{2\pi i k}} \left(e^{2i\delta_m} - 1 \right) e^{im\theta} \tag{5.40}$$

where these sum to the total scattering amplitude $f(\theta) = \sum_m f_m(\theta)$. Each partial amplitude contributes a partial cross section (here with units of length, not area) of

$$\begin{aligned} \Sigma_0(k) &= \frac{4}{k} \sin^2 \delta_0(k) \\ \Sigma_m(k) &= \frac{8}{k} \sin^2 \delta_m(k) \end{aligned} \tag{5.41}$$

and total cross section $\Sigma(k) = \sum_m \Sigma_m(k)$.

Thus the difficulty in solving a scattering system comes down to calculating the phase shifts $\delta_m(k)$ for a given potential. For a system where the potential is stated in terms of boundary conditions, such as a hard wall sphere system, calculating the phase shifts boils down to fulfilling the boundary conditions. However for smooth potentials, another approach is needed, such as the variable phase approach.

5.2.3 Variable Phase Equation

To solve for the phase shifts $\delta_n(k)$, one can artificially turn a problem with smooth potentials into a boundary condition problem by truncating the potential at some radius ρ. This approach is called the Variable Phase Method (see [15] for a complete treatment). Heuristically (see [98]), the method involves matching the inside wavefunction and its derivative at the radius ρ where the potential has been truncated. This allows the wavefunction inside the potential to be expressed in terms of the external free wavefunction, which may be written down in terms of Bessel fucntions and the phase shift δ_m. In combination with the Schrödinger equation, this leads to a differential equation for the phase shift as a function of the truncation radius, the "variable phase equation" (see [15] for a full derivation in 3D and [86] for the equation for a 2D system),

$$\delta_n'(\rho) = -\pi \frac{m}{\hbar^2} \rho V(\rho) \left[J_n(k\rho) \cos \delta_n(\rho) - N_n(k\rho) \sin \delta_n(\rho) \right]^2 \tag{5.42}$$

where the large $\rho \gg \sigma$ solution corresponds to the desired phase shift. The boundary condition $\delta_n(\rho = 0) = 0$ fixes the final phase shift. Numerically, this form of the boundary condition is not useful; more useful is the small ρ expression

$$\delta_n(\rho) \cong -\pi \frac{m k^{2n}}{2^{2n}(n!)^2 \hbar^2} \int_0^\rho V(\rho') {\rho'}^{2n+1} d\rho' \tag{5.43}$$

valid for $\rho \ll \lambda$.

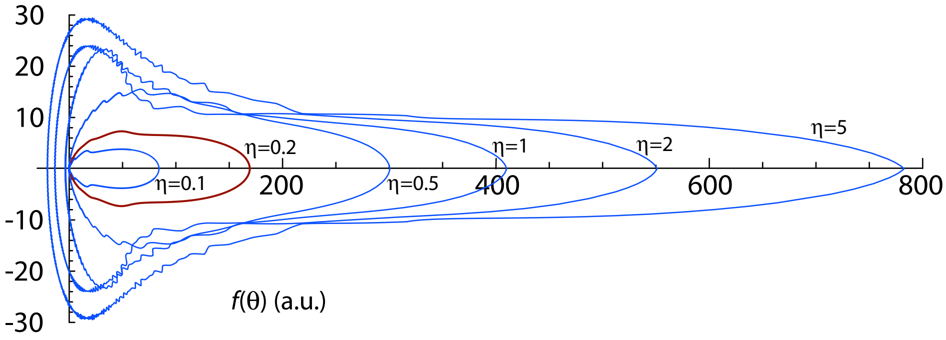

Figure 5.9: Scattering amplitudes of a Lorentzian tip at a variety of tip heights with respect to the Fermi energy, calculated using a partial wave expansion and variable phase method. In this calculation, $E_F = 13.7$ meV, so the Fermi wavelength $\lambda_F = 40$ nm. The relative tip height η varies from 0.1 to 5.0 E_F; the tip is $2\sigma = 100$ nm wide. In all cases, the scattering is very forward, but at stronger tip strengths lobes in the scattering, attributed to the linear caustics, are visible.

Using this expression as an initial condition, and an ordinary ODE solver, one can calculate the phase shifts in a fairly straightforward fashion. For a potential with long tails, such as a Lorentzian, convergence can be accelerated by multiplying the potential by a weakly decaying exponential, which would have physical significance in that it approximates Thomas-Fermi screening in a 2DEG.

5.2.4 Far-Field Tip Scattering Amplitudes

Putting all this machinery of scattering theory in 2D to work, we can calculate various scattering amplitudes of the local tip potentials relevant to the experimental data in Chapter (7). In Figure (5.9) we show the quantum scattering amplitudes $|f(\theta)|$ for a variety of Gaussian potential heights with respect to the Fermi energy E_F. The tip width is $2\sigma = 100$ nm, which is 2.5 λ_F; thus the scattering is close to being semiclassical and far from s-wave in character. In all cases the scattering is very forward in the far-field. This far-field result doesn't capture the existence of the shadow behind the tip that is seen in the classical results, and presumably in the near-field quantum case. Thus the far-field case is not completely adequate. As we have seen, in the case of a repulsive local potential, the shadow region tends to widen as $x^{1/3}$ for the Lorentzian, and logarithmically for the Gaussian, and hence in the far-field is not visible. In addition, the caustic structure in the far-field does show up in the quantum scattering results in Figure (5.9), particularly for higher tips. As such it provides a reasonably useful measure of the scattering amplitude in the semi-near field. We use the results for $\eta = 0.6$ in the semiclassical analysis of Chapter (7).

Chapter 6

General SPM Tip Scan Fringe Theory

Over the past few years, interesting results have been achieved by introducing a scanning probe microscope (SPM) tip above the surface of a semiconductor heterostructure which supports a two-dimensional electron gas (2DEG). As the SPM tip is moved around above the sample, an image of the underlying electron flow is produced [103, 101, 100, 102, 67]. These experiments are in addition able to resolve the coherent nature of the flow, with interference fringes present in the images, running perpendicular to the flow direction and spaced a distance $d = \lambda_F/2$.

In general, these experiments were two-terminal systems, with a quantum point contact (QPC) [111, 27, 10] in a low number of modes between source and drain contacts in the system. The QPC acts as a near point source of electron flow when open to a single transverse mode. As flow propagates through the system, it is backscattered by impurities in the system, or by the tip itself, when the central height of the tip potential $\eta = V(0)/E_F > 1.0$. The combination of amplitude backscattered to the source QPC by the tip, $A' = a(\vec{r})e^{i\phi(\vec{r})}$, plus a background amplitude A_o due to scattering from impurities for other fixed reflecting structures, will add coherently back at the source QPC. Semiclassically, the phase acquired along a path to a tip at a distance r from the source QPC is kr, so that in a region around a tip position r_o, the amplitude backscattered to the source QPC is

$$A \approx A_o + a(r_o)e^{i2k(r_o+\delta r)}.$$

The probability to return back to the source QPC is

$$|A|^2 \approx |A_o|^2 + 2|A_o||a(r_o)|\cos(2k\delta r + \phi_o).$$

As the tip is moved back and forth the backscattering probability varies sinusoidally with a spacing $d = 2\pi/2k = \lambda_F/2$. The flux transmitted back through the QPC, and hence the reflectance R, will also show such a variation with tip position. Since the system is a two-terminal system, then the transmission $T = 1 - R$ will also vary in this fashion, and hence the conductance of the system as a whole.

This approach to imaging flow in 2DEGs has been shown to be quite robust and useful for probing the electron flow. However it does require a specialized configuration. The system needs to be a two-terminal system, the SPM tip must backscatter the flow, and only small perpendicular magnetic fields can be used, since the backscattered flow is assumed to follow the same, or nearly the same path back to the source QPC.

In this Chapter we consider the fringing effect of an SPM tip in a more general context, building on the tip scattering theory from Chapter (5). This will include the possibility of a source and target QPC that are not colocated, of scattering into all angles, not just backscattering, and of fringing in a moderate perpendicular magnetic field. We begin by considering how the phase is changed as a scattering SPM tip is moved. This will lead us to a general fringe equation for the fringe structures resolved when a tip which scatters into any angle beats against a fixed background amplitude. We'll then consider various basic geometric cases and the fringe structures expected in these basic cases. Next we derive an expression for tip position offset for fringes observed at a certain position. Then we will consider experimental results that reveal deflection (i.e. non-backscattering) fringes, and compare with theory. Finally, in the next Chapter we use these results to address experiment fringes seen in a tip imaging system in the magnetic focussing [110] geometry.

6.1 General Fringing Theory

Here we consider the relation between the semiclassical action and the fringing structure. To begin, we consider the phase ϕ accumulated along a trajectory which originates at the source and propagates to the target QPC. This phase is taken to be locally a function $\phi(x, y)$ on the parameter field (x, y), where the coordinates (x, y) are some parameters, not necessarily the tip position. Ignoring Maslov phases, the phase is continuous on the plane, and we can linearize the phase expression in a region of interest. Along some direction θ of interest, we may linearize in the variable r, so that the phase variation

$$\delta\phi = \left|\frac{d\phi(x(r,\theta), y(r,\theta))}{dr}\right|_{(x,y)} \delta r.$$

For one cycle $\delta\phi = 2\pi$, so that the distance needed to complete one phase cycle, Δr, is

$$\Delta r = 2\pi \left|\frac{d\phi}{dr}\right|_{(x,y)}^{-1}.$$

We will take Δr to be the shortest spacing, so that the direction θ points parallel or antiparallel to the gradient of ϕ, along some direction $\hat{n}(x, y)$.

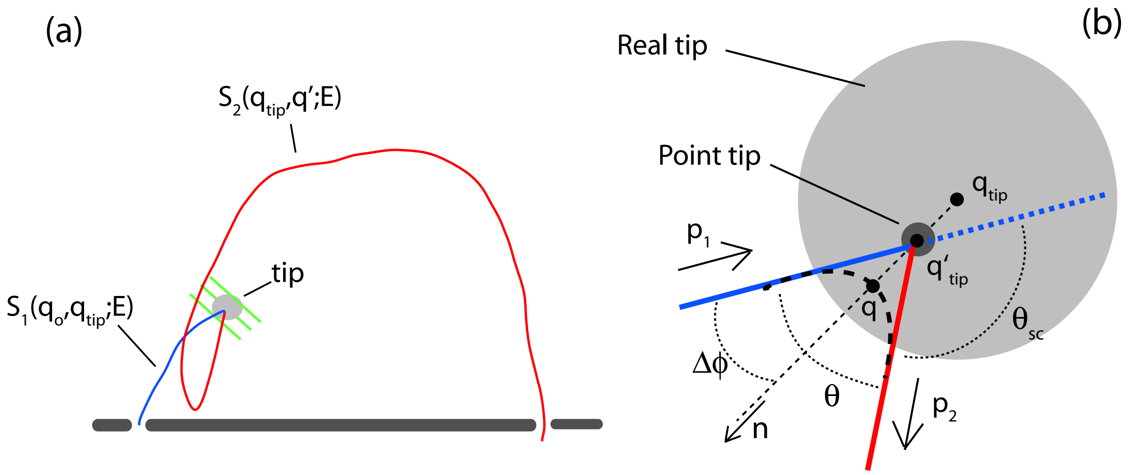

Figure 6.1: (a) A QPC to QPC trajectory which scatters from a tip (this is a real trajectory). This can be partitioned into two segments, and the action of each considered separately. (b) Approximating the scattering as being from a point tip, which lies a small distance from the real tip center.

If we consider the phase from one trajectory contribution, which beats against some background amplitude $ae^{i\phi_o}$, we may write the amplitude at the target

$$A = ae^{i\phi_o} + be^{i\phi(\vec{r})}$$

then the oscillatory part in the probability $|A|^2 \propto \cos(\phi_o - \phi(\vec{r}))$. Hence, when beating against a constant background, Δr is the fringe spacing. The direction of the fringes follows from the gradient of the phase, such that

$$\theta(x, y) = \tan^{-1}\left(-\frac{d\phi/dy}{d\phi/dx}\right).$$

When the fringes (or some component of them) are due to the interference between two trajectories whose cumulative phases both depend on tip position, then the Δr defined above is not the fringe spacing. Instead, we must consider the variation in the phase from both trajectories, which will not necessarily be collinear. Linearizing

$$\begin{aligned} 2\pi &= \Delta r |\nabla\phi_1 - \nabla\phi_2| \\ &= \Delta r \left|\frac{2\pi}{\Delta r_1}\hat{n}_1 - \frac{2\pi}{\Delta r_2}\hat{n}_2\right| \end{aligned} \tag{6.1}$$

so that the fringe spacing is

$$\Delta r = \left|\frac{\hat{n}_1}{\Delta r_1} - \frac{\hat{n}_2}{\Delta r_2}\right|^{-1}, \tag{6.2}$$

where Δr_1 and Δr_2 are the individual fringe spacings. The fringes are not uniquely defined by the gradients of the phases, and thus the mapping of fringe pattern to phase gradient will be ambiguous.

Semiclassically, the phase accumulated on the path from the source, at q_o, to the target QPC, at q', is proportional to the action accumulated along this path,

$$\phi = \frac{S(q_o, q'; E)}{\hbar};$$

here we will use "q" to represent (x, y). So to determine fringing, we need to know the gradient of the action in tip position, $\nabla_{\vec{r}_{tip}} S$. To do so, we partition a trajectory into two segments: one from the source QPC to a point q near the tip, with action $S_1(q_o, q; E)$, and one from the tip to the target QPC, with action $S_2(q, q'; E)$. This is depicted in Figure (6.1a). The total action accumulated along a transmitted path which strikes the tip is parameterized by q near the tip position,

$$S(q_o, q'; E) = S_1(q_o, q; E) + S_2(q, q'; E).$$

We choose the point q to be the position of nearest approach to the tip center. The difference $\delta q = q - q_{tip}$ may be on the order of the λ; however, away from a caustic the derivative in this value will be small, since this point of nearest approach depends on the incoming and outgoing momenta, which won't change dramatically. This q will "follow" the tip in the region where the scattering takes place. So while the discrepancy in action due to difference δq may be of order h, the discrepancy in the gradient of the action with tip position $\frac{\partial S}{\partial q_{tip}} - \frac{\partial S}{\partial q} = \frac{\partial S}{\partial q_{tip}} \left(1 - \frac{\partial q_{tip}}{\partial q}\right) = \frac{\partial S}{\partial q_{tip}} \frac{\partial \delta q}{\partial q}$, will usually be small, as long as $\left|\frac{\partial \delta q}{\partial q}\right| \ll 1$.

This slow change in the difference δq justifies a point tip approximation: we take the size of the tip to shrink to a point centered on the intersection of the incoming and outgoing trajectories, q'_{tip} (see Figure (6.1b)). Note that q'_{tip} lies between the tip position q_{tip} itself, and the real point of nearest approach q, improving the approximation.

Following this approximation, we replace q by q'_{tip} in the expression for the actions, and take the gradient; from now on we'll drop the prime, and take q_{tip} to mean the (shifted) tip position. The gradient reads

$$\frac{\partial S}{\partial x_{tip}} = \frac{\partial S_1(q_o, q_{tip}; E)}{\partial x_{tip}} + \frac{\partial S_2(q_{tip}, q'; E)}{\partial x_{tip}}$$

and similar for y. Now that we've set the endpoints of the trajectory segments to the tip position, we can greatly simplify this using the properties of the action $S(q_o, q; E)$,

$$\begin{aligned} \frac{\partial S(q_o, q; E)}{\partial q_o} &= -p_o \\ \frac{\partial S(q_o, q; E)}{\partial q} &= p. \end{aligned} \tag{6.3}$$

Thus the gradient of S in the tip position is

$$\nabla_{\vec{r}_{tip}} S = \vec{p}_1 - \vec{p}_2. \tag{6.4}$$

Furthermore, because the contribution to the canonical momentum from the vector potential is position dependent only, this contribution cancels, so that

$$\nabla_{\vec{r}_{tip}} S = m(\vec{v}_1 - \vec{v}_2) = -2\hbar k \sin(\theta_{sc}/2)\hat{n} \tag{6.5}$$

where θ_{sc} is the scattering angle, and $\hat{n}$ is the unit vector that bisects the angle θ (see Figure 6.1b).

Given the gradient of the action with tip position, the gradient in phase is trivial. It follows that the fringe spacing is

$$\Delta r = \frac{\lambda}{2} \left| \csc \frac{\theta_{sc}}{2} \right| \tag{6.6}$$

while the fringes run perpendicular to the unit vector $\hat{n}$, which lies at an angle

$$\Delta\phi_{fringe} = \frac{\pi - \theta_{sc}}{2} \tag{6.7}$$

with respect to the incoming trajectory. Geometrically, the fringes in the point tip approximation may be thought of as tracing out an effective reflecting wall that the trajectories reflect off elastically.

A great benefit of this result is the fringes provide both the direction and angle of scattering off the tip (to within a sign). If we suppose a locally flat background potential (or can average the fringes over an area much larger than the correlation length squared of the potential background), then the (averaged) fringe spacing Δr provides the scattering angle,

$$\theta_{sc} = 2 \sin^{-1} \left(\frac{\lambda}{2\Delta r} \right). \tag{6.8}$$

When a particle backscatters directly from the tip, then $\Delta r = \lambda/2$, and this expression correctly yields $\theta_{sc} = \pi$. When the trajectory is unscattered, the scattering angle is $\theta_{sc} = 0$, and the fringe spacing $\Delta r \to \infty$. Another important aspect of this result is that it holds true even in the presence of a magnetic field, as long as the field is not strong enough to effect the point tip approximation.

This simple model is true when the fringes are due primarily to trajectories beating against a strong enough background. When the background amplitude is smaller than the signal from the tip-scattered trajectories, then Δr cannot be so easily related to the scattering angle; the derivation needs to take into account more than one scattering angle. However, in smooth random potentials, the background signal often significant, the simplification usually holds. The point tip model as expressed also assumes that the trajectory strikes the tip only once; if multiple strikes occur, the simple mapping fails as well, because tip position doesn't simply relate to position in the coordinate space in which the electron moves.

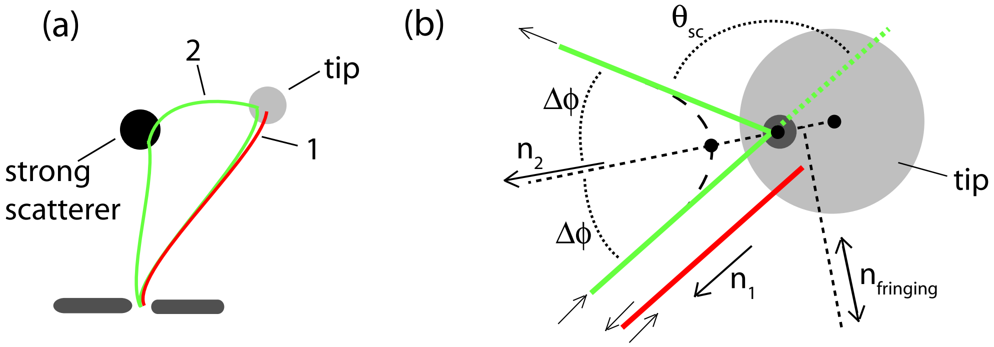

Figure 6.2: (a) Two trajectories which scatter from the tip: (1) which backscatters back to the source QPC, and (2) which deflects off the tip, scatters from another strong scatterer, and returns to the source QPC. (b) Geometric layout of the scattering process at the tip, in the point tip approximation.

6.2 Backscattering Interference

In the derivations in the previous section, we assumed that the fringes were due to interference patterns between the amplitude associated with a trajectory which scatters from the tip, and some background amplitude. We can alternatively ignore the background and consider interference between a deflected trajectory and a trajectory backscattered directly back to the source QPC by the tip (see Figure (6.2a)). In this case we have two phases which depend on the tip position, with two different phase gradient directions; the total spacing is

$$\Delta r = \left| \frac{\hat{n}_1}{\Delta r_1} - \frac{\hat{n}_2}{\Delta r_2} \right|^{-1} . \tag{6.9}$$

We will take the first trajectory to be the direct backscattered trajectory, and the second some deflected trajectory. The geometry of tip scattering is layed in in Figure (6.2b).

Since trajectory 1 is backscattered, we know that $\Delta r_1 = \lambda/2$, and that the two unit vectors are at an angle $\phi = (\pi - \theta_{sc})/2$ to each other, where θ_{sc} refers to the scattering angle of the second trajectory. Breaking up $\hat{n}_2$ into components parallel and perpendicular to $\hat{n}_1$, we may then simplify the expression,

$$\begin{aligned} \Delta r &= \left| \frac{\hat{n}_1}{\Delta r_1} - \frac{\hat{n}_2}{\Delta r_2} \right|^{-1} \\ &= \frac{\lambda}{2} \left| \hat{n}_1 - \sin \frac{\theta_{sc}}{2} \hat{n}_2 \right|^{-1} \\ &= \frac{\lambda}{2} \left| \left(1 - \sin^2 \frac{\theta_{sc}}{2}\right)^2 + \left(\cos \frac{\theta_{sc}}{2} \sin \frac{\theta_{sc}}{2}\right)^2 \right|^{-1/2} \end{aligned} \tag{6.10}$$

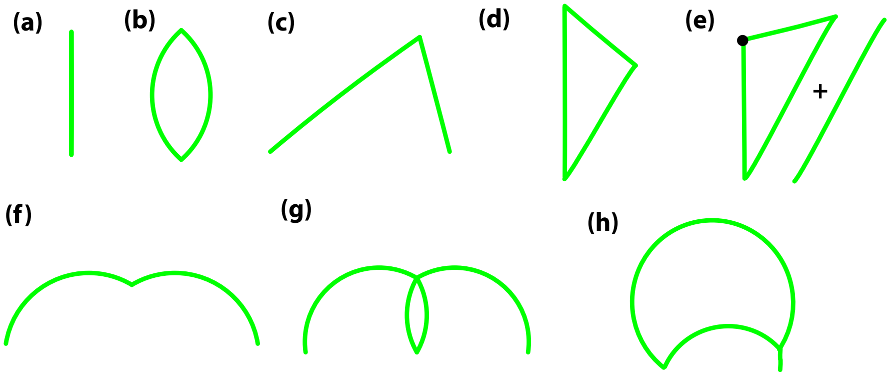

Figure 6.3: Various simple paths for which the fringe patterns are worked out in the text. Unless denoted by a "+", the paths are taken to interfere with a background amplitude. The blue dots are the QPCs, the red the tip, and black a strong fixed scatterer.

which simplifies to

$$\Delta r = \frac{\lambda}{2}\left|\sec\frac{\theta_{sc}}{2}\right|. \tag{6.11}$$

The direction of the fringes has been rotated by $\pi/2$ as well; the gradient of the total phase $\nabla\phi \propto \hat{n}_1 - \sin\frac{\theta_{sc}}{2}\hat{n}_2$ so that with respect to the backscattered trajectory $\frac{d\phi/dy_1}{d\phi/dx_1} = \tan\theta_{sc}/2$. Thus the fringes lie at an angle $\theta_{sc}/2$ with respect to the backscattered trajectory. This is $\pi/2$ from the fringe direction in the previous section. In systems where deflection of trajectories off the tip is common, one should expect to see a distorted checkerboard pattern in some places, when fringing due to interference against backscattered trajectories is of the same order of magnitude as that against the background amplitude.

While this case leads to a very convenient expression for the fringe spacing, it is clearly less general than in the previous section. The system must have source and target QPCs which are colocated, the tip must backscatter ($\eta > 1$), and the magnetic field must be weak. However, the case is relevant to many experiments in SPM imaging.

6.3 Basic Fringe Patterns

Here we consider a variety of geometries and derive the fringe patterns within the point tip model. Unless otherwise noted, we assume that a single trajectory interferences with an unperturbed background amplitude. In the following, refer to Figure (6.3) throughout.

(a) Direct Back-Scattering

The source and target QPCs are identical, and the electron follows the same path to and from the tip. The background may be clean or bumpy. The scattering angle $\theta_{sc} = \pi$, and the fringe spacing $\Delta r = \lambda/2$; the fringes are perpendicular to the electron trajectory at the tip position. In the clean case, the fringes form circular arcs with the QPC at the center. Multiple iterations n over the same path leads to a fringe spacing $\Delta r = \lambda/2n$

(b) Magnetic Back-Scattering

The source and target QPCs are identical, and the electron propagates in a uniform magnetic field in a clean system. The tip lies at a distance y from the QPC. The fringes are circular arcs, centered at the QPC, with spacing

$$\Delta r = \frac{\lambda}{2} \frac{2r_c}{\sqrt{(2r_c)^2 - y^2}} \tag{6.12}$$

Near the QPC, the spacing $\Delta r \to \lambda/2$, while at the edge of the classically allowed region, $y \to 2r_c$, then $\Delta r \to \infty$. In the center, when $y = r_c$, this becomes a typical value $\Delta r \approx \lambda/\sqrt{3}$.

(c) Elliptical Fringes 1

The source and target QPCs are separate, located at a distance D from one another. The tip is located at a position (x, y), with the origin at the midpoint between the QPCs. There is no magnetic field present, thus the path length determines the phase accumulated along the path. The resulting fringes can be trivially shown to be trace out ellipses, by considering what paths have the same path length. The semimajor axis is $2a = \sqrt{(x - D/2)^2 + y^2} + \sqrt{(x + D/2)^2 + y^2}$, and the semiminor axis $b = \sqrt{a^2 - (D/2)^2}$.

The scattering angle can be determined geometrically to be

$$\theta_{sc}(x, y) = \cos^{-1}\left(\frac{x + D/2}{\sqrt{(x + D/2)^2 + y^2}}\right) + \cos^{-1}\left(\frac{x - D/2}{\sqrt{(x - D/2)^2 + y^2}}\right) \tag{6.13}$$

which will be positive definite. The spacing then follows,

$$\Delta r(x, y) = \frac{\lambda}{\sqrt{2}} \left[1 + \frac{x^2 - (D/2)^2 + y^2}{\sqrt{((x - D/2)^2 + y^2)\,((x + D/2)^2 + y^2)}}\right]^{-1/2}. \tag{6.14}$$

A quick check, calculating the path length $L(x, y)$, finding the magnitude of the gradient of the phase, finds the same result. When centered between the QPCs, $x = 0$ and the fringe spacing expression simplifies to

$$\Delta r(x=0,y)=\frac{\lambda}{2}\sqrt{1+\left(\frac{D}{2y}\right)^2}; \tag{6.15}$$

This simplifies to $\lambda/2$ for $y \gg D$, and diverges for $y \to 0$.

The fringes follow ellipses with the two QPCs as foci; the equation for the ellipse is $(x/a)^2+(y/b)^2=1$, implying that the gradient to the phase is proportional to the gradient $\nabla\left((x/a)^2+(y/b)^2\right)$. Thus the normal to the fringes is at the angle

$$\phi=\tan^{-1}\left(\frac{y}{x}\frac{a^2}{b^2}\right), \tag{6.16}$$

where we take $0 \le \phi \le \pi$.

(d) Elliptical Fringes 2

The source and target QPCs are the same, and there is a strong scatterer located at a distance D from the QPC, perpendicular to the QPC wall; there is no magnetic field present. The tip is located at a position (x, y), with the origin at the QPC. This works out to be essentially the same geometry as previously done, but with some variables changed. The results are

$$\theta_{sc}(x,y)=\cos^{-1}\left(\frac{y}{\sqrt{x^2+y^2}}\right)+\cos^{-1}\left(\frac{y-D}{\sqrt{x^2+(y-D)^2}}\right) \tag{6.17}$$

$$\Delta r(x,y)=\frac{\lambda}{\sqrt{2}}\left[1+\frac{x^2+y^2-yD}{\sqrt{(x^2+y^2)\left(x^2+(y-D)^2\right)}}\right]^{-1/2}, \tag{6.18}$$

$$\Delta r(x,y=D/2)=\frac{\lambda}{2}\sqrt{1+\left(\frac{D}{2x}\right)^2}; \tag{6.19}$$

and

$$\phi=\tan^{-1}\left(\frac{y-D/2}{x}\frac{b^2}{a^2}\right), \tag{6.20}$$

Where now $-\pi/2 \le \phi \le \pi/2$.

(e) Hyperbolic Fringes

The setup is the same as in the previous section, but we consider the case where the phase is beating not against the background, but instead the trajectory backscattered directly from the tip. The is the case described in the section on backscattering interference, thus once we determine the scattering angle θ_{sc}, we can use the results there to determine the fringing.

The geometry for the deflected trajectory, however, is the same as for example (d), and thus we have the scattering angle. The fringe spacing follows directly, using $\Delta r = \frac{\lambda}{2}|\sec\theta_{sc}/2|$, to be

$$\Delta r(x,y) = \frac{\lambda}{\sqrt{2}}\left[1 - \frac{x^2+y^2-yD}{\sqrt{(x^2+y^2)\,(x^2+(y-D)^2)}}\right]^{-1/2}, \tag{6.21}$$

with

$$\Delta r(x, y = D/2) = \frac{\lambda}{2}\sqrt{1+\left(\frac{2x}{D}\right)^2}. \tag{6.22}$$

The fringe direction is perpendicular to the direction in example (d).

(f) Central Arc Fringes

The source and target QPCs are separate, located at a distance D from one another. The tip is located at a position $(x = 0, y)$, with the origin at the midpoint between the QPCs. There is a magnetic field present, implying a cyclotron radius r_c; we take $r_c > D/4$. Defining the angles

$$\begin{aligned} \alpha &= -\cos^{-1}\frac{\sqrt{(D/2)^2+y^2}}{2r_c} \\ \phi &= \cos^{-1}\frac{D/2}{\sqrt{(D/2)^2+y^2}}, \end{aligned} \tag{6.23}$$

where ϕ is the angle from the QPC to the tip, and α is the angle with which the arc crosses a line from the QPC to the tip (see Section (...)). The scattering angle is $\theta_{sc} = 2(\phi-\alpha)-\pi$ and the fringe spacing is

$$\begin{aligned} \Delta r &= \frac{\lambda}{2}\sec(\phi-\alpha) \\ &= \frac{\lambda}{2}\left[\frac{y}{2r_c}\sqrt{\frac{(2r_c)^2}{(D/2)^2+y^2}-1}-\frac{D}{4r_c}\right]^{-1}. \end{aligned} \tag{6.24}$$

Near the wall, the scattering angle $\theta_{sc} \to -2\alpha$, and spacing expression simplifies to $\Delta r \to \frac{2\lambda r_c}{D}$; this goes to the backscattering value only as $D \to 4r_c$, which is the classical limit in which such trajectories are possible. Far from the wall, when $y \gg D$, we may expand in the small parameter $D/2y$, with result

$$\Delta r \cong \frac{\lambda r_c}{\sqrt{(2r_c)^2-y^2}}\left[1+\frac{D}{\sqrt{(2r_c)^2-y^2}}\right] \tag{6.25}$$

which goes to the limit of the magnetic backscattering case (b) as D becomes negligible. Implicit in this limit, since $y \leq 2r_c$, is that D is small with respect to r_c as well; and thus that we are in a small magnetic field.

(g) Central Arc With Wall Fringes

This case is nearly the same as the above case (f), but now the tip scatters the electron to the wall and back before proceeding to the target QPC. In this case we may simplify things by recognizing that the value of interest is the accumulated phase, and that if we ignore any offsets in the tip position (i.e. we treat the tip as a true point tip), then we can think of the phase accumulation as due to two separate paths, one which scatters softly off the tip, as in case (f), and one which backscatters as in case (b). The unit vectors that describe the fringe direction are parallel or anti-parallel in this case, so we can uniquely determine the fringe spacing to be

$$\begin{aligned}\Delta r &= \left|\Delta r_1^{-1} \pm \Delta r_2^{-1}\right|^{-1} \\ &= \frac{\lambda}{2}\left|\frac{y}{2r_c}\left(\sqrt{\frac{4r_c^2}{y^2}-1} \pm \sqrt{\frac{4r_c^2}{(D/2)^2+y^2}-1}\right) \mp \frac{D}{4r_c}\right|^{-1}.\end{aligned} \tag{6.26}$$

When the QPCs are well spaced $D > 2r_c$ and the tip positions y is within r_c of the wall, then the first and third terms dominate the second, and we may simplify

$$\Delta r \cong \frac{\lambda}{2}\left|\sqrt{1-\left(\frac{y}{2r_c}\right)^2} + \frac{D}{4r_c}\right|^{-1}, \tag{6.27}$$

where we've taken the fringing directions to be antiparallel. Another limiting case is when the QPC spacing becomes small, so that the parts of the trajectory are nearly the same; then the fringe directions are parallel, and the limit becomes that of two magnetic backscatterings, $\Delta r = \frac{\lambda}{4}\frac{2r_c}{\sqrt{(2r_c)^2-y^2}}$.

(h) Free Magnetic Green Function Fringes

We add one last possible fringe pattern, which is due to the variation in amplitude at the tip itself from the magnetic Green function. A tip is near enough to the target QPC that nearly equal contributions from the two possible arcs are summed at the tip, while the background contribution is ignored. The tip is near enough the target QPC that as the tip is moved parallel to the wall, the phase due to the path from the tip to the target varies little and hence the tip acts to measure the phase difference between the two paths, and hence measures the Green function from the source to the tip.

The phase difference between the two paths is

$$\Delta\phi = 2k_f r_c(\alpha - \sin\alpha\cos\alpha) \tag{6.28}$$

where α is the angle with vertical at the source QPC over the longer trajectory. Near the target QPC,

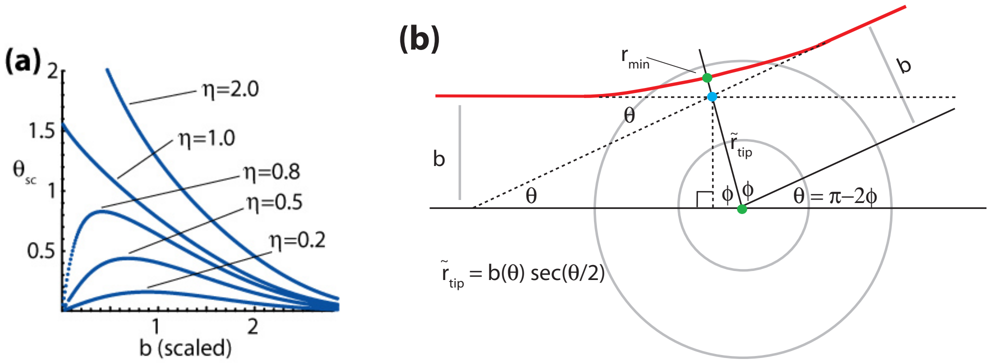

Figure 6.4: (a) Scattering angles $\theta_{sc}(b)$ for a Guassian tip potential. (b) Geometrical derivation of the effective tip shift $\tilde{r}_{tip}$, from the scattering angle θ and the numerically determined impact parameter $b(\theta)$. The point of closest approach r_{min} is determined numerically along with b.

then $D = 2r_c \cos\alpha$, where D is the distance between the QPCs. Then we may write

$$\Delta\phi = 4\pi \frac{r_c}{\lambda} \left[\cos^{-1} \frac{D}{2r_c} - \frac{D}{2r_c} \sqrt{1 - \left(\frac{D}{2r_c} \right)^2} \right]. \tag{6.29}$$

Linearizing in the standard way, one obtains the fringe spacing

$$\Delta r = \frac{\lambda}{2} \left[1 - \left(\frac{x - D}{2r_c} \right)^2 \right]^{-1/2} \tag{6.30}$$

as one moves the tip along the wall near the target QPC.

Because the fringes are due to the phase difference in the paths to the tip, one could conceivably replace the tip with a movable QC if possible. This case is interesting, because the amplitude at the tip due to the two paths is a measure of the magnetic Green function in the system. With a sufficiently collimated input distribution, effects of the reflections from the hard wall would be negligible and such a tip scan would probe the oscillations in the background magnetic Green function.

6.4 Effective Tip Position Shift

The fringe spacing has been shown to be directly related to the scattering angle θ_{sc}. This allows us to use classical scattering theory to determine the difference between the actual tip position, and the shifted "effective" point tip position, $\tilde{r}_{tip}$. From Chapter (5), we can determine the function $\theta_{sc}(b)$ numerically, where b is the impact parameter; for a backscattering tip, where $\eta > 1$, this is a monotonically decreasing function of impact parameter, and thus uniquely invertible. However, for a tip with $\eta < 1$, this function has a single peak, and thus its inverse will be double-valued, as shown in Figure (6.4a).

Given one of the inverted solutions $b = \theta^{-1}(\theta_{sc})$, we can geometrically determine the distance from the real tip to the effective tip (see Figure (6.4b) . The result reads

$$\tilde{r}_{tip} = b(\theta_{sc}) \sec(\theta_{sc}/2) \tag{6.31}$$

for each possible value b. Given the ambiguity in sign as well as the multi-valued nature of θ^{-1} for $\eta < 1$, the tip shift $\tilde{\vec{r}}_{tip}$ may take on two to four different possible values.

6.5 Experiment

Here we present experimentally measured elliptical fringes, obtained in an SPM imaging setup by Brian Leroy of the Westervelt group, and which appears in his Ph.D. thesis [68]. The results are easily reproducible in the lab, and represent the clearest examples of deflection-based fringing. We note that in addition to these results, in Chapter (7) we will present similar experimental fringes in the presence of a magnetic field, and more fully consider the fringing in that system there.

The layout of the device is shown in Figure (6.5a), and a micrograph of the device appears in Figure (6.5b). In the system, the Fermi wavelength is 45 nm, implying a backscattering fringe spacing of 23 nm. The elliptical fringes are spaced by $\Delta r = 38$ nm, so that $\Delta r/(\lambda_F/2) = 1.7$. With an inter-foci spacing of $D = 2000$ nm, and a $\Delta y = 700$ nm, this implies a scattering angle $\theta = 35°$, and a fringe spacing $\Delta r = 1.74\ (\lambda_F/2) = 39$ nm, in good agreement with experiment. The tip produces an effective tip height $\eta \equiv V(0)/E_F = 1.2$, and has a half width $\sigma = 67$ nm, thus the impact parameter $b = 96$ nm assuming a Gaussian tip profile, and $b = 74$ nm assuming a Lorentzian. Since in this case $\sec(\theta/2) \cong 1.0$, the tip shifts are nearly the impact parameters in both cases. We note in passing that the resolution of the data in the Figure is 2.47 nm/pixel.

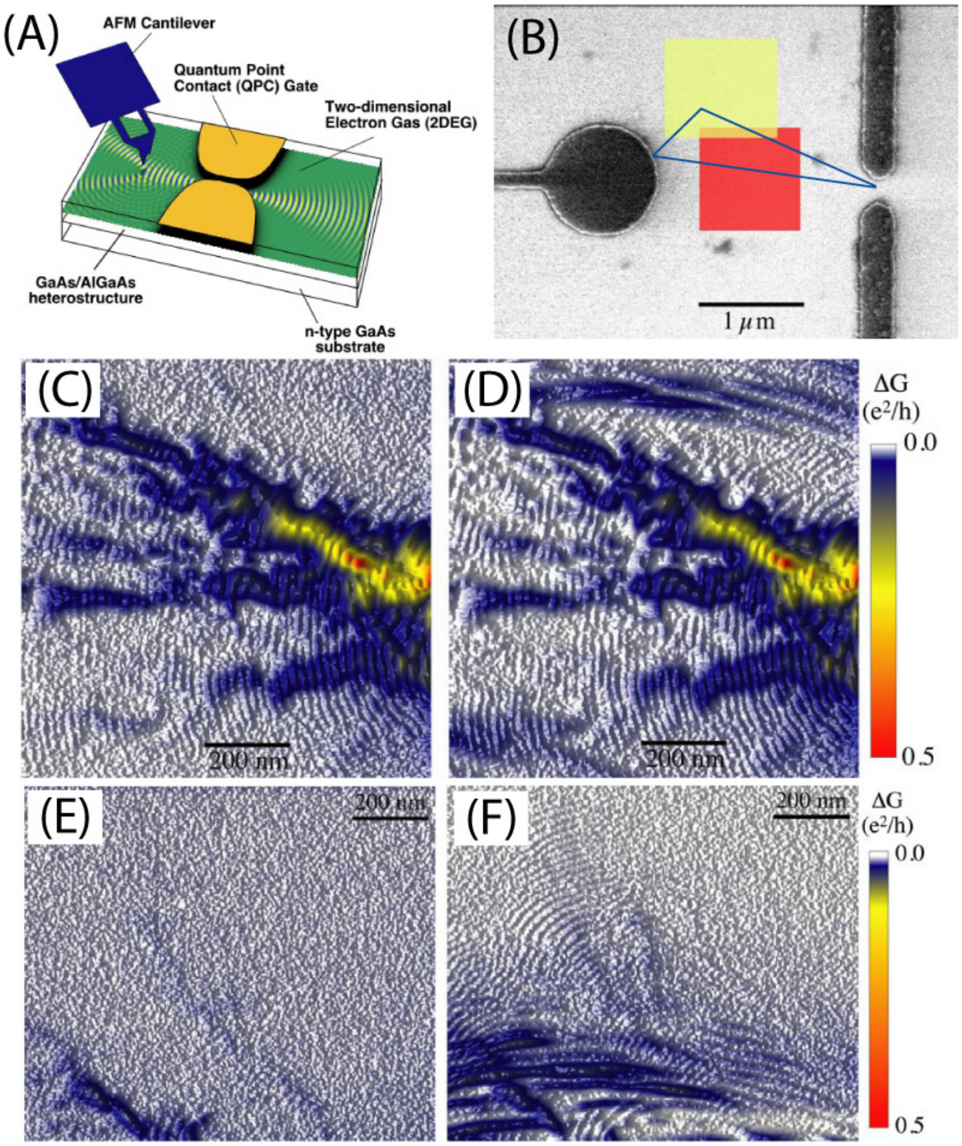

Figure 6.5: (A) The experimental device. (B) Micrograph of device, with SPM scan regions shown in red and yellow. The relevant elliptical trajectory is shown in blue. SPM tip scan in the red region is shown in (C) with the circular trace de-energized, and energized in (D). The SPM scan in the yellow region is shown for the circular trace de-energized (E) and energized (F).

Chapter 7

Deflection Imaging of Magnetic Focussing

7.1 Introduction

In the last two Chapters we considered the more general deflection scattering case as applied to SPM tip imaging system. In this Chapter we will consider more pointedly the effect of a finite-size tip on the electron flow, and what we can glean from SPM tip imaging experiments with arbitrary tip shapes. This we will do in the context of an experiment performed by Katherine Aidala in the Westervelt group at Harvard, aimed at the hspatial imaging of electron focussing in a perpendicular magnetic field.

We will begin by describing the experimental setup and results, and discuss how the experiment is conceptually different from other experiments. We will then explain the theory to be used to analyze the system. We begin by developing the classical and semiclassical billiard model of the system, and then discuss a quantum approach to simulating the system. We then simulate the conventional conductance scans in magnetic field, and compare the results to experiment. Continuing we simulate the tip scan experiment in a clean system, and comment on the relevance to the experiment. We conclude by simulating the system with a realistic bumpy background.

7.2 Experiment

The experimental setup is depicted schematically in Figure (7.1), and mimics the classic textbook magnetic focussing setup, pioneered by Sharvin and Tsoi [92, 105] in metals, where it has subsequently been used to study the shape of the Fermi surface, electron-phonon scattering,

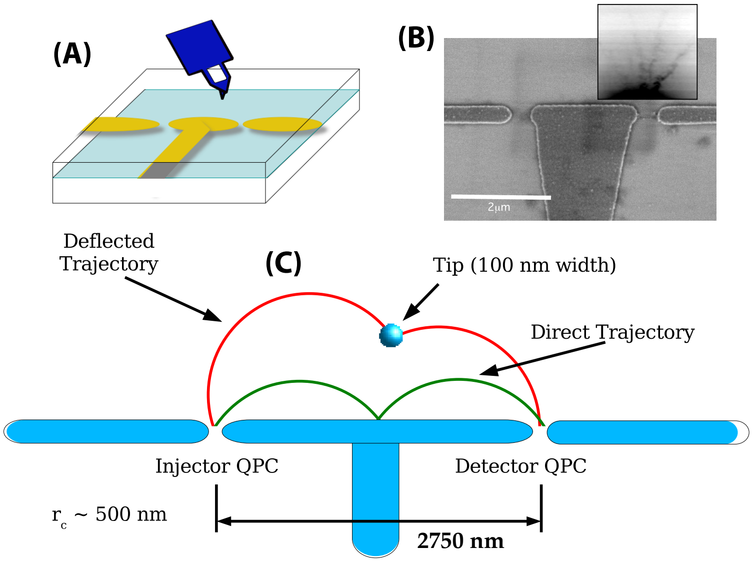

Figure 7.1: Classic magnetic focussing setup, with two collinear QPCs in a perpendicular magnetic field; here a SPM tip is also included. (A) shows the schematic of the experiment with the SPM tip. (B) shows a micrograph of the device; the inset is an SPM tip scan at zero field, showing the branched flow from the right QPC. In (C) we depict how the electron flows between the QPCs at moderate fields near a focussing peak, and how the SPM tip can deflect electron flow into the target QPC.

and surface scattering. In the context of 2DEGs the setup was first described almost 20 years ago [110]. The transmission through two colateral QPCs is measured as a perpendicular magnetic field is scanned in value up to the quantum Hall regime. Adding a new wrinkle to the system, a SPM tip energized to a large fraction of the Fermi energy was introduced above the surface of the sample, and scanned in the region of the electron flow between the two QPCs; the magnetic field and bias were held fixed during each scan. As the tip was scanned, the conductance between the QPCs was measured using a four-terminal measurement, creating a map of transconductance versus tip position.

The temperature in these experiments was at liquid Helium temperature, 4.2 K. The density was measured to be $n = 3.9 \times 10^{11}$cm^{-2}, implying a Fermi energy $E_F = 13.5$ meV and Fermi wavelength $\lambda_F = 40$ nm. A schematic of the experimental apparatus is shown in Figure (7.1a). The GaAs/AlGaAs heterostructure has a 2DEG 52nm below the surface in which the electrons conduct. Metal gates were deposited on the surface of the heterostructure to define the two QPCs, side by side and separated by a shared middle gate that is lithographically defined to be 2.5 μm long; a micrograph of the device is shown in Figure (7.1b). The electrons propagate almost ballistically through the system, but are strongly deflected by either the scanning tip or the metal gates (see Figure 7.1c). In addition, a bumpy background potential is present, due to imperfections in the crystal lattice, which causes small angle scattering of the electrons. Most measurements were performed with the voltage on the gates such that the QPCs were open to two transverse modes.

In the absence of a tip, the metal gates or other imperfections, the electron will move in a circle of radius

$$r_c = \frac{\hbar k_F}{eB} \tag{7.1}$$

where e is the electron charge, B is the perpendicular magnetic field, and k_F is the Fermi wavevector. While there is an initial spread in the momenta of the electrons emerging from the QPC, the magnetic field can focus them to a point of near convergence along the middle gate; the flux is greatest at the point $2r_c$ from the injection QPC. When this point of convergence intersects with the second QPC, a peak in the transmission is expected. Taking into account the possibility of $n-1$ bounces, this occurs when $L = 2nr_c$, so at field values

$$B_n = \frac{2\hbar k_F n}{eL} \tag{7.2}$$

where L is the spacing between the two QPCs. As one sweeps the magnetic field, periodic peaks are predicted when the spacing between the QPCs is equal to a multiple of the cyclotron diameter.

In Figure (7.2) we show the experimental focusing peaks. In (A) the darker sweep results from a measurement configuration in which the right QPC sources electrons and the left QPC acts as the collector. Upon switching the leads such that the left QPC is the source and the right is the collector, the lighter gray sweep is obtained. Note that there is reciprocity between the two, in that the fluctuations are nearly identical, but exist for the opposite field. This is expected from the Onsager-Casimir relations in the diffusive regime, extended to the ballistic regime of interest here by Büttiker [14]. One thing which distinguishes this experiment from other magnetic focussing experiments is the large size of the system, so that even a weak background bumpiness can scatter the focussing peaks. As a result, the experimental focussing peaks do not lie close to the peaks expected for a clean system. In Figure (7.2B), taken on a different day with the same sample, the peaks are more visible but still broadened and shifted. We will examine this is more detail in Section (7.5).

In Figure (7.3) we show tip scan experimental data performed near the first three focussing peaks. The tip was held at a height 35 nm above the surface of the sample, and hence 87 nm above the 2DEG, implying the effective tip potential was about $2\sigma \sim 170$ nm across. The voltage on the tip was -0.5 V, such that the effective tip strength $\eta \sim 0.5$ [96]. Because of the height of the tip, the scan could be continued over the QPCs themselves without hitting the metal gates. The QPC sources appear in the data as very bright or dark regions at the bottom of the scans. The resolution of the scans is $\Delta x = 9.4$ nm, which is just a quarter of the Fermi wavelength. The data in this

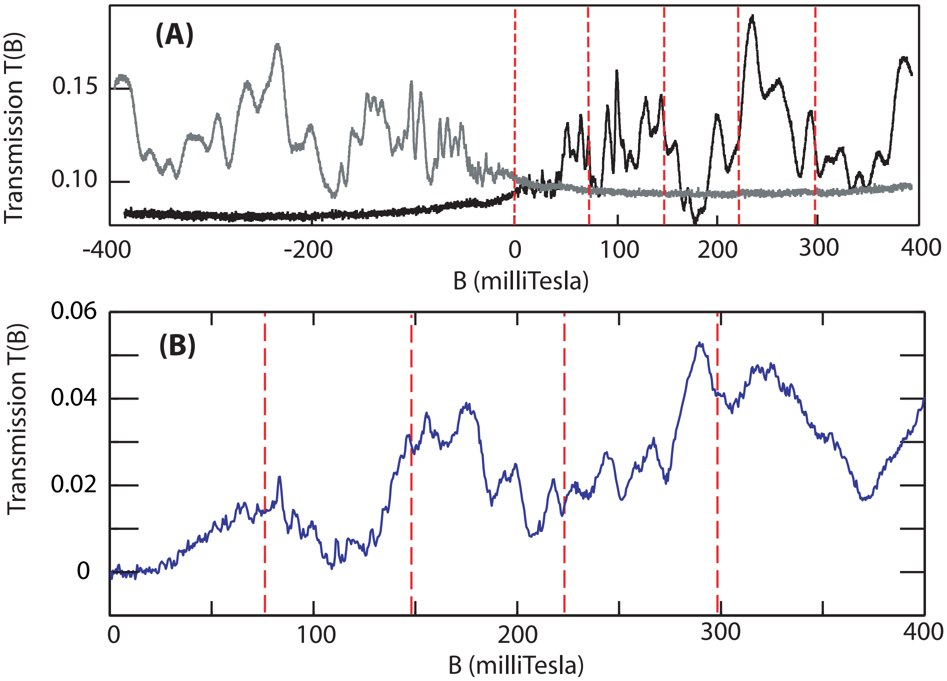

Figure 7.2: Transmission from the source to the target QPC as a function of magnetic field. (A) is for one scan, the data in grey is with both the magnetic field and the QPCs switched. The symmetry of the traces in B indicates that the fluctuations are due to conductance fluctuations and not to systematic noise. The red vertical lines indictes the field values that one would expect focussing peaks in the clean case. (B) is another scan, with focussing peaks closer to the expected spacing of 74 milliTesla in magnetic field.

case is not high resolution, and due to the configuration of the tip, does not reveal high frequency structure. Instead it serves mainly as a map of the classical structure of the flow.

As we proceed in field strength, the bouncing ball nature of the flow is readily apparent, with the number of bounces increasing with field strength. However, there is additional structure in the flow images. To begin, we know that there is a branching structure present in the system; for the lower field value, such a branching structure appears to be happening, as two distinct flows to the target QPC appear to be visible. However there are more consistent and generic patterns in the data. In particular, the center of the flow patterns tends to be reduced in transmission as compared to the tip-free (or distant tip) values. This region of reduced transmission is usually bordered by regions where the transmission is enhanced beyond the tip-free value. These patterns of reduction and enhancement, which have been seen before at low resolution by Crook and Smith [20], appear to follow the anticipated direction of the flow, and hence indicate that the pattern is a systematic feature of the tip imaging process. In Section (7.6) we shall consider the imaging of classical flow

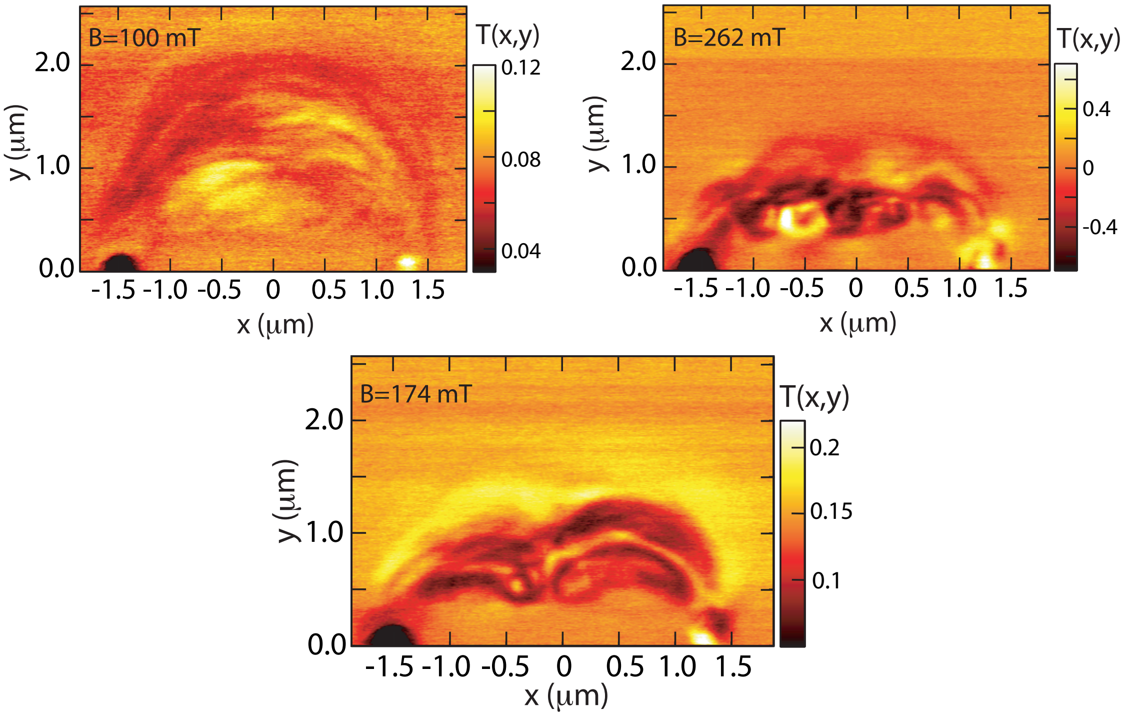

Figure 7.3: Experimental magnetic focussing tip scan data for a weak tip, at three magnetic field values that are near the classical focussing peak values. The tip height is well above the 2DEG surface, and thus the tip appears wider and weaker; this allows the gross structure of the flow to be imaged.

in the clean system, and find that these patterns are due to the finite sized tip either obstructing nascent flow by acting as a diffusive element, or enhancing the flow by deflecting flow that would otherwise not contribute into the target QPC.

In Figure (7.4) we show tip scan experimental data performed near the first three focussing peaks, but now with a tip that is much nearer the surface of the sample. Such a tip produces a sharper effective potential , and hence is able to resolve the flow at a higher resolution. The tip was held at a height 12 nm above the surface of the sample, and hence 64 nm above the 2DEG, thus the effective tip potential was about $2\sigma \sim 120$ nm across. The voltage on the tip was -0.3 V, such that the effective tip strength $\eta \sim 0.8$ [96]. The scan does not include the region near the metal gates because the tip would collide with them; the locations of the metal gates and QPCs are indicated schematically in the lowest plot. The resolution of the scans is $\Delta x = 3.8$ nm, much finer than the high tip results.

In contrast to the results with a higher tip, there is much finer structure visible in these

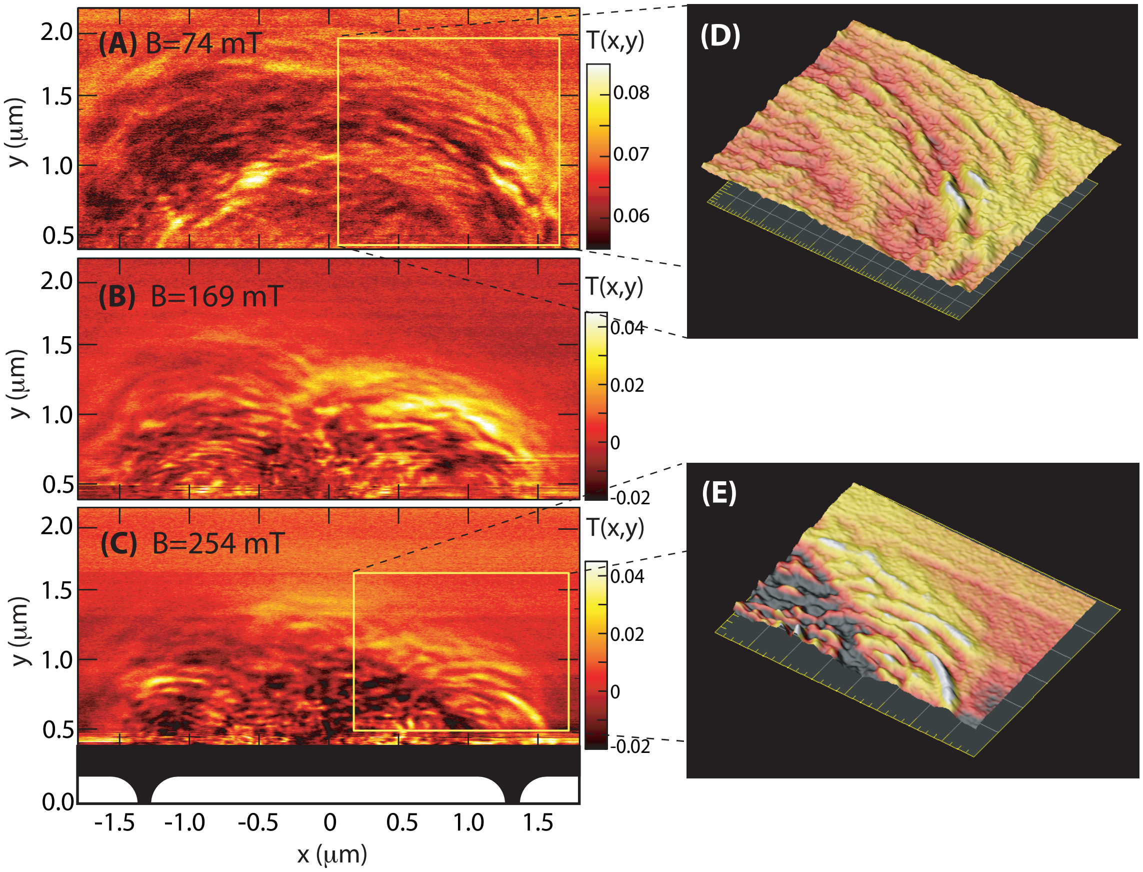

Figure 7.4: Experimental magnetic focussing tip scan data, at a resolution of 3.8 nm, with $E_F =$ 13.7 meV, and perpendicular field $B_z =$ (A) 74, (B) 169, and (C) 245 milliTesla. The effective potential from the tip was backscattering, with width $2\sigma \approx 100$ nm. The location of the QPCs and gates is indicated schematically in the bottom scan. The fringe structure in the data is blown up in the surface plots (D-E) to make more visible the regularity and pattern of the fringes.

scans, but the same overall bouncing ball-like flow. While the overall classical effects, seen in the high tip results, are still visible, much more obvious is the strong fringe-like patterns that run along the flow. However, carefully inspecting the fringes reveals that the patterns don't run exactly parallel to the expected flow direction, but instead run at a slight angle to the expected flow; this is particularly clear near the source or target QPCs.

In Figure (7.5) we plot the high resolution data with a grid overlay spaced by 100 nm. The minimum fringe spacing is $d \sim 80$ nm, with typical fringe spacings in the range $80 - 100$ nm. With a Fermi wavelength $\lambda_F = 40$ nm, this is twice the Fermi wavelength. In typical backscattering experiments, we would instead expect a fringe spacing of half the wavelength $d = 20$ nm. If we interpret the fringes as quantum in nature, but due to deflection scattering, then we can determine

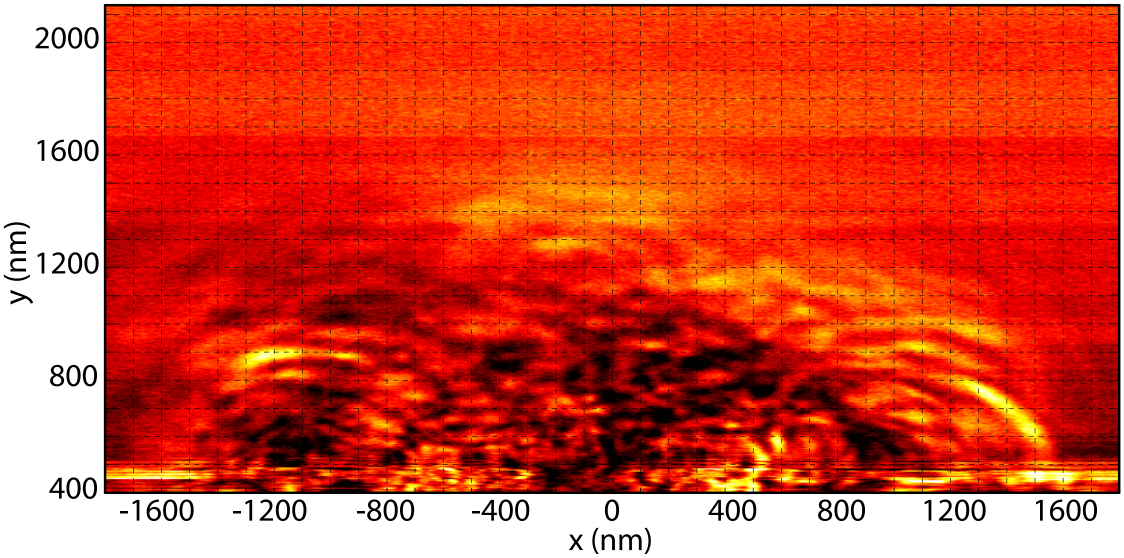

Figure 7.5: Experimental magnetic focussing tip scan data, at a resolution of 3.8 nm, with $E_F =$ 13.7 meV, and perpendicular field $B_z = 245$ milliTesla, plotted with a 100 nm grid overlay. The fringes have a minimum spacing of about 80 nm.

the scattering angle from equation (6.8) in Chapter (6), $\theta_{sc} = 2\sin^{-1}\left(\frac{\lambda}{2d}\right)$, to be $\theta_{sc} \sim 30°$. This implies that even though the tip can almost backscatter, the measurable effect of the tip in creating interference fringes is in the process of deflecting the electron by small to moderate angles as it flows along its arcing, bouncing ball orbit. Such a conclusion is a novel interpretation of the effect of tip scattering, and needs to justified via realistic simulations.

In subsequent sections we will simulate the system and compare to experiment. But before we do that, we will develop some of the results that we need in those simulations. We begin by treating the system as a billiard, and developing the semiclassics of the clean system.

7.3 Semiclassical Billiard Tip Scan

In this section we model the system in question as a billiard, with the QPCs modeled as a point source and target located on a hard flat wall; the tip is also assumed to be a point which is scanned around the system. The trajectories of the electron will hence be a series of connected arcs, connecting the source, some number of points along the wall, the tip, and the target QPC. The relevant classical and semiclassical quantities have been worked out in Appendix (D).

Since the tip may scatter at all angles, this simplifies the process. If we find all trajectories from the source to the tip, and then all trajectories from the drain to the tip, the set of combinations of these trajectories will be the set of all trajectories from QPC to QPC. We will assume that the system has some inherent disorder, so that there is a relevant decoherence length and mean free path. In addition, the QPCs are taken to have a fairly collimated angular distribution [93], so that trajectories injected along the walls may be ignored. This allows us to ignore the contributions from longer trajectories, and focus on the most direct trajectories.

In order to simulate a tip scan, we can use the hard-wall Green function we've calculated in Appendix (D) and basic scattering theory to calculate a total amplitude from the source QPC to the target, with a scattering tip placed at (x, y). We denote the tip-free hard wall Green function as $G_{o,B}(x, y)$, where we assume it starts at the source QPC along the wall. The finite size tip potential, parameterized by its central position $\vec{r}_{tip}$, we denote as $V_{\vec{r}_{tip}}(x, y)$; usually this is equivalent to $V_{\vec{r}_{tip}}(x, y) = V_0(x - x_{tip}, y - y_{tip})$ for central tip potentials. Then the scattering expansion for the full Green function from the source at $(0, 0)$ to the target at $(\mathcal{L}, 0)$, with the tip present in the system, reads

$$G_B(\mathcal{L}; x_{tip}, y_{tip}) = G_{o,B}(\mathcal{L}, 0) + \int dr'^2 G_{o,B}(x', y') V_{\vec{r}_{tip}}(x'y') G_{o,B}(\mathcal{L} - x', y') + \dots \tag{7.3}$$

where $\mathcal{L}$ is the distance along the wall from the source to the target QPC.

For convenience we will make a few approximations. To begin we take the tip potential to be a delta function at the tip position. However, this does not mean we assume the tip is an s-wave scatterer, since this is a semiclassical theory. Instead we have the luxury of replacing the integrations over the tip potential $V_{\vec{r}_{tip}}$ with a reasonably chosen function of the incoming and outgoing velocity and the tip position, $f(\vec{r}, \vec{v}, \vec{v}')$. This allows us to model the tip scattering process as we choose, and to model the summing up across all multiple scatterings with the wall present by using a "dressed" scattering amplitude. In general the presence of the wall will mean that this "dressed" scattering amplitude will be position dependent (on y).

Thus we have a collapsed, empirical Green function

$$G_B(\mathcal{L}; \vec{r}_{tip}) = G_{o,B}(\mathcal{L}, 0) + \sum_{\text{traj } j} \sum_{\text{traj } j'} G_{j,B}(\vec{r}_{tip}) f(\vec{r}_{tip}, \vec{v}, \vec{v}') G_{j',B}(\mathcal{L} - x_{tip}, y_{tip}) \tag{7.4}$$

where $G_{j,B}(\vec{r}_{tip})$ is the contribution to the Green function some trajectory j.

With this approach, we can analyze how the process of scattering from the tip affects where fringes are seen with significant amplitude, and what types of fringe patterns are seen in the clean system. Empirical quantities such as the injection weighting, the tip scattering amplitude,or dephasing length can be changed and modified to suit. Also the contributions from periodic orbits that "dress" the Green function can be controlled directly by adding or suppressing them in the sum over trajectories. In this sense the semiclassical hard wall billiard makes a convenient laboratory for studying the tip scan system.

The main drawback to this approach is that the finite size effects of the tip are not readily accessible; there is no mechanism for "blocking" or obstructing trajectories semiclassically, since the tip is of zero size. This problem is important only when there is significant amplitude at the target QPC without the tip; away from the focussing peaks, the tip will create new paths to the target QPC whose amplitude is large compared with the nascent flow. In addition this approach is directly relevant only for a clean system. While one could conceive of adding determinate disorder to the system by providing a momentum kick to the particle on the wall on on the tip, this approach doesn't adequately capture the effect of smooth bulk disorder in the system.

7.4 Quantum Simulation Method

In this section describe the use of quantum dynamic wavepacket approaches to simulate the propagation of the electron through the system; results will be discussed alongside classical simulations in the following sections. A wavepacket with a wide spread of energies around the Fermi energy (10 - 40 K) is launched outside the system of interest towards the first QPC; as it propagates, some amplitude passes through this source QPC, and some reflects off and is numerically attenuated, as described in Chapter (3). The history of the wavefunction is measured at a flux surface within the source QPC, and is used to reconstruct the flux entering the system as a function of energy, $\Phi_I(E)$. A similar flux surface and wavefunction measurement is performed at the target, "collector" QPC, to determine the outgoing flux, $\Phi_T(E)$. The ratio between the two is the transmission of the system,

$$T(E) = \frac{\Phi_T(E)}{\Phi_I(E)}.$$

From this we can determine the transconductance through the two QPCs by the L:andaur-Büttiker relation $G = \frac{2e^2}{h}T$ [21]. Using this approach, knowing the initial energy distribution of the wavepacket or the transmission of the first QPC is unimportant, because by measuring the incoming flux we measure the actual original energy distribution of the wavepacket while propagating through the system.

This transmission $T(E)$ is a sum over all the participating modes of the QPCs at energy E; as such we can't in general resolve the system by quantum number. To do so, we would also have to analyze the wavefunction passing through the flux surface into modes, by taking the overlap of the wavefunction with each transverse mode, and tracking each such mode separately. However, as is often the case in QPC system, our simulated QPC is restricted to the first plateau, allowing only a single mode through. In that case, the transverse quantum number is known to be $n = 1$, and because we know the energy distribution and the sign of the momentum, there is a one-to-one mapping between energy and longitudinal momentum $k_y = \sqrt{2m(E - E_1)}$; since we know the

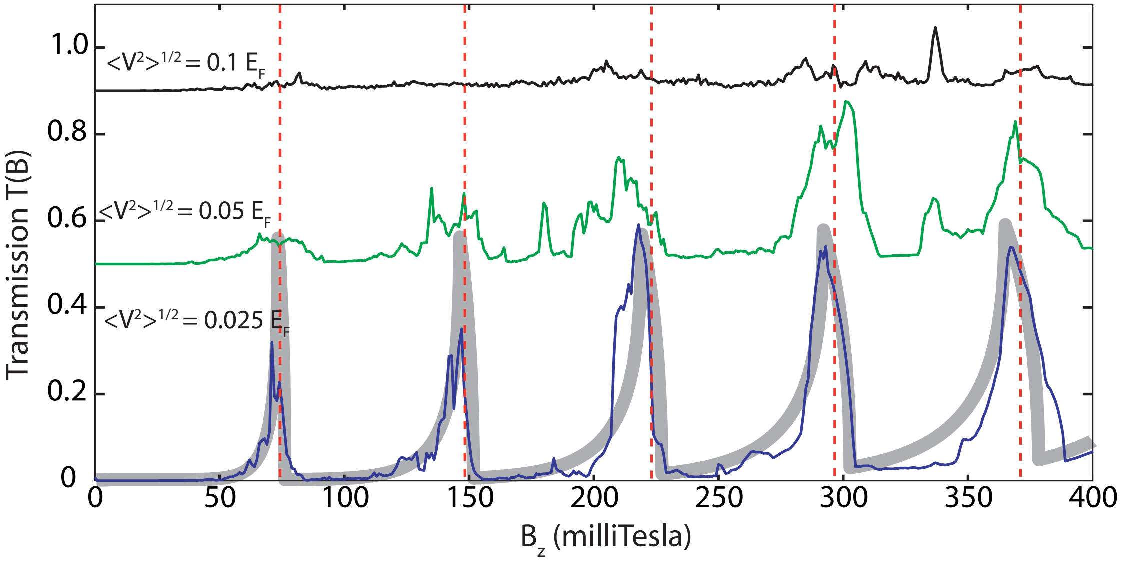

Figure 7.6: Classical results for the transmission with a clean billiard system (thick grey line) compared to a simulation of the billiard where a bumpy background potential has been included and trajectories run (black, green,and blue lines). The vertical dotted red lines are the focussing peak values. The sharply spiked structure in the clean case is replaced by a fluctuating background transmission. The QPCs are placed 2750 nm apart, the energy is $E = 13.7$ meV, and the source and target QPCs are 100 nm wide. The injection current distribution $w(\alpha) \propto \cos^8(\alpha)$.

energy distribution across the flux surface, we also know the distribution in quantum numbers in this case. Thus keeping the QPCs at a single mode allows us to determine the single mode transmission $T_{1,1}(E)$ unambiguously.

To simulate a scanning tip experiment, we introduce into this system at some point (x, y) a potential bump that approximates the effective potential induced by a charged tip. While the other parameters of the system are held fixed, the tip potential is moved about the system and the transmission function $T(E; x, y)$ measured. This data can then be evaluated at a specific energy to provide an energy resolved image of the conductance $G = \frac{2e^2}{h}T$, or convoluted by a thermal distribution in energy, $f(E) = \frac{4}{kT}\,\text{sech}^2(E/2kT)$ to determine the thermal conductance image.

7.5 Conductance Scans in Magnetic Field

Here we consider the measurement usually performed in these systems, where the conductance is measured as the perpendicular magnetic field is swept in value; there is no tip present. One can determine the transmission in the classical clean billiard case analytically. Such an analysis has been performed semiclassically [110] and quantum mechanically using billiard boundary conditions [106, 107, 108]. From [110], we can calculate the classical transmission through the system by considering the QPCs as point QPCs with infinitessimal width δw, and calculating the contribution from each trajectory that reaches the target QPC. For a given normalized injection distribution $f(\alpha)$ of current I_i injected from a point on the source QPC, the current into the target QPC I_c at a distance L is

$$\begin{aligned} I_c &= 2I_i\delta w \sum_{n\geq L/2r_c-1} f(\alpha_n)|\partial L/\partial\alpha|^{-1} \\ &= I_i\frac{2\delta w}{L}\sum_{n\geq L/2r_c-1} f(\alpha)\cot\alpha \end{aligned} \tag{7.5}$$

where $\int f(\alpha)d\alpha = 1$ for $\pi/2 \leq \alpha \leq \pi/2$. F We have taken into account the classical density $D(L,\alpha) = |\partial L/\partial\alpha|^{-1}$ on both paths which reach the target QPC, and the injection angle is related to the QPC distance as $L = 2r_c(n+1)\cos\alpha$. We can average over the finite widths w of the source and target QPCs; taking half-dipole injection distribution $f(\alpha) = \frac{2}{pi}\cos\alpha$, the average over finite width yields

$$T = \frac{2}{\pi}\sum_{n\geq L/2r_c-1} a\sqrt{1-a^2} - b\sqrt{1-b^2} - (\sin^{-1}a - \sin^{-1}b) \tag{7.6}$$

where $a = L/2(n+1)r_c$, $b = L_{min}/2(n+1)r_c$, and $L_{min} = \min[L+w, L(n+1)/n, 2(n+1)r_c]$. This result is a claim about the transmission from the source to the target QPC, and assumes that each QPC is ballistic. We take each QPC to be on the first plateau, so that the conductance of each is $2e^2/h$. The system will have negligible backscattering amplitude, so that we may take the resistances of the QPCs and the open system to add in serial; thus the conductance of the aggregate system should be $G = \frac{2e^2}{h}\frac{T}{2T+1} \approx \frac{2e^2}{h}T$ (which is a mixed classical and quantum result).

In Figure (7.6) we plot the clean classical transmission as a function of magnetic field, where the injection distribution has been taken to be a more collimated $f(\alpha) \propto \cos^8\alpha$. Also plotted is a simulation of the same billiard system, but where an experimentally realistic bumpy background potential has been added, with varying strength. On this potential landscape classical trajectories have been run in order to determine the classical transmission. In all cases the QPC width is 20 nm, which is typically $\lambda_F/2$, and thus consistent with a single moded QPC. The Fermi energy $E_F = 13.7$ meV, and mass $m = 0.067m_e$. The sharply spiked structure in the clean case, due to the caustics sweeping across the target QPC, is increasingly replaced by a fluctuating signal where the spikes are due instead in large part to the branch caustics sweeping across the target QPC.

Sharp structures in the bumpy classical case are due to some caustic branch sweeping into the target QPC. Analogous effects have been seen in quantum simulations from point scatterers [108]. In Figure (7.7) we show how the main caustic at the focussing peak in the clean case is

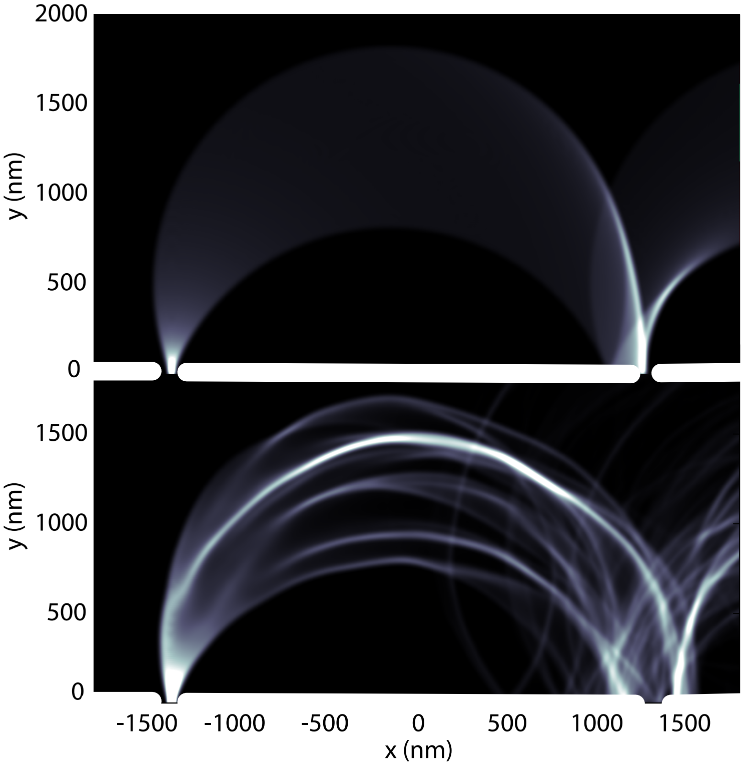

Figure 7.7: Classical simulations of the magnetic focussing process, in a clean (upper) and bumpy (lower) system. The main caustic formed in the clean case, which impinges on the target QPC here, is split into many caustic branches by the small angle scattering of the bumpy potential. This reduces the transmission on the focussing peak, but creates side peaks due to the branches.

split up into many caustic branches, reducing and shifting the peak, but also creating numerous side peaks. In both cases the focussing peaks are due to the passage of caustics across the target, but in the clean case the peaks are isolated and analytically predictable, while in the bumpy case the peaks are randomized by the effect of the bumpy background.

In Figure (7.8) we plot the semiclassical Green function $|G_o|^2$, which is proportional to the transmission probability T. This is obtained using the hardwall semiclassical Green function developed in Appendix (D). This result is for the amplitude from the center of one QPC to the other; since $T = 0$ and the simulations use point QPCs, the results aren't broadened as the classical or quantum cases. Plotted alongside is a classical result with a small aperture, and appropriately scaled. When thermal averaging is important, the interference oscillations see in the Figure tend to be washed out, and the main fluctuating signal will be due to caustic branching.

In Figure (7.9) we present a quantum version of the classical conductance vs. magnetic field simulation, along with the classical and experimental data. The bumpy background potential is

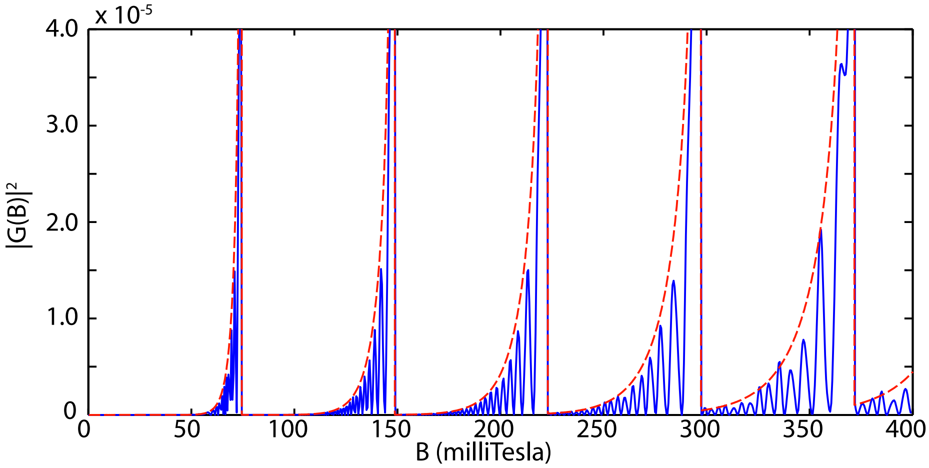

Figure 7.8: A semiclassical simulation of the Green function from a source point to a target QPC at a distance $\mathcal{L}$. The blue line is the clean, point-source semiclassical result, while the red dotted line is the accompanying classical result $T(B)$ for a very small target aperture, scaled for comparison. The injection distribution is fairly collimated, which exaggerates the focussing effects and results in a very spiked signal. The inclusion of a bumpy background (not done) would produce a more uniformly fluctuating signal, as in the classical and quantum simulations.

the same as in the classical case, but the QPC walls are more realistic smooth potentials. The plots are in addition thermally averaged for a temperature of 1.7 K. Even though this is a quantum simulation, we see no trace of high frequency interference structure in the clean results (shown in blue). This can be attributed to the finite size, but single moded, QPCs and thermal averaging effects. The focussing peaks are clearly present; towards higher fields they are shifted to the right. This effect is due to the use of soft walls instead of a hard billiard wall. Beyond the fourth focussing peak the simulation breaks down. The green lines are the bumpy results, and reproduce in a smoother fashion the randomization of the classical results. In all three cases wide focussing peaks are readily apparent near many focussing peaks, but not all. For stronger disorder, the peaks would be indistinguishable in most cases.

7.6 Tip Scan Simulations of a Clean System

Here we simulate the system and the process of scanning the SPM tip across the system, where we ignore the bumpy background, and take the 2DEG to be perfectly clean. This will allow us to identify the general mechanisms that lead to classical changes in the transmission, as well as quantum fringing, as it applies to the magnetic focussing geometry. To begin, we consider the effect of the SPM tip on the electron manifold. For a weak tip, the effective potential acts like a

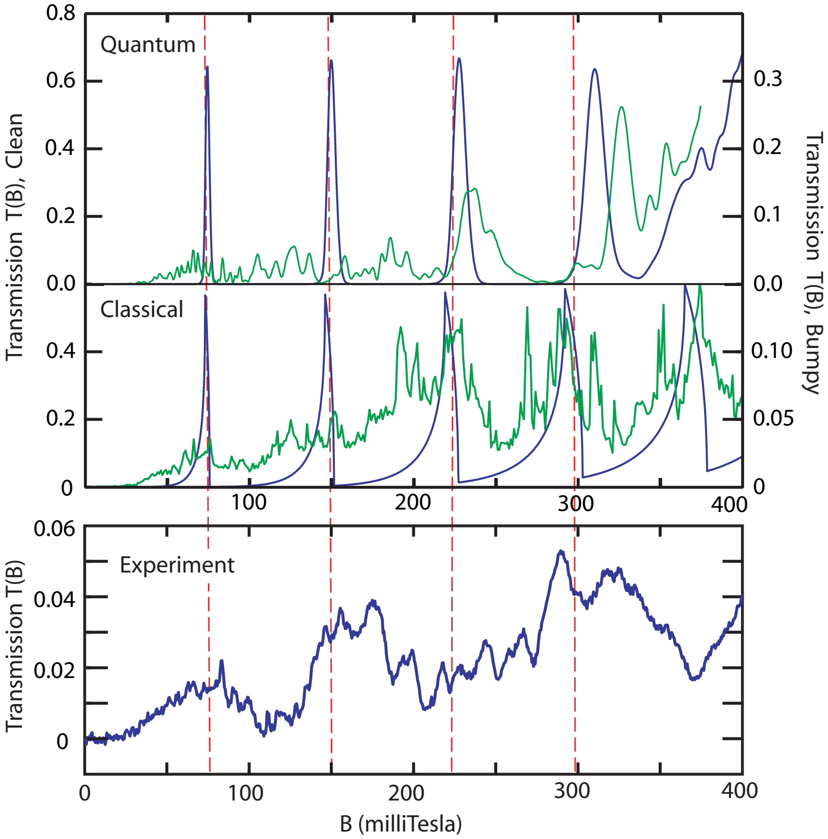

Figure 7.9: A quantum simulation of the same system as in Figure (7.6), but with a more realistic QPC wall, accompanied by the classical results and the experimental data. The blue line is for a clean system, the green for a bumpy system, with the same bumpy potential as in the classical simulation. The red dotted lines indicate the classical focussing peak field values B_n. While widened and shifted focussing peaks often appear in the bumpy and experimental cases, one can't always claim to see focussing peaks near every B_n value.

lens, convex or concave, and in the presence of a hard wall, the focussing effect will recur, though somewhat diffused, on the next arc (see Figure 7.10). The scattering process in the absence of a magnetic field has been examined in Chapter (5) in the absence of a magnetic field. In the presence of a weak to moderate magnetic such that the tip is small, $\sigma \ll r_c$, these results hold, modified by the cyclotron motion beyond the tip.

7.6.1 Classical Effects

To determine the classical effect of the tip on the electron flow and the transmission through the target QPC, we can run a manifold of trajectories in the presence of a tip, and rerun

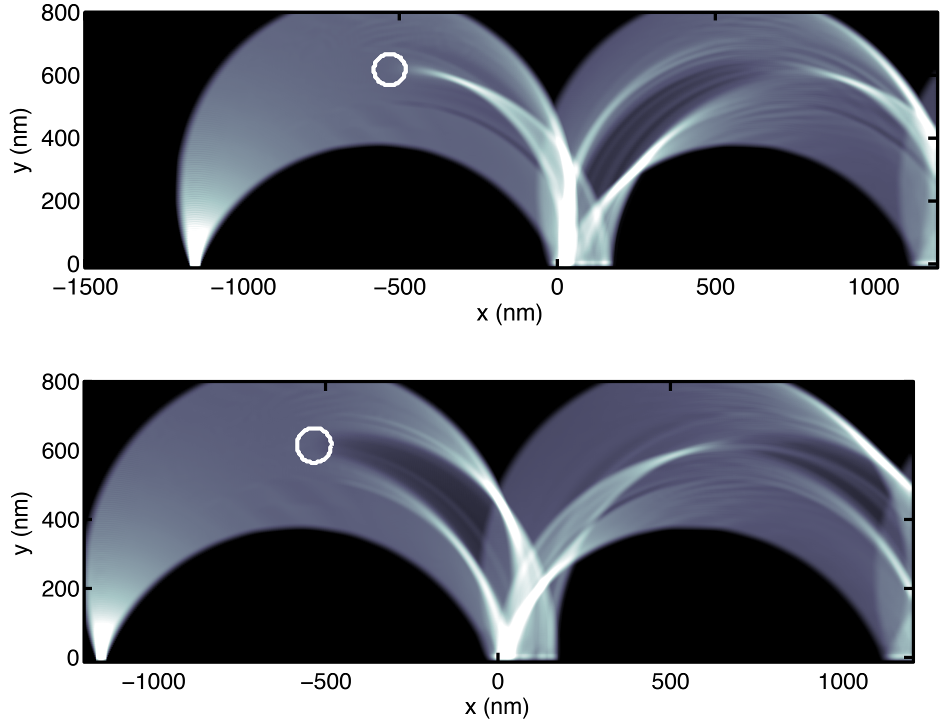

Figure 7.10: An attractive (a) or repulsive (b) tip of strength $\eta = 0.2$ and width $\sigma = 100$ nm, placed at the top of the first arc of a electron manifold in the magnetic focussing geometry.

the classical simulation at each tip position. This is similar to the simulation in Section (7.5), but with a fixed magnetic field and a tip introduced for each tip position. The results of such a simulation are shown in Figure (7.11), Here the parameters of the simulation are $B = 77$ milliTesla, $L_{QPC} = 2750$ nm, $E_F = 13.7$ meV, and the tip has strength $\eta = 0.6$ and width $2\sigma = 100$ nm; the effective electron mass is relevant for GaAs, $m = 0.067 m_e$.

In Figure (7.11a) we depict the effect of the tip on the electron flow (the grey sheet) and on individual trajectories. Here the tip is shading the target QPC from the flow, decreasing transmission. Figure (7.11b) shows a map of the transmission as a function of tip position. The main feature of the tip scan is the region of decreased transmission, where the tip has obstructed the nascent flow of the electron into the target QPC. By placing the tip in this region, the flow is scattered away from the target and strikes the wall away from the target QPC. This region of decreased transmission is bordered in turn by a region of enhanced transmission. This is due to the tip acting instead as a mirror, and redirecting trajectories into the target QPC instead. Such a pattern of reduction and enhancement of the classical transmission we've seen before in the zero field tip scan simulation in Chapter (5), Figure (5.7), and was also seen by Crook and Smith at low fields [20].

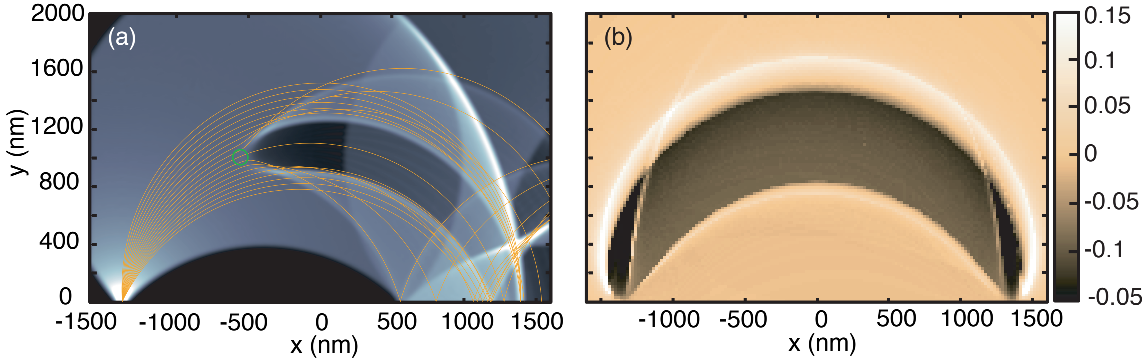

Figure 7.11: A classical tip scan of the magnetic focussing system with a tip $\eta = 0.6$ near the first focussing peak. In (a) we show the classical manifold scattering off the tip, along with some trajectories. In (b) we plot the transmission as a function of tip position.

Clearly there is a tradeoff between obstructing and enhancing the transmission from these competing effects. For a smooth tip and manifold, the effects will balance along some line between the two regions. In the figure, the enhancement region is stronger above the flow than below, and in a few cases such a border may not exist. However, in general these enhancement regions are a ubiquitous effect in the tip scans.

Note also that the caustics of the system are visible in the tip scan figure. The target QPC is just at the classically allowed region, $\mathcal{L} \cong 2r_c$, so nascent trajectories may both bounce against the wall or travel directly, with injectiion angle $\alpha \sim 0$ to transmit. By placing the tip near the center of the image, we block direct but not bouncing trajectories. By placing the tip near QPCs we may block both sets of trajectories, and significantly lower the transmission. The lighter line between the two regions is likely the signal of a caustic, since caustics occur between classically allowed and disallowed regions. The tip, when placed near this caustic, can focus this caustic into the QPC over a very narrow range of positions.

In Figure (7.12) we present a similar tip scan, but now near the second focussing peak. The obstruction vs. redirection effects are clearly evident in this case as well, and in this case enhanced below the obstruction more so than above. In the region near the wall bounce the caustic structure of the flowed creates sharp patterns in the tip scan. In addition, we can see additional structure in the slice of the transmission, shown in Figure (7.12a). This is due to the classical caustics as well; while the tip in general obstructs the flow in this region, it may redirect the caustics into the target QPC, for certain scattering angles, providing a temporary victory over the obstruction effect. This is even clearer near $x \sim 900$ nm, where the enhancement region follows the classical caustic.

These effects are not exclusive to the classical dynamics; the same effects are present

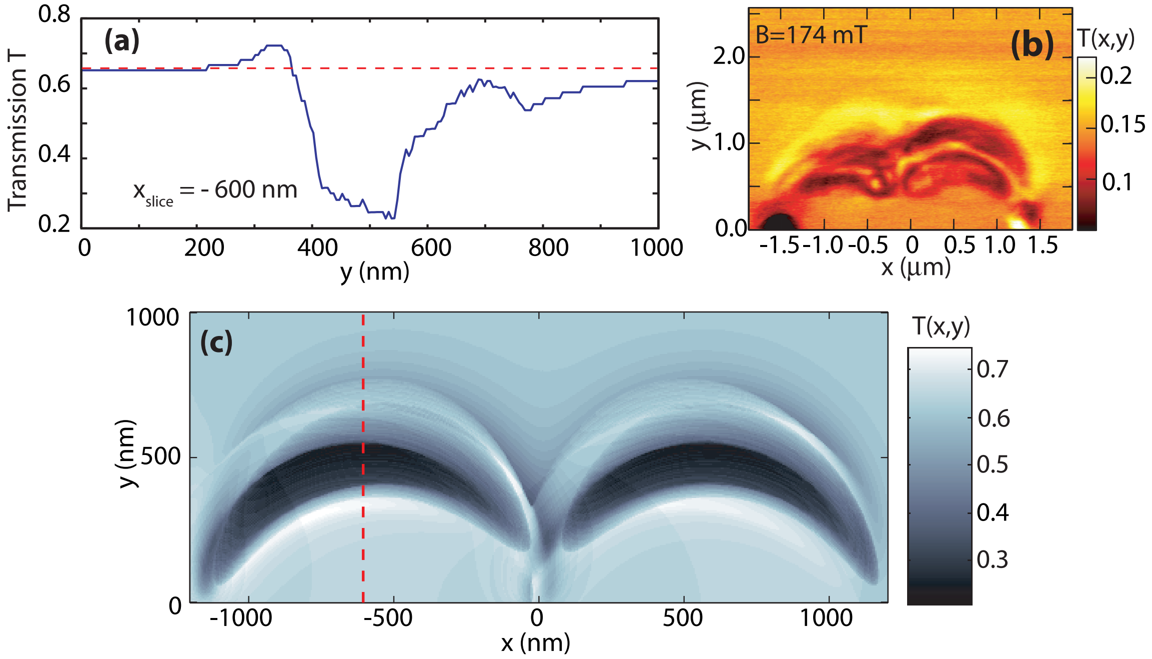

Figure 7.12: In (c) we present a classical tip scan of the magnetic focussing system with a tip $\eta = 0.2$ near the second focussing peak. The same structure is apparent as in the previous figure, but now doubled. In (a) we plot a slice of the transmission at $x = -600$ nm, as indicated by the dashed red line in (c). The tip scan reproduces surprisingly well the structures seen in the tip scan data with a high tip at the second focussing peak, $B = 174$ milliTesla, from Figure (7.3) and shown again in (b).

in quantum simulations in clean systems as well, when the conditions aren't right for fringing. In Figure (7.13) we show a number of quantum scan simulations with weak tips at varying fields. In all the cases fringes are not evident in the results, instead the tip scans appear very classical in nature. In (b) the same simulation in (a) has been done but with many open transverse modes in the QPCs, The result in this case is to amplify the signal, but the same classical structure is evident. In (c), which is far from the focussing peak, the only structure is an enhancement in transmission (which is nascently zero) when the tip is placed near the region where arcs from the QPCs meet. (d) shows the second focussing peak, which is remarkably similar to the classical simulation in Figure (7.12b).

7.6.2 Quantum Effects

Having become familiar with the classical effects of a finite size tip in the magnetic focussing system, we look into interference structures in the tip scans. Clearly such structures are not automatic, since we have yet to see them even in quantum data.

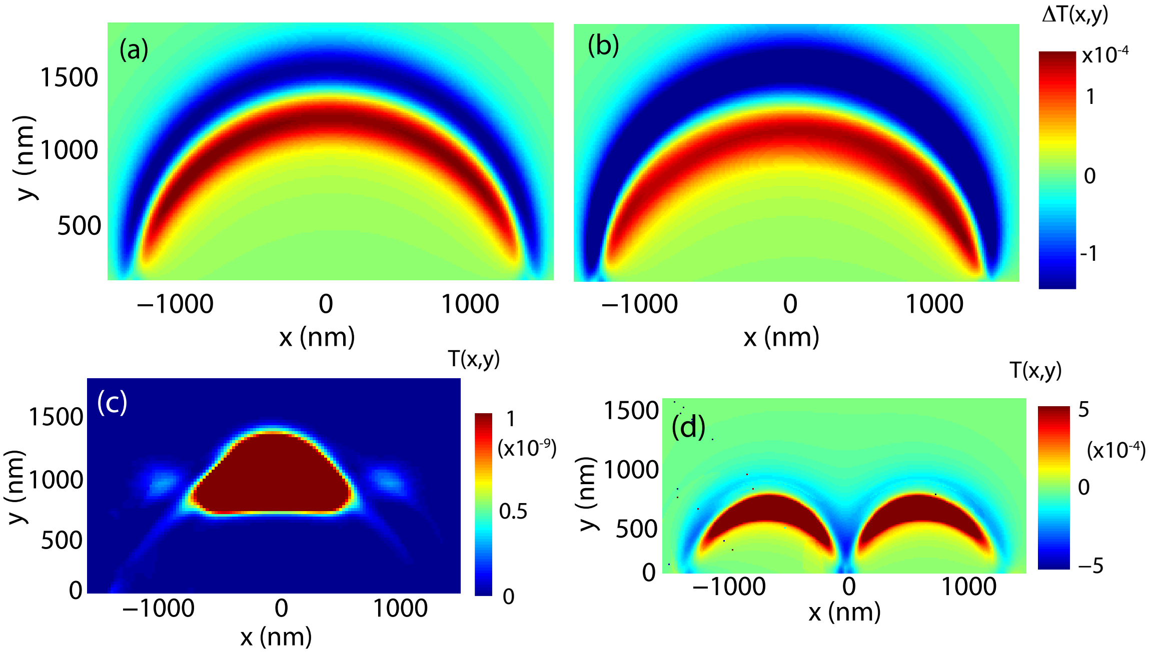

Figure 7.13: Quantum dynamics (wavepacket) tip scan simulation of the clean magnetic focussing configuration in a perpendicular magnetic field. Plotted is the change in transmission $\Delta T(x, y)$ due to the introduction of the tip. (a) is a full tip scan simulation of the system for a single open mode in the target QPC at the Fermi energy, while (b) is the same simulation but for many (> 5) open modes. The results have been thermally averaged. In these simulation, $E_F = 13.7$ meV, $T = 4$K, $B_z = 77$ milliTesla, so $r_c = 1327$ nm. The tip is Gaussian with peak height $V_o = 0.2E_F$, and width $2\sigma = 100$ nm. (c) is the same simulation, but with a magnetic field far from the focussing peak, $B = 60$ milliTesla, while (d) is at the second focussing peak, ~ 150 milliTesla.

To begin we examine some semiclassical tip scan simulations, on the first focussing peak using experimentally relevant values. The results are shown in Figure (7.14) for two different scattering profiles. On the left is a scattering profile for a forward scattering tip. This profile is taken from the results in Chapter (5), and corresponds to a tip with strength $\eta = 0.6$. The unphysical high signal at the edge of the classically allowed region is due to the caustics, and could be removed by standard uniformization techniques [112]. Near these caustics the fringing signal is high due to the amplitude oscillations in the free magnetic Green function, and seen in Figure (D.4). Because of the increase in amplitude near the caustics, the strength of this fringing is most likely unphysical, and these Green function fringes will most likely be small in more realistic systems. However there are fringe oscillations that follow the trajectory of the electrons across the sample, of the type seen experimentally. The fringes have a very large spacing in the center of the scan at a distance r_c from the wall. The fringe spanig becomes smaller, as does the amplitude, as the tip is brought closer to

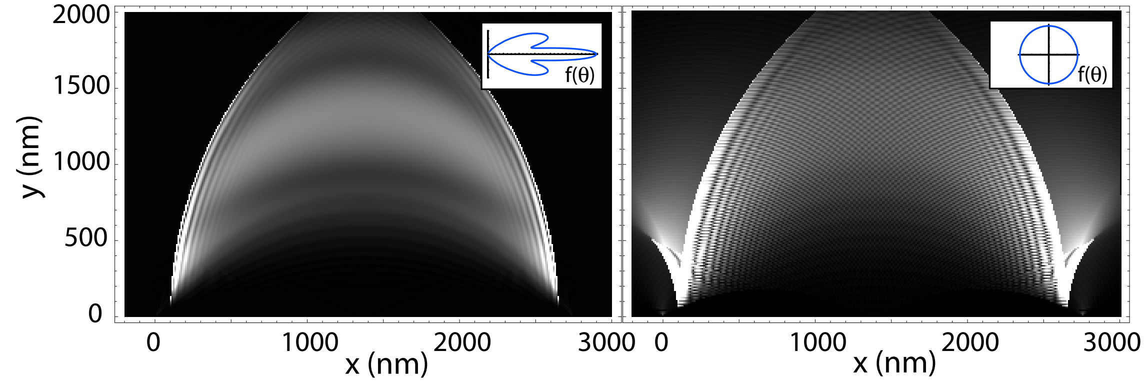

Figure 7.14: Semiclassical tip scans, $|G_B(\vec{r}_{tip})|^2$ for two different tip scattering functions. On the left is used a forward scattering function, equivalent to a $\eta = 0.6$ tip, while on the right is used an s-wave tip. The magnetic field $B = 77$ milliTesla and $E_F = 13.7$ meV.

the wall. These fringes are equivalent those worked out in Section (6.3f), depicted in Figure (6.3f).

In the right panel we present the same simulation, but with a uniform scattering amplitude. Most of the same fringing structure is present, but now with more oscillations. We can identify the high frequency horizontal oscillations as being due to trajectories that strike the tip, the wall, and then the tip again. These were worked out in Section (6.3g), and tend to have a spacing a little smaller than the backscattering spacing, $d < \lambda_F/2$. In addition we note that the amplitude beyond the central arc region is much higher in the uniform scattering case, due the scattering by the tip in all directions.

The scattering amplitude was taken to be "classical" in both cases, in that $f(\theta)$ was taken to be real, hence scattering angle dependent phase shifts were not considered. Note that these results are without thermal averaging, and with point QPCs, and so represent the finest clarity for the interference structure. A more realistic clean system will wash out some or all of the features.

In Figure (7.15) we examine a quantum dynamics (wavepacket) simulation of the clean system at $B = 77$ milliTesla, and at a energy $E_F = 13.7$ meV, given the experimental QPC spacing $L_{QPC} = 2750$ nm; the potential used in the rest of this Section, and in the quantum simulations in the previous Section, is shown in Figure (7.15a). The QPC walls are many multiples of the Fermi energy in height, and the QPCs admit just one mode when $E_F = 13.7$ meV. In Figure (7.15b-c) we perform a tip scan simulation at $B_z = 77$ milliTesla; the tip potential height is $\eta = 0.6$ and the tip potential is $2\sigma = 100$ nm across.

In the scan with no thermal averaging we again recover the caustic structures seen in classical simulations, but at 1.7 K this is mostly washed out. Interference structure is not in any obvious in these simulations, but closer inspection indicates that there is some signal. In Figure (7.15b),

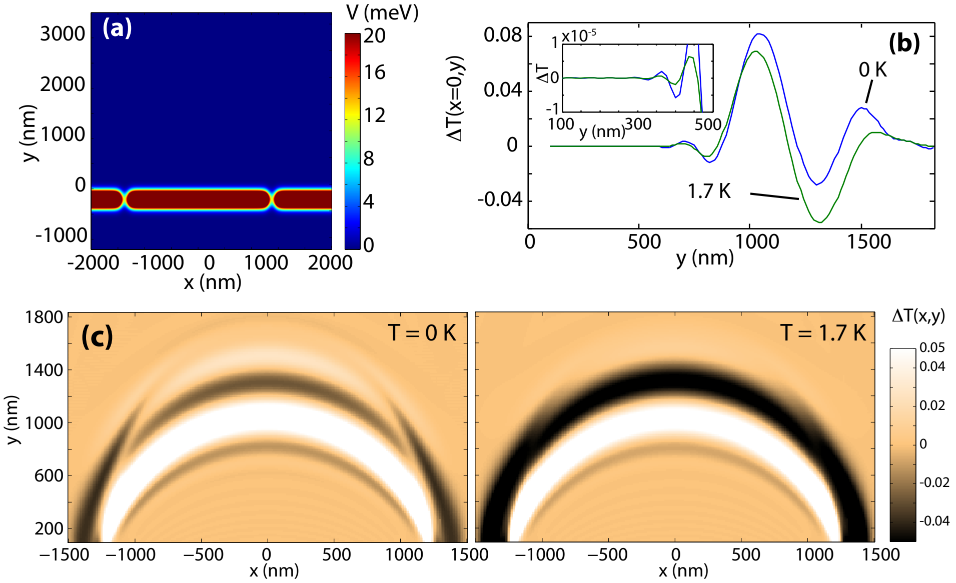

Figure 7.15: A quantum dynamics (wavepacket) tip scan simulation of the magnetic focussing configuration in a perpendicular magnetic field, $B_z = 77$ milliTesla, without a bumpy background potential. Plotted is the change in transmission $\Delta T(x, y)$ due to the introduction of the tip. (a) is the potential landscape used in the simulation; the source QPC is at lower left, the target at lower right. (b) is the tip scan results at $x = 0$ scanned in y. (c) depicts the full scan in (x, y) at the Fermi energy $E_F = 13.7$ meV, and thermally averaged at a temperature $T = 1.7$K. In this simulation, $r_c = 1327$ nm, and the tip is Gaussian with peak height $V_o = 0.6E_F$, and width $2\sigma = 100$ nm.

there are obvious oscillations in transmission due to classical effects, but there are oscillations that continue close to the wall beyond the range of classical effects. Assuming that the magnitude of the unperturbed wavefunction decreases monotonically toward the wall, there is no classical cause for these oscillations. The inset shows such oscillations continuing down to 300 nm from the wall, though quite attenuated. The oscillation spacing is ~ 200 nm, which with a Fermi wavelength of $\lambda_F = 40$ nm, implies a scattering angle from equation (6.8) in Chapter (6) of $2\sin^{-1}(1/10) \sim 11°$, a gentle deflection.

To understand whether these are fringes, and if so why so small, we need to better explore the parameter space of the tip strength. In the clean system for a single focussing peak, most of the structure can be understood by just considering a tip scan down the center of the sample. This is because, at the first focussing peak, the injection distribution mostly populates direct trajectories which don't bounce off the QPC wall, thus the tip scan is symmetric and reduced in complexity.

In Figure (7.16) we simulate central tip scans for a variety of tip heights, at the zero temperature and at a temperature of 1.7 K, and at a range of magnetic fields. For all magnetic

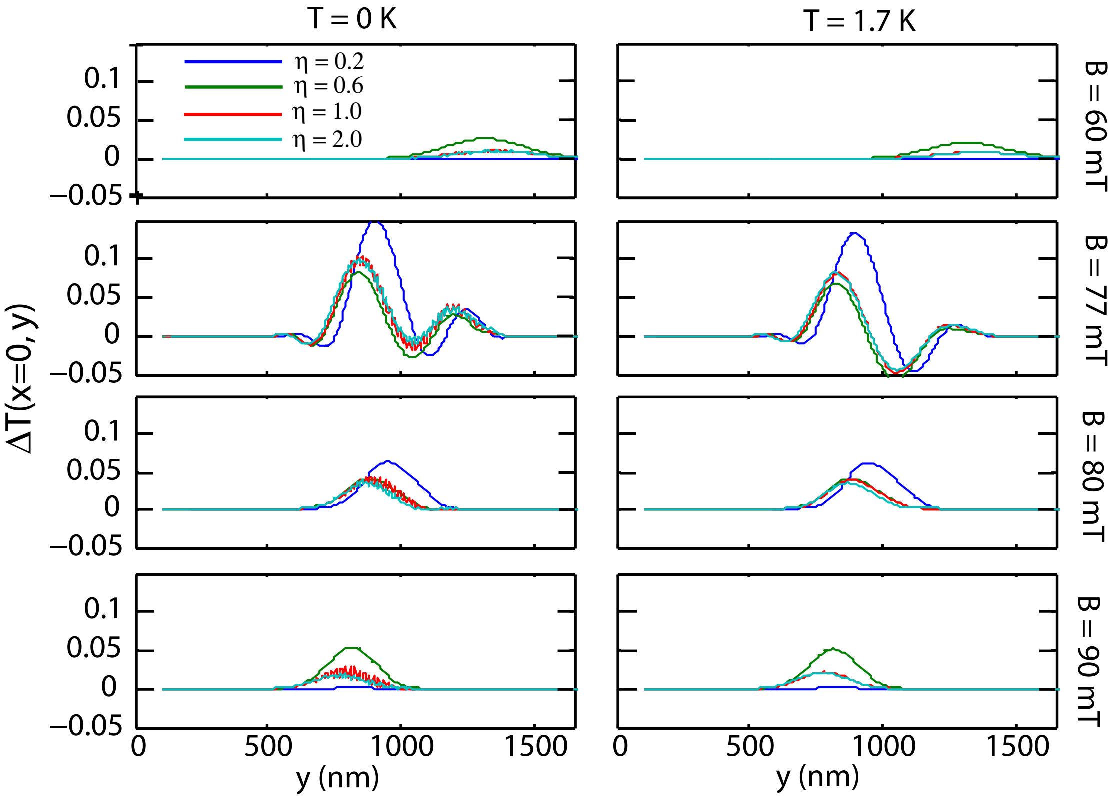

Figure 7.16: Tip scan simulations along the line of symmetry between the QPCs at a variety of tip potential heights and magnetic fields. Here $E_F = 13.7$ meV and the tip is Gaussian with width $2\sigma = 100$ nm as in previous figures.

fields, high frequency oscillations, of size $\lambda/2$, are visible for tip potentials that backscatter $\eta \geq 1$; however these oscillations diminish with thermal averaging. Of interest is that once a tip is strong enough to backscatter, then increasing the tip strength has little effect on the transmission. In the Figure, the data for $\eta = 1.0$ and $\eta = 2.0$ almost always lie on top of each other.

Of additional interest is that the response of the transmission to tip strength is not monotonic. For field values far from the focussing peaks, the highest transmission signal is at $\eta \sim 0.6$, while near the focussing peaks the transmission signal is largest for a very weak tip, $\eta \sim 0.2$. In neither case does a strong tip produce the strongest transmission signal; instead it produces in both cases a moderate signal. We may conclude that, more important than a large scattering cross section in the clean case, is the correct maximal scattering angle to accommodate the geometry. We hypothesize that the same holds at higher fields as well.

In Figure (7.17) we see a set of wavepacket tip scans where the tip height has been changed, and where the tip scan is kept at the Fermi energy or thermally at 1.7 K about the Fermi

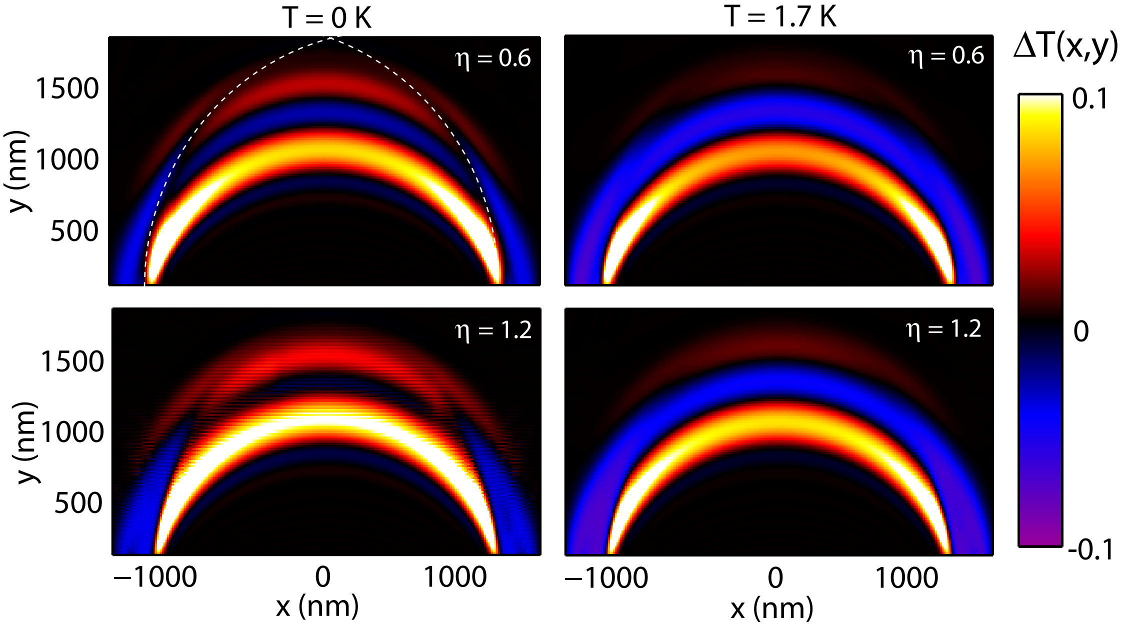

Figure 7.17: Tip scan simulations of the magnetic focussing configuration in a perpendicular magnetic field, $B_z = 77$ milliTesla, in a clean background. Plotted is the change in transmission $\Delta T(x, y)$ due to the introduction of the tip at $T = 0K$ and $T = 1.7K$, with two different tip potential heights, $\eta = 0.6$ and $\eta = 1.2$; black indicates no change in transmission. In the $T = 0$ K plots, the dotted lines indicate classical caustics; the slow oscillations along the y-axis are interference fringes. In the lower case, where $\eta = 1.2$, high frequency oscillations, of wavelength $< \lambda/2$, indicate interference effects due to the presence of the QPC wall. Thermal averaging effects remove a good deal of structure, including the caustics on either side, the higher frequency fringes, and diminish the strength of the long wavelength fringes. In this simulation, $r_c = 1327$ nm, the Fermi energy $E_F = 13.7$ meV, and the tip is Gaussian with width $2\sigma = 100$ nm.

energy. These scans are equivalent those in Figure (7.13a), but with stronger tip strength. At zero temperature the classical structure is clear, but is washed at higher temperature. For $\eta = 1.2$ at 0 K, there are horizontal fringes across the entire scan, all with nearly equal spacing, $d \sim 20$ nm. These are quickly washed out at 1.7 K. In addition at $\eta = 0.6$ there are much slower vertical oscillations that persist after thermal averaging, although they are noticeably fainter.

To understand the origin of the fringe structures, we need to examine the relevant flow and how the tip affects it. In Figure (7.18) we show the classical manifolds for three different tip strengths at three different points along the center line of the scans. For a tip of strength $\eta = 0.2$, the tip serves to obscure the target, reducing the transmission classically, but also serves to create two distinct bundles of trajectories above and below the tip position. While these two bundles of trajectories will have different phases on average, and hence interfere, the rate of change of the

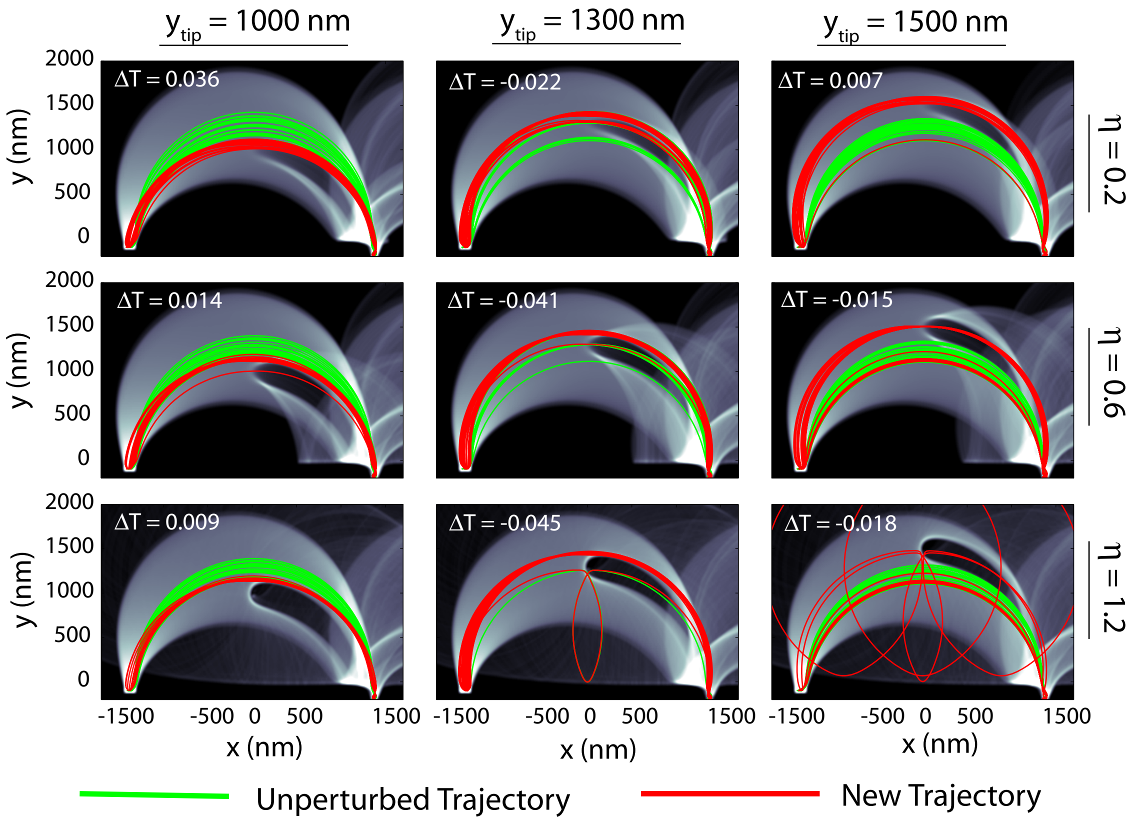

Figure 7.18: Classical trajectories in the same system as Figure (7.17), with a tip introduced at a variety of tip strengths and position along the central axis. This shows how the natively transmitted trajectories are disturbed by the tip, and how the tip creates new paths to the target QPC.

phase difference will be slow as the tip moves along the y-axis. Thus the fringe spacing will be large. Alternatively, we can consider the small angle deflection, in particular in the case at $y = 1500$ nm. Such a gentle deflection will lead to fringes that are too widely spaced to discern.

For the $\eta = 0.6$ case the same holds true, except that the stronger tip can separate trajectories more effectively, or alternatively can deflect into greater angles. The resulting fringe spacing is somewhat shorter, but not remarkable. In the $\eta = 1.2$ case, the strong tip can deflect into completely new paths, in particular into lenticular paths that bounce off the wall. These paths are the source of the horizontal fringes in the tip scan. In this sense the strong tip is imaging the wall instead of the electron momentum. From Chapter (6), Section (6.3g), these fringes should have a spacing $d \approx 0.7 \times \frac{\lambda_F}{2} \sim 15$ nm at one cyclotron radius from the wall.

7.6.3 Clean System Conclusions

From studying tip scans in clean systems, we have learned some counter-intuitive things about the effect of the tip on the transmission. The classical effect of the tip on the transmission has two main roles: one is to obstruct the nascent flow of electrons, reducing the transmission, and the other is to redirect into the target QPC flow that would have otherwise missed, increasing the transmission. In addition, because of the caustics that the tip generates and the caustic structures inherent to the classical flow, a finite-sized tip potential can resolve features that are much smaller than it is, even when deflecting and not backscattering flow. However, the precise location of the features is not usually clear from the scans, relative to the tip center.

Fringes are not necessarily present for $\eta < 1.0$; instead the geometry of the problem plays a role. New paths created by a weak deflection tip must intersect the target QPC for there to be a clear fringe signal. For the most part this means that the caustics shed by the tip must intersect the wall near the target QPC. For strong tips $\eta > 1.0$, fine scale fringes are present throughout the data, but they are usually washed away by thermal averaging.

The response of the system to the tip as its strength η is changed is non-monotonic, and near the first focussing peak, a very weak tip can show the largest response. This effect is again due to the finite size of the tip, and of the anisotropic scattering pattern of the flow off the tip.

In the clean case, fringes can be fairly evanescent and in most configurations just a small signal. However, in the bumpy case, the flow becomes much more complicated, and the distribution of trajectories more ergodic nature. The tip is more likely to have available a path to the target QPC to scatter into. Counter to intuition, as we increase the bumpy disorder in the system, the more likely we are to see clean and clear interference fringes somewhere in the scan region.

7.7 Simulations of a Bumpy System

In a realistic sample, the electron flux is non-uniform; due to the presence of the donor layer in our heterostructure, the electron moves over a smooth disordered potential landscape. The typical magnitude of this background is $V_{rms} = 0.05 - 0.1\ E_F$, and typical correlation length $l_{corr} = 40$ nm $\sim \lambda_F$. The small-angle scattering of the electron due to this smooth background potential produces caustic branches [100], where the density becomes very large classically. In the presence of a moderate magnetic field, such that the magnetic length $a_H =\equiv \sqrt{\hbar/m\omega_c} \gg l_{corr}$, classical branching due to the formation of caustics continues; this is depicted in Figure (7.19) for a case with a particularly strong branch, and in the lower panel of Figure (7.7).

One can imagine that as a magnetic field is applied, the branches bend over in the magnetic

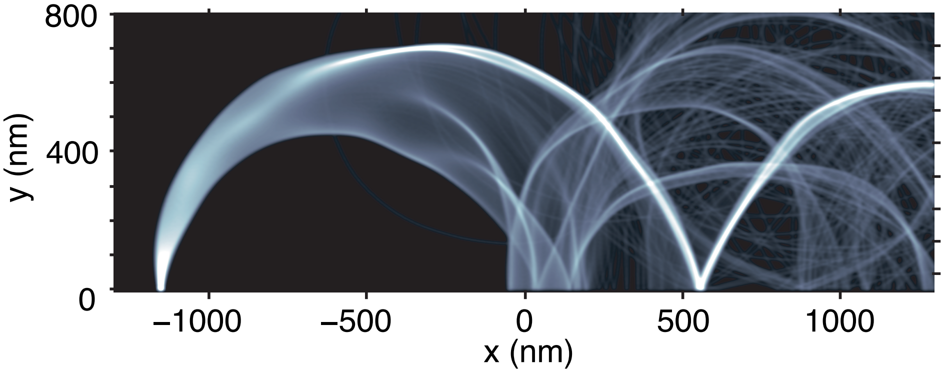

Figure 7.19: Branched caustics in a magnetic field. An electron trajectory manifold, injected from the target QPC at $x = -1350$ nm, is propagated through a random Gaussian background potential in a magnetic field of strength $B \sim 150$ milliTesla. The caustic branches develop even in the presence of a significant magnetic field, creating in particular a strong branch that bounces on the QPC wall at $x \sim 550$ nm. This indicates that transport in a magnetic field and bumpy background will be highly inhomogeneous, as in the $B = 0$ case.

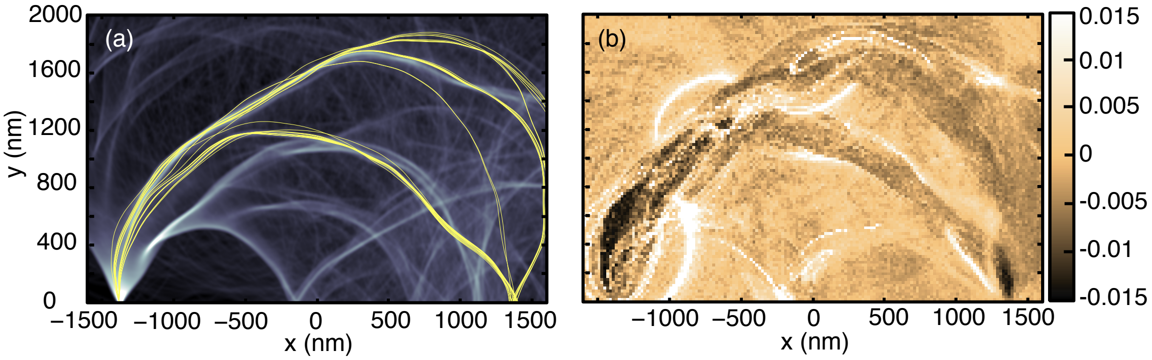

Figure 7.20: A bumpy classical tip scan simulation shown in (b), with the relevant transmitted nascent trajectories shown in yellow in (a), over top of an image of the nascent flow. The SPM tip resolves the nascent transmitted flow within about a half-tip width σ by diffusing the flow along the otherwise transmitting paths.

field and are swept across the collector QPC, causing the fluctuations in the measured transmission. In the presence of smooth disorder, the transmission in this system is mostly due to flux transported along specific branches in the flow; instead of being evenly distributed throughout the area, the flux “bundles” into the branches. This will create significant changes in the conductance as a function of B, as discussed in Section (7.5).

7.7.1 Classical Tip Effects in a Disordered System

This begs the question as to how this branched flow responds to the presence of a SPM tip, and how the transmission changes as a result of this response. In Figure (7.20b) we plot a classical tip scan with a just such a bumpy background potential. This is the same system as in the previous section, but now with a bumpy background. In this case, the bumpy background is a smooth random Gaussian distribution with correlation length $l_{corr} = 40$ nm and mean bump height $\sqrt{\langle V^2 \rangle} = 0.1 E_F$. What we see is the same type of pattern as in the clean classical case, where the are connected regions of reduced transmission, often bordered by narrow strips of enhancement. This is more remarkable, however, because even in the bumpy case, with a flow diffusing in momentum, the effect of the tip is once again to obstruct the nascently transmitted trajectories. Figure (7.20a) depicts a select, but dominant set of trajectories that are transmitted by the system with the tip absent; they are shown in yellow over top of an image of the nascent trajectory manifold. These "bundles" of trajectories carry enough flux through the target QPC in the undisturbed system, that by obstructing them even with a weak tip, there is a clear measurable change in the transmission.

This implies that a weak tip may be used to image nascent transmitted flow through a system. The diffusive effect that the tip has on the trajectories depopulates the region in phase space around the original trajectory. With a weak enough tip and a small enough system, these deflected trajectories will tend to strike the wall near the target QPC. Centered on these trajectories, the influence of the tip on nearby trajectories that would have missed the QPC is significantly less. The overall effect is to lower transmission.

Often bordering these channels of reduced transmission are highlighted strips, usually arc shaped. When the tip is placed over one of these regions, additional flux beyond the nascent flux is transmitted. In the bumpy case, these highlights are often located near nascent branch caustics that don't ordinarily carry transmitted flux. Placing the tip near these branches in these high flux regions allows some of the flux to be diverted along the nascent transmitting channel; even a small fraction of trajectories in this high flux region measurably increases the transmission.

7.7.2 Resolving Quantum from Classical Structure

In Figure (7.21a) we show a quantum tip scan simulation with a bumpy background. In this case a very weak tip $\eta = 0.2$ is used, and with thermal averaging at 4 K, fringe structure, if present, is not distinguishable from classical structure. However we assume that the overall structure is due to classical effects, since the familiar pattern of reduced transmission (in blue) bordered by an enhancement region (in red), in this case the flow, is visible. Figure (7.21b) depicts the same simulation but now with many open transverse modes in each QPC. One might conjecture that by

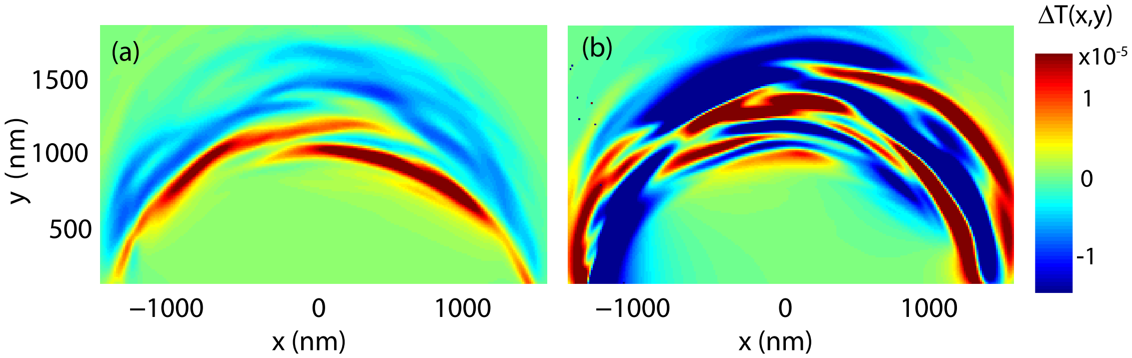

Figure 7.21: A quantum dynamics (wavepacket) tip scan simulation of the magnetic focussing configuration in a perpendicular magnetic field with a weak bumpy background potential. Plotted is the change in transmission $\Delta T(x,y)$ due to the introduction of the tip. (a) is a full tip scan simulation of the system for a single open mode in the target QPC at the Fermi energy, while (b) is the same simulation but for many (> 5) open modes. The results have been thermally averaged. In these simulation, $E_F = 13.7$ meV, $T = 4$K, $B_z = 77$ milliTesla, and so $r_c = 1370$ nm. The tip is Gaussian with peak height $\eta = 0.2$, and width $2\sigma = 100$ nm. The bumpy background potential has correlation length $l = 40$ nm and height $\sqrt{\langle V^2 \rangle} = 0.05 E_F$.

opening the QPCs, fringe structure would be reduced, since the flow occurs over many orthogonal modes, but that classical structure should persists even with many open modes. This would serve as a method to distinguish classical and quantum structure. However, the angular distribution is significantly widened as the QPCs are opened, in turn increasing the number and variety of classical allowed transmission paths. The upshot is that structure in the tip scan is significantly increased, without supplying a clear signal of the source of the structure, when using a weak tip to scan.

Another approach that proved unsuccessful was changing the value of $\hbar$ in the simulations. This could, in a simple enough system, have the effect of changing the spacing of the fringes by the factor $\tilde{\hbar}/\hbar$, where $\tilde{\hbar}$ is the new unphysical value of Planck's constant. Purely classical structure might remain unchanged. This approach, depicted in Figure (7.22), proved unfeasible in this system however. Changing $\hbar$ made a change in the relative phases of the wavefunction over a large enough region that it induced large scale modifications of the amplitude, not just on the scale of a wavelength. As such, the classical structure was not cleanly resolvable by this approach.

A potential alternative approach [49] may be to use the derivative in the signal, $\frac{\partial T}{\partial \hbar}$, to measure the "quantumness" of the signal. One would expect that the structures due mostly to quantum effects to vary linearly in $\hbar$, while classical structures should vary at higher orders. Thus using the difference between simulations at $\tilde{\hbar} = \hbar(1 \pm \epsilon)$ could provide a numerical derivative that could be used to discern classical from quantum structures.

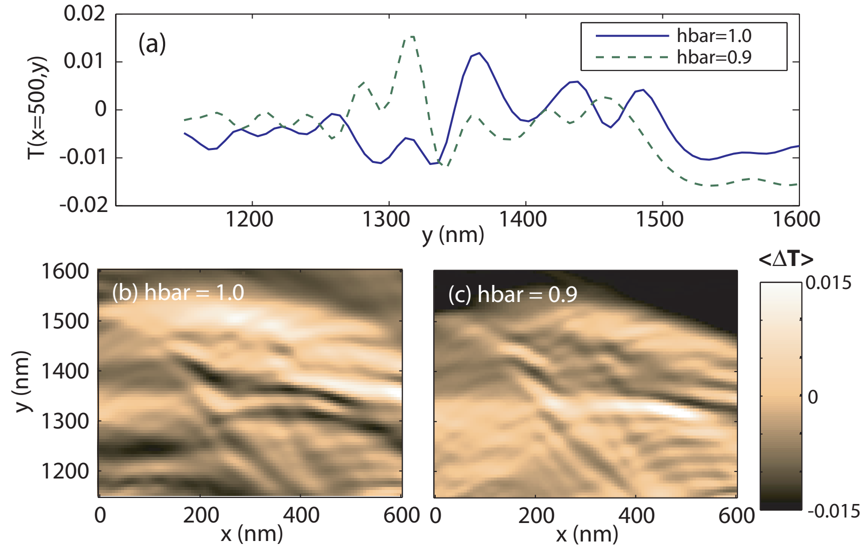

Figure 7.22: Tip scan simulations with a backscattering tip $\eta = 1.0$ and varying $\hbar$ numerically, in an attempt to distinguish fringe from classical structure. (a) is a slice through the data at $x = 500$ nm.

7.7.3 Effect of Tip Strength

While seemingly not possible to extract purely classical from quantum features directly, we can recall that the minimum size of the fringe structure depends on the maximum scattering angle from the tip, and that the scattering angle in turn depends on the tip strength. Thus by using a series of tip scans, we can progressively increase the fringe signal in the data, and at least qualitatively separate quantum from classical structures.

In Figure (7.23) we present such a tip strength series for the entire region of interest. The bumpy background is the same as used in the classical simulation in Figure (7.20), and the parameters of the system are the same as used in the clean wavepacket simulations in Section (7.6). For the weak tip, we recover a very similar result to that of the classical tip scan simulation in Figure (7.11): the weak tip has resolved what appears to be the nascent transmitted classical flow. We can further ask what are the transmitted trajectories in the system, and how does this match the tip scan. In Figures (7.24) and (7.29) we plot every classical trajectory transmitted through the target QPC using the same potential landscape as in the quantum simulation, superimposed over the quantum tip scan data. Clearly the weak tip scan has resolved the nascent transmitted trajectory “bundles” which have the highest density, and hence transmit the most flux. The gentle deflection of the tip, never more than 10°, is able to resolve with remarkable resolution the nascent flow. In this data, the flow is resolved to within a half-tip width, or 50 nm on average. In addition, the familiar enhancement

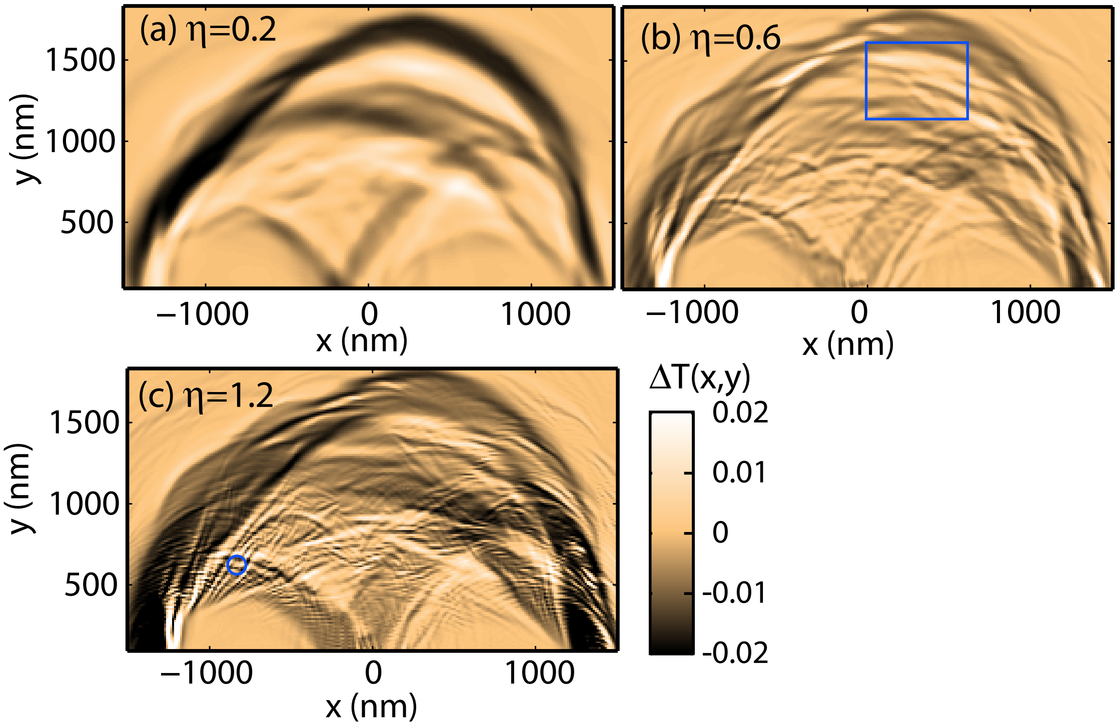

Figure 7.23: A series of tip scan simulations on the bumpy background with the tip strength η varied. The fringe structure grows more assertive in the scans with increasing tip strength, while the large scale "classical" structure becomes less well-defined. The box on the $\eta = 0.6$ scan indicates the region scanned in Figure (7.25), while the circle on the $\eta = 1.2$ scan indicates the tip position used in Figure (7.26).

is often present at borders of the flux bundles. The flux mapping breaks down when the tip acts to both obstruct and enhance flow, as is the case between the two main channels of trajectories.

With increasing tip strength η, the tip scans in Figure (7.23) also show finer features in the system, fringe structures that tend to follow the paths of the nascent flow. We note however that the amplitude of the change in transmission away from the QPCs does not increase with increasing tip strength: the strongest variations in T at the top of the arc occur at $\eta = 0.2$. At $\eta = 1.2$ the tip can backscatter, so we know that the fringes may have spacing as small as $d = \lambda_F/2$. At $\eta = 0.6$ the maximum fringe spacing is more like $d \sim 2\lambda_F = 80$ nm, while the weak tip has spacing that is indistinguishable from classical structures.

In Figure (7.25) we show a tip scan series in a small region of the system at a variety of tip strengths from backscattering to strongly attractive. At both attractive and repulsive weak potential strengths $\eta = \pm 0.2$, the features are clearly large scale. As the tip strength is increased,

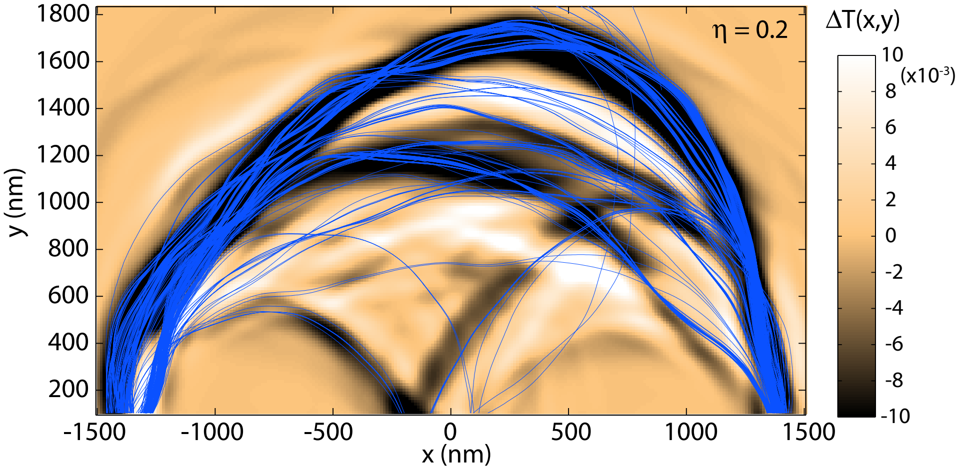

Figure 7.24: Classical trajectories on the bumpy background potential, with no tip present, superimposed on the $\eta = 0.2$ tip scan data. The weak tip scan clearly maps out the main trajectory "bundles" from the source to the target QPC. See also Figure (7.29) for a 3D rendering.

finer interference features are induced, until at backscattering and beyond the features resolve to about the wavelength. At backscattering, the finest possible fringes are $\lambda_F/2$, but this will only occur when backscattering will significantly contribute the the flow, i.e. near the QPCs. Further out from the walls, the relevant scattering angles are on the order of $\theta_{sc} \sim \pi/3$, such that the fringe spacings are $\sim \lambda_F$. As we've seen before. the relevant scattering angle depends on the geometry. In the previous cases, that was $\theta_{sc} = \pi$, but near the first focussing peak the angle is smaller.

While the weak tip scan can inform us about the nascent transmitted classical flow, the fringes obseved tell us about the scattering process with the tip, since their spacing can be converted into a scattering angle and a line parallel to the fringes can be thought of as following a "wall" off of which the trajectories bounce. Furthermore, if we already know the incoming angle θ_o from the weak tip scan, as well as the angle of the fringing ϕ, then we can conclude that the scattering angle is $\theta_{sc} = 2|\phi - \theta_o|$. The fringe spacing plus this information can be used to measure the wavelength and hence momentum of the scattered electrons,

$$\lambda_F = 2d \sin|\phi - \theta_o|. \tag{7.7}$$

This can be used as an independent measure of wavelength in a sample, and also as a sanity check on the accuracy of the fringe equation.

In Figure (7.26a,c) we show the nascent transmitted trajectories and the trajectory manifold, and in (b) the effect of a strong tip $\eta = 1.2$ on the flow density, and on the trajectories in (d). The tip position is the same as indicated on the scan in Figure (7.23c). The red trajectories indicate newly induced transmitted paths. In this case the tip been placed in a region of high flow density, but

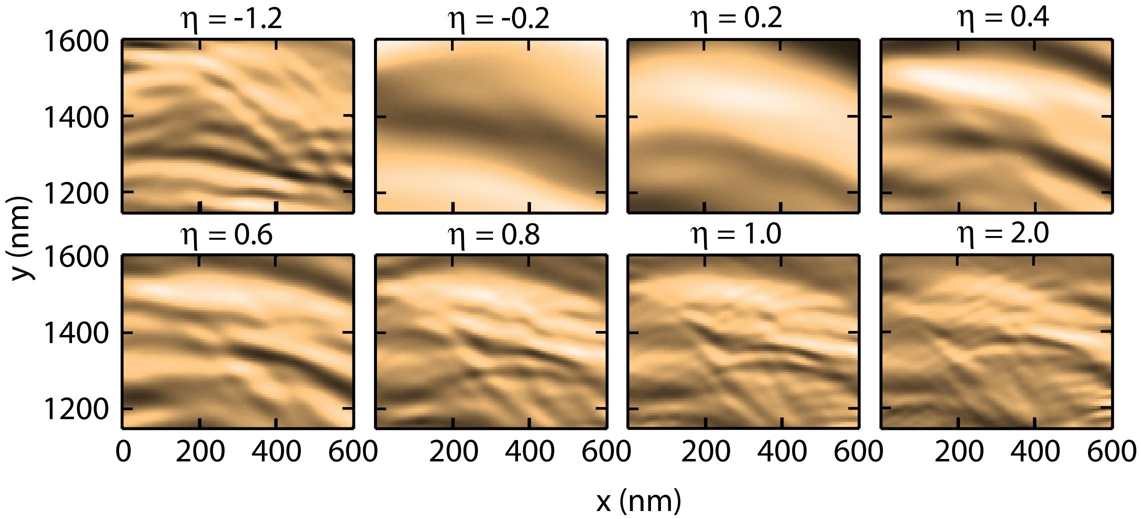

Figure 7.25: Wavepacket tip scan simulation of the magnetic focussing at a variety of tip strengths in a small region of Figure (7.23), indicated on the $\eta = 0.6$ scan by a box. The feature size changes significantly with tip strength up to $\eta = 1.0$.

where the flow will not actually transmit through the target QPC. By placing the tip in this region we have split the flow, and created new paths to the target. There are two main scattering processes here, one below with scattering angle $\theta_{sc} \sim \pi/3$, and one above with scattering angle $\theta_{sc} \sim \pi/4$, implying, with $\lambda_F = 40$ nm, a fringe spacing of $d = 40$ nm below and $d = 52$ nm above. Referring back to Figure (7.23), this is the consistent with the fringe patterns seen in the scan.

We note that for the weak attractive and repulsive cases $\eta \pm 0.2$, that the scans look almost shifted then inverted, with the local gradients in the transmission pointing in opposite directions. For weak scattering, the scattering angles are odd in the sign of η, such that $\eta \rightarrow -\eta$ implies that $\theta_{sc}(b) \rightarrow -\theta_{sc}(b)$. Suppose a weak repulsive tip $\eta > 0$ is placed at position $\vec{r}$, and deflects a single nascent transmitted trajectory out of the QPC. Then we place an attractive tip $\eta' = -\eta$ and looking for the same deflection of the trajectory, finding it at nearby position $\vec{r}'$. Then since the two tips deflect in opposite directions at the same impact parameter, we know that $|\vec{r} - \vec{r}'| = 2b$. Now suppose instead that the repulsive tip is brought to a distance b near a branch of trajectories and repulsively deflected the trajectories maximally into the target QPC, increasing the transmission. If the caustic branch were narrow enough, a weak repulsive tip would effect the same response in the transmission when placed at a distance b on the other side of the branch. Locally the gradients of the transmission would also have opposite directions as the tip was moved across the flow. This may be what is seen in Figure (7.25) for $\eta \pm 0.2$, and could potentially be used as differential measure of the local density of the flux.

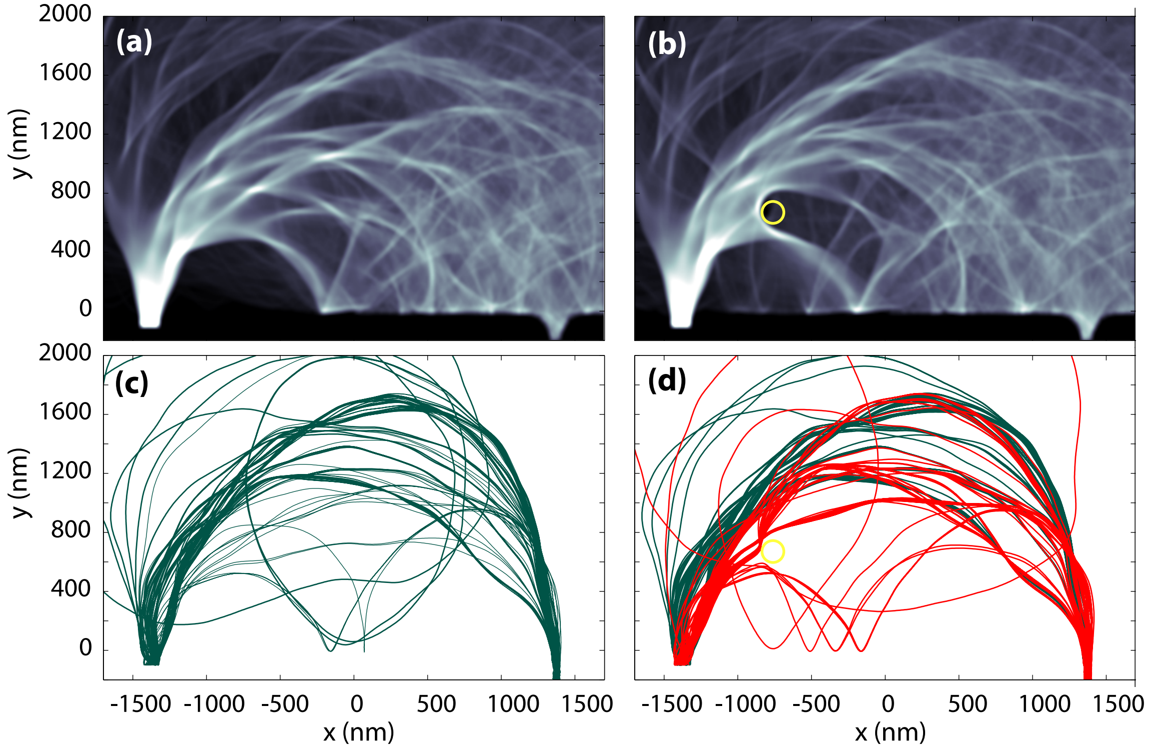

Figure 7.26: Classical trajectories on the bumpy background potential, with the exact same system as in Figure(7.23). In (a) we show the trajectory density with the tip absent, while in (b) the tip, with $\eta = 1.2$, is placed at $(-800, 650)$. In (c) we show the nascent transmitted trajectories in green, while in (d) we add the tip, removing some transmitted trajectories but also creating some new ones, shown in red.

Lastly we note that the strongly attractive case $\eta = -1.2$ produces fringe spacing on the order of those seen in the $\eta = 0.8$ scans, but not smaller. Clearly an attractive potential can't completely backscatter, since its scattering profile $\theta_{sc}(b)$ must have a maximum at some finite value $b > 0$. The fringes seen will decrease in spacing with a stronger attractive tip, but will do so at a different rate that the repulsive tip. One could use the typical fringe spacing for a repulsive and attractive tip with equal but opposite voltages to measure the scattering profile $\theta_{sc}(b)$ for each case. Coupled with a generic model of the tip potential, this could be used to create an empirical model of the tip scattering profile $\theta_{sc}(b)$ for the tip in the system. This could then be used as a calibration for measuring the flux in the system.

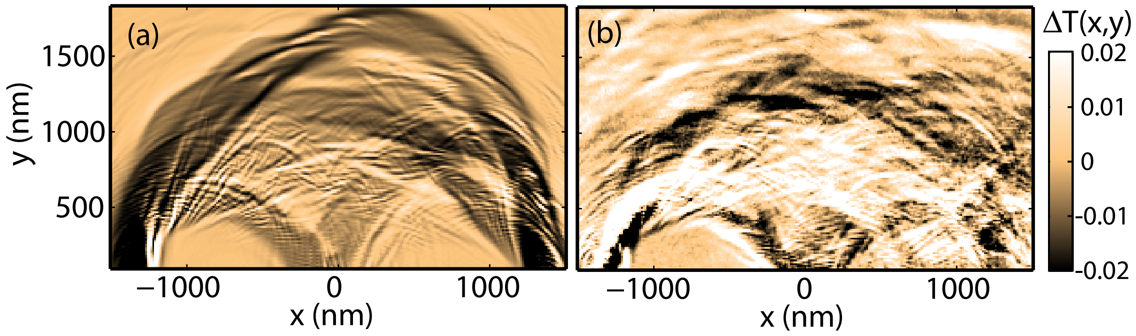

Figure 7.27: The tip scan simulation with $\eta = 1.2$ with one open transverse mode in each QPC (a), and with two open modes in each QPC (b). In (b) the fringes are still clearly present in some small isolated regions, but don't span the entire system as in (a).

7.7.4 Comparison With Experiment

An issue with comparing theory and experiment is that most of the simulations were performed with the QPCs open to at most one transverse mode, while the experiment was always run with at least three total transmitting modes in the system, and usually with two open transverse modes in each QPC. The effect of this will be to scramble the fringe structure, and perhaps to wash it out completely, leaving only a noisy signal of the classical flow. Since the experimental data does show fringing, to justify the simulations we must make sure that the results are consistent with experiment in this sense. In Figure (7.27) we compare the single moded QPC results from before, at $\eta = 1.2$, with the same tip scan simulations, but with the QPCs opened to two transverse modes each. The results look much noisier than the with single moded QPCs, and the angular range is much wider. But noticeably there are still regions in the scan where fringes are clearly apparent, but these regions are often fairly limited in size. This is typical of the fringes seen experimentally, and further justifies the simulation approach.

Finally we compare in Figure (7.28) the trend in fringe spacing with increasing tip strength in both theory and experiment. The strong similarity in fringe spacing at similar tip strengths η, and how the fringe spacing tends to go down with increasing tip strength, is striking. This is a strong indication that the fringe theory of Chapter (6) holds in moderate magnetic fields as well.

7.8 Conclusions

In this Chapter we have examined the issues involved with multi-terminal tip scan experiments in a magnetic field, and found that the mechanism that produces fringing in this case is

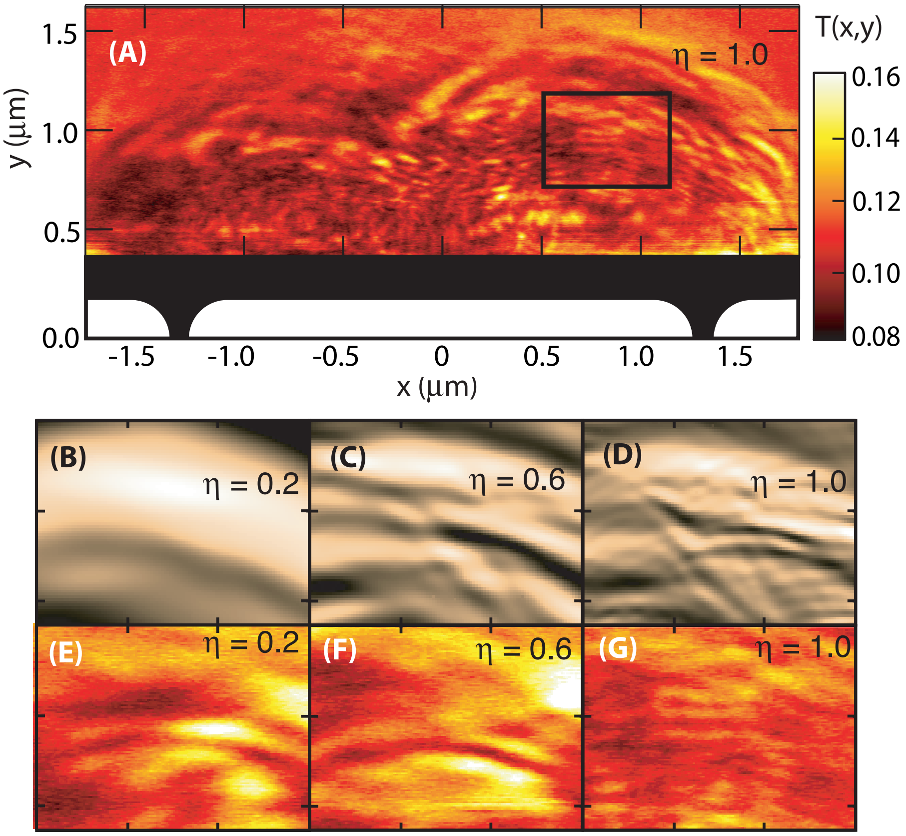

Figure 7.28: Experimental data compared to simulations showing a finer fringe structure with increasing tip strength. The simulation data is from Figure (7.25).

substantially different from previous tip scan experiments. The fact that the source and target QPCs are not colocated, and the presence of a moderate magnetic field have driven the need to consider the tip scattering process beyond backscattering. This in itself motivated the work in Chapters (5) and (6), with a significant result being the fringe equation (6.6), which relates the fringe pattern to the local properties of the scattering process.

We have developed classical, semiclassical, and quantum dynamics methods to simulate the tip scan process and to examine the flow of the electron in the system. The role of branching, seen in earlier works [101, 100, 103] continues to play a role in the determining the focussing peaks in the transmission as the magnetic fields is varies, $T(B)$. The classical caustics formed in the flow of electrons in a clean system give rise to the focussing peaks. In the bumpy disordered case the same holds true, but the branching of the electron flow splits and shifts the focussing peak into many smaller peaks in general, while at higher disorder the peaks cease to be discrete. At finite temperatures interference effects are negligible, and the structure of the focussing signal $T(B)$ is

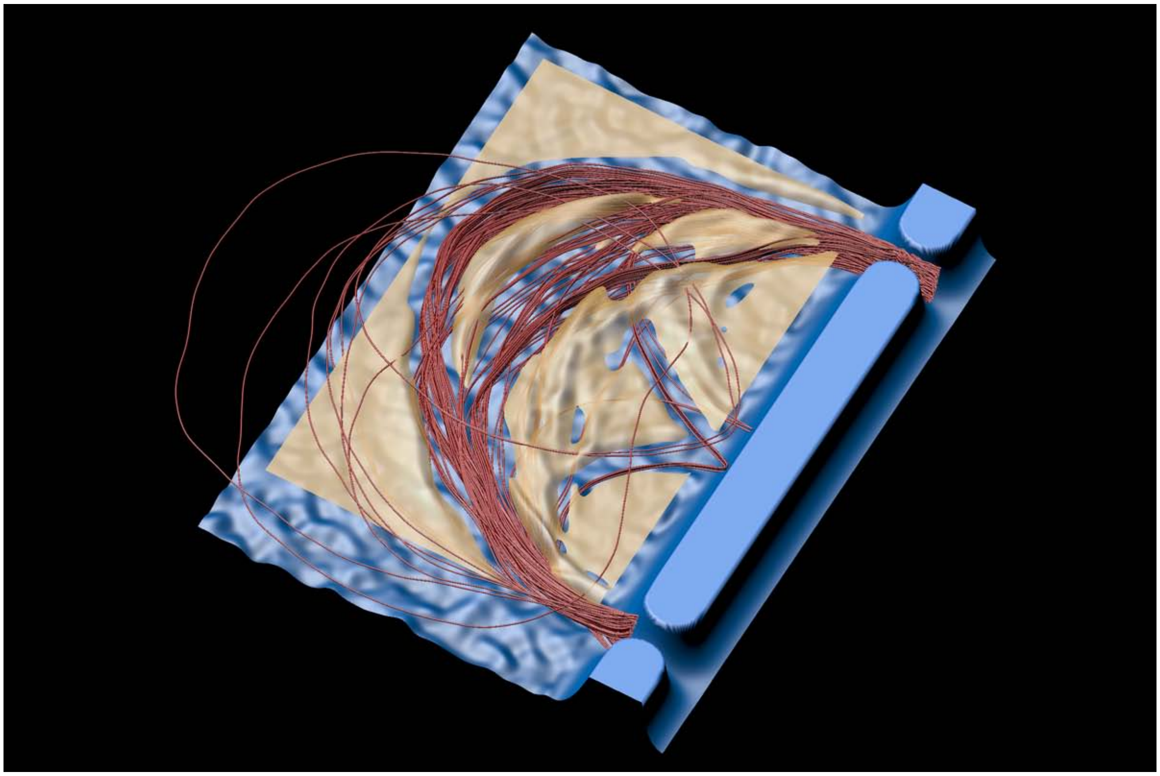

Figure 7.29: The weak tip scan (in tan) shown above the bumpy potential background (in blue), with the nascent transmitted trajectories. The tip scan has been clipped where its value $\Delta T < 0$, indicating regions where the tip obstructs the nascent transmitted flow.

determined mainly by classical processes.

The tip scan process in the system we've shown to be strongly dependent on the tip shape and strength. In particular, the signal in the transmission is highly non-monotoic in the tip strength η, for some cases the signal is highest for a very weak tip. In addition the transmission signal varies little once the tip backscatters, $\eta > 1$.

There are consistent classical signals in the tip scan system: as the tip passes over nascently transmitted flow, the transmission is reduced, while bordering these regions there are strips where the tip deflects more new flow into the QPC then obstructs it. These patterns are present in classical and quantum simulations. The scanning of a weak tip, attractive or repulsive, can use this effect to map the nascent transmitted flow in the system. It is important to point out the the tip will map transmitted flow only when used in this manner. This is different from the use of a backscattering tip to map the flow in two terminal systems at zero field [101, 100, 103].

Larger tip strengths will induce fringing, but in the clean system the fringing is often hard to discern from the classical signal and easily washed out by thermal averaging. However, the branching due to smooth disorder present in realistic systems tends focus the flow into “bundles” of transmitted trajectories. By “bundle” we mean a small continuous neighborhood of trajectories in phase space that remains nearby to a central trajectory over the course of the flow to the target QPC. While these bundles aren’t necessarily the caustic branches seen previously, they do form discrete regions in phase space of transmitted trajectories. This bundling enhances fringing; each trajectory in the bundle accumulates nearly the same phase as it propagates through the system, and as such discretizes the amplitude into “bundles” as well. If we parameterize trajectories by their initial angle α, then the nascent semiclassical amplitude at the target QPC may be approximated

$$A_o = C \int d\alpha A(\alpha) e^{i\phi(\alpha)} \approx C \sum_{\text{traj } j} A_j e^{i\phi_j} \tag{7.8}$$

where C is some constant, and where the sum is over the typical bundle trajectories j. Weak tips will diminish or remove one of the terms when placed over a bundle, lowering the transmission but not creating a tip position dependent interference effect (i.e fringe).

When a strong tip deflects flow into a new bundle (or bundles), this new discrete amplitude term is a function of tip position, $A'(\vec{r}_{tip})e^{i\phi(\vec{r}_{tip})}$. Varying the tip position will vary the phase of the bundle in accordance with the arguments in Chapter (6), where would we use the typical bundle trajectory, with the amplitude sum over nascent bundles serving as the background amplitude. The interference of the new bundle amplitude with the nascent amplitude produces the fringes we see. When these bundles happen to coincide, or nearly coincide with caustic branches, the response may be very large, and the fringe signal stronger than expected.

Lastly, we note that the use of varying tip strengths can also be used as a calibration for the systems. By measuring the range of fringes seen, one can empirically derive a typical scattering function $\theta_{sc}(b)$ and use this to understand the effective tip potential. One can use the knowledge of the flow direction from weak tip scattering, along with the fringe direction for stronger tips, to calculate the wavelength of the electron. Finally, it may be possible to use the differential signal of alternating weak attractive and repulsive tips to gain further information about the electron flow density from the tip scan data.

Appendix A

Atomic Units

Here we tabulate for convenient conversion factors for atomic units [76]. This is a table of physical constants in atomic units:

Physical constant	**Dimensionless value**
$\hbar$	1.0
Electron mass m_e	1.0
Bohr radius $a_B = \frac{\hbar^2}{m_e e^2}$	1.0
Fine structure constant $\alpha = \frac{e^2}{\hbar c}$	$0.007297351 \approx 1/137$
speed of light $c = \frac{e^2}{\hbar \alpha}$	137.036
Boltzmann's constant k	3.16666×10^{-6} (1/Kelvin)
Electrostatic constant k	1.0
Proton mass m_p	1836.1527557
Proton or positron charge	1.0
Lepton cyclotron period (@ 5.4 T)	2.73×10^5

Note that we use the unit of mass as the electron rest mass, and ignore the difference between that and the reduced mass, $\mu = 0.999456 m_e$.

Here is a table of conversion factors from atomic units to SI and CGS units:

Physical quantity	**Atomic to SI factor**	**Atomic to CGS factor**
time	2.41888×10^{-17} secs	2.41888×10^{-17} secs
length	$5.29177249 \times 10^{-11}$ m	$5.29177249 \times 10^{-9}$ cm
area	$2.80029 \times 10^{-21}\ m^2$	$2.80029 \times 10^{-17}\ cm^2$
volume	$1.48185 \times 10^{-31}\ m^3$	$1.48185 \times 10^{-25}\ cm^3$
speed	2.18769×10^{6} m/sec	2.18769×10^{8} cm/sec
momentum	$1.99285151 \times 10^{-24}$ kg m/sec	$1.99285151 \times 10^{-19}$ kg cm/sec
energy (Hartree)	$4.3597438 \times 10^{-18}$ J	$4.3597438 \times 10^{-11}$ ergs
electric potential	27.2113834 V	0.0907674 StatV
electric field	$5.14220624 \times 10^{11}$ V/m	5.14220624×10^{9} V/cm
magnetic field (B)	$2.350517349 \times 10^{5}$ T	$2.350517349 \times 10^{9}$ Gauss
magnetic dipole	$1.854801799 \times 10^{-23}$ J/T	$1.8548018 \times 10^{-19}$ erg/Gauss
charge	$1.6021773349 \times 10^{-19}$ C	$4.803206814 \times 10^{-10}$ ESU
mass	$0.9105953 \times 10^{-30}$ kg	$0.9105953 \times 10^{-27}$ g
action	$1.054571596 \times 10^{-34}$ J s	$1.054571596 \times 10^{-27}$ erg s

In addition, energy is converted as 1 Hartree $= 27.2116$ eV, which is twice the ground state energy of the hydrogen atom.

Appendix B

Integrable Motion in a Uniform Magnetic Field

Here we consider some basic cases of motion in a uniform magnetic field, and derive various relevant quantities. We also consider the systems in guiding center action-angle coordinates, which are usually the most appropriate coordinate systems in which to express the motion.

B.1 Charged Particle in a Uniform Magnetic Field

To begin we consider the general case of a particle moving in a potential and a uniform magnetic field. In the symmetric gauge, ($\vec{A} = \vec{B} \times \vec{r}/2$ or $A_\theta = rB/2$), the Hamiltonian for a system in a uniform $\vec{B} = B\hat{z}$ field is

$$H = \frac{1}{2m}(\vec{p} - \frac{q}{c}\vec{A})^2 + V(\vec{r}) = \frac{1}{2m}(\vec{p} + \frac{m\eta\omega_c}{2}\vec{r} \times \hat{z})^2 + V(\vec{r}) \tag{B.1}$$

where $\omega_c \equiv \frac{|qB|}{mc}$ is positive definite, and $\eta = qB/|qB|$, the sign of the product of the charge and magnetic field.

From Hamilton's equations of motion, $m\dot{\vec{r}} = \vec{p} + m\eta\omega_c\vec{r} \times \hat{z}/2$ and $\dot{\vec{p}} = \frac{m\omega_c}{2}\dot{\vec{r}} \times \hat{z} + q\vec{E}(\vec{r})$, the equation of motion for $\vec{r}$ is:

$$\ddot{\vec{r}} = \eta\omega_c\dot{\vec{r}} \times \hat{z} + \frac{q}{m}\vec{E}(\vec{r}, t). \tag{B.2}$$

When $\vec{E}$ vanishes this has a transverse solution that is completely circular, and the solution is trivial. With $v_{x,o} = -v\sin\delta_o$ and $v_{y,o} = v\cos\delta_o$, we find

$$\vec{r}(t) \quad = \quad \vec{r}_{center} + \eta r_c \left[\hat{x}[\cos(\eta\omega_c t + \delta_o) + \hat{y}\sin(\eta\omega_c t + \delta_o)\right]$$

$$\vec{v}(t) \;=\; \omega_c r_c[-\hat{x}\sin(\eta\omega_c t+\delta_o)+\hat{y}\cos(\eta\omega_c t+\delta_o)] \qquad \text{(B.3)}$$

where $r_c = |\vec{v}_\perp|/\omega_c$ is the cyclotron radius, and $\vec{r}_{center}$ is the center of the circle of motion. The canonical momentum is

$$\begin{aligned}\vec{p} &= m\vec{v}+q\vec{A}/c = m\vec{v}-\frac{m\eta\omega_c}{2}\vec{r}\times\hat{z}\\ &= \frac{m}{2}\vec{v}-\frac{m\eta\omega_c}{2}\vec{r}_o\times\hat{z}\end{aligned} \qquad \text{(B.4)}$$

when only a uniform magnetic field $\vec{B}$ and no other fields present. Thus the canonical momentum depends on the initial position; in particular it depends on the initial position with respect to the center of the gauge (which we've taken to be the origin here).

We can calculate the action $S(q,q';E)$ from the definition ([45, 12]),

$$\begin{aligned}S(q_o,q';E) &= \int_{q_o}^{q'}\vec{p}\cdot d\vec{q}\\ &= m\int_{q_o}^{q'}\vec{v}\cdot d\vec{q}-\frac{m\eta\omega_c}{2}\int_{q_o}^{q'}(\vec{r}\times\hat{z})\cdot d\vec{q}.\end{aligned} \qquad \text{(B.5)}$$

by considering the angle covered by the motion, and counting the number of complete cycles. The first term depends only on the relative distance covered, $|\vec{r}'-\vec{r}_o|$, while the second term depends on the gauge, and hence on the absolute initial and final position. The first integral, being position independent, can be shifted and rotated to simplify the calculation, and evaluates to

$$m\int_{q_o}^{q'}\vec{v}\cdot d\vec{q} = \frac{\eta 2E}{\omega_c}\left[\xi\sqrt{1-\xi^2}+\sin^{-1}\xi\right] \qquad \text{(B.6)}$$

where $\xi \equiv |\vec{r}'-\vec{r}_o|/2r_c$. The second term becomes $m\eta\omega_c(x'y_o-x_oy')/2$, so that the full action is

$$S(q_o,q';E) = \frac{2\pi n_{cyc}E}{\omega_c}+\frac{\eta 2E}{\omega_c}\left[\xi\sqrt{1-\xi^2}+\sin^{-1}\xi\right]+\frac{m\eta\omega_c}{2}(x'y_o-x_oy') \qquad \text{(B.7)}$$

where we note that $\xi=\xi(|\vec{r}'-\vec{r}_o|,E)$. Note that for a complete cycle, $\xi=|\vec{r}'-\vec{r}_o|/2r_c=0$, and the action becomes simply $S(q,q;E)=\frac{2\pi n_{cyc}E}{\omega_c}$ with no position dependence.

The time of travel, $T=\frac{\partial S}{\partial E}$ can be seen to be the total cumulative angle, divided by the cyclotron frequency; taking the derivative, and noting that the angle subtended by an arc on radius r_c who endpoints are $\vec{r}_o$ and $(\vec{r}'$ is $\Delta\theta = 2\sin^{-1}|\vec{r}'-\vec{r}_o|/2r_c$, then we can identify the time of travel as $T=\frac{1}{\omega_c}(2\pi n_{cyc}+\Delta\theta)$. (Note also that there is a $\Delta\theta=\pi-2\sin^{-1}|\vec{r}'-\vec{r}_o|/2r_c$ solution as well, when $\pi<\Delta\theta<2\pi$). Thus the total time of travel is the total angle accumulated by the motion, divided by the angular frequency, the expected result $T=(\theta'-\theta_o)/\omega_c$.

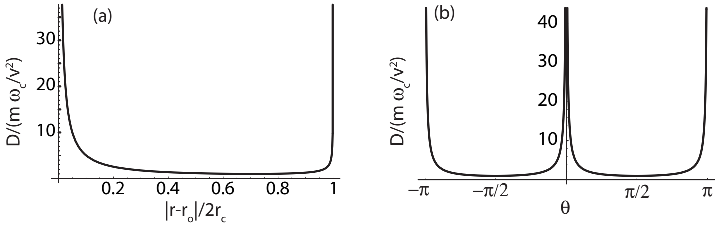

Figure B.1: Classical density on the energy surface for a free particle in a magnetic field. In (a) we plot the scaled density versus the distance traveled, while in (b) we plot the density as a function of the angle accumulated. In both cases we see divergences, indicative of caustics, at the origin and extremum of the motion.

It is also useful to consider the classical density, which is derived from the action $S(q,q';E)$ as [45, 12]

$$D(q,q';E) = -\begin{vmatrix} \frac{\partial^2 S}{\partial q_i \partial q'_j} & \frac{\partial^2 S}{\partial q_i \partial E} \\ \frac{\partial^2 S}{\partial q'_i \partial E} & \frac{\partial^2 S}{\partial E \partial E} \end{vmatrix} = -\begin{vmatrix} \frac{\partial^2 S}{\partial x \partial x'} & \frac{\partial^2 S}{\partial x \partial y'} & \frac{\partial^2 S}{\partial x \partial E} \\ \frac{\partial^2 S}{\partial y \partial x'} & \frac{\partial^2 S}{\partial y \partial y'} & \frac{\partial^2 S}{\partial y \partial E} \\ \frac{\partial^2 S}{\partial E \partial x'} & \frac{\partial^2 S}{\partial E \partial y'} & \frac{\partial^2 S}{\partial E \partial E} \end{vmatrix} \tag{B.8}$$

in two-dimensions. Performing the appropriate derivatives, we find the result

$$D(q,q';E) = \frac{m\omega_c}{v^2}|\csc\theta| = \frac{m\omega_c}{2v^2}\frac{1}{\xi\sqrt{1-\xi^2}} \tag{B.9}$$

where θ is the total angle accumulated, and ξ is defined as above. Note that while the action itself was position dependent, the classical density depends only on the relative distance travelled. When the classical density diverges, the system has a classical caustic at that point. Here, the density diverges when $\xi = 0$ or $\xi = 1$, implying caustics at the starting point $\vec{r}_o$ and at the furthest classical accessible distance $2r_c$ from the starting point. The classical density is plotted in Figure (B.1), versus the relative distance covered, and the angle subtended.

B.2 Rotating Frame

When $V = V(\rho, z)$ is cylindrically symmetric, we can use polar coordinates to solve the system. The symmetric gauge in polar coordinates for axial $\vec{B}$ is $\vec{A} = \frac{\rho B}{2}\hat{\theta}$, with Hamiltonian

$$H = \frac{p_z^2}{2m} + \frac{p_r^2}{2m} + \frac{1}{2m\rho^2}\left(p_\theta - \frac{m\eta\omega_c\rho^2}{2}\right)^2 + V(\rho,z); \tag{B.10}$$

note here that the p_θ is the canonical angular momentum, conjugate to θ in the presence of a magnetic field, and not the kinetic angular momentum $mr^2\dot{\theta}$.

The generating function to change to a frame rotating at frequency ω is

$$F_2(\vec{p}', \vec{q}) = p'_r r + p'_z z + p'_\theta(\theta - \omega t). \tag{B.11}$$

For generating function $F_2(\vec{p}', \vec{q})$, the transformation equations are $p_i = \frac{\partial F_2}{\partial q_i}$ and $q'_i = \frac{\partial F_2}{\partial p'_i}$ and $H' = H + \frac{\partial F_2}{\partial t}$. With this generating function, one finds that the canonical momenta are unchanged, the new angular position is $\theta' = \theta - \omega t$, and the Hamiltonian in the rotating frame is $H_R(\omega) = H - \omega p_\theta$. This reflects the cost in energy to "spin up" the system to the new rotating frame. When the potential is cylindrically symmetric, the total canonical angular momentum is conserved by a rotation about the center of the potential.

Noting that $p_\theta = L_z = m v_\theta \rho + \frac{m\eta\omega_c}{2}\rho^2$ in the lab frame, the rotating frame Hamiltonian reads

$$H_R(\omega) = \frac{p_z^2}{2m} + \frac{p_r^2}{2m} + \frac{1}{2m\rho^2}\left(p_\theta - \frac{m(2\omega + \eta\omega_c)}{2}\rho^2\right)^2 + V(\rho, z) - \frac{m\omega(\omega + \eta\omega_c)}{2}\rho^2 \tag{B.12}$$

From this Hamiltonian, it is clear that if we choose a frame rotating at $\omega = -\eta\omega_c/2$, we can remove the apparent magnetic field from the Hamiltonian. This choice is essentially choosing a rotating frame where the Coriolis force balances the magnetic force; in this frame, $m\vec{v}' = \vec{p}$. We are left with an extra harmonic potential, the magnetic confining term,

$$H_R(-\eta\omega_c/2) = \frac{\vec{p}^2}{2m} + V(\rho, z) + \frac{m\omega_c^2\rho^2}{8}. \tag{B.13}$$

If we can ignore the radial part of the external potential $V(z)$, the transverse solutions are simple motion in a 2D harmonic potential.

B.3 Trivial Action-angle coordinates ($\vec{E} = 0$)

In the case of $\vec{E} = 0$, and uniform axial $\vec{B}$, the cyclotron motion is completely cyclic, implying that a change to action-angle coordinates is warranted. We will ignore the decoupled axial motion. The cyclotron action J_c is

$$\begin{aligned} J_c &= \frac{1}{2\pi}\oint \vec{p}\cdot d\vec{q} \\ &= \frac{1}{2}m\omega_c r_c^2 \end{aligned} \tag{B.14}$$

Note that the action is the same as the angular momentum of the motion perpendicular to the plane of the motion, $L = |\vec{r} \times \vec{p}| = J_c$, that this is proportional to the energy in the cyclotron motion, $E = J_c\omega_c$, and that J_c is proportional to the square of the cyclotron radius, $r_c^2 = \frac{2J_c}{m\omega_c}$. This indicates that the cyclotron action will provide a useful measure of the energy stored in the cyclotron motion.

The canonical transformation to these coordinates is

$$\begin{aligned} x &= \alpha\sqrt{2J_c}\cos\theta_c \\ y &= \alpha\sqrt{2J_c}\sin\theta_c \\ p_x &= -\frac{1}{2\alpha}\sqrt{2J_c}\sin\theta_c \\ p_y &= \frac{1}{2\alpha}\sqrt{2J_c}\cos\theta_c \end{aligned} \tag{B.15}$$

where $\alpha \equiv 1/\sqrt{m\eta\omega_c}$. In these coordinates, the Hamiltonian is trivial, as are the equations of motion:

$$\begin{aligned} H &= \omega_c J_c \\ \frac{dJ_c}{dt} &= 0 \\ \frac{d\theta_c}{dt} &= \omega_c. \end{aligned} \tag{B.16}$$

Note that if the rotation is clockwise, so that $\eta = -1$, then α is imaginary.

B.4 Guiding Center Action-Angle Coordinates

For general transverse coordinates where the fast motion is dominated by the cyclotron cycle, it makes sense to separate the fast cyclotron motion from the slow, guiding center motion. Define guiding center coordinates as [43]

$$\begin{aligned} X &= x - \alpha\sqrt{2J_c}\cos\theta_c \\ Y &= y - \alpha\sqrt{2J_c}\sin\theta_c, \end{aligned} \tag{B.17}$$

where we attempt to separate the fast cyclotron motion from the average movement of the particle. The action angle coordinates provide two variable (J_c, θ_c), while in Cartesian coordinates we have 4 transverse variables, (x, y, p_x, p_y). Thus we need two more variables (P, Q) in the canonical transform. A natural variable to choose is the X position of the guiding center, $Q \equiv X$; however, this leads to an asymmetric transform. Instead we choose $Q \equiv X/\alpha$, where $\alpha \equiv 1/\sqrt{m\eta\omega_c}$ as before. Then we require that this new position coordinate Q is independent of the action-angle coordinates. This is tantamount to demanding that the guiding center position X is independent of the cyclotron motion, and thus that the Poisson relations $\{Q, J_c\} = \{Q, \theta_c\} = 0$ holds. This requirement leads to the conclusion that the Y coordinate of the guiding center acts like a canonical momentum, $P = Y/\alpha$. The full canonical transform reads

$$x = \alpha\left(Q + \sqrt{2J_c}\cos\theta_c\right)$$

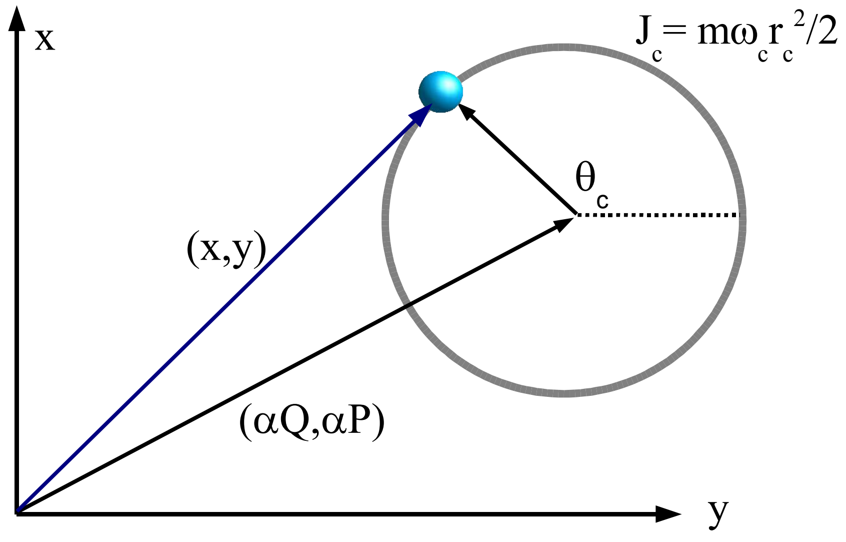

Figure B.2: Action-angle coordinates useful for describing particle dynamics when the cyclotron motion is dominant.

$$\begin{aligned} y &= \alpha\left(P+\sqrt{2J_c}\sin\theta_c\right) \\ p_x &= \frac{1}{2\alpha}\left(P-\sqrt{2J_c}\sin\theta_c\right) \\ p_y &= \frac{1}{2\alpha}\left(-Q+\sqrt{2J_c}\cos\theta_c\right). \end{aligned} \tag{B.18}$$

Note the factor of one half in the canonical momenta $p_{x,y}$ from above. The inverse transform is

$$\begin{aligned} Q &= \frac{1}{2\alpha}(x-2\alpha^2 p_y) \\ P &= \frac{1}{2\alpha}(y+2\alpha^2 p_x) \\ J_c &= \frac{1}{8\alpha^2}\left[(x+2\alpha^2 p_y)^2+(y-2\alpha^2 p_x)^2\right] \\ \theta_c &= \tan^{-1}\left(\frac{y-2\alpha^2 p_x}{x+2\alpha^2 p_y}\right). \end{aligned} \tag{B.19}$$

The full Hamiltonian in these transformed coordinates is

$$H(Q,\theta_c,z;P,J_c,p_z) = \frac{p_z^2}{2m} + J_c\eta\omega_c + V(Q,\theta_c,z;P,J_c) \tag{B.20}$$

and equations of motion

$$\begin{aligned} \dot{Q} &= \frac{dV}{dP} \\ \dot{\theta}_c &= \eta\omega_c + \frac{dV}{dJ_c} \end{aligned}$$

$$\begin{aligned}
\dot{z} &= \frac{p_z}{m} \\
\dot{P} &= -\frac{dV}{dQ} \\
\dot{J}_c &= -\frac{dV}{d\theta_c} \\
\dot{p_z} &= -\frac{dV}{dz}
\end{aligned} \tag{B.21}$$

In these new coordinates, the transverse kinetic energy is wrapped up in the cyclotron motion, $\eta\omega_c J_c$, and the motion of the guiding center itself does not appear as a kinetic energy term. Also, the transformation is such that if $\eta = -1$, then both the guiding center coordinates become imaginary, but the action and angle coordinates remain real; the action J_c takes on the sign of η.

B.5 Free Motion in Guiding Center Coordinates

We consider again the trivial case of transverse with no external potentials, hence

$$H(Q, \theta_c, z; P, J_c, p_z) = J_c \eta \omega_c \tag{B.22}$$

so that the equations of motion read $\dot{J}_c = \dot{P} = \dot{Q} = 0$ and $\dot{\theta}_c = \eta\omega_c$. While the equations of motion are trivial, the position dependence of the canonical momenta implies that the action is not so simple. The total transverse action $S(q, q'; E)$ is the integral over the momenta, with respect to the coordinates,

$$S(q, q'; E) \equiv \int_{\theta}^{\theta'} J_c(\theta) d\theta + \int_{Q}^{Q'} P(Q) dQ. \tag{B.23}$$

In the case of free motion in a uniform magnetic field, $V(Q, \theta_c, P, J_c) = 0$, then from the equations of motion there is no action accumulated in the guiding center motion, and the action is simply $S(q, q'; E) = \frac{E}{\omega_c}(\theta' - \theta) = ET$, where T is the time of motion. Clearly this describes free motion in the angle coordinate; the derivative $\frac{dS}{dE} = T$ is clearly the time of travel.

The system is integrable with two ignorable coordinates. The standard expression for the classical density is singular in this case, and of no use. However, from the equations of motion we know that $Q' = Q_o$ and $\theta' = \theta_o + \eta\omega_c T$. Hence the time dependent density is simply

$$D(q_o, q'; t) = \delta(\theta' - \theta_o - \eta\omega_c T)\delta(Q' - Q_o). \tag{B.24}$$

A Fourier transform to energy space yields a uniform distribution in energy,

$$D(q_o, q'; E) = \frac{1}{2\pi}\delta(Q' - Q_o). \tag{B.25}$$

B.6 Uniform Electric Field: Drift Velocity

As a next step up in complexity, we apply a constant electric field $(E_x, E_y, 0)$ by adding a potential $V(\vec{r}) = -q\vec{E}\cdot\vec{r}$, and no other fields beside the uniform magnetic field. Then the tranverse Hamiltonian in canonical guiding center coordinates is

$$H_\perp = J_c\eta\omega_c - q\alpha E_x(Q + \sqrt{2J_c}\cos\theta_c) - q\alpha E_y(P + \sqrt{2J_c}\sin\theta_c); \tag{B.26}$$

the axial motion remains decoupled. The equations of motion yield a simple solution for the guiding center coordinates,

$$\begin{aligned} \dot{Q} &= -\alpha q E_y \\ \dot{P} &= \alpha q E_x \end{aligned} \tag{B.27}$$

so that the actual guiding center coordinates move with a constant drify velocity (and recalling that $\alpha = 1/\sqrt{m\eta\omega_c} = 1/\sqrt{qB/c}$),

$$\begin{aligned} \vec{X}_\perp &= \frac{c\vec{E}\times\vec{B}}{B^2}t + \vec{X}_{\perp,o} \\ &= \vec{v}_D t + \vec{X}_{\perp,o} \end{aligned} \tag{B.28}$$

which is devoid of the fast cyclotron oscillation. We've defined here the drift velocity

$$\vec{v}_D \equiv \frac{c\vec{E}\times\vec{B}}{B^2}. \tag{B.29}$$

Meanwhile, the action and angle are oscillating rapidly about their average values. Without loss of generality, we will consider the case where $E_x = 0$, so that P is a constant of the motion (in general some combination of Q and P is constant of the motion); this is just a rotation in space to align the y direction with the electric field direction. Then the equations of motion yield

$$\begin{aligned} \frac{d}{dt}\sqrt{J_c} &= \frac{\alpha q E_y}{\sqrt{2}}\cos\theta_c \\ \frac{d\theta_c}{dt} &= \eta\omega_c - \frac{\alpha q E_y}{\sqrt{2J_c}}\sin\theta_c \end{aligned} \tag{B.30}$$

By conservation of energy, we can solve for $\sin\theta_c$ in terms of energy values and J_c.

B.7 Harmonic Potential

We now turn to cylindrically symmetric potentials. Starting with the simplest case, we consider a harmonic potential. The motion in such a system is completely integrable, and may serve as a starting point for an expansion for other transversely symmetric potentials (i.e. Coulomb).

We denote the potential in terms of frequencies $\omega_x = \sqrt{k_x/m}$,

$$V(\vec{r}) = \frac{1}{2}m\omega_z^2 z^2 + \frac{1}{2}m\omega_r^2(x^2+y^2). \tag{B.31}$$

Here we've written it for an attractive potential. If we're in an Penning trap, where the potential is repulsive in the transverse direction, we just replace every occurence of ω_r^2 by $-\omega_r^2$ (i.e. make ω_r imaginary). We also note that in an ideal Penning trap, $\omega_z = \sqrt{2}\omega_r$, but here we consider the more general case.

The axial motion is completely decoupled, and in this potential is just simple harmonic motion, so we consider only the transverse coordinates. We can further simplify the system by considering a rotating frame of reference where the resulting effective potential terms just cancel the external harmonic potential (not the magnetic force, as we did earlier). From before, the harmonic effective potential term, in a frame rotating at ω, is $V_R(\rho) = -m\omega(\omega+\eta\omega_c)\rho^2/2$, so that the total apparent harmonic potential which we want to vanish is

$$V(\rho) = \frac{m\rho^2}{2}\left(\omega_r^2 - \omega(\omega+\eta\omega_c)\right) \tag{B.32}$$

This effective harmonic potential will vanish when we rotate at a frequency $\omega = -\omega_m$ which solves this; thus this “magnetron” frequency [13] is

$$\omega_m \equiv -\frac{\eta}{2}\left[\sqrt{\omega_c^2 + 4\omega_r^2} - \omega_c\right]. \tag{B.33}$$

Note that for an attractive potential, the magnetron and cyclotron frequencies are of opposite sign, while for a repulsive potential the signs are the same. Rewriting the transverse Hamiltonian in polar coordinates rotating at the magnetron frequency, we have only a kinetic energy term left,

$$H_{\perp,m} = \frac{1}{2m}\left(\vec{p} - \frac{m\eta\tilde{\omega}_c}{2}\rho\hat{\theta}\right)^2 \tag{B.34}$$

where in the rotating frame the cyclotron frequency is $\tilde{\omega}_c = \sqrt{\omega_c^2 + 4\omega_r^2}$ and $\tilde{\eta} = \eta$. The frequencies are interrelated, so that $\omega_m = \eta(\omega_c - \tilde{\omega}_c)/2$ and $\tilde{\omega}_c = \omega_c - 2\eta\omega_m$.

In the magnetron frame, the change to action-angle variables is trivial, with $\tilde{\theta}_c$ a cyclic coordinate, so that

$$H_{\perp,m}(\tilde{\theta}_c, \tilde{J}_c, \tilde{Q}, \tilde{P}) = \eta\tilde{\omega}_c\tilde{J}_c \tag{B.35}$$

with the guiding center coordinates $(\tilde{Q}, \tilde{P})$ cyclic as well (here our tilde indicates the magnetron frame).

Now the question arises as to how this system looks in the lab frame. The generating function

$$F_2(J_c, \tilde{\theta}_c, P, \tilde{Q}) = J_c(\tilde{\theta}_c + \omega_m t) - \frac{1}{2}(\tilde{Q}^2 + P^2)\tan(\omega_m t) + P\tilde{Q}\sec(\omega_m t) \tag{B.36}$$

preserves the action, and hence the canonical angular momentum, but generates a rotation $-\omega_m$ back to the lab frame:

$$\begin{aligned} Q &= \tilde{Q}\cos\omega_m t - \tilde{P}\sin\omega_m t \\ P &= \tilde{Q}\sin\omega_m t + \tilde{P}\cos\omega_m t \\ J_c &= \tilde{J}_c \\ \theta_c &= \tilde{\theta}_c + \omega_m t. \end{aligned} \tag{B.37}$$

The associated Hamiltonian in the lab frame is then

$$H = H_m + \frac{\partial F_2}{\partial t} = (\eta\tilde{\omega}_c + \omega_m)J_c + \frac{\omega_m}{2}(P^2 + Q^2) \tag{B.38}$$

We can clearly use action-action variables for the guiding center motion as well,

$$\begin{aligned} Q &= \sqrt{2J_m}\cos\theta_m \\ P &= \sqrt{2J_m}\sin\theta_m \end{aligned} \tag{B.39}$$

where the magnetron action is related to the radius of the magnetron orbit by

$$\sqrt{\frac{2J_m}{m\omega_m}} = r_m \tag{B.40}$$

where the constant parameter ω_m is the magnetron frequency. The Hamiltonian is now completely reduced,

$$H = (\eta\tilde{\omega}_c + \omega_m)J_c + \omega_m J_m. \tag{B.41}$$

In this form, the motion is completely separable, and we note that the problem is clearly identical to that of a two-dimensional harmonic oscillator.

The classical density is not derivable from the action $S(q_o, q; E)$ in the standard way, but we can instead utilize the time independence of the equations of motion to write the classical density as

$$D(q_o, q; t) = \delta\left[\Delta\theta_c - (\eta\tilde{\omega}_c + \omega_m)t\right] \quad \delta\left[\Delta\theta_m - \omega_m t\right]. \tag{B.42}$$

We can rewrite this as a delta function related the angular displacements, and one involving time; taking the Fourier transform, we find

$$D(q_o, q; E) = \frac{1}{2\pi}\delta\left(\Delta\theta_c - \frac{\eta\tilde{\omega}_c + \omega_m}{\omega_m}\Delta\theta_m\right). \tag{B.43}$$

The system has uniform probability to be in any state, as long as the displacement in angles obeys a certain ratio.

The coordinates in the lab frame transform back to be

$$\begin{aligned} x &= \alpha\left(\sqrt{2J_m}\cos\theta_m + \sqrt{2J_c}\cos\theta_c\right) \\ y &= \alpha\left(\sqrt{2J_m}\sin\theta_m + \sqrt{2J_c}\sin\theta_c\right). \\ p_x &= \frac{1}{2\alpha}\left(\sqrt{2J_m}\sin\theta_m - \sqrt{2J_c}\sin\theta_c\right) \\ p_y &= \frac{1}{2\alpha}\left(-\sqrt{2J_m}\cos\theta_m + \sqrt{2J_c}\cos\theta_c\right) \\ \rho &= \alpha\sqrt{2(J_c+J_m) + 4\sqrt{J_cJ_m}\cos(\theta_c-\theta_m)}. \end{aligned} \tag{B.44}$$

with full inverse transformation

$$\begin{aligned} J_m &= \frac{1}{8\alpha^2}\left[\left(y+2\alpha^2p_x\right)^2 + \left(x-2\alpha^2p_y\right)^2\right] \\ \tan\theta_m &= \frac{y+2\alpha^2p_x}{x-2\alpha^2p_y} \\ J_c &= \frac{1}{8\alpha^2}\left[\left(y-2\alpha^2p_x\right)^2 + \left(x+2\alpha^2p_y\right)^2\right] \\ \tan\theta_c &= \frac{y-2\alpha^2p_x}{x+2\alpha^2p_y}. \end{aligned} \tag{B.45}$$

In this case $\alpha \equiv 1/\sqrt{m\eta\tilde{\omega}_c}$.

Transforming back from the action-angle representation, we get Hamiltonian rotated back from the magnetron frame by $\omega = -\omega_m$,

$$H = \frac{p_r^2}{2m} + \frac{1}{2m\rho^2}\left(p_\theta - \frac{m(\omega_c - 2\omega_m)}{2}\rho^2\right)^2 + \frac{m\omega_m(\omega_c-\omega_m)}{2}\rho^2 \tag{B.46}$$

The cyclotron action, and hence the angular momentum in the cyclotron action, is conserved by the transformation back to the lab frame, $J_c = \tilde{J}_c$. In addition, in the trivial magnetron frame we know that the cyclotron radius $\tilde{r}_c$ remains related to the cycltron action as $\tilde{r}_c = \sqrt{\frac{2J_c}{m\eta\tilde{\omega_c}}}$. Thus the cyclotron radius in the magnetron frame $\tilde{r}_c$ remains dependent on $\eta\tilde{\omega}_c$, and hence on ω_r, even when the magnetic field B is held fixed. Since a rotation preserves radial length, the range of ρ values that the orbiting particle covers will remain the same in all rotating frames; hence this range of values is $\Delta\rho = 2\tilde{r}_c$. This implies that the cyclotron radius in the lab frame, defined as $r_c \equiv |\vec{v}_\perp|/\omega_c$, is not a good indicator of the particle motion, since the effects of the radial field and the guiding center motion are not taken into account.

If we neglect the radial potential and write $r_c = \sqrt{\frac{2J_c}{m\eta\omega c}}$, we can derive the ratio between the potential-free and magnetron cyclotron radii as

$$\frac{\tilde{r}_c}{r_c} = \sqrt{\frac{\omega_c}{\tilde{\omega}_c}} = [1 \pm 4(\frac{\omega_r}{\omega_c})^2]^{-\frac{1}{4}}, \tag{B.47}$$

where again plus is for attractive, minus for repulsive potentials.

An important point to note here is that by identifying the magnetron frame, we identify a natural set of action-angle coordinates to use to describe the cyclotron motion. Using these coordinates as a basis, we transform back into the lab frame, and identify the action-angle coordinates that describe the guiding center motion directly. The resulting Hamiltonian is not one which would be written down immediately; however, it identifies correctly the contribution to cyclotron and magnetron energies due to each action.

In the case of a harmonic potential, the individual actions are each conserved separately, and hence the guiding center approximation is exact. Thus the harmonic case serves as a starting point for approximations to other more general cylindrically symmetric potentials.

Appendix C

The Guiding Center Approximation

Here we consider how to perform a guiding center approximation (GCA) in the Hamiltonian dynamics. Normally, the guiding center approximation is performed by separating out the faster and slow motion of a particle in a magnetic field, and time averaging over the fast cyclotron motion to derive an equation of motion for the guiding center of the particle [66, 82]. While this procedure is fairly straightforward and is easy to integrate numerically, it has the drawback that the resulting equations of motion are not derived from a Hamiltonian, and are not symplectic. It also is fairly difficult to perform an expansion to higher order in the guiding center approximation.

The approach that follows, which is not completely novel [43] but rarely used, identifies clearly the adiabatic invariants in the problem, and is readily amenable to classical perturbation theory. We consider the Hamiltonian guiding center approximation mainly in the context of motion in cylindrically symmetric potentials and uniform magnetic fields. Ultimately we examine the case of a Coulomb well, and the "guiding center atom."

C.1 Non-Hamiltonian Formulation of GCA

Traditionally [66, 82] the guiding center approximation is the assumption that the kinetic energy of the cyclotron motion is an adiabatic invariant of a particle moving in a strong magnetic field, taken to be uniform here. The fast motion of the particle about the center of the cyclotron motion, the "'guiding center"', is taken to be so fast that the position of the particle may be replaced by the the averaged, guiding center value. After subtracting out the fast cyclotron motion, an expansion in small velocity leads to equations of motion for the particle (here upper case indicates guiding center values),

$$\vec{v}_D \equiv \vec{V} \quad = \quad \frac{c\vec{E} \times \vec{B}}{|B|^2}$$

$$\begin{aligned} \vec{\delta v}(t) &= r_c\omega_c(-\hat{x}\sin\omega_c t + \hat{y}\cos\omega_c t) \\ v_z &= p_Z/m \\ \dot{p}_z &= -\frac{\partial V}{\partial z} \end{aligned} \tag{C.1}$$

where the position of the particle is taken to be $\vec{r} = \vec{R} + \delta\vec{r}$. The guiding center approximation is essentially the expansion of the guiding center position $\vec{r} - \delta\vec{r}$.

The fact that this formulation of the guiding center approximation doesn't conserve energy can be easily illustrated by an example. Consider the completely transverse potential

$$V(x,y) = \frac{1}{2}\left[\left(\frac{x}{a}\right)^2 + \left(\frac{y}{b}\right)^2\right]$$

in a strong magnetic field, and a particle that begins at $(x,y) = (a,0)$. The electric field is hence $\vec{E} = -(x/a^2, y/b^2)$. Then the initial energy, including the cyclotron kinetic energy, the drift kinetic energy $mv_D^2/2$, and the potential energy is clearly

$$E_i = E_{cyc} + \frac{mc^2}{2a^4B^2} + \frac{1}{2}.$$

As time progresses, the particle will drift along the same equipotential, since the drift velocity is perpendicular to the electric field (which is the gardient of the potential). After a time, it will reach the y-axis, at point $y = b$. The guiding center approximation states that E_{cyc} is a constant of the motion, so that the energy at this point is

$$E_f = E_{cyc} + \frac{mc^2}{2b^4B^2} + \frac{1}{2}$$

clearly energy is not conserved unless $a = b$. When the transverse potential is rotationally invariant, or when the electric field is constant, this formulation of the guiding center approximation does conserve energy; however these are special cases, and is not true in general.

This lack of energy conservation arises from the fact the the system is not Hamiltonian; instead the equations of motion arise from an expansion about the true equations of motion.

C.2 Hamiltonian Formulation of GCA

Previously, the non-Hamiltonian approach has been adequate, because it was applied to system where the guiding center approximation held very well. However in considering the atoms in a strong magnetic field ([113] and Chapter (2)), there is a competition between the magnetic field and the Coulomb well. Thus studying the Hamiltonian dynamics of the system, in particular how the GCA fails, is useful.

By changing to action-angle variables using equations (B.18) and (B.19), we can isolate the correct actions that will be conserved, or nearly conserved, in the Hamiltonian system. Once this transformation is effected, the guiding center approximation becomes the assumption that the canonical momentum J_c, which is nearly equal to the angular momentum, is conserved. This makes the cyclotron angle a trivial coordinate and reduces the dimensionality of the problem. The full transformed Hamiltonian in guiding center action-angle coordinates reads

$$H(Q, \theta_c, z; P, J_c, p_z) = \frac{p_z^2}{2m} + J_c \eta \omega_c + V(Q, \theta_c, z; P, J_c).$$

Thus the Hamiltonian guiding center approximation amounts to replacing the real potential by some potential $V = V(J_c; Q, z; P, z)$ independent of θ_c and now parameterized by J_c. We will only consider cylindrical potentials below.

C.3 Cylindrically Symmetric Potentials

We now consider the presence of a cylindrical potential well and a transverse harmonic well (which may be of infinitessimal strength), with full Hamiltonian, transformed to action-angle variables from the previous section,

$$H = \frac{1}{2m}\left(\vec{p} - \frac{m\eta\omega_c\rho}{2}\hat{\theta}\right)^2 + V(\rho, z) + \frac{m\omega_r^2\rho^2}{2} \tag{C.2}$$

where the magnetronmotion here is due to some external field, not the Coulomb well; the Coulomb well will have an additional effect on the guiding center motion. In action-angle variables,

$$\rho = \alpha\sqrt{2J + 4\sqrt{J_m J_c}\cos(\theta_c - \theta_m)} \tag{C.3}$$

where $J = J_m + J_c$, the total angular momentum. So we can write in action-angle variables

$$H = \frac{p_z^2}{2m} + (\eta\tilde{\omega}_c + \omega_m)J_c + \omega_m J_m + V(|\theta_c - \theta_m|, J_m, J_c, z) \tag{C.4}$$

The Hamiltonian depends on the angle variables as $H = H(|\theta_c - \theta_m|)$ only, which implies from Hamilton's equations of motion that $\frac{dJ_c}{dt} = -\frac{dJ_m}{dt}$. Since each action represents an angular momentum, this is a restatement of conservation of angular momentum in a cylindrically symmetric potential, and is exactly true for all cases. Such a conservation law indicates that we can reduce the dimensionality of the problem, as expected.

We tend to be most interested in the dynamics of the guiding center itself, so we want to eliminate (θ_c, J_c). Defining a canonical transformation

$$F_2 = \tilde{J}_m(\theta_m - \theta_c) + \tilde{J}_c\theta_c \tag{C.5}$$

we get new transverse coordinates

$$\begin{aligned}\tilde{J}_m &= J_m \\ \tilde{J}_c &= J_c + \tilde{J}_m = J \\ \theta &= \theta_m - \theta_c \\ \tilde{\theta}_c &= \theta_c,\end{aligned} \tag{C.6}$$

where the variable θ is conjugate to momentum J_m, and the total angular momentum J is conjugate to θ_c, which becomes an ignorable coordinate. The transformed Hamiltonian in just two coordinates (θ, z) is

$$H = (\eta\tilde{\omega}_c + \omega_m)J - \eta\tilde{\omega}_c J_m + \frac{p_z^2}{2m} + V(\rho(\theta), z) \tag{C.7}$$

Here J is the total angular momentum of the system, hence the first term is a constant.

We can interpret the kinetic energy terms as follows. If we were to drop the potential $V(\rho, z)$, ignore the axial motion, and bring the guiding center to the origin so that $J_m = 0$, then the first term is the only energy in the problem. Hence $E_o \equiv (\eta\tilde{\omega}_c + \omega_m)J$ is the cyclotron energy of the particle moving at the bottom of the harmonic well and modifed by the magnetron motion. If we now move the particle's guiding center to some radius ρ_m, then we must increase the magnetron action J_m; the energy required to do this is the second term, $E_{\rho_m} \equiv -\eta\tilde{\omega}_c J_m$. These two terms comprise the "bare" energy of the (harmonic) system with no axial motion or additional fields, where the actions are decoupled and individually conserved. To this we add the transverse kinetic energy and the potential to arrive at the full Hamiltonian.

C.4 Coulomb Well

We now consider the presence of a Coulomb well and a transverse harmonic well (which may be of infinitessimal strength), with the Hamiltonian in guiding coordinates,

$$\begin{aligned}H &= \frac{1}{2m}\left(\vec{p} - \frac{m\omega_c\rho}{2}\hat{\theta}\right)^2 - \frac{e^2}{r} + \frac{m\omega_r^2\rho^2}{2} \\ &= \frac{p_z^2}{2m} + (\eta\tilde{\omega}_c + \omega_m)J - \eta\tilde{\omega}_c J_m \\ &\quad - \frac{e^2}{\alpha\sqrt{2J + (z/\alpha)^2 + 4\sqrt{J_m(J - J_m)}\cos(\theta)}}\end{aligned} \tag{C.8}$$

where again the magnetron motion here is due to some external field, not the Coulomb well; $J = J_c + J_m$; and $\theta = \theta_m - \theta_c$. We've utilized the fact that the Coulomb well is cylindrically symmetric, and hence that the total angular momentum is conserved, to write the Hamiltonian is a simplified form, with only two explicit coordinates, θ and z.

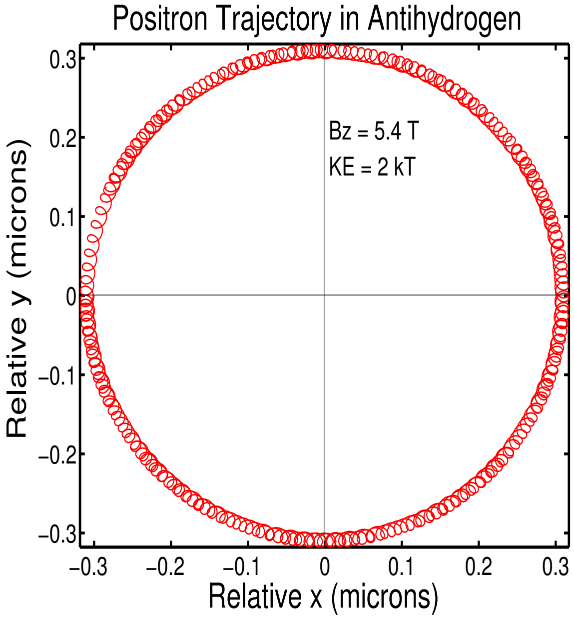

Figure C.1: Trajectory of a positron in a Coulomb well in the presense of a very strong magnetic field, projected onto the x-y plane. Motion is strongly guiding center.

In the general case, it doesn't make much sense to use action-angle coordinates to describe the dynamics of a particle in a Coulomb potential, since the magnetron frame concept depends on the local electric field which may be changing rapidly. However if the trajectory of the particle is restricted in the range of ρ values so that the local electric field has a small variation, then it can make sense to speak of a magnetron frame, and the representation can be a useful one.

The associated equations of motion are

$$\begin{aligned}
\dot{\theta} &= -\eta\tilde{\omega_c} + \frac{\alpha^2 e^2 (J - 2J_m)\cos\theta}{\sqrt{J_m(J-J_m)}\,(z^2+\rho^2)^{3/2}} \\
\dot{J}_m &= \frac{2e^2\alpha^2\sqrt{J_m(J-J_m)}\sin\theta}{(z^2+\rho^2)^{3/2}} \\
\dot{\theta}_c &= \eta\tilde{\omega_c} + \omega_m + \frac{\alpha^2 e^2}{(z^2+\rho^2)^{3/2}}\left(1 + \sqrt{\frac{J_m}{J-J_m}}\cos\theta\right) \\
\dot{J} &= 0 \\
\dot{z} &= p_z/m \\
\dot{p}_z &= m\ddot{z} = -\frac{e^2 z}{(z^2+\rho^2)^{3/2}},
\end{aligned} \tag{C.9}$$

where now $\rho^2 = 2\alpha^2 J + 4\alpha^2\sqrt{J_m(J-J_m)}\cos\theta$. Since the angle here is defined as $\theta = \theta_m - \theta_c$, then the magnetron angle equation of motion is

$$\dot{\theta}_m = \omega_m + \frac{\alpha^2 e^2}{(z^2+\rho^2)^{3/2}} \left(1 + \sqrt{\frac{J - J_m}{J_m}}\right). \tag{C.10}$$

We can physically interpret this result as follows: at large radius, the second term vanishes, and the magnetron motion is that the of external harmonic potential. For small radius cyclotron motion, the second term becomes $cE_r/\rho B = v_D/\rho$, the drift motion for the locally linear radial Coulomb electric field.

We can now dispense with the external electric field if appropraite, and instead consider just the magnetron motion due to the Coulomb field; we set the constant parameter $\omega_m \to 0$ and the cyclotron frequency $\tilde{\omega}_c \to \omega_c$.

C.5 Guiding Center Atom

In the simplest approximation, we consider the case of a tight cyclotron orbit, so that $J \gg J_c$; the cyclotron motion has little angular momentum in comparison to the total angular momentum (this is not necesarily true of the energy, however). Thus we may drop the oscillating part of the Coulomb term. We also disregard the external harmonic field, thus $\omega_m \to 0$ and the cyclotron frequency $\tilde{\omega}_c \to \omega_c$., and our guiding center Hamiltonian reads

$$H = \frac{p_z^2}{2m} + \eta\omega_c J - \eta\omega_c J_m - \frac{e^2}{\sqrt{2\alpha^2 J + z^2}}. \tag{C.11}$$

With this simplest Hamiltonian, the actions J_m, J_c, and thus the cyclotron radius and guiding center radius are constants of the motion:

$$\begin{aligned}
\dot{\theta} &= -\eta\omega_c \\
\dot{\theta}_c &= \eta\omega_c + \frac{\alpha^2 e^2}{(z^2+\rho_m^2+\rho_c^2)^{3/2}} \\
\dot{z} &= p_z/m \\
\dot{J} &= 0 \\
\dot{J}_m &= 0 \\
\dot{p}_z &= m\ddot{z} = -\frac{e^2 z}{(z^2+\rho_m^2+\rho_c^2)^{3/2}}
\end{aligned} \tag{C.12}$$

where we've identified the square of the magentron radius and cyclotron radii $\rho_m^2 + \rho_c^2 = 2\alpha^2 J$. A more physical approximation, of the same order, is to replace $\rho_m^2 + \rho_c^2$ by just ρ_m^2 in the denominator. Under this guiding center approximation, the transverse motion is a constant rotation of relative angle θ between the cyclotron and magnetron angles. The magnetron angle obeys the motion equation,

$$\dot{\theta}_m = \frac{\alpha^2 e^2}{(z^2 + \rho_m^2)^{3/2}}, \tag{C.13}$$

where again $\alpha \equiv 1/\sqrt{m\eta\omega_c} = 1/\sqrt{eB/c}$. Hence the motion of the guiding center is radial at a fixed angular frequency, determined by the initial position of the particle about the Coulomb well. Thus we have the effective magnetron frequency

$$\omega_{m,\text{Coulomb}} = \frac{\alpha^2 e^2}{(z^2 + \rho_m^2)^{3/2}}. \tag{C.14}$$

due to the Coulomb well.

We will take this as the definition of a "'guiding center atom"', that the cyclotron action J_c and the orbital action J_m are conserved independently, which implies that the cyclotron and orbital radii are in addition constants of the motion.

C.5.1 Corrections to the Guiding Center Approximation

If we want to consider the case where such an approximation will just break down, we can focus on what the average change in the action J_c (and hence, for a cylindrical potential, the action J_m as well). In such a case, we consider the approximation $J_m \gg J_c$ (in reality this is for the case $J_m + J_c \gg 2\sqrt{J_m J_c}$, so the expansion holds if $J_c \gg J_m$ as well). We expand the Coulomb term about the radius

$$r_T \equiv \sqrt{2\alpha^2 J + z^2} \tag{C.15}$$

so that, for arbitrary central force

$$r^p \cong r_T^p \left[1 + \frac{p}{2}\left(\frac{4\alpha^2\sqrt{J_m J_c}}{r_T^2}\right)\cos\theta + \frac{p(p-2)}{8}\left(\frac{4\alpha^2\sqrt{J_m J_c}}{r_T^2}\right)^2 \cos^2\theta\right]. \tag{C.16}$$

To first order, the Hamiltonian is

$$H = \frac{p_z^2}{2m} + (\eta\tilde{\omega}_c + \omega_m)J - \eta\tilde{\omega}_c J_m - \frac{e^2}{r_T} + \frac{2\alpha^2 e^2\sqrt{J(J - J_m)}}{r_T^3}\cos\theta \tag{C.17}$$

so that the equation of motion for the cyclotron action reads

$$\dot{J}_c = -\dot{J}_m = -\frac{2\alpha^2 e^2\sqrt{J J_c}}{(2\alpha^2 J + z^2)^{3/2}}\sin\theta. \tag{C.18}$$

Rewriting the derivative as

$$\frac{d}{dt}\sqrt{J_c} = -\frac{\alpha^2 e^2\sqrt{J}}{(\rho_T^2 + z^2)^{3/2}}\sin\theta. \tag{C.19}$$

we can change from action to radii in the equation,

$$\frac{d\rho_c}{dt} = -e^2\alpha^2\rho_T \frac{\sin\theta}{(\rho_T^2 + z^2)^{3/2}}. \tag{C.20}$$

Thus for purely transverse motion, the cyclotron radius depends only on the relative angle $\theta = \theta_m - \theta_c$.

As a first stab at an approximation, we can guess that the sine will contribute a factor of $1/\omega_c\sqrt{2}$, and that for large ρ_T, the the axial part plays a small role, so taking $\rho_T \approx \rho_m$,

$$\langle \Delta\rho_c \rangle \approx \frac{e^2\alpha^2}{\sqrt{2}\rho_m^2\omega_c} = \frac{1}{\sqrt{2}\rho_m^2 m\omega_c^2} \tag{C.21}$$

So we expect the fluctuations $\Delta\rho_c$ to go as ρ_m independent of ρ_c for large orbits.

C.5.2 Simulations of the Breakdown of the GCA

In this section we simulate a 2D atomic potential, and analyze numerically how the GCA breaksdown as the particle comes closer to the $1/r$ singularity. In Figure (C.2) we consider how the cyclotron radius varies as a function of the the magnetron radius in a Coulomb field. The units used are hydrogenic scaled coordinates, discussed in Chapter (2).

In (a) we plot a trajectory where $\rho_c > \rho_m$ while in (c) we plot a typical guiding center trajectory where $\rho_c \ll \rho_m$. In (b) we plot an interesting trajectory where $\rho_c \sim \rho_m$, and opposing magnetic and Coulombic forces create a pear-shaped orbit. In (d) we show the results of classical simulations of particle motion, showing how the cyclotron radius changes from the initial value to a final steady-state value. For each point, the center of the guiding center is started at a certain distance from the Coulomb center on the x-axis, while the particle is placed an additional $\rho_{c,o}$ cyclotron radius perpendicular to the x-axis. The subsequent change in cyclotron radius, or magnetron radius, is plotted at steady state. The result shows an abrupt breakdown of the GCA between $\rho_m = 2 - 3$ units; while a larger cyclotron radius implies a breakdown for larger magnetron radius, the results for large and small lie within a reasonably small range. This is due to the quality of the GCA, and the singular nature of the Couomb potential. The dotted line in (d) plots the analytic approximation to the GCA breakdown, equation (C.21).

Plotted in Figure (C.3) is a series of 2D wavepacket simulations in a Coulomb field and a perpendicular magnetic field. Each simulation start with the same wavepacket at a certain magnetron radius, and then plots the wavepacket after one magnetron cycle. The breakdown of the GCA is apparent quantum mechanically here as well.

In Chapter (2), we consider more carefully the breakdown of the GCA in the hydrogen atom.

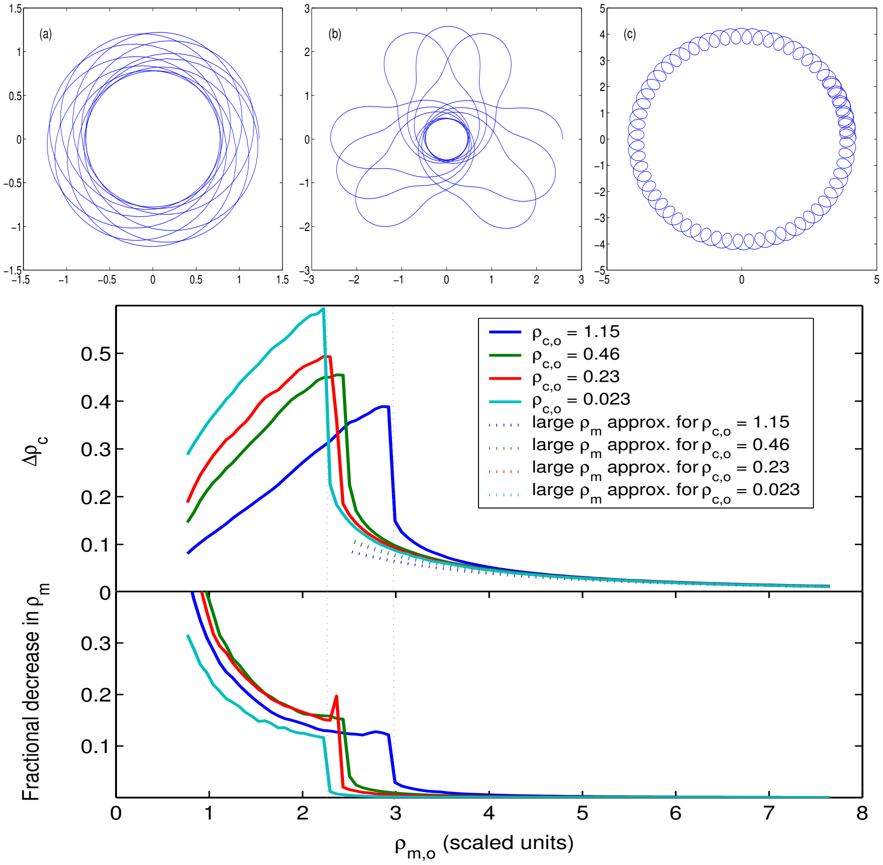

Figure C.2: Transverse simulations, using the action-angle representation and $z = 0$, $p_z = 0$, of the evolution of $\rho_c(t)$ for various initial cyclotron radii over a range of magnetron radii. The transverse approximation, equation (C.21), is compared without a fitting parameter to the simulation values, and agree well up to $\rho_m \approx 3.5$, which corresponds to 0.25μm at 5.4 Tesla. In addition, the data is nearly independent of ρ_c down to this value.

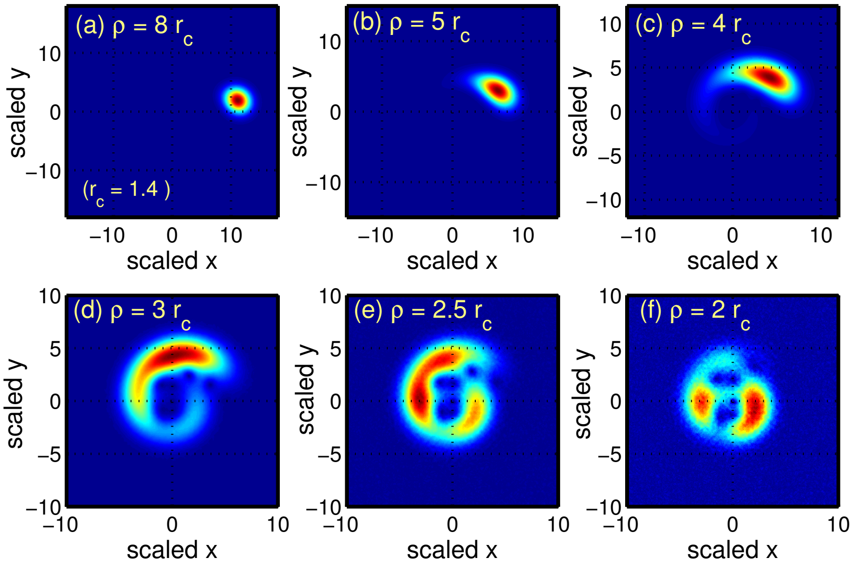

Figure C.3: Wavepackets introduced into a Coulomb potential and a perpendicular magnetic field. Clear is the breakdown of the GCA with decreasing magnetron radius. In each frame, the wavepacket was prepared in the same initial state $|\psi_o\rangle$. Each frame is taken after the completion of one cyclotron period.

Appendix D

Hard Wall Billiard System

In this section we examine a billiard model of the magnetic focussing system considered in Chapter (7), where a source is located along an infinitely hard billiard wall in a magnetic field, and we want to know the various semiclassical values of propagation to a scatterer at point $\vec{r}$ located somewhere in space off of the wall, as well as a point on the wall a distance $\mathcal{L}$ away. The trajectories of the electron will be a series of connected arcs, connecting the source, some number of points along the wall, the scatterer, and the target point. Thus we engage in an exercise in geometry.

Usually such a semiclassical billiard model of motion is considered in terms of motion on the wall [110, 51]. However, in our case we will be interested in the semiclassical Green function from a source on the wall to a point off the wall. This generalization of the approach is a novel one, motivated by new experimental imaging techniques. Because these are new results, we will derive them here, and reference the previous results as we go. As an added feature of the model, we will take into account a collimated, non-uniform injection weighting $w(\alpha)$, and similarly a target amplitude $w'(\alpha)$ along the wall; such an amplitude is needed in general in order to fulfill boundaries conditions on the hardwall of the billiard.

D.1 Basic Geometry

The geometry and definitions of angles and distances are depicted in Figure (D.1) for a trajectory connecting a source to a point. Note that the α here has opposite sign to that in reference [110]. To determine the triplet of values (n, α, θ) that uniquely describe a QPC to tip trajectory, one must solve a set of equations,

$$\begin{aligned} x/r_c &= (2n+1)\cos(\alpha) + \cos(\alpha - \theta) \\ y/r_c &= \sin(\alpha - \theta) - \sin(\alpha) \end{aligned} \tag{D.1}$$

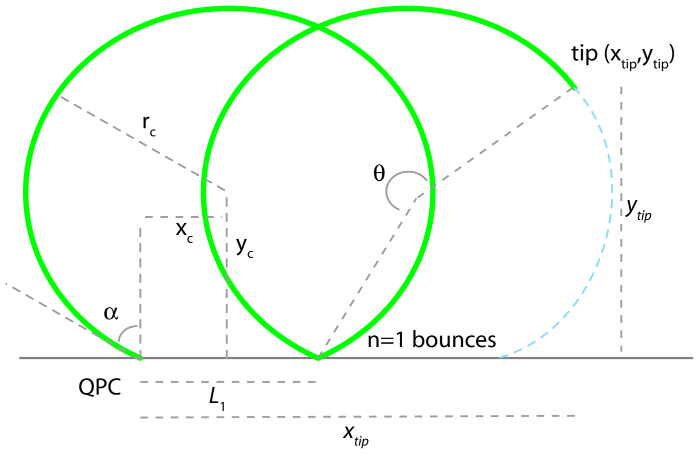

Figure D.1: Geometry for the magnetic focussing billiard system, depicting a trajectory between a point source (a QPC) and a point off the wall (for example an SPM tip). Every trajectory can be uniquely parameterized by the triplet (n, α, θ), however the free parameters are the position (x, y). Note that α is defined in the standard manner as a counterclockwise angle, but θ is a clockwise angle.

where it is assumed that the QPC is at the origin. The minimum possible number of bounces has a lower limit,

$$n \geq \frac{x - \sqrt{r_c^2 - y^2}}{2r_c} - \frac{1}{2}. \tag{D.2}$$

There are usually two solutions for each n value.

Note that if we want to consider only trajectories from the source on the wall to another point on the wall a distance $\mathcal{L}$ away, we can use the above by setting $y = 0$ and setting the $x = \mathcal{L}$, in which case we get simply

$$\begin{aligned} \alpha_{wall} &= \pm\cos^{-1}\left(\frac{\mathcal{L}}{2(n+1)r_c}\right) \\ n_{wall} &\geq \mathcal{L}/2r_c - 1. \end{aligned} \tag{D.3}$$

Given a trajectory triplet (n, α, θ), one can calculate the properties of the trajectory directly. The distance from the source on the wall to a point in space $\vec{r}$ is clear from equation (D.1). The distance between bounces, $\mathcal{L}_1$, and the position of the center of the arcs with respect to the preceding bounce point (x_c, y_c) are

$$\begin{aligned} \mathcal{L}_1 &= 2r_c\cos(\alpha) \\ x_c &= \mathcal{L}_1/2 = r_c\cos(\alpha) \\ y_c &= r_c\sin(\alpha) \end{aligned} \tag{D.4}$$

The sign of α is important, since it determines if the arcs are centered above or below the wall.

The length of a trajectory $\mathcal{C}$ is

$$\mathcal{C} = nr_c(\pi + 2\alpha) + r_c\theta \tag{D.5}$$

while the area, defined as the area below the trajectory but above the wall (the usual area in the sense of integration) is

$$A = \frac{r_c^2}{2}\left[n(\pi + 2\alpha + \sin(2\alpha)) + \theta - \sin\theta + \frac{1}{2}\sin(2\alpha) - \sin(2\alpha - \theta) + \sin(2\alpha - 2\theta)\right] \tag{D.6}$$

Again, if we would rather consider only wall to wall orbits, then we may take $\theta = \pi + 2\alpha$, and these expressions simplify to:

$$\begin{aligned} \mathcal{C}_{wall} &= (n+1)r_c(\pi + 2\alpha) \\ A_{wall} &= \frac{r_c^2}{2}(n+1)(\pi + 2\alpha + \sin(2\alpha)). \end{aligned} \tag{D.7}$$

D.2 Classical Action

In anticipation of modelling the system using semiclassical methods, we consider the classical action and amplitude for propagation from the source on the wall to a position off the wall $\vec{r}$. The classical action is defined as [45]

$$S(\vec{r}_o, \vec{r}) = \int_{\vec{r}_o}^{\vec{r}} \vec{p}\cdot d\vec{r} = \int_{\vec{r}_o}^{\vec{r}} m\vec{v}\cdot d\vec{l} - \frac{e}{c}\vec{A}\cdot d\vec{l} \tag{D.8}$$

The action $S(\vec{r}_o, \vec{r})$ is gauge dependent, but when dealing with phase differences this is irrelevant, since the gauge choice adds a constant action. As such we can choose the most convenient gauge to work in, in this case the Landau gauge $\vec{A} = -By\hat{x}$, with the origin chosen so that the hard wall lies on $y = 0$. With this choice, the magnetic part of the action amounts as usual to being proportional to the flux through the area between the curve and the hard wall. The action from the source at the origin to some point (x, y) is

$$\begin{aligned} S(x,y) &= \hbar k\mathcal{C} - eBA/c \\ &= \frac{n\hbar k r_c}{2}(\pi + 2\alpha - \sin 2\alpha) + \frac{\hbar k r_c}{2}\theta + \\ &\quad \frac{\hbar k r_c}{2}\left[\sin\theta - \frac{1}{2}\sin 2\alpha + \sin(2\alpha - \theta) - \sin(2\alpha - 2\theta)\right]. \end{aligned} \tag{D.9}$$

where n, α and θ depend on the independent variables (x, y). In the case of a trajectory which returns to the wall after n bounces, the action is simply

$$S(\mathcal{L}) = \frac{(n+1)\hbar k r_c}{2}(\pi + 2\alpha - \sin 2\alpha) \tag{D.10}$$

where $\alpha(\mathcal{L}) = \pm\cos^{-1}(\mathcal{L}/(2r_c))$.

D.3 Classical Density and Amplitude

Free motion in a uniform magnetic field can be described as a trivial motion in action-angle coordinates (Section (B)), and as such the classical density from any point $\vec{\theta}_o$ to $\vec{\theta}$ is simply unity, when expressed in action-angle variables. In Cartesian coordinates, the same is not true; from equation (B.9) the classical density in free space depends on the distance traveled $R = |\vec{r}' - \vec{r}_o|$ according to

$$D_{free}(E;R) = \frac{m}{\omega_c r_c^2} |\csc\theta| = \frac{2m}{\omega_c} \frac{1}{R\sqrt{4r_c^2 - R^2}} \tag{D.11}$$

where θ is the angle traveled around the orbit. As noted before there are two angles θ and $2\pi - \theta$ that produce the required distance R. The classical amplitude is $\sqrt{D}$. This amplitude is valid even in the hard wall case, as long as the number of bounces $n = 0$.

If we consider the just wall to wall trajectories, so that the final position in y is at the wall and $R = \mathcal{L}$, then the classical density may be found by considering the variation in $\mathcal{L}$ (see [110]). Considering a local coordinate system that follows the trajectory, the classical may be expressed as $D = \frac{1}{v}\frac{\partial^2 S}{\partial \tilde{x}^2}$, where the rotated coordinate $\tilde{x}$ runs perpendicular to the velocity. In our case, $\tilde{x}$ lies at an angle α to the wall, so that $d\tilde{x} = d\mathcal{L}/\cos\alpha$. Thus we may rewrite $D = \frac{1}{v\cos^2\alpha}\frac{\partial^2 S}{\partial \mathcal{L}^2}$. from the expression for the wall to wall action, equation (D.10). This evaluates to

$$D_{wall}(E,\mathcal{L}) = \frac{m}{(n+1)\omega_c r_c^2} |\csc 2\alpha|. \tag{D.12}$$

If we consider the $n = 0$ free propagation case, and recognize that the angle subtended $\theta = \pi + 2\alpha$, then since $\csc\theta = -\csc 2\alpha$ the expressions agree.

This result implies that the density due to n bounces can be thought of a reciprocal sum of the density contributions from each bounce, i.e. that $D_n^{-1} = \sum_n D_o^{-1}$. This suggests a generalization to the classical density for a trajectory from an arbitary point $\vec{r}_o$, to a point $\vec{r}$. Assuming that the angles from $\vec{r}_o$ to the wall, $-\theta_o$, and from the wall to $\vec{r}$, θ, as well as the angle α and number of bounces n have been previously determined, the density could be written as

$$D = \frac{m}{\omega_c r_c^2} \left| n\sin 2\alpha - \sin(\theta - \theta_o) \right|^{-1} \tag{D.13}$$

and in particular for a source on the wall to an arbitrary (classical allowable) point off the wall

$$D = \frac{m}{\omega_c r_c^2} \left| n\sin 2\alpha - \sin\theta \right|^{-1}. \tag{D.14}$$

These expressions show the correct behavior as the point are moved to the walls (at which time $\theta - \theta_o \to \pi + 2\alpha$), and in the case of $\alpha = 0$ correctly recover the free propagation case. While not

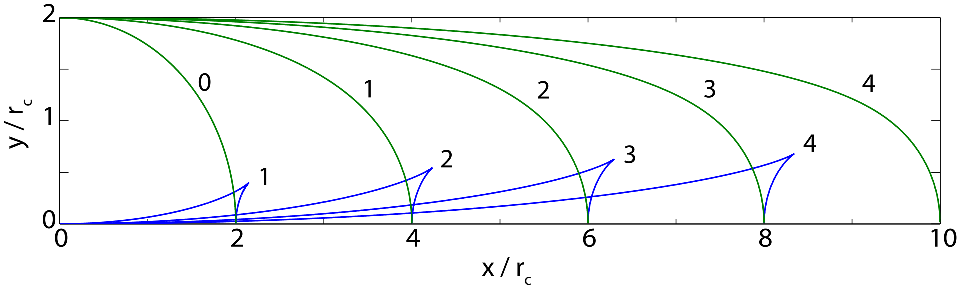

Figure D.2: Classical classics for the magnetic billiard system. The source is at the origin on the left of the figure. The caustics are labeled by the number of reflections from the hard wall that happen before the trajectories cross. The first caustic in the upper series (in green) is a circular arc of radius $2r_c$ centered at the source, and is the only caustic that results from free propagation.

a proof of the correctness of the expression, this should motivate this ansatz for the classical density in later sections. Our ansatz for the classical amplitude is hence

$$A = \sqrt{\frac{m}{\omega_c r_c^2}} \frac{1}{\sqrt{|n \sin 2\alpha - \sin(\theta)|}}. \tag{D.15}$$

D.4 Caustics

As outlined in [110] the caustics may be found by varying an initial condition, and determining where in the sample the two nearby trajectories cross. The position of the particle can be determined by parameters (n, α, θ) from equation $D.1$. By varying the initial angle parameter α, and demanding that the position remain the same, we determine the equation for the caustics

$$\begin{aligned} x &= r_c \left[\sin\alpha + (1-u^2)^{-1/2} \right] \\ y &= r_c \left[(2n+1)\cos\alpha + u(1-u^2)^{-1/2} \right] \end{aligned} \tag{D.16}$$

where $u \equiv \frac{1}{(2n+1)\tan\alpha}$. The caustic is at a final accumulated angle

$$\theta_c(n,\alpha) = \frac{\pi}{2} + \alpha - \tan^{-1}\left(\frac{\cot\alpha}{2n+1}\right) \tag{D.17}$$

with respect to the start of the last arc.

These caustics are plotted in Figure (D.2), and come in two families, lower and upper caustics, and are ordered by the number of relfections from the wall. All the lower caustics are due to reflections off the hard wall, while the upper are due to $n-1$ reflections, plus the “turnaround” caustic present in the free case.

For a trajectory which starts and ends on the wall, as in the tip-free case, the number of caustics crossed is $n_c = n+1$ for a longer trajectory, $\alpha > 0$, and $n_c = n$ for a shorter trajectory with $\alpha < 0$; generally $n_c(n, \alpha) = n + \Theta(\alpha)$, where $\Theta(x)$ in the Heaviside step function. The number of reflections is clearly $n_r = n$. Tolopogically each caustic crossing retards the semiclassical phase by $-\pi/2$ and each reflection advances or retards the phase by π. Thus for a wall-to-wall trajectory, the phase index is

$$\mu_{w-to-w}(n, \alpha) = -n + \Theta(\alpha) \tag{D.18}$$

and the total phase is $-\pi\mu/2$. For a trajecory which starts at the wall and ends at some point above the wall, the index will depend on whether the particle has crossed the last caustic. Thus for point off the wall,

$$\mu(n, \alpha) = -n + \Theta(\alpha) + 1 - \Theta(\theta - \theta_c). \tag{D.19}$$

D.5 Free Semiclassical Green Function

In section we approach the system from a semiclassical point of view. When the magnetic fields involved are moderate, and the geometry open, the length scale of the system is much larger than that of the wavelength of the electron, and such an approach is justified.

We begin by determining the semiclassical Green functions in the clean system. Then, making an assumption for the angular amplitude of the source, we calculate the amplitude for propagating through the system as a function of magnetic field, in the tip-free case, and as a function of the probe point $\vec{r}$. To begin we consider the free semiclassical Green function in a magnetic field.

In the free B-field case, trajectories emanating from a point source with energy E will return back to the point source, following a circle of radius r_c. As we have seen, there are only two arcs from a point $\vec{x}_o$ to a second point $\vec{x}$ at a distance $\mathcal{L} < 2r_c$; at $\mathcal{L} = 2r_c$ there is one orbit, and none for $\mathcal{L} > 2r_c$. *Note*: in this section we use $\mathcal{L}$ and α to indicate the correspondence with the no-bounce magnetic focussing case. For a well-collimated injection distribution, most of the transmitted amplitude will be due to direct orbits when at low magnetic fields, and one can argue that such a magnetic focussing experiment is actually measuring the free magnetic Green function with disorder.

In the absence of a magnetic field, the semiclassical free Green function is straightforward [87], and in one and three dimensions is the same as the quantum Green function. However in magnetic field the Green function is more complicated, and the existence of caustics implies that it will diverge significantly from the quantum expression [24, 51] near these caustics. The semiclassical Green functions is the sum of phases accumulated along classical trajectories, weighted by the

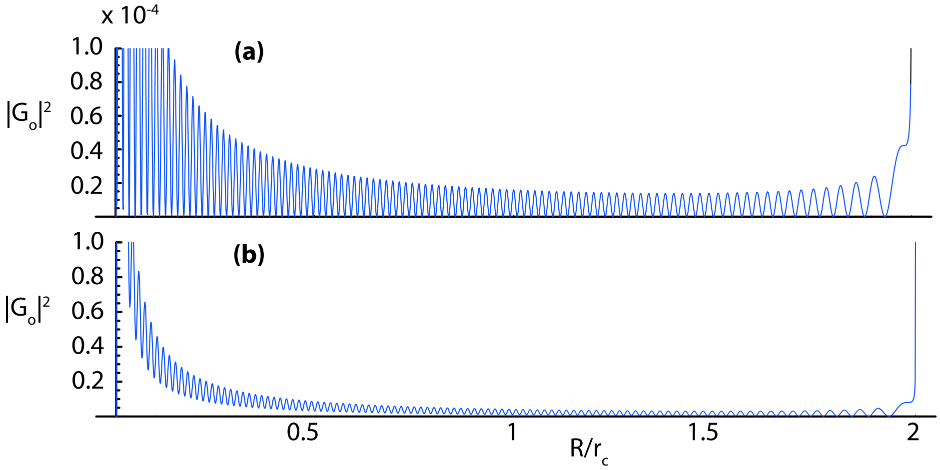

Figure D.3: Plot of the magnitude of the free Green function without (a) and with (b) decoherence. The parameters are relevant to the experiment in Chapter (7): $E_F = 13.7$ meV, $B = 77$ milliTesla, so that $r_c = 1327$ nm and $\lambda_F = 40$ nm. In (b) the dephasing length is taken to be 5000 nm, which is 3.8 r_c.

classical amplitude of each trajectory [45, 12],

$$G_{sc} = \sum_{\text{trajs } j} \frac{2\pi}{(2\pi i\hbar)^{(d+1)/2}} A_j \; e^{\phi_j + \pi\mu_j/2} \tag{D.20}$$

where μ is the phase index, and d is the dimension. The prefactor evaluates to $e^{-i3\pi/4}\hbar^{-3/2}(2\pi)^{-1/2}$. Following the preceding sections, the two primary orbits are arcs of phase

$$\phi(\mathcal{L}) = \frac{kr_c}{2}(\pi \pm 2\alpha \mp \sin 2\alpha)$$

where $\mathcal{L} = 2r_c \cos\alpha$; for a complete circle the injection angle $\alpha = \pi/2$, and we get $\phi_C = \pi k_f r_c$. If the trajectory traveled a distance $\mathcal{L}$, we know that $\alpha = \pm\cos^{-1}(\mathcal{L}/2r_c)$, so that the difference in phase between the shorter and longer trajectories is

$$\Delta\phi(x,y) = 2k_f r_c(\alpha - \sin\alpha\cos\alpha).$$

The shorter primary orbit, for which $\alpha < 0$, will not cross a caustic, while the longer primary orbit will cross a caustic when $\mathcal{L} = 2r_c$, thus for n iterations of the orbit, the Maslov phase will be

$$\pi\mu/2 = n\pi + \begin{cases} 0 & \text{if } \alpha < 0 \\ \pi/2 & \text{if } \alpha > 0. \end{cases}$$

The classical amplitude for every orbit is the same,

$$A = \sqrt{\frac{m|\csc 2\alpha|}{\omega_c r_c^2}} = \sqrt{\frac{m^2|\csc 2\alpha|}{\hbar k_F r_c}}.$$

Hence the free semiclassical Green function in a magnetic field is

$$G_B(E;\mathcal{L}) = \frac{2\pi}{(2\pi i\hbar)^{3/2}}\sqrt{\frac{m^2|\csc 2\alpha|}{\hbar k_F r_c}}\sum_{\text{traj } j} e^{i(\phi_j+\pi\mu_j/2)}.$$

We have seen that there are only two primary trajectories to any classically allowed point $\vec{r}$, and each can have n repetitions of the cyclotron orbit. Thus we can sum across repetitions n of the primary orbit instead, with result

$$G_B(E;\mathcal{L}) = \frac{4\pi e^{i\pi/4}}{(2\pi i\hbar)^{3/2}}\sqrt{\frac{m^2|\csc 2\alpha|}{\hbar k_F r_c}}\cos(\Delta\phi/2+\pi/4)e^{i(\phi_o+\Delta\phi/2)}\sum_n e^{in\pi},$$

where ϕ_o is the phase of the shorter orbit. We can thus write the Green function as a product of position depdenent and independent parts,

$$G_B(E;\mathcal{L}) = \frac{4\pi e^{i\pi/4}}{(2\pi i\hbar)^{3/2}}A(E;\mathcal{L})D(E), \tag{D.21}$$

where the position dependent part is explicitly in terms of α

$$A(E;\mathcal{L}) = \sqrt{\frac{m^2|\csc 2\alpha|}{\hbar k_F r_c}}\cos[k_f r_c(\alpha - \sin\alpha\cos\alpha)+\pi/4]e^{ik_F r_c(\pi/2+\sin(2\alpha)/2)}. \tag{D.22}$$

The $D(E)$ terms can be evaluated by carefully summing over al the poles; refer to [51] for a more careful general derivation. We plot the free Green function in Figure (D.3).

The position dependence of the amplitude of the Green function will depend on the phase difference between the two paths, i.e.

$$|G_B(\mathcal{L})|^2 \propto \frac{\cos^2\left[k_f r_c\left(\cos^{-1}\lambda - \lambda\sqrt{1-\lambda^2}\right)\right]}{\lambda\sqrt{1-\lambda^2}} \tag{D.23}$$

where $\lambda \equiv \mathcal{L}/2r_c$.

If a probe of the local density of states were placed at a distance r from the source, we could measure the spatial variation in the Green function $|G(\vec{r})|^2$, and see “fringes.” The fringe spacing is derived in Section (6.3) of Chapter (6), with the relevant case, depicted in Figure (6.3h), and written down in equation (6.30). The fringe pattern can be seen in the striped region of Figure (D.4); without the hard wall, the stripes appear in a circular pattern centered on the point source. Near the classical turning point the oscillation spacing becomes large, but for distances well under $2r_c$, the spacing becomes independent of the magnetic field in general, and is just $\lambda/2$, the same fringe spacing seen in the backscattering experiments.

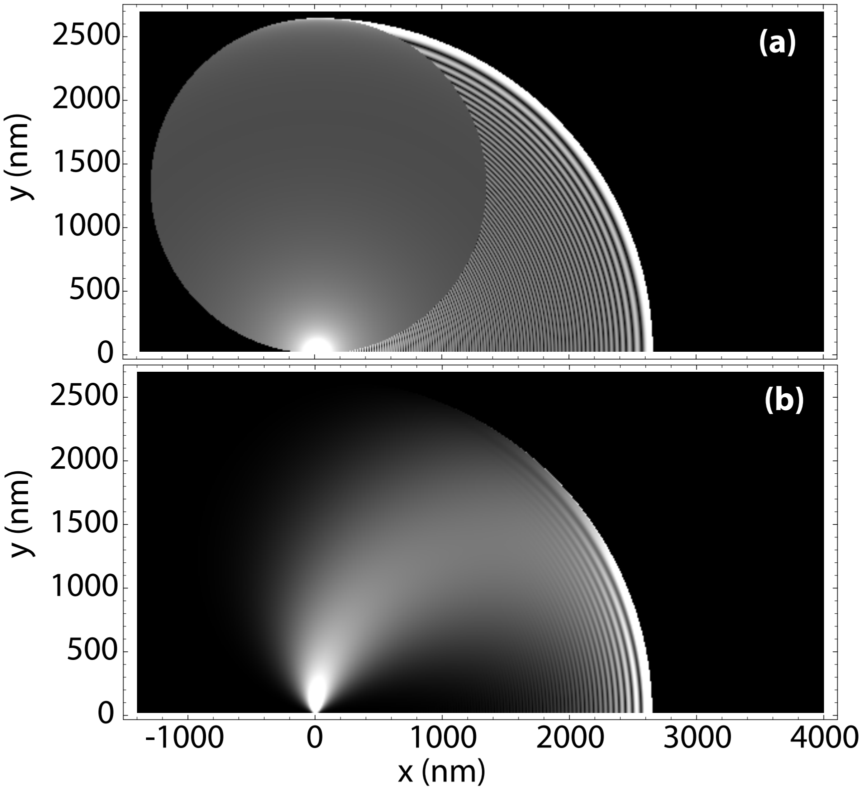

Figure D.4: The semiclassical Green function $|G(\vec{r})|^2$ from a point on a straight billiard wall, but with no bounces; this study is intended to explain how the free Green function in a B field is modified by the hard wall limiting the initial distribution of angles. In (a) the effect of the hard wall is only to truncate the range of initial angles to $-\pi/2 < \alpha < \pi/2$, while in (b) we also impose a collimated initial amplitude $w(\alpha) \propto \cos^4(\alpha)$. Here $E_F = 13.7$ meV, and $B = 77$ miliTesla.

D.6 Hard-Wall Semiclassical Green Function

In this section we calculate the semiclassical Green function for an infinite hard wall, assuming the ansatz in equation (D.15). For simplicity we consider the source to be on the wall, and the endpoint anywhere in classically allowable space $0 \le y \le 2r_c$; the more general case is a straightforward generalization.

To calculate the hardwall semiclassical Green function, one must solve the transcendental equations (D.1) for the parameters (n, α, θ) for each trajectory. In general there will be at most 2 trajectories for each n value. Once obtained, the semiclassical Green function can be calculated directly, using the expressions for the classical amplitude (D.15), the action (D.9), and the phase index (D.19).

In order to manage the number of trajectories, we can use the fact that the length of

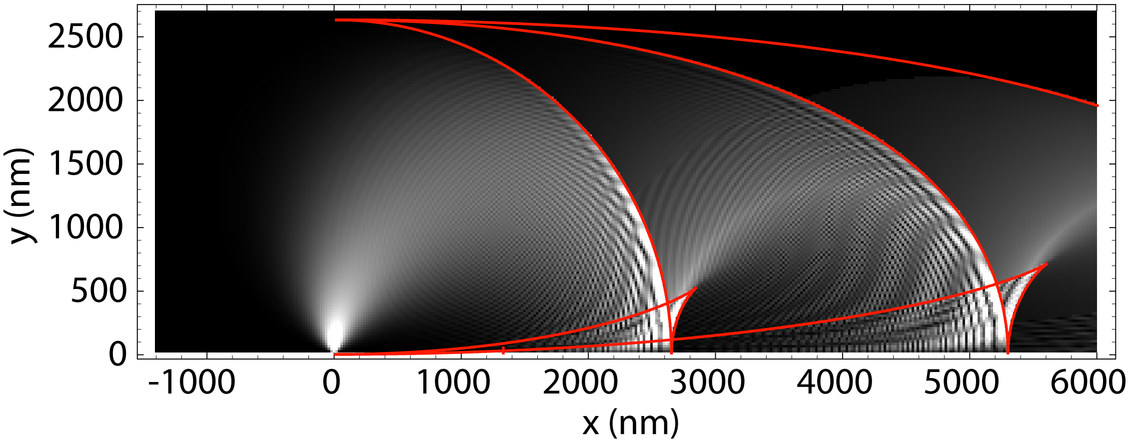

Figure D.5: The semiclassical Green function $|G(\vec{r})|$ from a point on a straight billiard wall. The classical cuastics are plotted in red. As is relevant for the experiment in Chapter (7), we set parameters $E_F = 13.7$ meV, and $B = 77$ miliTesla, and the injection amplitude $w(\alpha) \propto \cos^4(\alpha)$.

the trajectories will scale linearly with n for large n, and that the system will have some inherent dephasing, to truncate the sum over trajectories. For consistency we can include a factor e^{-L_j/l_ϕ}, where l_ϕ is the dephasing length, to formalize the truncation. In addition, any trajectory with large number of bounces will have an initial angle α close to $\pm\pi/2$. Including a weighting factor $w(\alpha)$ that models a collimated injection distribution will further enhance convergence, since for any such physical distribution, $\lim_{|\alpha|\to\pi/2} w(\alpha) \to 0$. Both considerations imply that the most relevant trajectories will be those for which n is small.

To begin, we consider the intermediate case where the free magnetic Green function G_B is used, but where the half-plane nature of the injection QPC plays a role in limiting and weighting the amplitudes of the trajectories. In Figure (D.4a) we plot the free magnetic Green function, but only included trajectories where the y-velocity $v_{y,o} > 0$; This is equivalent to including a weighting function $w(\alpha) = \frac{1}{\sqrt{2\pi}}\Theta(\pi/2 - \alpha)\Theta(\alpha + \pi/2)$ in each term in the semiclassical Green function. There is a circular region of radius r_c that is free of oscillations; in this region only one trajectory is available. To the right of this region two trajectories are available, and hence oscillations, out to a distance of $2r_c$.

If we use a more realistic, collimated weighting function of the form $w(\alpha) \propto \cos^n(\alpha)$, we can see the combined effect of the trajectory interference and injection weighting. The region of maximum fringing due to the Green function is about $2r_c$ to the right of the injection QPC and between a cyclotron radius from the wall to the wall.

In Figure (D.5) we include multiple bounces with the weighted injection distribution. The clear fringing continues periodically at a distance of $\sim 2nr_c$ from the source on the wall. The Green function is still limited to being non-zero only within $2r_c$ of the wall, while the amplitude is strongest near the wall. In this sense, the magnetic focussing experiment may be thought of as a direct measure of the Green function of the system $|G_B|^2$. The caustic structures are still visible in the hard-wall Green function, as indicated by the red lines. In addition, the injection weighting creates extra structures that extend the cusp caustics near the wall further away from the wall, following semicircular paths of radius r_c. Such structures should be visible in a tip scan such as considered in Chapters (6) and (7).

Appendix E

Numerical Codes

In support of the work done to produce the numerical results in this dissertation, we submit the following numerical codes as additional material on CD-ROM and on the web:

- **matlab-wavepackets**: MATLAB code that sets up and propagates wavepackets on customizable potential landscapes, and can measure fluxes and LDOS. Used to prototype and setup simulations. Creates a netCDF [109] binary data file use with the C++ simluation code. Described in Chapter (3) and used in Chapters (4) and (7);
- **meso-wavepackets-src**: C++ code that propagates wavepackets and measures flux and related values. Highly optimized to be fast, but a serial code. Intended to be used parametrically (many runs with parameters of the problem changed with each run, such as in a tip scan). Described in Chapter (3) and used in Chapters (4) and (7);
- **matlab-2d-classical**: Classical mechanics, and semiclassics, MATLAB code that runs trajectories in 2D mesoscopic-like systems. Can also do search for periodic orbits in a 2D potential. Used in Chapters (4), (5) and (7);
- **SemiclassicalBands.nb**: Mathematica code for computing the semiclassics of the magnetic billiard, used in Chapter (4); and
- **SemiclassicalFocussing.nb**: Mathematica code for computing the semiclassical hard-wall billiard model of tip scan imaging of the magnetic focussing experiment. The approach in layed out in Appendix (D) and used in Chapter (7).

Bibliography

[1] Sadhna K. Adhikari. Quantum scattering in two dimensions. *American Journal of Physics*, 54(4):362–367, April 1985.

[2] K. E. Aidala, R. E. Parrott, E. J. Heller, and R. M. Westervelt. Imaging electrons in a magnetic field. *Physica E, in press (available at http://arxiv.org/abs/cond-mat/0603035).*

[3] George Arfken. *Mathematical Methods for Physicists*. Academic Press, Inc., Harcourt Brace Jovanovich, Publishers, 3rd edition edition, 1985.

[4] V.I. Arnol'd. *Mathematical methods of classical mechanics*. Springer-Verlag, 1980.

[5] J.E. Avron, I.W. Herbst, and B. Simon. *Annals of Physics*, 114:431, 1978.

[6] M. Baranger, K.T.R. Davies, and J.H. Mahoney. *Annals of Physics*, 186:95, 1988.

[7] J. Bardeen. Tunnelling from a many-particle point of view. *Physical Review Letters*, 6(2):57–59, January 1961.

[8] A.H. Barnett, M. Blaauboer, A. Mody, and E.J. Heller. Mesoscopic scattering in the half plane: Squeezing conductance through a small hole. *Physical Review B*, 63:245312, June 2001.

[9] M.H. Beck, A. Jäckle, G.A. Worth, and H.-D. Meyer. The multiconfiguration time-dependent hartree (mctdh) method: a highly efficient algorithm for propagating wavepackets. *Physics Reports*, 324:1–105, 2000.

[10] C. W. J. Beenakker and H. van Houten. *Solid State Physics*, 44:1, 1991.

[11] M. Belloni, M.A. Doncheski, and R.W. Roberts. Exact results for 'bouncing' gaussian wave packets. *http://arxiv.org/abs/quant-ph/0408182*, 2004.

[12] Matthias Brack and Rajat K. Bhaduri. *Semiclassical Physics*, volume 96 of *Frontiers in Physics*. Addison Wesley Publishing Company, 1997.

[13] Lowell S. Brown and Gerald Gabrielse. Geonium theory: Physics of a single electron or ion in a penning trap. *Review of Modern Physics*, 58(1):233, 1985.

[14] M. Büttiker. Four-terminal phase-coherent conductance. *Physical Review Letters*, 57:1761, 1986.

[15] F. Calogero. *The Variable Phase Approach To Potential Scattering*. Academic Press, 1967.

[16] B.P. Carter. *Journal of Mathematical Physics*, 10:788, 1969.

[17] Hong Chen, J. J. Heremans, J. A. Peters, A. O. Govorov, N. Goel, S. J. Chung, and M. B. Santos. Spin-polarized reflection in a two-dimensional electron system. *Applied Physics Letters*, 86:032502, 2005.

[18] C.W. Clark and K.T. Taylor. *Journal of Physics B*, 13:L737, 1980.

[19] R. Crook, C. G. Smith, A. C. Graham, I. Farrer, H.E. Beere, and D. A. Ritchie. Imaging fractal conductance fluctuations and scarred wavefunctions in a quantum billiard. *Physical Review Letters*, 91:246803, 2003.

[20] R. Crook, C. G. Smith, M. Y. Simmons, and D. A. Ritchie. Imaging cyclotron orbits and scattering sites in a high mobility two-dimensional electron gas. *Physical Review B*, 62:5174, 2000.

[21] Supriyo Datta. *Electronic Transport in Mespscopic Systems*, volume 3 of *Cambridge Studies in Semicondicutor Physics and Microelectronics Engineering*. Cambridge University Press, first edition edition, 1995.

[22] D. Delande and J.C. Gay. *Physical Review Letters*, 57:2006, 1986.

[23] O. Dippel, P. Scmelcher, and L.S. Cederbaum. *Physical Review A*, 49:4415, 1994.

[24] V.V. Dodonov, I.A. Malkin, and V. Man'ko. The Green function of the stationary Schrödinger equation for a particle in a uniform magnetic field. 51:133–134, 1975.

[25] M.L. Du and J.B. Delos. *Physical Review A*, 38:1896, 1988.

[26] Daniel H. E. Dubin and T. M. O'Neil. *Rev. Mod. Phys.*, **71**:87, 1999.

[27] D. A. Wharam et al. *Journal of Physics C*, 21:L209, 1988.

[28] G. Gabrielse et. al. *Physics Letters B*, 507:1, 2001.

[29] G. Gabrielse et. al. *Physical Review Letters*, 89:213401, 2002.

[30] G. Gabrielse et. al. *Physical Review Letters*, 89:233401, 2002.

[31] G.Muller et al. *Physical Review Letters*, 75:2875, 1995.

[32] M. Amoretti et. al. *Nature (London)*, 419:456, 2002.

[33] T.M. Fromhold et al. *Physical Review Letters*, 72:2608, 1994.

[34] T.M. Fromhold et al. *Physical Review B*, 51:18029, 1995.

[35] P.O. Fedichev. *Physics Letters A*, 226:289, 1997.

[36] G. Finkelstein, P. I. Glicofridis, R. C. Ashoori, and M. Shayegan. Topographic mapping of the quantum Hall liquid using a few-electron bubble. *Science*, 289:90, 2000.

[37] J. A. Folk, R. M. Potok, C. M. Marcus, and V. Umansky. A gate-controlled bidirectional spin filter using quantum coherence. *Science*, 299, 2003.

[38] G. Gabrielse. *Fundamental Symmetries*, page 59. Plenum, New York, 1987.

[39] G. Gabrielse, S.L. Rolston, L. Haarsma, and W. Kells. *Physics Letters A*, 129:38, 1988.

[40] T. F. Gallagher. *Rydberg Atoms*. Cambridge University Press, New York, 1994.

[41] Barry M. Garraway and Kalle-Antti Suominen. Wave-packet dynamics: New physics and chemistry in femto-time. *Reports on Progress in Physics*, 58:365–419, 1995.

[42] M. Glinsky and T. O'Neil. *Physics of Fluids B*, 3:1279, 1991.

[43] B.E. Granger. Private communication, 2002.

[44] C. Grosche and F. Steiner. *Handbook of Feynmann Path Integrals*, volume 145 of *Springer Tracts in Modern Physics*. Springer, 1998.

[45] Martin C. Gutzwiller. *Chaos in Classical and Quantum Mechanics*, volume 1 of *Interdisc-plinary Applied Mathematics*. Springer-Verlag, 1990.

[46] E. J. Heller. Time-dependent variational approach to semiclassical dynamics. *J. Chem. Phys.*, 64:63, 1976.

[47] E.J. Heller. Bound-state eigenfunctions of classically chaotic hamiltonian systems: Scars of periodic orbits. *Physical Review Letters*, 53(16):1515, October 1984.

[48] E.J. Heller. *Proceedings of the 1989 Les Houches Summer School on "Chaos and Quantum Physics"*, chapter Semiclassical wave packet dynamics and chaos in quantum mechanics, pages 547–663. Elsevier Science Publishers B.V., North-Holland, 1991.

[49] E.J. Heller. Private communication, 2006.

[50] E.J. Heller, K.E. Aidala, B.J. Leroy, A.C. Bleszynski, A. Kalben, R.M. Westervelt, K.D. Maranowski, and A.C. Gossard. Thermal averages in a quantum point contact with a single coherent wave packet. *Nano Letters*, 5(7):1285–1292, 2005.

[51] Klaus Hornberger and Uzy Smilanksy. Magnetic edge states. *arKiv:nlin*, nlin(0201012v1):1–170, January 2002.

[52] W. Ihra, F. Mota-Furtado, and P. F. O'Mahony. Ionization of atoms in parallel electric and magnetic fields: The role of classical phase space. *Physical Review A*, 58(5):3884, November 1998.

[53] A. Jäckle and H.-D. Meyer. Time-dependent formulation of reactive flux employing complex absorbing potentials: General aspects and application within the multiconfiguration time-dependent hartree wave approach. *Journal of Chemical Physics*, 105(16):6778, October 1996.

[54] L. Kaplan and E.J. Heller. Measuring scars of periodic orbits. *Physical Review E*, 59(6):6609, June 1999.

[55] E.H. Kennard. Zur quantenmechanik einfacher bewegungstypen. *Zeitschrift für Physik*, 44:326–352, 1927.

[56] J. Könemann, P. König, T. Schmidt, E. McCann, Vladimir I. Fal'ko, and R.J. Haug. Correlation-function spectroscopy of inelastic lifetime in heavily doped gaas heterostructures. *Physical Review B*, 64:155314, 2001.

[57] Leo Kouwenhoven and Charles Marcus. Quantum dots. *Physics World*, 11:35, June 1998.

[58] Leo P. Kouwenhoven, Charles M. Marcus, Paul L. McEuen andSeigo Tarucha, Robert M. Westervelt, and Ned S. Wingreen. *Mesoscoic Electron Transport*, chapter Electron Transport in Quantum Dots. Proceedings of the Advanced Study Institute. Kluwer, 1997.

[59] Tobias Kramer. Personal Communication., 2006.

[60] Kenneth C. Kulander and Eric J. Heller. Time dependent formulation of polyatomic photofragmentation: Application to h3+. *Journal of Chemical Physics*, 69(6):2439–2449, September 1978.

[61] J.C. Lagarias, J. A. Reeds, M. H. Wright, and P. E. Wright. Convergence properties of the nelder-mead simplex method in low dimensions. *SIAM Journal of Optimization (as implemented in MATLAB R14)*, 9(1):112–147, 1998.

[62] L.D. Landau and E.M. Lifshitz. *Mechanics*. Pergamon Press, New York, 1976.

[63] L.D. Landau and E.M. Lifshitz. *Quantum mechanics : non-relativistic theory*. Pergamon Press, 3rd edition edition, 1991.

[64] R. Landauer. *IBM J. Res. Dev.*, 1:233, 1957.

[65] I.R. Lapidus. Quantum-mechanical scattering in two dimensions. *American Journal of Physics*, 50(1):45–47 45–47, January 1982.

[66] B. Lehnert. *Dynamics of Charged Particles*. Wiley, New York, 1964.

[67] B.J. LeRoy, M.A. Topinka, R.M. Westervelt, K.D. Maranowski, and A.C. Gossard. Imaging electron density in a two-dimensional electron gas. *Applied Physics Letters*, 80:4431, 2002.

[68] Brian J. Leroy. *Imaging Coherent Electron Flow Through Semiconductor Nanostructures*. PhD thesis, Harvard University, 2003.

[69] A.J. Lichtenberg and M.A. Lieberman. *Regular and Chaotic Dynamics*. Springer-Verlag, New York, 1994.

[70] R.G. Littlejohn. *Physics Reports*, 138:193, 1986.

[71] G. Littman, M.M. Kash, and D. Kleppner. *Physical Review Letters*, 41:103, 1978.

[72] J. Main, G. Wiebusch, A. Holle, and K.H. Welge. *Physical Review Letters*, 57:2789, 1986.

[73] C. M. Marcus, R. M. Westervelt, P. F. Hopkins, , and A. C. Gossard. Conductance fluctuations and quantum chaotic scattering in semiconductor microstructures. *Chaos*, 3(4):643–653, October 1993.

[74] C.M. Marcus, A.J. Rimberg, R.M. Westervelt, P.F. Hopkins, and A.C. Gossard. Conductance fluctuations and chaotic scattering in ballistic microstructures. *Physical Review Letters*, 69(3):506, July 1992.

[75] E. McCann and V.I. Falko. Parametric correlations of local density-of-states fluctuations in disordered pillars, wires, and films. *Journal of Physics C*, 13:6633–6648, 2001.

[76] Peter J. Mohr and Barry N. Taylor. *Review of Modern Physics*, 72:351, 2000.

[77] N. Moiseyev. Quantum theory of resonances: calculating energies, widths and cross-sections by complex scaling. *Physics Reports*, 302(5-6):211–293, 1998.

[78] E.E. Narimanov and A. Douglas Stone. Quantum chaos in quantum wells. *Physica D*, 131:221–246, 1999.

[79] E.E. Narimanov and A.D. Stone. Origin of strong scarring of wave functions in quantum wells in a tilted magnetic field. *Physical Review Letters*, 80(1):49, January 1998.

[80] E.E. Narimanov and A.D. Stone. Theory of the periodic orbits of a chaotic quantum well. *Physical Review B*, 57(16):9807, April 1998.

[81] E.E. Narimanov, A.D. Stone, and G.S. Boebinger. Semiclassical theory of magnetotransport through a chaotic quantum well. *Physical Review Letters*, 80(18):4024, May 1998.

[82] T.G. Northrop. *The Adiabatic Motion of Charged Particles*. Interscience, New York, 1963.

[83] M.C. Payne. Transfer hamiltonian description of resonant tunnelling. *Journal of Physics C*, 19:1145–1155, 1986.

[84] F.M. Penning. *Physics (Utrecht)*, 3:873, 1936.

[85] Aaron D. Peters, Charles Jaffé, and John B. Delos. Closed-orbit theory and the photodetachment cross section of H^- in parallel electric and magnetic fields. *Physical Review A*, 56(1):331, 1997.

[86] M. E. Portnoi and I. Galbraith. Variable-phase method and levinson's theorem in two dimensions: Application to a screened coulomb potential. *Solid State Communications*, 103(6):325–329, 1997.

[87] Klaus Richter. *Semiclassical theory of mesoscopic quantum systems*. Springer, New York, 2000.

[88] L. P. Rokhinson, V. Larkina, Y. B. Lyanda-Geller, L. N. Pfeiffer, and K. W. West. Spin separation in cyclotron motion. *Physical Review Letters*, 93:146601, 2004.

[89] P. Schmelcher and L.S. Cederbaum. *Comments Modern Physics D*, 2:123, 2000.

[90] T. Schmidt, R.J. Haug, V.I. Fal'ko, K.v. Klitzing, A. Förster, and H. Lüth. *Europhys. Lett.*, 36:61, 1996.

[91] T. Schmidt, R.J. Haug, V.I. Fal'ko, K.v. Klitzing, A. Förster, and H. Lüth. *Physical Review Letters*, 78:1540, 1997.

[92] Y. V. Sharvin and L. M. Fisher. Observation of focused electron beams in a metal. *JETP Letters - USSR*, 1:152, 1965.

[93] K.L. Shepard, M.L. Roukes, and B.P. Van der Gaag. Direct measurement of the transmission matrix of a mesoscopic conductor. *Physical Review Letters*, 68(17):2660, April 1992.

[94] G. A. Steele, R. C. Ashoori, L. N. Pfeiffer, and K. W. West. Imaging transport resonances in the quantum hall effect. *Physical Review Letters*, 95:136804, 2005.

[95] M. Stopa. Quantum dot self-consistent electronic structure and the coulomb blockade. *Physical Review B*, 54(19):13767, November 1996.

[96] Michael Stopa. Personal Communication., 2006.

[97] B. Su, V.J. Goldman, and J.E. Cunningham. *Physical Review B*, 46:7644, 1992.

[98] John R. Taylor. *Scattering Theory*. John Wiley & Sons, Inc., 1972.

[99] Steven Tomsovic and Eric J. Heller. Long-time semiclassical dynamics of chaos: The stadium billiard. *Physical Review E*, 47:282–299, January 1993.

[100] M. A. Topinka, E. J. Heller, and R. M. Westervelt. Imaging electron flow. *Physics Today*, 56:12, 2003.

[101] M. A. Topinka, B. J. LeRoy, R. M. Westervelt, S. E. J. Shaw, R. Fleischmann, E. J. Heller, K. D. Maranowski, and A. C. Gossard. Coherent branched flow in a two-dimensional electron gas. *Nature*, 410:183, 2001.

[102] M.A. Topinka, B.J. LeRoy, R.M. Westervelt, K.D. Maranowski, and A.C. Gossard. Imaging coherent electron wave flow in a two-dimensional electron gas. *Physica E*, 12:678, 2002.

[103] M.A. Topinka, B.J. LeRoy, R.M. Westervelt, S.E.J. Shaw, E.J. Heller, K.D. Maranowski, and A.C. Gossard. Imaging coherent electron flow from a quantum point contact. *Science*, 289:2323, 2000.

[104] Mark A. Topinka. *Imaging coherent electron wave flow through 2-D electron gas nanostructures*. PhD thesis, Harvard University, 2002.

[105] V.S. Tsoi. Focusing of electrons in a metal by a transverse magnetic field. *JETP Letters*, 19:70, 1974.

[106] Tsuyoshi Ueta. *Journal of the Physical Society of Japan*, 61:4314, 1992.

[107] Tsuyoshi Ueta. *Journal of the Physical Society of Japan*, 63:4506, 1994.

[108] Tsuyoshi Ueta. Quantum-mechanical study of electron focusing spectrum and quantized billiard model. *Journal of the Physical Society of Japan*, 64(12):4813–4823, 1995.

[109] Unidata. http://www.unidata.ucar.edu/software/netcdf/. Web Site.

[110] H. van Houten, C. W. J. Beenakker, J. G. Williamson, M. E. I. Broekaart, P. H. M. van Loosdrecht, B. J. van Wees, J. E. Mooij, C. T. Foxon, and J. J. Harris. Coherent electron focussing with quantum point contacts in a two-dimensional electron gas. *Physical Review B*, 39(12):8556–8575, April 1989.

[111] B. J. van Wees et al. *Physical Review Letters*, 60:848, 1988.

[112] Jiri Vanicek. *Uniform semiclassical methods and their applications*. PhD thesis, Harvard University, May 2003.

[113] D. Vrincineau, B.E. Granger, R. Parrott, H.R. Sadeghpour, L.S. Cederbaum, A. Mody, J. Tan, and G. Gabrielse. Strongly magnetized antihydrogen and its field ionization. *Physical Review Letters*, 92(13):133402–1, April 2004.

[114] P. B. Wilkinson, T. M. Fromhold, L. Eaves, F. W. Sheard, N. Miura, and T. Takamasu. Observation of 'scarred' wavefunctions in a quantum well with chaotic electron dynamics. *Nature (London)*, 380:608, 1996.

[115] A. Yacoby, H.F. Hess, T.A. Fulton, L.N. Pfeiffer, and K.W. West. Electrical imaging of the quantum hall state. *Solid State Communications*, 111:1, 1999.

[116] C. Zimmerman and T.W. Hänsch. *Hyperfine Interactions*, 76:47, 1993.

[117] D.M. Zumbuhl, C.M. Marcus, M.P.Hanson, and A.C. Gossard. Asymmetry of nonlinear transport and electron interactions in quantum dots. *arXiv:cond-mat*, (0508766v1):1–4, August 2005.